SAPIENZA
UNIVERSITÀ DI ROMA

Neutrino emission via proton-proton interaction and magnetic field screening in GRBs

Università di Roma “La Sapienza”, Dipartimento di Fisica

Dottorato di Ricerca in Astrofisica Relativistica, IRAP Ph.D. – XXXII Ciclo

Candidate

Stefano Campion
ID number 1344868

Thesis Advisor

Prof. Ruffini Remo

Co-Advisor

Prof. Rueda Hernandez Jorge Armando

15 February 2021

Thesis defended on 15 February 2021
in front of a Board of Examiners composed by:

Prof. De Bernardis Paolo (chairman)

Prof. Longo Francesco

Prof. Della Valle Massimo

The external evaluators of the thesis:

Prof. Pittori Carlotta

Prof. Araudo Anabella

Neutrino emission via proton-proton interaction and magnetic field screening in GRBs
Ph.D. thesis. Sapienza – University of Rome
ISBN: 000000000-0

This thesis has been typeset by LaTeX and the Sapthesis class.

Version: February 10, 2021

Author's email: stefano.campion@uniroma1.it

To my sister, Serena

“And as her image
Wandered through my head
I wept just like a baby
As I lay awake in bed
And I know what it’s like
To lose someone you love
And this felt just the same”

Dream Theater, “Through her eyes”

Abstract

Gamma-Ray Bursts (GRBs) are one of the most energetic astrophysical events of our Universe and a precise study of all the physical mechanisms occuring in these systems involves different branches of physics (from particles physics to General Relativity). The main subjects of this thesis concern the particles physics and the plasma physics fields. I study two different physical processes, operated by elementary particles as protons, electron/positron paris, photons and neutrinos, occuring in GRBs.

In Ch. (1) I give a general introduction to GRBs, with some of their structural physical generalities and properties (as their different emission phases, spectral and temporal properties etc.). I introduce also the *fireshell model*, which has been developed during the years by Prof. Ruffini, R. and his group, in order to study and understand the several mechanisms behind the GRB emission. I will also highlight the principal differences between this model and the *fireball model* (which was the first model adopted in order to study the GRBs emission).
The structure of the fireshell model considers a Reissner-Nordoström Black Hole, with a strong electric field that converts part of the BH total energy in e^+e^- plasma by the vacuum polarization process. These particles are accelerated and emit photons, and this leads to the formation of a relativistic optically thin fireshell of $e^+e^-\gamma$ plasma (the "PEM–pulse"). This shell interacts with baryons, deposited in the ambient near the BH due to the collapse event, forming a new accelerated optically thick plasma of $e^+e^-\gamma$-baryons (PEMB–pulse). The transparency of this shell brings to the formation of the *proper* GRB emission (P-GRB emission).

In Ch. (2) I introduce a classification of the GRBs in classes and subclasses. They differ from each other principally for their different progenitors, formation process, their isotropic energy $E_{\rm iso}$, their rest-frame spectral peak energy $E_{p,i}$ and local observed rate.
In the Thesis, I have focused my attention principally on a particular type of long GRB class: the type I Binary-driven HyperNova (BdHN). The physical scenario and process, that leads to the formation of the BdHN class, is the *Induced Gravitational Collapse* (IGC), with the *hypercritical accretion process* paradigm. The two original studies of the Thesis, developed in Chs. (3) and (4), are based on the physical scenario of BdHN. In this chapter, I also show the connections between the several observations of a GRB event and the basic processes of the BdHN model.

In Ch. (3), the first topic of the Thesis is presented, namely the neutrinos and photons production by proton-proton interaction, between accelerated protons and protons at rest. Keeping in mind the above discussed scenario for the dynamics of the $e^+e^-\gamma$-baryons plasma, recent numerical simulations have shown that the SN ejecta becomes highly asymmetric. Therefore, the electron-positron ($e^\pm$) plasma created in the BH formation, during its isotropic and self-accelerating expansion, engulfs different amounts of ejecta baryons along different directions, leading to a direction-dependent Lorentz factor. In this configuration, I have studied the pp interaction occurring in two regions: an high density region and a low density region. In the conclusion of this chapter I also try to give an estimate of a possible, direct or indirect, detection of the neutrinos and photons created throught the above mechanism. From this analysis it came out that a possible detection of these neutrinos with currently operating detectors is plausible only for sources several order of magnitude more energetic than the ones considered in this work, and very-high energy ineracting protons (this subject is treated in App. (D) and will be better developed in future works). It also came out that an indirect detection of these neutrinos by means of the related photons emission is possible.

The second subject of the Thesis is presented in Ch. (4) and concerns the study of the screening process of an electromagnetic field near a BH operated by electron-positron pairs. It has been shown that a rotating BH immersed in a test background magnetic field, of initial strength B_0 and aligned parallel to the BH rotation axis, generates an induced electric field, whose strength is proportional to the background magnetic field, $E = 1/2\ \Upsilon B$ (where Υ is the BH spin parameter). In this analysis, I consider the configuration of crossed fields: $\mathbf{B} = B\hat{z}$ and $\mathbf{E} = E\hat{y}$. In this system, an huge number of e^+e^- pairs can

be emitted by vacuum polarization process, start to be accelerated to high energies by the induced electric field and emit synchrotron photons. These photons interact with the magnetic field via the magnetic pair production process (MPP): $\gamma + B \rightarrow e^+ + e^-$. The motion of all these particles around the magnetic field lines generates also an induced magnetic field oriented in the opposite direction to the background one, which implies a reduction of the background magnetic field. The principal results are that the combination of the processes described above can reduce the magnetic field in a small time scale, even if the production of pairs is not so efficient due to the low energy of the emitted photons, for the selected initial conditions of the field strengths and particles densities.

Acknowledgments

I express my gratitude to my Master degree thesis advisor Prof. Merafina MArco for directed me to the IRAP-PhD program. In particular, I would like to express my gratitude to Prof. Ruffini Remo and to the International Center for Relativistic Astrophysics Network (ICRANeT) for offered me the opportunity to get the Ph. D. degree, to work with them and for his financial support.

I would like to thank especially the brilliant Prof. Jorge Armando Rueda Hernandez, for standing me, for supporting me and because he has been a guide during my Ph. D. course. His wide knowledge of phsyics and astrophysics was precious for the development of my work and made me grow as a scientist. It has been a pleasure to work with him.

I would like to thank to the Profs. SheSheng Xue and Vereshchagin Gregory (in the ICRANeT center of Pescara, Italy) for the discussions about the magnetic field screening process and Prof. SheSheng also for his help in the final part of the PhD., even if not directly related to the Thesis. I also would like to thank the secretaries, administators and system manager of this center, respectively: Cesare, Cinzia, Elisabetta, Silvia, Cristina and Gabriele.

I want also to thank much for their helpfulness and time they spent to read and evaluate my Thesis, for their suggestions and comments, the external referees: Prof. Pittori Carlotta and Prof. Araudo Anabella. Thanks to their suggestions, the Thesis has much improved.

During the years of this Ph. D. I met many great students and researchers. It has been important for me to meet good people from different cultures and from all over the world, to spend time and good moments with them. I would like to thank Dr. Melon Fucksman David and, in particular, Dr. Aimuratov Yerlan and Dr. Tychengulova Aliya for their friendship. I also thank Yerlan for the permission that he gave me to use part of his Thesis for the development of part of chapter I of my Thesis.

I am not able to express with words my gratitude, my affection and my love to my girlfriend Ezgi Soylan, maybe just a "thanks for her love" says much more than I am able to express.

A special thanks is devoted to my closest friends: Fabrizio Orsini, Laura Marceddu, Danio Vona, Emanuele Ermanni, Matteo Boezi, Roberto Cotesta, Francesco Bucciarelli. They have always played an important part in my life and they have always been close to me, in good moments and in all the difficult moments of my life. My gratitude and my affection to them goes beyond these simple words.
I would like to thank my friends Dr. Altilio Rosa, Dr. Riccardo Eugenia, Vittoria Pagani, Francesca Campanile, Andrea Ciotti and Ludovica Benedetti, for their friendship and for being close to me in the most difficult moment of my life.

A special thanks is also devoted also to my close friends Daniele Racanelli, Dr. Calvanese Strinati Marcello and Giovanni Taietta. I met them in the beginning of my university career eleven years ago and, since this graduation corresponds to the end of this part of my life, I would like to thank them for their freindship during all these years. A special thanks is also dedicated to my dear friend Kim Valerie, for her beauty.

My infinite gratitude and invaluable thanks goes to Loris, for making me become who I am.

Last but not least, I would like also to thank my mother, my brother and my grandparents for their affection.

List of Tables

List of Figures

List of Publications

Journal Articles

Submitted

- Campion, S., Melon Fuksman, J. D. & Rueda, J. A., Neutrino production from proton-proton interactions in binary-driven hypernovae, ArXiv preprint:1910.10439C (2019) (submitted to *Physical Review D*);

- Campion, S., Rueda, J. A., Xue, S. S. & Ruffini, R., On the magnetic field screening in strong crossed electromagnetic fields, (presented on the 4^{th} Zeldovich meeting in September 2020 and will appear in *Astronomy Reports* as part of the Conference report)

Preprints

- Campion, S., Rueda, J. A., Xue, S.S. & Ruffini, R., Magnetic field screening process in a Kerr Black Hole, ArXiv preprint arxiv:2002.11681C (2020);

- R. Ruffini, Liang Li, R. Moradi, J.A. Rueda, Yu Wang, S.S. Xue, C.L. Bianco, S. Campion, J.D. Melon Fuksman, C. Cherubini, S. Filippi, M. Karlica, N. Sahakyan, Self-similarity and power-laws in GRB 190114C, ArXiv preprint:1904.04162R.

Contents

Introduction

Gamma-ray Bursts (GRBs) are one of the most energetically powerful events in our Universe and they are the breeding ground of many physical processes that correlate several branches of physics: General Relativity (GR), High Energy Particles Physics (HEP), Fields Theory (FT), High Energy Astrophysics (HEA) and Plasma Physics. In these events, indeed, the presence of Black Holes (BHs, hereafter), surrounded by plasma of matter particles and radiation, gives rise to a plethora of phenomena of different nature which correlate all of those branches of physics. This Thesis explore the connection between a few of these fields.

The elaborate is based on the work that I have developed during my Ph.D. course. It is divided in two principal themes: 1) in the first part of my Ph.D. I studied the neutrino emission via the proton-proton (pp) interaction mechanism between accelerated protons and protons at rest present in a region with high (low) matter density inside (outside) the GRB site (developed in Ch. (3)); 2) in the second part of the Ph.D. I focused my attention to the screening process of an electromagnetic field near a BH operated by accelerated electron-positron pairs emerging from the BH (developed in Ch. (4)).

In Ch. (1) I expose some generalities and features (spectral, temporal etc) of GRBs. I will give an overview the "*fireshell model*" for GRBs introduced and developed by Prof. Ruffini, R. and his group during the last twenty years. A few characteristics and mechanisms of this model are exposed and, also, the salient differences compared to the old traditional "*fireball model*". The *fireshell model* is the physical framework over which this group built, and improved during the years, a wide range of binary system models in order to explain the observed differences in the GRBs spectra and light curves.

In Ch. (2) I start to introduce the series of GRBs classes and subclasses, introduced by Prof. Ruffini, R. *et al.*. The classification is principally based on: the GRB progenitors, the Out-State, the peak energy of the prompt emission $E_{p,i}$ (MeV), the isotropic Gamma-ray energy $E_{\rm iso}$ (erg), the isotropic emission of ultra-high energy photons (GeV), $E_{\rm iso,\ GeV}$ (erg) and their local observed rate $\rho_{\rm GRB}$ $\left(\mathrm{Gpc}^{-3}\ \mathrm{yr}^{-1}\right)$. The principal features and physical mechanisms of *induced gravitational collapse scenario* (IGC hereafter) are exposed. This scenario was introduced by the group in order to explain the formation of the binary systems which leads to the different stages of the GRB emission. Consequently, I will introduce the BdHNe systems emerging from the IGC scenario, that constitutes the basic model upon which this Thesis is developed. The final part of this chapter is devoted to the connection between the physical processes of the BdHNe framework and the observational counterparts detected at Earth.

In Ch. (3) the problem of photons γ and neutrino ν emission via the decay of neutral and charged $\pi-$mesons and $\mu-$lepton emerging from proton-proton (pp) interaction is considered. Due to the asymmetry of the matter around the BH (the SN-ejecta, as I will explain in Ch. (2)), in the equatorial plane of the system (the orbital plane of the BH+NS system) there are regions with a high and low matter density. In this scenario, I study the pp interaction, occurring in the equatorial plane, in the following two cases: 1) the interaction occurs when a relativistic plasma of leptons and radiation, accelerated by the BH electric field, impacts on baryons at rest positioned surrounding the BH (at a distance $r \sim 10^{10}$ cm from the BH site), the so called Circum-Burst Medium, CBM, which is characterized by a high particles number density ($n_h \simeq 10^{23}$ particle/cm^{-3}). The plasma swallows up (with a baryon load $B \equiv M_b c^2/E_{e^+e^-} = 51.75$, where M_b is the expelled ejecta mass and $E_{e^+e^-}$ is the e^+e^- isotropic energy) and accelerate protons that impact, at

every radius, with the protons at rest (in the laboratory frame) ahead of the plasma front. The energy of the interacting protons is not so high (the proton Lorentz factor varies between $2 \leq \gamma_p \leq 6$ inside the impact region), but enough to overcome the meson production threshold and to produce photons and neutrinos by $\pi-$mesons and $\mu-$leptons decay; 2) differently from the first case, in this second case the interaction occurs far from the BH site, where the target baryons are the component of the InterStellar Medium (ISM) (at a distance from the BH site of $10^{16} < r < 10^{17}$ cm), which has small particles number density ($n_h = 1$ particle/cm^3). Here the interacting particles are the protons charged by the leptonic-radiation plasma, when it expands in the region with low matter density near the BH (with a baryon load $B = 10^{-3}$). In this case, the interacting protons acquire a Lorentz factor of $\Gamma \sim 10^3$, which leads to the production of GeV or TeV photons and neutrinos when they interact with the ISM target protons.

In Ch. (4) the screening process of an electromagnetic field near a BH is studied. I consider the physical system where a rotating BH is immersed in a background strong magnetic field of strength $B_0 \sim 10^{14}$ Gauss. It is well known (see [152]) that a rotating BH immersed in a background magnetic field [1] generates an induced electric field on the BH, that is proportional to the parent magnetic field (at least in a region close to the BH horizon) (see [130, 136, 105]). In these conditions, I consider the interaction between photons (emitted by already existing electron/positron pairs created via the vacuum polarization process, which are accelerated by the electric field, principally through curvature/synchro-curvature/synchrotron processes) and the magnetic field, which generate an electron-positron pair through the *magnetic pair production* process (MPP hereafter), $\gamma + B \rightarrow e^- e^+$. These pairs are accelerated due to the presence of the induced electric field, positrons are accelerated outward, while electrons inward (or vice versa depending on the induced electric field direction). The motion of the pairs around the magnetic field lines leads to the creation of an induced magnetic field, in the direction opposite to the background one. Consequently there is a reduction of the total magnetic field and, due to their proportionality, of the induced electric field too (even if the physical reasons for the decrease of the two fields are different). This process will end when: 1) the magnetic field is reduced enough in such a way that the MPP cross-section σ_{MPP} is too low and the pairs creation stops; 2) because of the electromagnetic field reduction, the already existing pairs are not even more accelerated and will radiate all of their energy.
This process can be fundamental to understand the emissions of a GRB, since in a strong magnetic field photons are trapped inside the system. If the magnetic field reduces its strength, the transparency conditions are reached and photons will be free to escape from the region. Then, this process can be important to understand the different emissions of GRBs from both energetic and temporal point of view.

In Ch. (5) I summarize the principal results and the conclusions of the works developed and presented in this Thesis.

After Ch. (5), a large number of appendixes are also included. In these appendixes are reported all the calculations related to the works developed in Chs. (3) and (4), as the parameterization for the pp cross-sections, particles spectra, kinematic limits for particles or the basic calculations for the development of future works. The appendices from App. (A) to App. (E) are related to the work developed in Ch. (3), while the appendices from App. (F) to App. (H) are related to the work developed in Ch. (4). In particular:

- In App. (A) I report the proton-proton cross-section (from [25]), for the case of low energetic interacting protons, that I will use in the first part of Ch. (3).
- In App. (B), the calculations of the kinematic limits for the daughter particles (muonic and electronic νs and photons) emerging from the pp interactions, namely $\pi-$mesons, $\mu-$leptons, are reported.
- The structure of the spectra for the daughter particles emerging from pp interaction (from [70]), that I will use in the second part of Ch. (3), are shown in App. (C).

[1] The study developed in this chapter it has to be considered applied to the BdHN model, whose characteristics are widely explained in the Ch. (2). As will be explained in that chapter, these are binary systems composed by a SuperNovae (SN) (that, after the explosion, becomes a neutron star) and a companion neutron star (NS) that, after an accreation process of the material expelled by the SN, collapses in a BH. The cited background magnetic field derived by the old magnetized collapsed NS.

- In App. (D) I give only an introduction to the problem of photons/neutrinos production via the pp interaction, for the case of very high energy protons ($E_p \sim 10^{21}$ eV) when they are emitted along the BH rotation axis and interact with the ISM protons. This is only a preliminary study for the considered interaction in this specific configuration, since the parameterization nor for the daughter particles spectra nor for the pp cross-section for these very high energetic protons is not known yet. I just wanted to provide an order of magnitude for the energy and flux of the daughter particles.

- In order to understand if we are able to detect the photons created by the π^0 decay, created via the pp interaction studied in Ch. (3) and App. (D), in App. (E) I calculate the probability of the possible interactions between these photons with protons, electrons and positrons in the considered different physical conditions.

- In App. (F) I show all the calculations necessary to relate the momentum of a photon (emitted by the pairs) in the *rest frame* of the emitting electrons, with the photon momentum received by an observer at rest at infinity, *laboratory frame*. This calculation is necessary in order to get the right expression for the magnetic pair production rate, for the study of the screening process in Ch. (4).

- In App. (G) I give only an overview on the equations that need to be used in order to study the screening process for two other configurations of the magnetic and electric field: 1) parallel fields (oriented along the $z-$direction); 2) when an angle is present between the direction of the two fields ($\vec{B}$ is oriented along the $z-$axis, while $\vec{E}$ lies on the $y-z$ plane). These further studies will be developed in future works.

- In App. (H) I report the preliminary study that I developed concerning the magnetic field screening. Notwithstanding the differences in the expression of the equations and in some assumptions, compared to the right one exposed in Ch. (4), this study has been important to better understand the approach to the problem and its analytical formulation.

Chapter 1

Introduction on Gamma-Ray-Bursts and to the *fireshell* model

In this chapter we introduce the Gamma-Ray-Bursts (GRBs hereafter), one of the most energetic and powerful event of our Universe. In Sec. (1.1) we describe some general features of GRBs, from their temporal properties to the spectral one.

In Sec. (1.2) we give the description of the different phases of a GRB event and its observational counterparts (*precursor* emission, *prompt* emission, *afterglow* emission): we focus and expose the "*fireshell*" model, under the *induced gravitational collapse* scenario (that we will analyze in Ch. (2)), for the explanation of the *prompt* phase. This model was formulated by Ruffini *et al.* in a series of papers [116, 115, 114], in contrast with the *fireball* model, which presents a few incongruences with the data. The fireshell is based on physical processes of energy extraction from a black hole, already known and developed in 1970s [28, 36], where the black hole was used as a central engine to power the GRB emission.

We will dedicate a subsection for the explanation of the dynamic of a (initially) leptonic plasma, created via the process of energy extraction from a BH, in self-acceleration that passes through a region filled by matter expelled by a SN-event. The expansion inside this medium will gives rise to the *prompt* phase and part of the *afterglow*. Instead, the *precursor* emission originates from the explosion of that SN and the consequently accretion on the companion star.

Part of the next section on the general properties of *gamma-ray bursts* is based on the Aimuratov Yerlan Ph. D. thesis [13].

1.1 Common GRB features

As we stated above, the GRBs are one of the most energetic astrophysical events in the entire Universe. On Earth, the event of a GRB consists in a series of radiation impulses, which span a wide range of energies: from the optical to the X-ray, from $\gamma-$ray to the GeV emission. These several radiations emerge from distinct physical processes occurring at different time intervals. In this chapter we briefly present the physical processes behind all of these radiations (and we will refer the reader to the specified papers), basing our exposition within the framework of BdHNe family for GRBs.

Some basic general characteristics of GRBs are:

- they can last from fractions of a second to thousands of seconds [11]. Consequently, they are classified as transient sources;
- they all occur at cosmological distances, usually between redshift $0.0085 \lesssim z \lesssim 9.4$ (at least for the already known sources). Then, we can surely say that they have a cosmological origin.

- they all have an incredibly high energy emission $10^{46} \lesssim E_{iso} \lesssim 10^{55}$ erg, where different values depend on the different classes of GRBs (see the next chapter);
- notwithstanding there are of a few theoretical models that try to explain GRBs, they all share, as common feature, the presence of compact astrophysical systems and strong events with almost the same actors on scene: the event of Super-Novae (SN) explosion, neutron stars (NSs), pulsars, white dwarfs (WD) or Black Hole (BH) formation, merging between one of the previous components, (highly or midly)-relativistic jets of particles;

These features are mostly common to all GRBs and their values differ correspondingly to the different classes of GRBs. In Ch. (2), we will introduce a series of subclasses of GRBs and their characteristics within the theoretical framework of the "*fireshell*" model.

During the years, from the first discovery of a Gamma-Ray Brust phenomenon made it by the *Vela* satellite in 1967 [73] until today, the observations of these events (made it by different satellites and detectors as: the *Burst and Transient Source Experiment* (BATSE) instrument [44] onboard of *Compton Gamma-Ray Observatory*, the *Large Area Telescope* (LAT), *AGILE*, *Fermi*-GBM and others) highlight some temporal and spectral features common to all the GRBs. In the following paragraphs we describe some of their common temporal and spectral characteristics.

Temporal properties

Little by little the number of GRBs detection increased during the last 50 th years, astrophysicist tried to define a classification of these events. It grew up the evidence of a separation based on the total duration of the event, the latter defined as the time from onset of the burst to the latest time when a significant flux is detected, of a temporal *bimodal* nature of GRB (see Mazets et al. (1981) [81]). The temporal separation between the two modes has been seen to occurs at ≈ 2 s from the trigger ([44, 55]). This classification was corroborated by a spectral counterpart based on the *spectral hardness ratio*. Furthermore, a parameter connecting these two evidences has been established to account for this bimodal property: the T_{90} defined as the time during which the cumulative counts increase from 5% to 95% above the background level. Thus, the period of time of the event encompasses 90% of the total counts became an intensity-independent measure of the duration of the event itself.

Notwithstanding the above properties, GRBs present different temporal structures. The light curve varies from event to event and there are no typical time profile. But the time profiles exhibit an overlapping behaviour with multiple peaks and statistically significant fine structure on milliseconds time scale.

In accordance with the temporal characteristic stated above, a GRB event can be divided in two main phases: the *prompt* and the *afterglow*. The *prompt* phase includes the majority of the energy release detected by the instrument in the keV–MeV range. The *afterglow* phase is active in the eV–keV and MeV–GeV ranges, but is less energetic than the prompt and it is associated to the counterparts of first phase.

Not all the bursts present a *precursor* phase. This phase is characterized by a weak excess of photons before, from a few to hundred of seconds ([76]), the main energetic episode. Even if the mechanism generating the precursor phase is still not completely clear, it came out that they are tightly connected to the main event, but just a proportionality factor less energetic than the entire burst and, probably, they derive from the formation event which brings to the system generating the other two emissions.

Spectral properties

Notwithstanding the temporal profiles of GRBs differ from one to another, the spectral behaviour presents some common features. Indeed, analyzing the spectra of all the bursts during the decades, it came out the evidence of a similar spectral behaviour. Despite their emission across the entire electromagnetic spectrum, the *Spectral Energy Distribution* (SED, or spectrum) shape of a typical GRB implies that most

of the energy is received in γ-rays. The SED shows the intensity of radiation over a range of energies and it is usually represented in a plot as $\log\left(E^2 \frac{dN}{dE}\right)$ *vs* $\log(E)$ in units of $[\,\mathrm{erg}\cdot\mathrm{cm}^{-2}\cdot\mathrm{s}^{-1}\cdot]$.

The spectra [1] of gamma-ray bursts are similar in shape with energy distribution having a prominent peak though not fixed to particular value and varies around 1 MeV, after correcting for the $(1+z)$ cosmological redshift [68, 56]. There is also a trend for bursts of higher luminosity to have a higher value for E_{peak}. The spectra are highly variable in time and have a complex variability. The SED are the hardest initially and soften to later phases, the hard-to-soft spectral evolution. The shape of the spectra differs significantly depending on the energy domain and tends to be a power law at high energies and almost exponential at low energies. Thus, the burst spectra have been typically modeled as a power-law times an exponential cut-off at low energy, $N_E(E) \propto E^{\alpha}\exp(-E/E_0)$, and a power-law at high energies, $N_E(E) \propto E^{\beta}$, with $\alpha > \beta$. Then, the shape of the spectra cannot be represented by a single simple law.

The GRB spectra are described by several observational characteristics. Among them there are the *Energy Fluence* in units of $[\,\mathrm{erg\ cm}^{-2}]$, the *Peak Energy Flux* in units of $[\,\mathrm{erg\ cm}^{-2}\ \mathrm{s}^{-1}]$ and *Spectral Hardness*. They define many properties, tell immediately how intense is a given event and, together with a redshift and a total duration, serve to derive the energy component of the emission. Therefore these values become essential in any spectral catalog of bursts.

These observational characteristics are useful to understand the physical mechanisms behind the emission itself. Then, one needs to look at the physical processes acted by high-energetic particles emitted in the system and how these processes emit a radiative counterpart.

Radiative processes in astrophysics concern the particles acceleration, deceleration and deviation of their trajectories. The principal radiative processes for a particle in relativistic or ultra-relativistic motion are: Compton scattering (due to the scattering of a low energy photon on a charged particle), Inverse Compton scattering (when the charged particle and the photon have comparable energy), Synchrotron emission (the radiation emitted by a relativistic charged particle immersed in a magnetic field), Bremsstrahlung (radiation due to the acceleration of a charge in the Coulomb field of another charge). For a complete description of these processes see, *i.e.*, [138, 75]. Then, if an observer at Earth is able to catch the right energy of the emitted photons by the source and the energy distribution of the arrival photons, he would be able to understand their producing mechanisms and, then, get informations about the physical hidden system behind them [2]

In order to reproduce the GRB spectrum one needs to make a few assumptions for the principal and characterizing physical quantities (as the energy and spatial distribution of the emitting particles, the configuration of the electric and magnetic fields and so on) and put boundary conditions (or, at least, initial conditions). The most used assumption for these type of sources concern the dynamic of the particles. They are described moving as a relativistic, or midly-relativistic, plasma. Usually this plasma is considered to be in self-acceleration and the radiation is emitted by different interactions inside or by this plasma (as particles interaction, the acceleration itself, the mutual interaction between shells with different velocities and interaction between this plasma and the external material ahead of it). The above mechanisms, once applied to the plasma dynamic, allow us to construct the theoretical energy spectrum and compare it with the observative one.

Then, the whole typical broad-band spectrum of a GRB, in prompt phase, can be synthetically repoduced by three components: two non-thermal components (one is a cut-off power-law (CPL), while the other one is a power-law (PL)) and a thermal one (usually a black-body, BB). Usually the PL component serves for extension of the distribution to high energies. The BB component cannot explain the whole spectrum, but it has been found that it can significantly contribute for a large amount of energy [139, 140].

[1] Here we talk about continuum spectra with no features of emission/absorption lines.

[2] For "right energy of photons" I mean that, since every cited process have a specific photons spectrum, with its peak or flat regions (as for the Synchrotron or Bremsstrahlung), if we consider the best conditions and, then, only the peak energy of the photons spectrum (with a correction due to the cosmological distance), detecting these photons or part of the spectrum, we are able discriminate which process produced them.

This is a schematization of the complete GRB spectrum of the prompt+high energy phases. On the other end, the light-curve of the prompt phase consists of several peaks of different intensity and duration forming a unique pattern for every event. In order to see from where these radiative peaks come from, one needs to study each peaks looking at the specific particle physical mechanism producing this radiation.

The *afterglow phase* of a GRB is an important trace of the event [3], comparable with the *prompt* phase. This phase occurs after the *prompt* emission and it extends in a wide range of wavelengths: from optical to radio, from X- and $\gamma-$ray to high-energy emission. Notwithstanding this phase covers a wide range of the electromagnetic spectrum, it is usual to refer to the *afterglow* phase as it X-ray band emission.
In Fig. (1.1) we show a typical example of an afterglow detected by *Swift* telescope for the GRB 090510. The top panel show the *Swift*-XRT afterglow spectrum, in normalized counts per second per keV, for the *Photon Counting* mode (PC, the red curve) and the *Window Timing* mode (WT, the blue curve). The bottom panel, show the *Swift*-XRT light curve for the same GRB. It is shown the flux in $\left[\mathrm{erg/cm^2/s}\right]$ as a function of time sicne the BAT trigger.

The characteristic equation describing the afterglow flux density is $F_\nu(t,\nu) \propto t^{-\alpha}\nu^{-\beta}$, where indices α and β denote the *temporal decay* rate and *spectral index*, respectively. Consequently, each episode of X-ray afterglow is defined by range of index values typical for it. The *afterglow* light curve can be described by three power-law plus two other components. They are divided as a *steep* decay, a *plateau*, a *flare*, *normal* decay and *late* decay. A common feature of the *afterglow* phase is the time separation of the optical observation in "early" and "late" time afterglow. This separation is corroborated by temporal and spectral proprieties of the received radiation. Spectra of late time of optical radiation can be fitted by a simple power-law, with spectral index ~ -1 and follows a gradual decay trend. The late time emission most probably represents an environment where the GRB is placed and what initial high energy plasma and photons interacts with in order to be re-emitted in the form of low energy optical afterglow. The early afterglows (the first few hours post-trigger) show an active energy release through optical flares, some of which are claimed to correlate with ones of X-ray and even γ-ray bands.

The others energy band of the *afterglow* consist in the *radio* and in the *high-energy* emission. The *radio* emission can last from hours to years after the first detection of the event. This radiation is thought to originate in the ambient of the GRB, has a fast rising and a later decay as a power-law. The percentage of GRBs with radio *afterglow* is$\sim$ 30%. The *high-energy* emission concerns photons energies from MeV to GeV, with an arrival delay, in regard to the prompt, of the order 10^3 s (or more). This high-energetic component of the afterglow has a very low counting rate and the physical reason of this emission is still matter of debate.

1.2 Fireshell model for GRBs

The "*fireshell*" model was proposed by Prof. Ruffini, R. *et al.* in a series of papers ([116, 115, 114]) in order to describe the physical process behind the *prompt* emission of GRBs. This model is proposed in contrast to the "*fireball*" model (see [159]), usually adopted for the description of the GRBs. This traditional model presents some inconsistencies with respect to the GRB data. We will discuss in the introduction of Ch. (2) about the problems of the fireball model, which brought to the introduction of this fireshell model and the induced gravitational collapse scenario, that we will discuss in the same chapter.

The structure of the fireshell model considers a Reissner-Nordoström Black Hole, where a strong electric field is present and converts part of the BH total energy in e^+e^- plasma by the vacuum polarization process. This energy extraction process corresponds to the energy source of the GRB. After the pairs creation, the plasma of electron-positron and photons (called PEM–pulse, see below) forms an optically thin fireshell which accelerates and expands relativistically. This shell interacts with baryons, deposited in the ambient near the BH due to the collapse of the progenitor star (the SN-explosion). These baryons are

[3] It is thanks to the afterglow that we are able to determine the redshift of the GRBs.

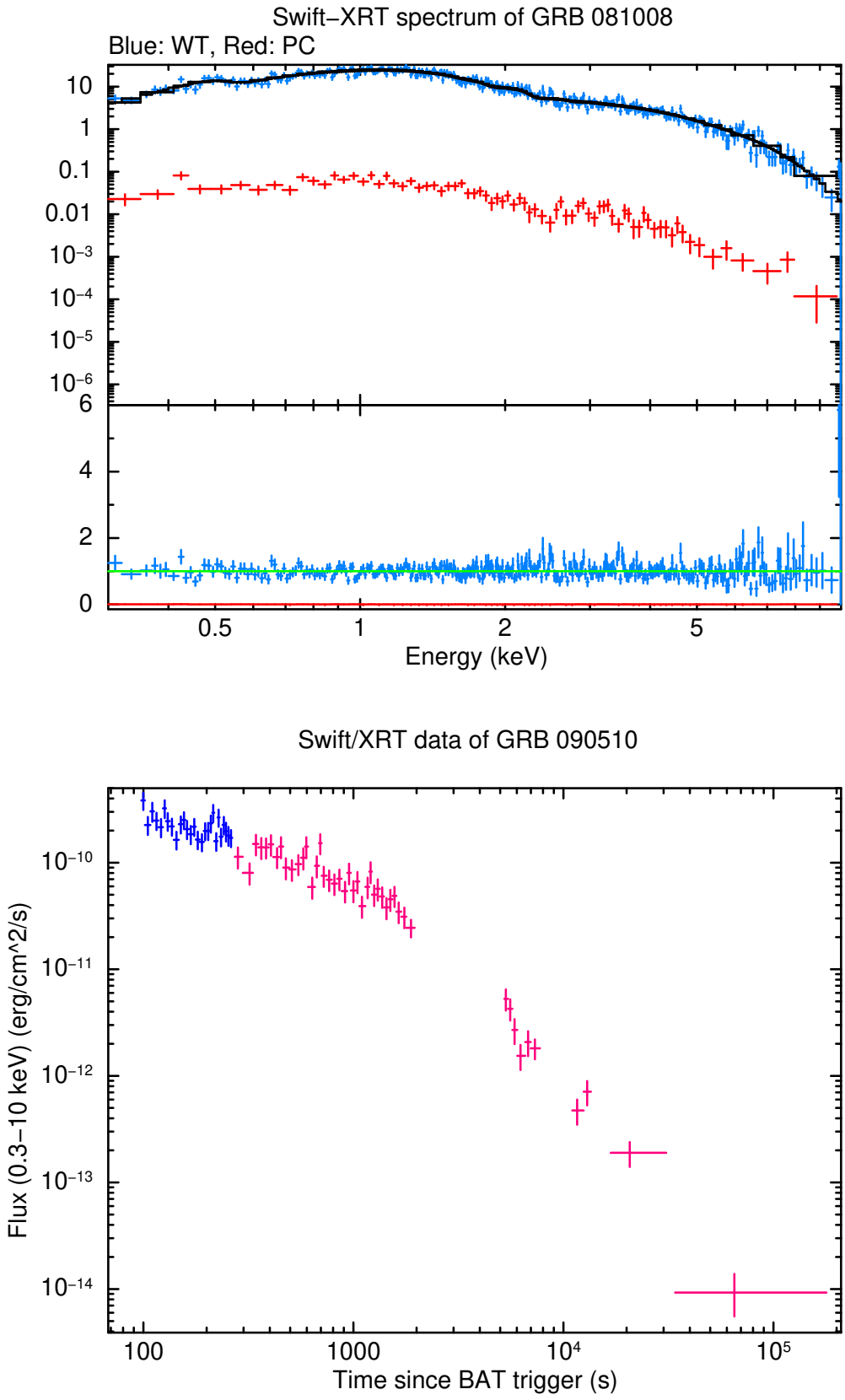

Figure 1.1. Example of afterglow detected by *Swift* telescope for the GRB 090510. **Top panel:** *Swift*-XRT afterglow spectrum, in normalized counts per second per keV, for the PC mode (the red curve) and the WT mode (the blue curve). **Bottom panel:** *Swift*-XRT light curve for the same GRB. The flux, in $\left[\mathrm{erg/cm^2/s}\right]$, is shown as a function of time sicne the BAT trigger.

swallowed up by the PEM and a new optically thick plasma of e^+-e^--γ-baryons (PEMB–pulse) is created and starts again to accelerate. The transparency of this shell leads to the formation of the *proper* GRB emission (P-GRB emission). In the next section we describe briefly these dynamics acting in the fireshell model.

1.2.1 Dynamic of the Fireshells

In the fireshell model, the creation of e^+e^- pairs via vacuum polarization is the physical engine of the GRB, whose occurence is due to the presence of a strong electric field of a Kerr-Newman Black Hole ([72]; [89]; [102]; [36]). The Kerr-Newman Black Hole (BH) has three degrees of freedom: mass M, charge Q and angular momentum L (or J). The fireshell model considers a BH without rotation ($L = 0$) [4]. The maximum energy extractable from the Kerr-Newman BH via pair creation process *à la* Sauter-Heisenberg-Euler-Schwinger (1936) is

$$E_{\max} = 1.8 \times 10^{54} \left(\frac{M_{BH}}{M_\odot} \right) \quad \text{erg}, \tag{1.1}$$

where M_{BH} is the mass of the BH. From this extractable energy, a plasma of electron-positron pairs is created in a shell around the BH and its external radius is fixed where the electric field is equal to the critical one $\left(E_c = m_e^2 c^3/\hbar e\right)$. The region of space where this plasma is created is called "*dyadosphere*" (see [100, 112]). The assumption of the fireshell model is that the total energy of the created pairs is equal to the isotropic energy emitted by the GRB, $E^{\rm tot}_{e^+e^-} = E_{\rm iso}$. When the pairs are created, they thermalize and, due to their optical thickness, self-accelerate. This fireshell of expanding plasma is composed by electrons-positrons-photons and is called "Pair ElectroMagnetic pulse" (PEM-pulse) (see [120]).

After the previous expansion of the pairs-photons shell (that corresponds to the first phase of the fireshell model), with an enhancement of the global Lorentz factor (until $\Gamma \sim 10^2 - 10^3$), the second phase involves the decrease of the Lorentz factor (until to $\Gamma \lesssim 4$) due to the impact of the plasma on the baryonic matter surrounding the BH and deposited by the progenitor collapsed star (the so called "SN-ejecta"). During this last phase, the pairs energy is partially converted into kinetic energy of the baryons, that have been swallowed by the pairs plasma and start to be accelerated (third phase), with an increase of their Lorentz factor. In Sec. (1.2.2) we will describe better the dynamic of this interaction between the e^+e^--pair plasma and the matter in the SN-ejecta. The series of these processes leads to the formation of an optically thick pairs-photons-baryons plasma (PEMB–pulse). The amount of baryons incorporated by the plasma is measured by the dimensionless parameter B, called *baryon load*,(that should not be confused with the magnetic field) defined as

$$B = \frac{M_b c^2}{E^{\rm tot}_{e^-e^+}}, \tag{1.2}$$

where M_b is the baryonic mass inside the plasma and $E^{\rm tot}_{e^-e^+}$ is the energy of the pairs, which corresponds to the energy of the dyadosphere E_{dya}. Smaller is the values of B, smaller is the decrease of the plasma Lorentz factor, due to the inertia of the fireshell. For $B > 10^{-2}$ turbulences start to act and the dynamical solution of the fireshell model is not valid any more.

After the third phase, the PEMB-pulse becomes optically thin and the *proper gamma ray bursts* (P-GRB) is emitted. This corresponds to the first emission seen in the light curve and brings a thermal component with it [115]. Smaller is the value of B ($B < 10^{-5}$), smaller is the value of the pairs energy converted into baryons kinetic energy and, then, stronger is the emission when the shell becomes optically thin. Vice versa, larger values of B lead to a larger fraction of the pairs energy converted to baryons kinetic energy and, then, to a low energetic emission.

[4] We remind that a Kerr solution with $L = 0$ reduce to the so called Reissner-Nordström BH ([103]; [91]; [28]), where the only two parameters that describe the system are the mass M and the charge Q.

After the transparency of the shell, the fourth phase starts, where an optically thin fireshell interacts with the baryons of the *circum burst medium* (CBM). This interaction leads to the emission of the Extended Afterglow (EA), which covers a wide range of the spectrum energy (from low energies, to optical, to X- and γ−ray), it lasts longer than the P-GRB emission and it occurs subsequently to this one. This emission is due to the dissipation of the baryons kinetic energy of the fireshell in radiation. Then, the total GRB emission (called "GRB *prompt emission*") is given by P-GRB+EA. Consequently, the whole energy of the dyadosphere is shared between these two components $E^{tot}_{e^+e^-} = E_{P-GRB} + E_{EA}$. From what we stated above, we get that for lower values of B, the majority of the emission is released in the P-GRB phase, while for higher values of B the energy is released principally during the EA phase. The Afterglow spectrum is a convolution of thousand of thermal spectra with different temperatures and it is described by a power-law times a thermal spectrum.

Summarizing, the fireshell model predicts a canonical bolometric light curve composed by two principal emissions: the P-GRB, which occurs when an optically thick shell reaches the transparency; the EA, due to the interaction of an optically thin fireshell with the baryons of the *circum burst medium* (CBM). Both the intensity of these components are governed by the baryon load parameter B. For values of $B < 10^{-5}$, the P-GRB component is the dominant one ($\sim 50\%$ of the total energy) and these type of GRBs are called *genuine short*-GRB. For $3 \times 10^{-4} \leq B \leq 10^{-2}$, the dominant component is the Afterglow. These type of GRBs are denominated as *long*-GRB. In the light curve for these type of GRBs, the P-GRB has only a small amount of energy and occurs before the EA phase, while the several peaks in the EA phase are produced by inhomogeneities of the CBM.

1.2.2 Dynamic of the interaction between e^+e^-plasma and matter: X-ray flares

As we stated above, when the pairs are created, this plasma accelerates to a high Lorentz factor ($\Gamma \sim 10^2 - 10^3$) and phagocytizes baryonic matter encountered during its expansion. In this case the baryon load is $B < 10^{-2}$ and the baryons are accelerated. When the transparency of this plasma occurs: 1) it emits radiation that explain the entire prompt emission of the GRB, that corresponds to the most energetic part of the plasma total energy $E_{e^+e^-}$; 2) the accelerated baryons interact with the circum-burst medium clouds.

There is a second episode of radiation emission related to the pair plasma. This emission emerges due to the transparency of the plasma with a Lorentz factor $\Gamma \lesssim 4$. The latter low value is reached because the relativistic e^+e^- plasma enters in a region with high matter density and starts to acquire baryons, converting part of its energy into baryons kinetic energy. In this section we describe the dynamic of the impact between the e^+e^- plasma onto this baryonic denser region, which is characterized by a baryon load $10 \lesssim B \lesssim 10^2$. The radiation emitted at the transparency of this plasma corresponds only to a fraction of the pairs plasma energy $E_{e^+e^-}$ (between $2\% - 20\%$) and gives rise to the X-ray flares.

In order to study the expansion of the plasma inside SN-ejecta, hydrodynamical simulations have been made using one-dimensional relativistic hydrodynamical (RHD) module included in the freely available PLUTO code (see [86]). This code integrates partial differential equations in the only two variables: radius and time. In this way, one can follow the evolution of the plasma inside the ejecta. The equations to integrate are the ones of a relativistic fluid in absence of gravity, that can be written as

$$\frac{\partial(\rho\Gamma)}{\partial t} + \nabla.(\rho\Gamma\mathbf{v}) = 0, \tag{1.3}$$

$$\frac{\partial m_r}{\partial t} + \nabla.(m_r\mathbf{v}) + \frac{\partial p}{\partial r} = 0, \tag{1.4}$$

$$\frac{\partial \mathcal{E}}{\partial t} + \nabla.(\mathbf{m} - \rho\Gamma\mathbf{v}) = 0, \tag{1.5}$$

where ρ and p are, respectively, the comoving fluid density and pressure, $\mathbf{v}$ is the coordinate velocity in natural units ($c = 1$), $\Gamma = (1 - \mathbf{v}^2)^{-\frac{1}{2}}$ is the Lorentz gamma factor, $\mathbf{m} = h\Gamma^2\mathbf{v}$ is the fluid momentum, m_r its radial component, $\mathcal{E}$ is the internal energy density, and h is the comoving enthalpy density defined by

$h = \rho + \epsilon + p$ (where ϵ is the internal energy density measured in the comoving frame). We define the internal energy density $\mathcal{E}$ as:

$$\mathcal{E} = h\Gamma^2 - p - \rho\Gamma, \tag{1.6}$$

where the first two terms on the right hand side coincides with the T^{00} component of the fluid energy-momentum tensor $T^{\mu\nu}$, while the last one is the mass density in the laboratory frame.

This plasma-fluid satisfies the equation of state of an ideal relativistic gas, which can be expressed by the enthalpy

$$h = \rho + \frac{\gamma p}{\gamma - 1}, \tag{1.7}$$

with $\gamma = 4/3$, if the following conditions are satisfied: 1) the process of pair-production and annihilation is in equilibrium $e^+ + e^- \rightleftarrows \gamma + \gamma$, which implies the equivalence between the electron and positron chemical potential $\mu_{e^+} = \mu_{e^-} \equiv \mu$; 2) the plasma is chargeless, namely the baryon number density $Z\, n_{\rm B}(\mu, T) = n_{e^-}(\mu, T) - n_{e^+}(\mu, T)$, where $n_{e^\pm}$ is the positron/electron number density and Z is the average number of electrons per nucleon. Under the above conditions, and considering that the matter density can be written as $\rho = m_p n_{\rm B} + m_e\,(n_{e^-} + n_{e^+})$, it can be shown that the value $\gamma = 4/3$ satisfies Eq. (1.7), with a small error.

The variables ($n_{e^\pm}$, $\epsilon_{e^\pm}$, $p_{e^\pm}$) are calculated through the Fermi-Dirac distribution

$$f(z, T, m, \mu) = \frac{1}{e^{\sqrt{z^2+(m/T)^2}-\mu/T} + 1}, \tag{1.8}$$

while $\epsilon_\gamma = aT^4$, $p_\gamma = aT^4/3$, $\epsilon_{\rm B} = 3/2\, n_{\rm N} T$, $p_{\rm B} = n_{\rm N} T$, where T is the temperature, $n_{\rm N}$ the nuclei number density and $a = 8\pi^5 k_B^4/15h^3c^3 = 7.5657 \times 10^{-15}$ erg cm^{-3} K^{-4} the radiation constant (see [129] for more details).

The integration of the above system of equations, along a selected radial direction, starts after that the physical structure of the system is established by the induced gravitational collapse event and, principally, when the shape and the profile of the SN-ejecta is setted. A description of the induced gravitational collapse event is given in the next chapter, but the principal results that we need to emphasize here are: 1) the SN-ejecta has enough angular momentum to circularize for a short time and forms a disk-like structure around the NS; 2) the presence of a NS companion gives rise to a large asymmetry in the distribution of the ejecta. This asymmetric behaviour allows the X-ray photons to be emitted.
We refer the reader to [46, 52, 19] for more details about the simulations and their improvement during the years, from the first simulation [46] to the last one [19].

The simulations start assuming the following binary parameters values: the NS has an initial mass of 2.0 $M_\odot$; the $CO_{\rm core}$ obtained from a progenitor with a zero-age-main-sequence mass $M_{\rm ZAMS} = 30\ M_\odot$ leads to a total ejecta mass 7.94 $M_\odot$, and follows an approximate power-law profile $\rho^0_{\rm ej} \approx 3.1 \times 10^8 (8.3 \times 10^7/r)^{2.8}$ g cm^{-3}. The orbital period is $P \approx 5$ min, i.e. a binary separation $a \approx 1.5 \times 10^{10}$ cm. For these parameters the NS reaches the critical mass and collapses to form a BH.

Fig. (1.2) shows the SN ejecta mass enclosed within a cone of 5 degrees of semi-aperture angle, whose vertex is at the position of the BH at the moment of its formation (see the lower left panel of Fig. 6 in [19]), and whose axis is along various directions, measured counterclockwise with respect to the line of sight. Fig. (1.3) shows instead the cumulative radial mass profiles within a selected number of the aforementioned cones. From these plots we deduce how the e^+e^- plasma swallows different amounts of baryonic mass along different directions due to the asymmetry of the SN-ejecta created by the presence of the NS binary companion and the accretion process onto it [19]. At the time $t = 0$, the e^+e^- plasma has an energy of $E_{e^+e^-} = 3.16 \times 10^{53}$ erg, which is distributed homogeneously in a region between $10^8 - 10^9$ cm from the BH site and expands in a region with negligible baryon load. The SN-ejecta has a negligible pressure and its mass profile is given by $\rho \propto (R_0 - r)^\alpha$, with R_0 and $2 \le \alpha \le 3$ are parameters chosen properly.

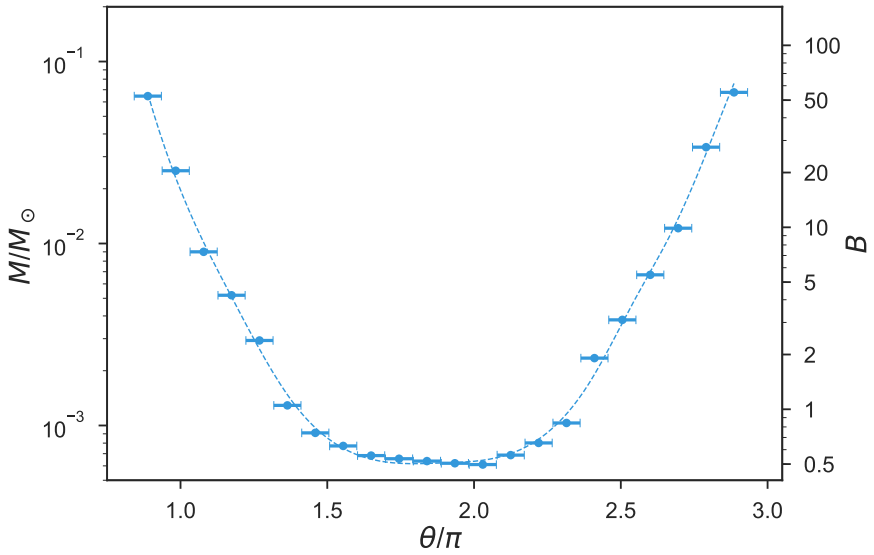

Figure 1.2. The SN ejecta mass enclosed within a cone of 5 degrees of semi-aperture angle, whose vertex is at the position of the BH at the moment of its formation (see the lower left panel of Fig. 6 in [19]), and whose axis is along various directions measured counterclockwise with respect to the line of sight. The binary parameters of this simulations are: the NS has an initial mass of 2.0 $M_\odot$; the CO_{core} obtained from a progenitor with a zero-age-main-sequence mass M_{ZAMS} = 30 $M_\odot$ leads to a total ejecta mass 7.94 $M_\odot$, and the orbital period is $P \approx 5$ min, i.e. a binary separation $a \approx 1.5 \times 10^{10}$ cm. The vertical axis on the right side gives, as an example, the corresponding value of the baryon load B assuming a plasma energy of $E_{e^+e^-} = 3.16 \times 10^{53}$ erg.

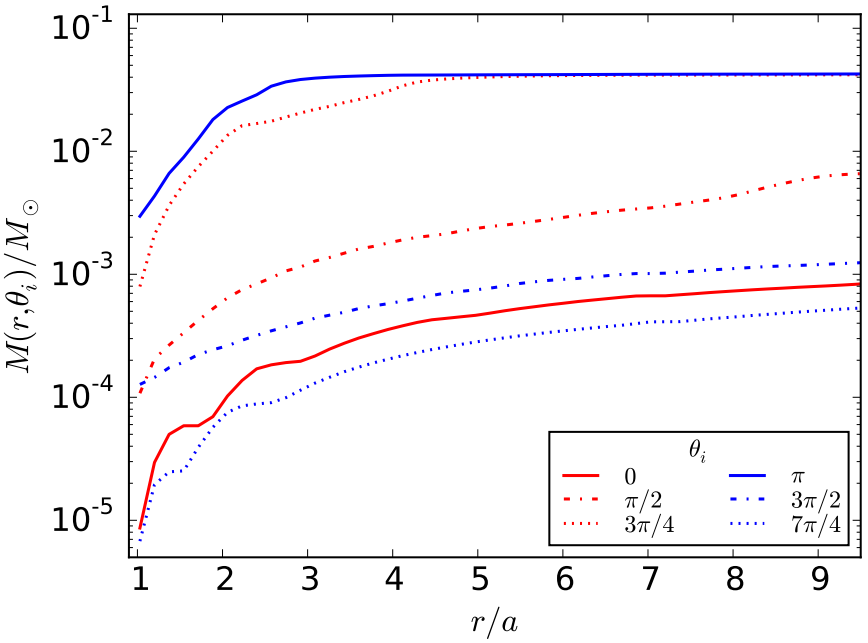

Figure 1.3. Cumulative radial mass profiles within selected cones among the ones used in Fig. (1.2). We note that the final value for the cumulative mass reached at the end of each direction, namely the value when each curve flattens, is consistent with the total integrated mass value of the corresponding direction shown in Fig. (1.2). The binary parameters of these simulations are the same of Fig. (1.2).

The expansion of the plasma inside the SN-ejecta leads to the formation of a shock that propagates all inside the ejecta. In Fig. (1.4) the radial distribution profiles of the velocity and the mass density, in the laboratory frame, inside the ejecta are shown as a function of the distance r at two specific moments: t_1 corresponds to the moment before the plasma crosses the entire SN-ejecta, while t_2 the moment when the plasma have crossed the whole ejecta and reaches its external surface. The baryon load adopted for this plot is $B = 200$. The peaks of the velocity profiles correspond to the front of the shock and we can see that behind the shock a tail of accelerated material (with $0.1 \leq \beta \leq 1$) is formed.

The transparency radius R_{ph} is setted by the point when the optical depth $\tau = \int_{R_{ph}}^{\infty} \sigma_T n_{e^-}(r)\, dr = 1$ (where σ_T is the Thomson cross-section and the electron number density is given by $n_{e^-} = \rho\Gamma/m_p$, with m_p the proton mass).

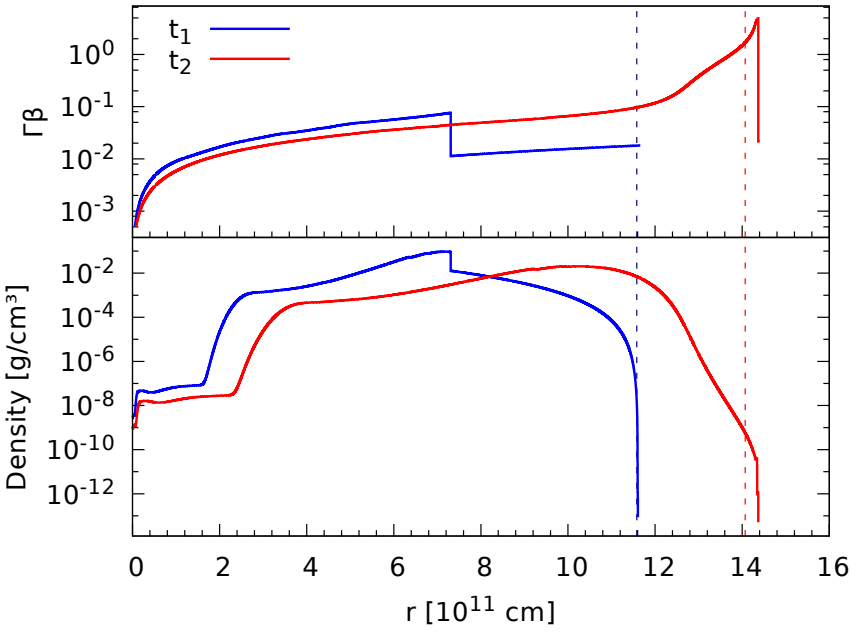

Figure 1.4. Above: Distribution of the velocity inside the SN ejecta at the two fixed values of the laboratory time t_1 (before the plasma reaches the external surface of the ejecta) and t_2 (the moment at which the plasma, after having crossed the entire SN ejecta, reaches the external surface). We plotted the quantity $\Gamma\beta$, recalling that we have $\Gamma\beta \sim \beta$ when $\beta < 1$ and $\Gamma\beta \sim \Gamma$ when $\beta \sim 1$. **Below:** Corresponding distribution of the mass density of the SN ejecta in the laboratory frame ρ_{lab}. These particular profiles have been done using a baryon load $B = 200$. The dashed vertical lines correspond to the two values of the transparency radius R_{ph}. In particular, we see that at t_1 the shock front did not reach R_{ph} yet and the system is optically thick(see [129]).

From these results we can conclude that, when the e^+e^- plasma expands into the whole SN-ejecta region, it acquires and accelerates matter until it reaches the transparency at the outermost part of the ejecta, at the radius R_{ph}, with a Lorentz factor $\Gamma \leq 4$. The transparency of the plasma allows to emit X-ray photons: the X-ray flares.

The Ch. (3) of this thesis is based on the simulations described in this section, but with a different value for the baryon load. There we will study the neutrino emission via the proton-proton interaction occurring during the expansion of the pair-plasma inside the ejecta. The protons at rest inside the ejecta are accelerated by this expanding plasma and interact with protons, still at rest, placed ahead of the plasma front. In order to study this phenomenon, the simulations have been done setting a baryon load value of $B = 51.75$, which derives from the initial conditions setted for the stars that form the BdHN system.

Chapter 2

The framework of the BdHNe

In this chapter we give an overview on the salinet features of the class of binary-driven hypernovae (BdHNe) within the induced gravitational collapse (IGC) scenario for the explanation of the long GRBs. The building blocks of this chapter are based principally to the paper [110].

There is an increasing observational evidence that Gamma-ray bursts (GRBs) originate in different subclasses, each one with specific energy release, spectra, duration, etc. and all of them with binary progenitors. The binary components involve carbon-oxygen cores (CO_{core}), neutron stars (NSs), black holes (BHs), and white dwarfs (WDs).

In this introduction we try to summarize the principal events concerning the BdHNe model, within the IGC scenario proposed by Prof. Ruffini, R. *et al.* in [114, 124]. The progenitor of a BdHNe is a CO_{core}-NS binary. The supernova (SN) explosion of the CO_{core}, producing at its center a new NS (νNS), triggers onto the NS companion a hypercritical, i.e., highly super-Eddington, accretion process, accompanied by a copious emission of neutrinos. By accretion the NS can become either a more massive NS or reach the critical mass for gravitational collapse with consequent formation of a BH. The SN explosion and the hypercritical accretion onto the NS explain the X-ray precursor. The feedback of the NS accretion, the NS collapse and the BH formation produce asymmetries in the SN ejecta, that has been studied by 3D simulations and analysis for GRBs. The newborn BH, the surrounding matter and the magnetic field inherited from the NS, comprise the *inner engine* of the GRB from which the electron-positron (e^+e^-) plasma and the high-energy emission are initiated and start to propagate inside and outside the system. The impact of the e^+e^- plasma on the asymmetric ejecta transforms the SN into a hypernova (HN). The dynamics of the plasma in the asymmetric ejecta leads to signatures on the emitted radiation depending on the observational viewing angle. This explains the ultra-relativistic prompt emission in the MeV domain and the mildly-relativistic flares in the early afterglow in the X-ray domain. Instead, the feedback of the pulsar-like emission of the νNS onto the hyper-novae explains the X-ray late afterglow. In addition, the BdHNe, in their different flavors, lead to binary systems composed by νNS-NS or νNS-BH. Moreover, the gravitational waves emission drives these binaries to merge and producing short GRBs. It is thus established a previously unthought interconnection between long and short GRBs and their occurrence rates.

This sequence of events that characterize this scenario has been introduced in order to avoid the problems that emerged from the usual interpretation of GRBs with the traditional "*fireball*" model. In this model, the GRB is assumed to originate from a SN explosion by the collapse of a very fast rotating and massive star and the GRB dynamics is drive by a *fireball*, a single ultra-relativistic collimated jet. Some of the salient problems of this model are:

- the lack of observations for the existence of a very small beaming angle θ (of the order of 1°), necessary in order to explain the reduction of the observed energy of the system from $\sim 10^{54}$ erg to $\sim 10^{51}$ erg expected from the model ([34, 141, 26]);

- the request for this scenario of a dense and strong wind-like circumburst medium (CBM). This is in contrast with the observations in most GRBs of a CBM density of $\sim$ 1 particle/cm^3 [113]. Indeed, in order to have for the e^+e^--plasma a Lorentz factor of $\Gamma \sim 100$ ([142, 98, 83]), it should incorporates a limited amount of matter, that is regulated by a baryon load $\lesssim 10^{-2}$ (see Eq. (1.2)) [121];

- the energy emitted by a SN explosion lies in the range $10^{49} - 10^{51}$ erg, while the GRB emits in the range $10^{49} - 10^{54}$ erg. Then, the formation of a stellar-mass BH it is necessary to explain this surplus of energy.

These are the principal problems concerning the *fireball* model. In order to solve these and others problems, the IGC scenario was introduced by Ruffini *et al.* ([114, 124]). The scenario is based on this scheme: the explosion of a Ib/c SN triggering an accretion process onto a NS companion. The NS, reaching the critical mass value, gravitationally collapses leading to the formation of a BH. The formation of the BH consequently leads to the emission of the GRB. From the initial proposal, during the years, many modifications, theoretical improvements and the necessity for observational verifications have led to the development of a wide range of phenomenology for GRBs, that we are going to resume in the next section.

2.1 GRB subclasses

The principal basic distinction of GRBs consists between *long*- and *short*-GRB. This separation is based on: 1) the different duration of the spikes in the prompt emission: this difference depends on the values of the baryon Lorentz factor which are accelerated by the e^+e^- plasma (long bursts have $\Gamma \sim 10^2 - 10^3$, while short burst $\Gamma \sim 10^4$); 2) long bursts have $T_{90} > 2$ s, while for short burst $T_{90} < 2$ s; 3) in the framework of the fireshell model, they have different baryon load: for long burst $10^{-4} \leq B < 10^{-2}$ [63, 93, 96, 95], while in short burst $10^{-5} \leq B \leq 10^{-4}$ [87, 126, 127]. Notwithstanding this basic classification, several classes of GRB have been found, basing on their energetics characteristics.

Here we summarize the different subclasses of GRBs, dividing them in two groups: binary-driven hypernovae (BdHNe) and compact-object binary mergers (BM) (see [110]). Old names previously assigned to some subclasses (see [128, 111, 106]) are also inserted. All the subclasses, some of their properties, their new and old names are listed in Tab. (2.1) in Sec. (2.6). The first group corresponds to the BdHNe and is composed by three elements.

i. **X-ray flashes (XRFs)**. These systems have CO_{core}-NS binary progenitors in which the NS companion does not reach the critical mass for gravitational collapse [19, 20]. Thus the XRFs lead either to two NSs ejected by the disruption of the CO_{core} through a SN-event, or to binaries composed of a newly-formed $\sim$1.4–1.5 $M_\odot$ NS (hereafter νNS) born at the center of the SN, and a massive NS (MNS) which accreted matter from the SN ejecta. Some observational properties are: Gamma-ray isotropic energy $E_{iso} \lesssim 10^{52}$ erg, rest-frame spectral peak energy $E_{p,i} \lesssim 200$ keV and a local observed rate of $\rho_{XRF} = 100^{+45}_{-34}$ Gpc^{-3} yr^{-1} [128]. We refer the reader to [128, 131] for further details on this class. In [153], this class has been divided into BdHN type II, the sources with $10^{50} \lesssim E_{iso} \lesssim 10^{52}$ erg, and BdHN type III, the sources with $10^{48} \lesssim E_{iso} \lesssim 10^{50}$ erg.

ii. **Binary-driven hypernovae (BdHNe)**. Originate in compact CO_{core}-NS binaries where the accretion onto the NS becomes high enough to bring it to the point of gravitational collapse, hence forming a BH. Most of these binaries survive to the SN explosion, have a short orbital period ($P \sim 5$ min) and remain a bound system. Therefore, BdHNe produce νNS-BH binaries. Some observational properties are: $E_{iso} \gtrsim 10^{52}$ erg, $E_{p,i} \gtrsim 200$ keV and a local observed rate of $\rho_{BdHN} = 0.77^{+0.09}_{-0.08}$ Gpc^{-3} yr^{-1} [128]. In [153] this class has been renominated as BdHN type I.

iii. **BH-SN**. These systems originate in CO_{core} (or Helium or Wolf-Rayet star)-BH binaries, hence the hypercritical accretion of the SN explosion of the CO_{core} occurs onto a BH previously formed in the evolution path of the binary. If the binary survives to the SN explosion, the BH-SNe system produces or νNS-BH, or BH-BH binaries, depending on the fate of the central remnant of the SN (see, although, [144, 145]). Some observational properties are: $E_{iso} \gtrsim 10^{54}$ erg, $E_{p,i} \gtrsim 2$ MeV and an upper limit to their rate is $\rho_{BH-SN} \lesssim \rho_{BdHN} = 0.77^{+0.09}_{-0.08}$ Gpc^{-3} yr^{-1}. In [153] this class has been renominated as BdHN type IV.

Instead, the following three subclasses derive from the compact-object binary mergers (BMs) group and it is thought that they give rise to short-GRBs

iv. **Short Gamma-ray flashes (S-GRFs)**. They are produced by NS-NS mergers leading to a MNS, namely when the merged core does not reach the critical mass of a NS in order to collapse as a BH. Some observational properties are: $E_{iso} \lesssim 10^{52}$ erg, $E_{p,i} \lesssim 2$ MeV and a local observed rate of $\rho_{S-GRF} = 3.6^{+1.4}_{-1.0}$ Gpc^{-3} yr^{-1} [128]. In [153] this class has been renominated as BM type I.

v. **Authentic short GRBs (S-GRBs)**. They are produced by NS-NS mergers, that leads to a BH when the merged core reaches the critical mass for a NS to forms a BH [127, 126, 88]. Some observational properties are: $E_{iso} \gtrsim 10^{52}$ erg, $E_{p,i} \gtrsim 2$ MeV and a local observed rate of $\rho_{S-GRB} = \left(1.9^{+1.8}_{-1.1}\right) \times 10^{-3}$ Gpc^{-3} yr^{-1} [128]. In [153] this class has been renominated as BM type II.

vi. **Ultra-short GRBs (U-GRBs)**. This is a theoretical GRB subclass subjected for observational verification. U-GRBs are expected to be produced by νNS-BH mergers, with a merger time scale of $\sim 10^4$ yr or less [51], whose binary progenitors can be the outcome of BdHNe type I (see point II above) or of BdHNe type IV (BH-SN; see point III above). The following observational properties are expected: $E_{iso} \gtrsim 10^{52}$ erg, $E_{p,i} \gtrsim 2$ MeV and a local observed rate similar to the one of BdHNe type I, since it has been shown that most of them are expected to remain bound [51], i.e. $\rho_{U-GRB} \approx \rho_{BdHN} = 0.77^{+0.09}_{-0.08}$ Gpc^{-3} yr^{-1} [128]. In [153] this class has been renominated as BM type V.

In addition to these subclasses, there are two others subclasses of GRB that consider the presence of, at least, one white dwarf (WD).

vii. **Gamma-ray flashes (GRFs)**. These sources have hybrid properties between long and short bursts and have no associated SNe [41]. It has been proposed that they are produced by NS-WD mergers [128], which form a MNS but not a BH [128]. Some observational properties for this type of GRBs are: $10^{51} \lesssim E_{iso} \lesssim 10^{52}$ erg, $0.2 \lesssim E_{p,i} \lesssim 2$ MeV and a local observed rate of $\rho_{GRF} = 1.02^{+0.71}_{-0.46}$ Gpc^{-3} yr^{-1} [128]. Most NS-WD mergers are probably under the threshold of current X-ray and Gamma-ray instruments since only one detection has been identified (GRB 060614 [27]). In [153] this class has been renominated as BM type III.

viii. **Fallback kilonovae (FB-KNe)**. This is a recently introduced GRB subclass having as progenitors WD-WD mergers [111, 106], that leads to a massive ($M \sim 1$ M$_\odot$), fast rotating ($P \sim$ 1–10 s), highly-magnetized ($B \sim 10^9$–10^{10} Gauss) WD. Some observational properties are: $E_{iso} \lesssim 10^{51}$ erg, $E_{p,i} \lesssim 2$ MeV and a local observed rate $\rho_{FB-KN} = (3.7\text{–}6.7) \times 10^5$ Gpc^{-3} yr^{-1} [111, 106, 79, 80].

2.2 The BdHNe class

In this section we concentrate our attention to the case of the BdHNe subclass, which contains the two cases of BdHNe I (**BdHNe**) and BdHNe II (**XRFs**).

As we explained in the previous section, the progenitors of these systems are CO_{core}−NS binaries. The CO_{core} explodes as a SN and produces an accretion process onto the NS companion. If the binary

system is not disrupted by the SN explosion and if it is compact enough, namely it has a fast orbital period (a few minutes), the accretion becomes hypercritical. The accretion process leads to the formation of a massive NS (MNS) or to a BH. The latter comes out through the induced gravitational collapse of the progenitor-NS. Consequently, the emerging binary-system is composed by a new NS (νNS), formed at the center of the SN, and a MNS or a BH.

A schematic reproduction of the SN-NS binary system and the process of the IGC is shown in Fig. (2.1). The figure shows the moment when the SN explosion occurs and the companion NS reaches the critical mass for the formation of a BH and the emission of the GRB. It is also shown the Bondi-Hoyle region related to the NS, namely the region after that the material of the SN-ejecta falls onto the NS surface, and the neutrino sphere, namely the region where a copious number of $\nu\bar{\nu}$ are created (by the electron-positron annihilation process), which take out most of the gravitational energy gained by the NS from the infalling material.

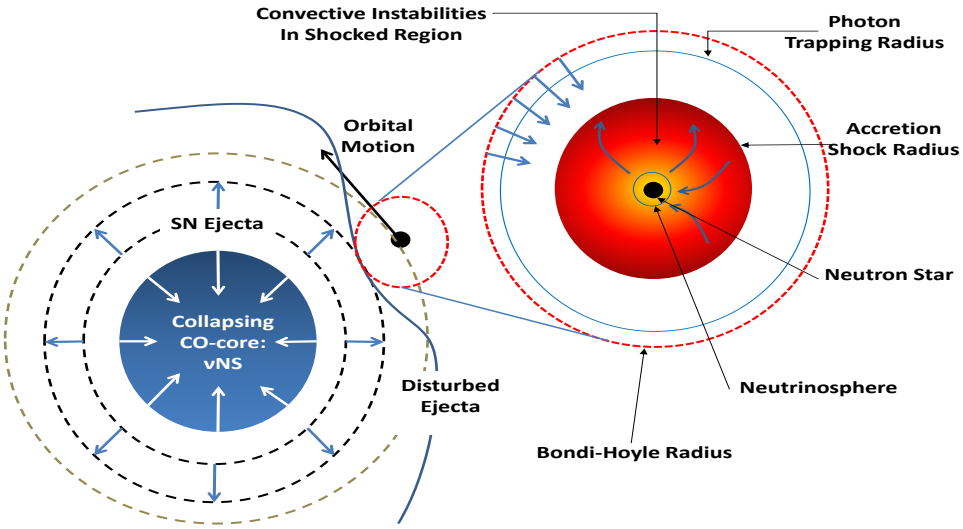

Figure 2.1. Scheme of the induced gravitational collapse (IGC) scenario (taken from Figure 1 in [52]). The CO_{core} undergoes supernova (SN) explosion, the neutron star (NS) accretes part of the SN ejecta and then reaches the critical mass for gravitational collapse to a black hole (BH), with consequent emission of a GRB. The SN ejecta reaches the NS Bondi-Hoyle radius and fall toward the NS surface. The material shocks and decelerates while it piles over the NS surface. At the neutrino emission zone, neutrinos take away most of the gravitational energy gained by the infalling matter. The neutrinos are emitted above the NS surface and allow the material to reduce its entropy to be finally incorporated to the NS. For further details and numerical simulations of the above process see [52, 20, 19].

Let's concentrate on the specific case of BH formation. In this binary system of νNS-BH, the so called *inner engine* model has been introduced in order to explain the high-energy emission [135, 136, 137, 118]. The *inner engine* is drove by the rotation of the BH together with the presence of a magnetic field inherited from the NS and the surrounding matter. The electromagnetic field of the engine is mathematically described by the Wald solution [152]. This physical configuration of the source induces an overcritical electric field around the BH generated by the presence of a background magnetic field and by the rotation of the BH. The break-down of this overcritical electric field leads to the creation of a huge amount of electron-positron (e^+e^-) pair plasma which self-accelerates to ultra-relativistic velocities.

This brief explanation of the physical processes behind the BdHNe model has its observative counterpart. Indeed the different wavelength emissions of a GRB event can be explained as follow:

1. The GRB prompt emission in the Gamma-rays region of the spectrum can be explained by the transparency of the e^+e^- pair plasma.

2. The induced electric field is able to accelerate protons that, if they are emitted along the rotation axis of the BH, lead to the formation of ultra high-energy cosmic rays (UHECRs) of up to energies of $\sim 10^{21}$ eV (see App. (D)).

3. In connection with the previous point, the acceleration process along directions at a certain angle to the polar direction leads to proton-synchrotron radiation which explains the GeV emission [135, 136].

4. The optical emission can be explained by the interaction/feedback of the GRB into the SN, which makes it become the hypernova (HN) [134, 21]. This emission is powered by nickel decay and occurs a few days after the GRB trigger.

5. The observed X-ray precursors [19] can be explained as due to the SN shock breakout and the hypercritical accretion.

6. The e^+e^- feedback onto the SN ejecta also produces gamma- and X-ray flares observed in the early afterglow [129].

7. The synchrotron emission by relativistic electrons from the νNS into the expanding magnetized HN ejecta and the νNS pulsar emission explain the early and late X-ray afterglow [117].

In the following sections we summarize the cornerstone physical points of the model, which concern the IGC scenario, which is at the base of the BdHNe model.

2.3 The IGC framework

After the first proposal of the IGC scenario (formulated in 2012 [109]), a lot of theoretical work and many numerical simulations have been done in order to: relax, little by little, several assumptions of the initial model, always to add new elements to the problem, to better describe and to have a complete view of the complex scenario.

In the beginning, the model had some assumptions as: (1) a uniform density profile of the pre-SN CO_{core}; (2) the ejecta was evolved following an homologous expansion; (3) the mass of the NS and the CO_{core} were assumed nearly constant. The first numerical simulations were implemented in 2014 [52] via a *1-D* code. From this analysis the accretion rate was inferred in the range $10^{-3} - 10^{-1}$ $M_\odot$ s^{-1}.

Later, *2-D* simulations have been done (see [20]) where: 1) some of the previous assumptions were released as the adoption of a power-law in distance for the ejecta density profile and which evolves with an homologous expansion; 2) new elements have been added to the model as: the inclusion of the angular momentum transferred from the ejecta material to the NS, the general relativistic effects to the calculations of the NS structural parameters (mass, radius, spin), NS gravitational binding energy and to the angular momentum transferred by the matter particles. The results of these simulations showed that the infalling particles of the ejecta start to circularize around the NS before being accreted and that there is a maximum orbital period (P_{max}) for which the NS reaches the critical mass for the gravitational collapse into a BH. This parameter became the threshold for the definition of specific classes of GRB: the **XRF**, where the NS does not reach the critical mass; the **BdHNe**, where the critical mass is reached and the formation of BH is triggered.

The *3-D* simulations has been studied in Becerra *et al.* 2015 [20] and Becerra *et al.* 2016 [19] through smoother-particles-hydrodynamics (SPH)-like simulations, where the mass and the number of particles in each layer of the SN-ejecta were assigned according to the power-law density profile and their velocities follow a radial distribution. The NS is assumed in circular motion around the CO_{core}, which constitutes the center of mass of the system. In this simulations the neutrino emission has been taken into account and results that the dominant process of ν production is the electron-positron annihilation, $e^+e^- \rightarrow \nu\bar{\nu}$. The ν

luminosity can reach values of the order $\sim 10^{52}$ erg s^{-1}, with neutrino energy of ~ 20 MeV. The principal result of this simulation is that the evolution of the SN-ejecta around the NS has been obtained: the matter, with an initial spherical distribution, becomes highly asymmetric due to the accretion process and gravitational field of the NS. It is also showed that the SN-ejecta circularize for a short time and form a disk-like structure before to be accreted by the NS. In Fig. (2.2) we show some plots of these simulations kept from [21]. The basic process of these simulations is the hypercritical accretion that we are going to describe in the next section.

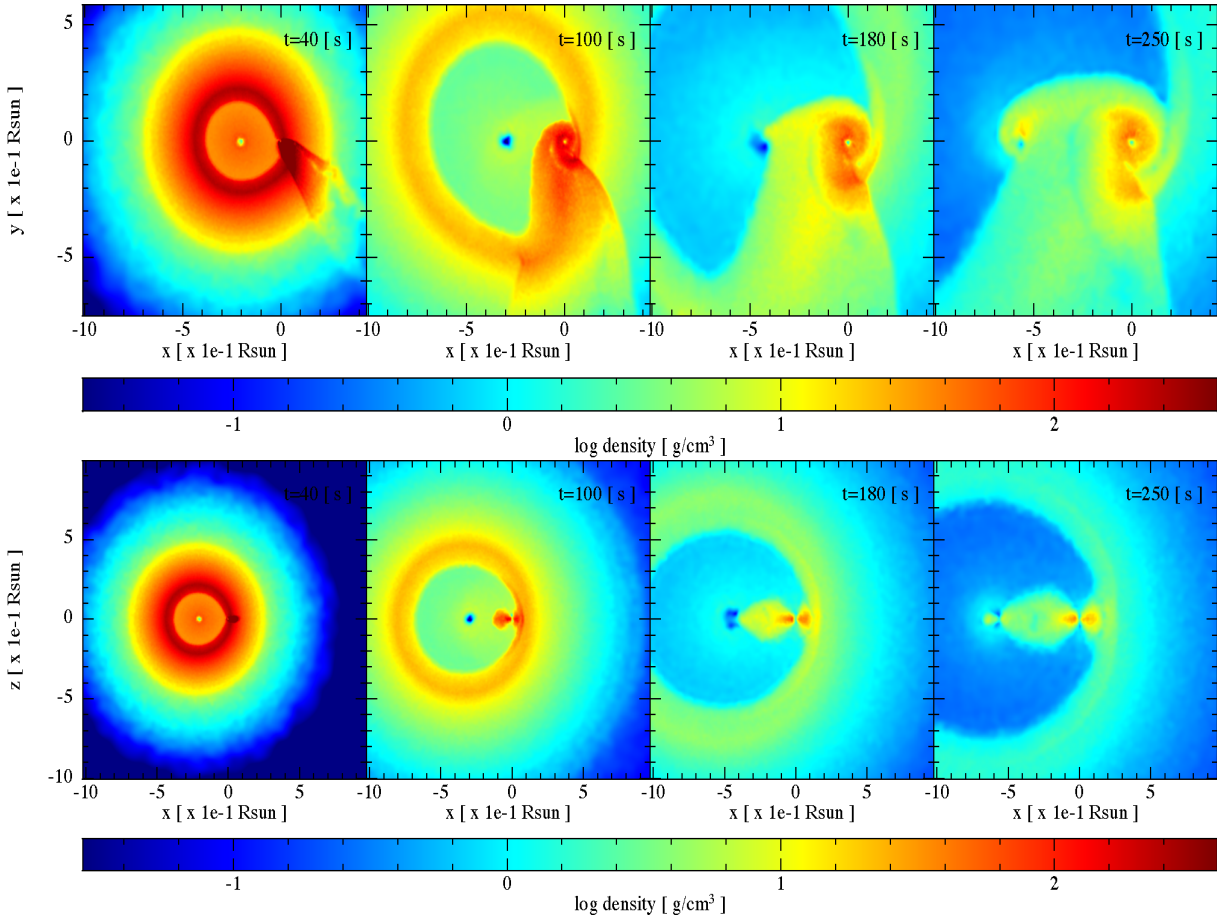

Figure 2.2. Snapshots of the 3D SPH simulations of the IGC scenario (taken from Figure 2 in [21]). The initial binary system is formed by a CO_{core} of mass ≈ 6.85 $M_\odot$, from a ZAMS progenitor star of 25 $M_\odot$, and a 2 $M_\odot$ NS with an initial orbital period of approximately 5 min. The upper panel shows the mass density on the equatorial (orbital) plane, at different times of the simulation. The time $t = 0$ s is set in our simulations at the moment of the SN shock breakout. The lower panel shows the plane orthogonal to the orbital one. The reference system has been rotated and translated for the x-axis to be along the line joining the νNS and the NS centers, and its origin is at the NS position.

2.4 The hypercritical accretion process

The main physical conditions for which the hypercritical (i.e. highly super-Eddington) accretion process occurs onto the NS (for the XRF and BdHNe systems) are that: 1) the photons are trapped in the inflowing material of the ejecta; 2) the shocked atmosphere of the NS has a very high temperature ($T \sim 10^{10}$ K) and density ($\rho \gtrsim 10^6$ g cm^{-3}) and this brings to a highly efficient $\nu\bar{\nu}$ production which cools rapidly the system allowing the hypercritical accretion to continue.

If these two conditions are satisfied, the accretion process goes on with a rate given by

$$\dot{M}_B(t) = \pi \rho_{\rm ej} R_{\rm cap}^2 \sqrt{v_{\rm rel}^2 + c_{\rm s,ej}^2}, \qquad R_{\rm cap}(t) = \frac{2GM_{\rm NS}(t)}{v_{\rm rel}^2 + c_{\rm s,ej}^2}, \tag{2.1}$$

where G is the gravitational constant, $\rho_{\rm ej}$ and $c_{\rm s,ej}$ are the density and sound speed of the ejecta, $R_{\rm cap}$ and $M_{\rm NS}$ are the NS gravitational capture radius (Bondi-Hoyle radius) and gravitational mass, and $v_{\rm rel}$ the ejecta velocity relative to the NS: $\vec{v}_{\rm rel} = \vec{v}_{\rm orb} - \vec{v}_{\rm ej}$; $|\vec{v}_{\rm orb}| = \sqrt{G(M_{\rm core} + M_{\rm NS})/a}$, and $\vec{v}_{\rm ej}$ is the velocity of the supernova ejecta (see Fig. (2.1)). Typical values of the $CO_{\rm core}$ mass are (3.5–9.5) $M_\odot$, which corresponds to (15–30) $M_\odot$ zero-age-main-sequence (ZAMS) progenitors (see [52, 20] for details). The binary period is limited by the request to do not have any Roche lobe overflow by the $CO_{\rm core}$ before the SN explosion [52]. For a $CO_{\rm core}$ of 9.5 $M_\odot$ that forms a binary system with a 2 $M_\odot$ NS, the minimum orbital period allowed by this condition is $P_{\rm min} \approx 5$ min. For these typical binary and pre-SN parameters, Eq. (2.1) gives accretion rates 10^{-4}–10^{-2} $M_\odot$ s^{-1}.

The numerical simulations of the SN explosions suggests the adoption of a homologous expansion of the SN, i.e., $v_{\rm ej}(r,t) = nr/t$, where r is the position of each layer from the SN center and n is the expansion parameter. The density of the ejecta evolves as

$$\rho_{\rm ej}(r,t) = \rho_{\rm ej}^0(r/R_{\rm star}(t), t_0)\frac{M_{\rm env}(t)}{M_{\rm env}(0)}\left(\frac{R_{\rm star}(0)}{R_{\rm star}(t)}\right)^3, \tag{2.2}$$

where $M_{\rm env}(t)$ the mass of the $CO_{\rm core}$ envelope, $R_{\rm star}(t)$ is the radius of the outermost layer, and $\rho_{\rm ej}^0$ is the pre-SN $CO_{\rm core}$ density profile; $\rho_{\rm ej}(r,t_0) = \rho_{\rm core}(R_{\rm core}/r)^m$, where $\rho_{\rm core}$, $R_{\rm core}$ and m are the profile parameters obtained from numerical simulations.

The NS mass and angular momentum evolve as [20, 30]:

$$\dot{M}_{\rm NS} = \left(\frac{\partial M_{\rm NS}}{\partial M_b}\right)_{J_{\rm NS}} \dot{M}_b + \left(\frac{\partial M_{\rm NS}}{\partial J_{\rm NS}}\right)_{M_b} \dot{J}_{\rm NS}, \qquad \dot{J}_{\rm NS} = \xi\, l(r_{\rm in})\dot{M}_{\rm B}, \tag{2.3}$$

where M_b is the NS baryonic mass, $l(r_{\rm in})$ is the specific angular momentum of the accreted material at $r_{\rm in}$ (the radius where the accretion process starts), which corresponds to the angular momentum of the last-stable orbit (LCO), and $\xi \leq 1$ is a parameter that measures the efficiency of angular momentum transfer. In this picture we have $\dot{M}_b = \dot{M}_B$.

In order to integrate Eqs. (2.1) (2.2), we need to provide the derivatives of $M_{\rm NS} = M_{\rm NS}(M_b, J_{\rm NS})$. These relations are given by (see [29, 30, 20]):

$$\frac{M_b}{M_\odot} = \frac{M_{\rm NS}}{M_\odot} + \frac{13}{200}\left(\frac{M_{\rm NS}}{M_\odot}\right)^2\left(1 - \frac{1}{137}j_{\rm NS}^{1.7}\right), \tag{2.4}$$

where $j_{\rm NS} \equiv cJ_{\rm NS}/(GM_\odot^2)$, and

$$l_{\rm lco} = \frac{GM_{\rm NS}}{c}\left[2\sqrt{3} - 0.37\left(\frac{j_{\rm NS}}{M_{\rm NS}/M_\odot}\right)^{0.85}\right]. \tag{2.5}$$

The NS continues the accretion process until it reaches an instability limit or up to when all the SN ejecta overcomes the NS Bondi-Hoyle region. Two main instability limits for rotating NSs have been taken into account: the mass-shedding or Keplerian limit and the secular axisymmetric instability limit (for more details on the accretion process see [19]). The latter limit defines the critical mass that can be reached, which is given by

$$M_{\rm NS}^{\rm crit} = M_{\rm NS}^{J=0}(1 + k j_{\rm NS}^p), \tag{2.6}$$

where k and p are parameters that depends on the specific Equation of State (EOS) considered. The values of k varies between $10^{-3} - 10^{-2}$, while p between $(2.20 - 2.8)$, for the EOS: NL3, TM1 and GM1 (see [30, 20]).

The accretion rate of the SN-ejecta onto the NS can be as high as $\sim 10^{-2} - 10^{-1}$ $M_\odot$ s^{-1}. For these conditions: 1) the magnetic pressure is much smaller than the random pressure of the infalling material and, then, the magnetic field has no effects on the accretion process; 2) the photons are trapped within the infalling matter, with a trapping radius given by $\dot{M}_{\rm B} k/(4\pi c) \sim 10^{13} - 10^{19}$ cm (where k is the opacity); 3) the above physical conditions lead to an efficient neutrino cooling, which radiates the gained gravitational energy by the infalling material.

The accretion shock moves outward as the material piles onto the NS. Since the post-shock entropy is inversely proportional to the shock radius position, the NS atmosphere is convective unstable and these instabilities might drive high-velocity outflows from the accreting NS [50, 47]. The entropy at the base of the atmosphere is [49]:

$$S_{\rm bubble} \approx 16 \left(\frac{1.4\,M_\odot}{M_{\rm NS}}\right)^{-7/8} \left(\frac{M_\odot\,{\rm s}^{-1}}{\dot{M}_{\rm B}}\right)^{1/4} \left(\frac{10^6\,{\rm cm}}{r}\right)^{3/8} k_B/{\rm nucleon}, \tag{2.7}$$

where k_B is the Boltzmann constant. The material expands and cools down adiabatically, i.e., $T^3/\rho =$ constant. For a spherically symmetric expansion, $\rho \propto 1/r^3$ and $k_B T_{\rm bubble} = 195\, S^{-1}_{\rm bubble} \left(10^6\,{\rm cm}/r\right)$ MeV. While if the material expands laterally [48]: $\rho \propto 1/r^2$, i.e. $T_{\rm bubble} = T_0(S_{\rm bubble})\,(r_0/r)^{2/3}$. This implies a bolometric blackbody flux at the source from the rising bubbles:

$$F_{\rm bubble} \approx 2\times 10^{40} \left(\frac{M_{\rm NS}}{1.4\,M_\odot}\right)^{-7/2} \left(\frac{\dot{M}_{\rm B}}{M_\odot\,{\rm s}^{-1}}\right) \left(\frac{R_{\rm NS}}{10^6\,{\rm cm}}\right)^{3/2} \left(\frac{r_0}{r}\right)^{8/3} {\rm erg\,s^{-1}cm^{-2}}. \tag{2.8}$$

The above thermal emission has been shown [52] to be a plausible explanation of the early X-ray (precursor) emission observed in some GRBs.

We stated above that the neutrino emission play a crucial role in the cooling process of the system. The ν cooling is the principal responsible for the release of the NS binding energy gained by the infalling material. In the next subsection we briefly report the result of the analysis of the ν emission.

2.4.1 Neutrino emission

The neutrino emission process by the electron-positron annihilation dominates over the others processes (see [19]). The e^+e^- pairs, which produce the neutrinos, are thermalized at the matter temperature that is approximately given by:

$$T_{\rm acc} \approx \left(\frac{3P_{\rm shock}}{4\sigma/c}\right)^{1/4} = \left(\frac{7}{8}\frac{\dot{M}_{\rm acc} v_{\rm acc} c}{4\pi R^2_{\rm NS}\sigma}\right)^{1/4}, \tag{2.9}$$

where $P_{\rm shock}$ is the pressure of the shock developed on the accretion zone above the NS surface, $\dot{M}_{\rm acc}$ is the accretion rate, $v_{\rm acc}$ is the velocity of the infalling material, σ is the Stefan-Boltzmann constant and c the speed of light. For the accretion rates range of interest, $10^{-4} - 10^{-2}$ $M_\odot$ s^{-1}, the system develops temperatures and densities around $T \gtrsim 10^{10}$ K and $\rho \gtrsim 10^6$ g cm^{-3}, respectively.

Under these physical conditions, the neutrino emissivity by the e^+e^- annihilation process can be estimated by the simple formula [158]:

$$\epsilon_{e^-e^+} \approx 8.69\times 10^{30} \left(\frac{k_B T}{1\,{\rm MeV}}\right)^9 {\rm MeV\,cm^{-3}\,s^{-1}}, \tag{2.10}$$

where k_B is the Boltzmann constant.

Because of this dependence by the temperature, most of the neutrinos are emitted from a spherical shell around the NS of thickness

$$\Delta r_\nu = \frac{\epsilon_{e^-e^+}}{\nabla \epsilon_{e^-e^+}} = \frac{\Delta r_{\rm ER}}{9} \approx 0.08 R_{\rm NS}. \tag{2.11}$$

Then, using Eqs. (2.10) and (2.11), we can get the neutrino luminosity

$$L_\nu \approx 4\pi R_{\rm NS}^2 \, \Delta r_\nu \, \epsilon_{e^-e^+}. \tag{2.12}$$

For example, for $M_{\rm NS} = 2\ {\rm M}_\odot$ and $T \sim 1 - 10$ MeV, results a neutrino luminosity of $L_\nu \approx 10^{48} - 10^{57}$ MeV s^{-1} and a neutrino density of $\sim 10^{-1}$ cm^{-3}.

In Ch. (3) we study in more details another mechanism of neutrino production occurring in the BdHNe model, which does not enter in the cooling process during the evolution of the system, but it is related to the energy loss of the pair-photons-baryons plasma, emitted outward by the BH, in the interaction with the SN-ejecta.

2.5 Observations-Processes connection

In this section we briefly describe the connection between the frequency of the detected photons and their production process within the BdHNe model. The GRBs present different emission frequencies; in a time-series they can be summarized as follow: an early X-Ray precursors, $\gamma-$rays from the prompt emission, the GeV emission, the early and late X-Ray afterglow emission. Let's analyze each of these emissions and try to connect them with the specific physical production processes.

2.5.1 X-ray Precursor

The X-ray precursor can be explained by the SN-schock breakout (where the conversion of the SN shockwave kinetic energy into photons implies that almost an energy of $\sim 10^{50}$ erg can be emitted) or/and by the accretion of the SN-ejecta into the NS surface until the latter reaches the critical mass for the gravitational collapse into a BH, since the accretion triggers the emission and expansion of thermal convective bubbles placed on the surface of the NS, see [62, 52, 19, 153]).

2.5.2 GRB Prompt Emission

In the BdHNe model, the prompt emission of the GRB is explained by the transparency of e^+e^- highly relativistic plasma. Here we explain how this emission is created.

As we stated in Sec. (2.1), the class of BdHN I is composed by a νNS-BH binary surrounded by an asymmetric distribution of the SN-ejecta, which comprises a cavity of radius 10^{11} cm around the newly formed BH with a very low baryonic density (see [118]).

The BH is also immersed in a background magnetic field B_0 (derived by the old magnetized collapsed NS). This configuration of the system corresponds to what has been defined as the "*inner engine*" (see [130]). As demostrated by the Wald solution [152], a BH immersed in a test strong magnetic field generates an induced electric field whose radial component, evaluated in the polar direction ($\theta = 0$), assumes the following form (written in Boyer-Lindquist (BL) coordinates) (see [130, 136, 105] for the full expresison of electromagnetic field in BL coordinates):

$$E_{\hat{r}} = -\frac{2B_0 J G}{c^3} \frac{\left(r^2 - \hat{a}^2\right)}{\left(r^2 + \hat{a}^2\right)^2} \approx -\frac{1}{2}\alpha B_0 \frac{r_+^2}{r^2}, \tag{2.13}$$

that, when is evaluated at the BH horizon, $r_+ = (G/c^2)(\hat{M} + \sqrt{\hat{M}^2 - \hat{a}^2})$, becomes

$$E_{\hat{r}} \approx -\frac{1}{2}\alpha B_0 \approx 6.5 \times 10^{15}\, \alpha \left(\frac{B}{B_{cr}}\right) \quad \frac{\mathrm{V}}{\mathrm{cm}}. \tag{2.14}$$

Here $\hat{M} = GM/c^2$ and $\hat{a} = a/c = J/(M\,c)$, where J is the dimensionless angular momentum of the BH, M the BH mass and G the gravitational constant. $\alpha = J/M^2$ is the spin of the BH ($\alpha \leq 1$), while $B_{cr} = E_{cr} = m_e^2 c^3/e\hbar \simeq 4.4 \times 10^{13}$ Gauss is the critical magnetic/electric field [1].

The strong value of the electric field in Eq. (2.14) ensures the production of a huge amount of e^+e^- pairs in the spherical cavity around the BH by the quantum electrodynamics (QED) process of vacuum polarization (see [122]). This plasma expands from the BH site in all the directions and impacting with different amount of matter along its path due to the asymmetry of the SN-ejecta. Then, the plasma experience different dynamic depending on the expansion directions. The engulfed amount of matter along different angles in the equatorial plane is shown in Figs. (1.2) (1.3).

In the direction pointing from the $\mathrm{CO_{core}}$ to the NS, in the orbital plane, the cavity around the BH allows the pair-plasma to expand relativistically with a Lorentz boost $\Gamma \sim 10^2 - 10^3$, due to the low baryonic density ([118, 137]). These conditions bring the palsma to reach easily the transparency at a distance from the source of $10^{15} - 10^{17}$ cm, where MeV-photons are emitted and are observed in the ultrarelativistic prompt emission. The plasma of e^+e^- and γ impacts also to the matter present in the circum burst medium (CBM) ([100, 119, 121]), which can leads to the production of photons and neutrino via the photo-hadronic interaction ($\gamma + p \rightarrow \pi^0/\pi^\pm \rightarrow \gamma/\nu\bar{\nu}$).

2.5.3 Early X-ray Afterglow: Flares

The thermal emission observed in the early X-ray flares of the early afterglow of BdHNe implies that it is emitted at a distance from the source of $\sim 10^{12}$ cm, by a midly-relativistic plasma wiht a Lorentz boost $\Gamma \lesssim 4$ [129]. This scenario contrasts with the "fireball" model which needs an ultra-relativistic expansion of the plasma between the prompt emission and the afterglow.

In the directions where more matter is present (see Sec. (2.5.2)), the e^+e^- plasma impacts on the SN-ejecta at a distance of $\sim 10^{10}$ cm. The Lorentz boost of the plasma decreases proportionally to the amount of matter that the plasma encounters during the expansion until the value $\Gamma \lesssim 4$, reached at the transparency of the $e^+e^-\gamma$-baryon plasma.

The midly-relativistic emission emerging from this dynamic is observed in the thermal radiation of the early X-ray afterglow and X-ray flares. Some examples of this dynamic and emission has been observed, in the early hundreds of seconds, for GRB 090618 which has a velocity of $\beta \sim 0.8$ [125, 92], GRB 081008 has a velocity $\beta \sim 0.9$ [129], and GRB 130427A has a velocity of $\beta \sim 0.9$ as well [123, 154, 117].

2.5.4 Late X-ray Afterglow

It is shown in [117] that the X-ray afterglow is powered by: 1) the synchrotron emission of relativistic electrons (emitted by the νNS) inside the magnetized HN ejecta; 2) the νNS pulsar emission which extracts its rotational energy.

The analysis of the afterglow data allows to deduce the strength and the structure of the νNS magnetic field and its rotation period (see [153] for the procedure which comprises the derivation of the orbital period of the system, also through the prompt emission data, the $\mathrm{CO_{core}}$ rotation period and the assumption of the angular momentum conservation).

[1] In Gaussian units, the electric and magnetic field have the same dimension.

2.5.5 High-Energy GeV emission

In the BdHN model, the GeV emission can be explained by the protons synchrotron emission, when they are accelerated toward off-polar axis directions.

Let's consider again the "*inner engine*". As we stated in Sec. (2.5.2), the action of the background magnetic field and the rotation of the BH induce an electric field with an electric potential [135, 136]:

$$\Delta\phi = -\int_{\infty}^{r_+} E dr = E_{r_+} r_+ = 9.7\times 10^{20}\cdot\alpha\left(\frac{B_0}{B_c}\right)\left(\frac{M}{M_\odot}\right)(1+\sqrt{1-\alpha^2}) \quad \frac{\mathrm{V}}{e}. \tag{2.15}$$

This electric potential is able to accelerate protons to ultra-relativistic velocities and energies up to $\epsilon_p = e\Delta\phi \approx 10^{21}$ eV. Along the BH rotation axis there are no radiation emitted and, then, protons can reach very high energies and being emitted as UHECR and Neutrinos (see App. (D) for the description on how these neutrinos are created in this configuration and their detectability). On the off-polar directions, the protons emit synchrotron radiations with energy depending on the angle between their direction and the magnetic field. The smaller the angles, the higher the synchrotron photons energies.
The available electrostatic energy to accelerate protons is

$$\mathcal{E} = \frac{1}{2}E_{r_+}^2 r_+^3 \approx 7.5\times 10^{41}\cdot\alpha^2\left(\frac{B_0}{B_c}\right)^2\left(\frac{M}{M_\odot}\right)^3(1+\sqrt{1-\alpha^2})^3 \quad \mathrm{erg}, \tag{2.16}$$

so that the number of protons that the *inner engine* can accelerate is

$$N_p = \frac{\mathcal{E}}{\epsilon_p} \approx 4.8\times 10^{32}\alpha\left(\frac{B_0}{B_c}\right)\left(\frac{M}{M_\odot}\right)^2(1+\sqrt{1-\alpha^2})^2. \tag{2.17}$$

The time scale of the first elementary process is given by the time necessary to accelerate protons, i.e.:

$$\Delta t_{\mathrm{el}} = \frac{\Delta\phi}{E_{r_+}c} = \frac{r_+}{c} \approx 4.9\times 10^{-6}\left(\frac{M}{M_\odot}\right)(1+\sqrt{1-\alpha^2}) \quad \mathrm{s}. \tag{2.18}$$

Thus, finally, the emission power of the *inner engine* is approximately given by:

$$\frac{d\mathcal{E}}{dt} \approx \frac{\mathcal{E}}{\Delta t_{\mathrm{el}}} = 1.5\times 10^{47}\cdot\alpha^2\left(\frac{B_0}{B_c}\right)^2\left(\frac{M}{M_\odot}\right)^2(1+\sqrt{1-\alpha^2})^2 \quad \mathrm{erg}\cdot\mathrm{s}^{-1}. \tag{2.19}$$

The timescale of the subsequent processes depends on the time required to rebuild the electric field. This is guaranteed by the circumburst ionized medium, which supplies the protons that are accelerated outward of the system and the electrons that fall to the BH. Then, it is essential to know the density profile of this circumburst matter and its evolution with time [136, 137].

For a BH mass of $M \sim 2.2\ \mathrm{M}_\odot$ and spin $\alpha \sim 0.3$, it comes out a magnetic field $B \sim 6.7\, B_{cr} \approx 10^{14}$ Gauss, a number of protons $N_p \sim 10^{34}$ and electric power of $\frac{d\mathcal{E}}{dt} \sim 10^{49}$ erg s^{-1}. These numbers are in agreement with the GeV emission data (see [136] and [137], respectively, for the details of the analysis of GRB 130427A and GRB 190114C).

2.6 Summary

In this chapter we have summarized the basic differentiation between GRBs. They have been divided in eight subclasses and we summarized the principal features of each GRBs. In [153] the GRB subclasses introduced in [128] and in [111, 106], have been renominated and they have been divided into two main groups: binary-driven hypernovae (BdHNe) and compact-object binary mergers (BMs). The old and the new nomenclature, together with some principal characteristics, are summarized in Tab. (2.1). We have

Table 2.1. Summary of the Gamma-ray bursts (GRB) subclasses. This table is an extended version of the one presented in [153] with the addition of a column showing the local density rate, and it also updates the one in [128, 131]. We unify here all the GRB subclasses under two general names, BdHNe and BMs. Two new GRB subclasses are introduced: BdHN Type III and BM Type IV. In addition to the subclass name in "Class" column and "Type" column, as well as the previous names in "Previous Alias" column, we report the number of GRBs with known redshift identified in each subclass updated by the end of 2016 in "number" column (the value in a bracket indicates the lower limit). We recall as well the "in-state" representing the progenitors and the "out-state" representing the outcomes, as well as the peak energy of the prompt emission, $E_{\rm p,i}$, the isotropic Gamma-ray energy, $E_{\rm iso}$ defined in the 1 keV to 10 MeV energy range, the isotropic emission of ultra-high energy photons, $E_{\rm iso,Gev}$, defined in the 0.1–100 GeV energy range, and the local observed rate $\rho_{\rm GRB}$ [128]. We adopt as definition of kilonova a phenomenon more energetic than a nova (about 1000 times). A kilonova can be an infrared-optical counterpart of a NS-NS merger. In that case the transient is powered by the energy release from the decay of r-process heavy nuclei processed in the merger ejecta [77, 85, 148, 23]. FB-KN stands for fallback-powered kilonova [111, 106]: a WD-WD merger can emit an infrared-optical transient, peaking at ∼5 day post-merger, with the ejecta powered by accretion of fallback matter onto the newborn WD formed in the merger. The density rate of the GRB subclasses BdHN III (HN) and BM IV (FB-KN) have not yet been estimated.

Class	Type	Previous Alias	Number	*In-State*	*Out-State*	$E_{\rm p,i}$ (MeV)	$E_{\rm iso}$(erg)	$E_{\rm iso,Gev}$ (erg)	$\rho_{\rm GRB}$ (Gpc^{-3} yr^{-1})
Binary-driven	I	BdHN	329	$CO_{\rm core}$-NS	νNS-BH	∼0.2–2	$\sim10^{52}$–10^{54}	$\gtrsim10^{52}$	$0.77^{+0.09}_{-0.08}$
hypernova	II	XRF	(30)	$CO_{\rm core}$-NS	νNS-NS	∼0.01–0.2	$\sim10^{50}$–10^{52}	–	100^{+45}_{-34}
(BdHN)	III	HN	(19)	$CO_{\rm core}$-NS	νNS-NS	∼0.01	$\sim10^{48}$–10^{50}	–	–
	IV	BH-SN	5	$CO_{\rm core}$-BH	νNS-BH	$\gtrsim2$	$>10^{54}$	$\gtrsim10^{53}$	$\lesssim0.77^{+0.09}_{-0.08}$
	I	S-GRF	18	NS-NS	MNS	∼0.2–2	$\sim10^{49}$–10^{52}	–	$3.6^{+1.4}_{-1.0}$
Binary	II	S-GRB	6	NS-NS	BH	∼2–8	$\sim10^{52}$–10^{53}	$\gtrsim10^{52}$	$\left(1.9^{+1.8}_{-1.1}\right)\times10^{-3}$
Merger	III	GRF	(1)	NS-WD	MNS	∼0.2–2	$\sim10^{49}$–10^{52}	–	$1.02^{+0.71}_{-0.46}$
(BM)	IV	FB-KN	(1)	WD-WD	NS/MWD	<0.2	$<10^{51}$	–	–
	V	U-GRB	(0)	NS-BH	BH	$\gtrsim2$	$>10^{52}$	–	$\approx0.77^{+0.09}_{-0.08}$

concentrated our attention on the subclasses of BdHNe (type I and II) and XRFs. BdHNe I and II have as a common progenitor a $CO_{\rm core}$-NS binary. The $CO_{\rm core}$ explodes as type Ic SN, forming at its center a new NS, which we denote νNS, and produces onto the NS companion a hypercritical accretion process accompanied by an intense neutrino emission. The intensity of the accretion process and the neutrino emission depend mainly on the binary period, being more intense for tighter binaries. The NS companion in such an accretion process can reach or not the critical mass for gravitational collapse, i.e., to form a BH. The former binaries leading to a BH by accretion are the BdHNe I, while the ones in which the NS companion becomes just a more massive NS, are the BdHNe II (the old XRFs) (see Tab. (2.1)).

We described the theoretical aspects of the *induced gravitational scenario* (IGC) applied to the formation and evolution of the BdHN class.

We provided briefly some observational features of the model, namely which process and at what time of the evolution observable photons are produced.

The simulations, from $1-D$ to $3-D$ simulations, provided many informations about the physics of the GRB and highlighted new results as the evolution of the SN-ejecta from a spherical to an asymmetric distribution due to the accretion process.

We reviewed, and recall here, the fundamental processes occurring in the BdHNe model:

(1) the SN explosion;

(2) the hypercritical accretion onto the NS companion;

(3) the NS collapse with consequent BH formation;

(4) the initiation of the *inner engine*;

(5) the e^+e^- plasma production;

(6) the e^+e^- plasma feedback onto the SN, which converts the SN into a HN;

(7) the formation of the cavity around the newborn BH;

(8) the transparency of the e^+e^- plasma along different directions;

(9) the HN emission powered by the νNS;

(10) the action of the *inner engine* in accelerating protons leading to UHECRs and to the high-energy emission.

Some of these physical processes listed above for the BdHN leave specific observable signatures in the long GRB multiwavelength lightcurves and spectra. For each process we have recalled its energetics, spectrum, and associated Lorentz factor: from the mildly-relativistic X-ray precursor, to the ultra-relativistic prompt Gamma-ray emission, to the mildly-relativistic X-ray flares of the early afterglow, to the mildly-relativistic late afterglow and to the high-energy GeV emission.

Concerning the latter emission, it is related to the process of rotational energy extraction from a BH. The ingredients necessary for this procedure are: a rotating BH, a background magnetic field where the BH is immersed, the presence of matter surrounding the BH which feeds it with baryonic and leptonic particles. The BdHN model presenting these characteristics and this structure has been called the "*inner engine*" of the high-energy emission (see [135, 136, 137, 118]). The presence of a background magnetic field and the rotation of the BH induce a strong electric field, because of the Wald's mechanism [152], which is able to accelerate protons and positrons to high energy. The particles accelerated along the polar axis of the BH will leave the system as UHECRs, while the one propagating to a certain angle, with respect to the magnetic field, will emit synchrotron radiation which explain (depending on the value of the angle) the high energy radiation.

In the next chapters we focus our attention to two different processes which occur in the BdHN model. These processes concern baryonic (Ch. 3) and leptonic (Ch. 4) particles, occurring in different moments and regions of the system, that can lead to a direct (Ch. 3) or indirect (Ch. 4) observational counterpart:

(1) In Ch. (3), we study the neutrino production from pp interaction, occurring in the equatorial plane of the νNS-BH system, between protons engulfed and accelerated by the e^+e^- plasma (which becomes a leptonic-baryonic-radiation plasma) with protons, at rest, ahead of the plasma and not yet phagocytozed by it. We study also the interaction of this plasma (with higher energy) with protons in the interstellar medium.

(2) In Ch. (4), we study the process of magnetic field screening operated by e^+e^- pair accelerated in the polar direction of the BH. The particles start to circularize around the magnetic field lines and create an induced magnetic field in the opposite direction with respect to the background one. This leads to a reduction of the total magnetic field which leads to the transparency of the $e^+e^-\gamma$ plasma and, then, to the emission of observable radiation.

Chapter 3

Neutrino and gamma-ray emission from pp interaction in the BdHN model

3.1 Introduction

Multi-messenger astronomy is a fundamental technique to get complementary information about the physical processes, dynamics, evolution and structure behind the cosmic sources emission [31]. With the advent of new facilities generating high-quality data of cosmological energetic sources such as supernovae (SNe), gamma-ray bursts (GRBs) and active galactic nuclei (AGN), the analysis of the multi-messenger emission becomes a necessity. Our aim here is to present, for the case of long GRBs, the emission of the neutrino messenger from the process of proton-proton (pp) interactions occurring in the source.

Many studies about neutrino emission from GRB has been made since the pioneering work of Waxman & Bahcall [155]. They study the production of neutrinos of energies $E_\nu \sim 10^{14}$ eV coming from the photomeson process by the interaction between very-high energy accelerated protons ($E_p \lesssim 10^{20}$ eV) and photons emitted by means of synchrotron/IC radiation by accelerated electrons. Other works followed specifically studying the neutrino production in the traditional *fireball* model of GRBs (see for example: [17], [84], [156], [157]). In these works, it is shown that within the *fireball* the νs are produced by the decay of pions and muons created by the internal shock, mainly by two dominant processes: 1) photomeson production ($p + \gamma \rightarrow \pi, \mu \rightarrow \nu_{\mu,e}$) between very-high energies Fermi accelerated protons and synchrotron/IC photon ($\sim$ 1 MeV) from accelerated electrons. The neutrinos created via this channel have energies $\sim 10^{14}$ eV [156]. If the protons are accelerated up to $\sim 10^{20}$ eV and interact with photons of few eV (Optical-UV photons), neutrinos emerge with energies $\sim 10^{18}$ eV [157]; 2) π and μ production via the proton-neutron interaction channel, between accelerated protons and coasting neutrons [17] [84], once these two components of the same expanding fireball are decoupled. This channel gives rise to νs with energies of $5 - 10$ GeV. In order for this channel to occur some conditions need to be satisfied: the fireball needs a certain amount of neutrons, the dimensionless entropy parameter $\eta = (L/\dot{M}c^2)$ needs to be greater than a specific value ($\eta \gtrsim 400$), the relative velocity between p and n needs to be $v_{rel} \rightarrow c$.
Other two ways of neutrino production that have been investigated in the GRB literature are the n decay and νs associated to a stellar collapse or to a merging event which leading to a GRB (see [84] and references therein). Both of these ways are less efficient compared to the previous channels and produce neutrinos of energies $10 \leq E_\nu \leq 100$ MeV, that would be difficult to detect due to the low values of νN cross section for low E_ν.

As already stated above, in this work we study the neutrino production from pp interaction following, instead of the fireball model, the BdHN model, whose characteristics have been already stated in Ch. (2) and, specifically for our purposes, are exposed in the next sections. The typical energies of the escaping νs are $\sim$ GeV and, as we will show in this chapter, the interaction dynamics is different with respect to the one of the *fireball* model.

3.1.1 BdHN I: from MeV to GeV and TeV neutrinos

There are two principal classes of GRBs (see [128] or Tab. (2.1) for the subdivision of long and short GRBs in seven different subclasses). The "short bursts" originate in the mergers of binaries composed of a neutron star (NS) accompanied either by another NS, or a white dwarf (WD) or a black hole (BH), or mergers of binary WDs. The "long bursts" split in four different subclasses, all of them originating from binaries which have been called *binary-driven hypernovae* (BdHNe) of type I, II, III and IV [153].

We are here interested in BdHNe I (see Tab. (2.1) for further quantitative details about this and other GRB classes and subclasses). The progenitor is composed of a pre-SN carbon-oxygen star (hereafter CO_{core}) and a NS companion in close orbit [19, 52, 109]. The explosion of the CO_{core} as SN forms a newborn NS (hereafter νNS) at its center and, at the same time, ejects material that triggers a hypercritical accretion process onto the NS companion. Depending on the binary parameters, the system leads to the following subclasses (see Fig. (3.1) and [19, 21, 153]). In compact binaries with orbital periods ~ 5 min, the accretion onto the NS is sufficient to bring it to the critical mass, forming a BH by gravitational collapse. These are the BdHNe I, and they explain energetic long bursts with isotropic energy in gamma-rays $E_{\rm iso} \gtrsim 10^{52}$ erg and peak energy $E_{p,i} \gtrsim 200$ keV. We refer the reader to [110, 153] for details on the BdHNe II–IV.

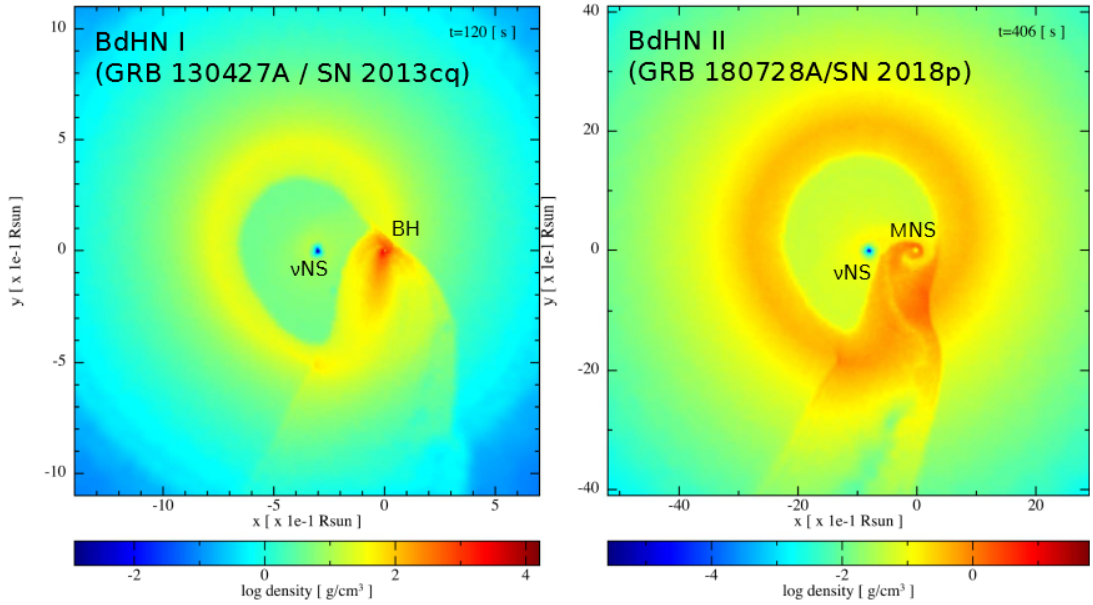

Figure 3.1. Selected SPH simulations from [21] of a CO_{core} exploding as SN in presence of a NS companion: Model '25m1p08e' with $P_{\rm orb} = 4.8$ min (left panel) and Model '25m3p1e' with $P_{\rm orb} = 11.8$ min (right panel). The pre-SN star is a CO_{core} of mass $M_{\rm CO} = 6.85\ M_\odot$, evolved from a $25\ M_\odot$ zero-age main-sequence (ZAMS) progenitor. The initial mass of the NS companion is $M_{\rm NS} = 2\ M_\odot$. The plots show the density colormap on the orbital plane. The coordinate system has been rotated and translated to place the NS companion at the origin $(0, 0)$ and the νNS along the x-axis. The binary in the left panel is a BdHN I [153] and the snapshot is at the time of the collapse of the NS companion to a BH, $t = 120$ s from the SN shock breakout ($t = 0$ s of the simulation). The right-panel binary leads to a BdHN II and the snapshot corresponds to $t = 406$ s after the SN trigger.

Formation channel and occurrence rate of BdHN

The BdHN I forms NS-BH binaries and the parameters for which the hypercritical accretion leads the NS to the critical mass, with consequent gravitational collapse forming a rotating BH, have been widely explored (see, e.g., [52, 19, 21]). This knowledge, in turns, has allowed to envisage possible evolutionary paths for these binaries.

The evolutionary path leading to BdHN is thus expected to be closely related to the ones known for the formation of compact-object binaries, e.g., NS-NS or NS-BH, as introduced by the X-ray binary and SN communities. Thus, a plausible BdHN formation channel starts with a binary composed of, e.g., $\gtrsim$ 10-12 $M_\odot$ zero-age main-sequence (ZAMS) components [109, 20]. After the core-collapse of the primary, the binary is formed by a newly born NS and the secondary, ordinary star. The system then evolves through mass-transfer episodes and possibly multiple common-envelope epochs [150]. These binary interactions lead to the ejection of the hydrogen and helium outermost layers of the secondary star. At this stage, the binary is composed of a CO_{core} (or a helium star) and a NS companion. The X-ray binary and SN communities dubbed these systems "*ultra-stripped*" binaries [150]. These binaries are thought to produce the 0.1–1% of the SN population [149].

Therefore, the binary progenitors of the BdHN are expected to be formed in an evolutionary path very similar to the one of *ultra-stripped* binaries. The majority of population synthesis simulations lead to *ultra-stripped* binaries with orbital periods 3×10^3–3×10^5 s [150], which are longer than the ones of BdHN. It is then clear that the BdHN progenitors must be a small subset of the binary progenitors of *ultra-stripped* binaries. This conforms with the fact that GRBs are indeed a rare phenomenon, i.e. their density rate is much lower with respect to other astrophysical sources, therefore the population of binaries that end with the appropriate physical conditions to produce a BdHN must be low [51].

The observed occurrence rate of BdHN I and II are, respectively, ~ 1 Gpc^{-3} yr^{-1} and ~ 100 Gpc^{-3} yr^{-1} [128]. Therefore, they are 0.5% and 0.005% of the SNe Ibc rate, which is 2×10^4 Gpc^{-3} yr^{-1} [58]. Since (0.1–1%) of the SN Ibc are expected to be produced by *ultra-stripped* binaries [149], their density rate is expected to be in the range (20–200) Gpc^{-3} yr^{-1}. This implies that $\lesssim 5\%$ of this population is enough to explain the BdHN I population. Interestingly, these estimates agree with traditional population synthesis analyses concluding that only $\sim$ 0.001–1% of massive binaries lead to double compact-object binaries [53, 42, 99].

Baryonic content available for proton-proton interactions in a BdHN I

A copious neutrino emission is one of the crucial physical phenomena characterizing the BdHN scenario [52]. Thanks to the neutrino-antineutrino flux, the accretion process onto the NS can proceed at hypercritical, super-Eddington rates, leading to neutrinos of energies 20–30 MeV with luminosities of up to 10^{51} erg s^{-1} (see, e.g., [19]). Interestingly, neutrino flavour oscillations owing to neutrino self-interactions have been also shown to be relevant during this hypercritical accretion process [22].

In this work, we focus on the emission of neutrinos of higher energies than the aforementioned ones. Specifically, we show that BdHN I also produce neutrinos (and photons), in the GeV and TeV energy domains, via pp interactions.

In order to set up the possible pp interactions occurring in a BdHN I, we start by analyzing the structure of the baryonic matter present. For this task, we make use of recent three-dimensional simulations of this system [19, 21]. Fig. (3.1) shows a snapshot of the BdHN I-II formation taken from [21, 153] (see also Fig. (2.2) for a time sequence of the event). The SN ejecta, although starts expanding in a spherically symmetric way, becomes highly asymmetric by the accretion process onto the NS [19, 21] and the BH formation [118]. Due to this morphology, the electron-positron (e^+e^-) plasma created in the process of BH formation, which expands isotropically from the newborn BH site, experiences a different dynamics along different directions due to the different amounts of baryonic matter encountered [129].

In the direction pointing from the CO_{core} to the accreting NS, outwards and lying on the orbital plane, the NS and the BH formation cave a region characterized by very poor baryon pollution, a *cavity* (see Figs. (3.1) and (3.2); see also [19, 21, 118]). The production of the e^+e^- plasma and its subsequent evolution and transparency leading to sub-MeV emission, overcoming the so-called GRB *compactness problem*, has been extensively studied in the theoretical framework of the *fireshell* model, which fully solves the hydrodynamic equations of motion of the plasma (see [101, 119, 121, 24]). We refer to these

references for details. The formation of the e^+e^- pair plasma is governed by quantum electrodynamics, i.e. $\hbar/(m_e c^2) \sim 10^{-21}$ s, while the collapse of the NS into a BH occurs on a gravitational timescale $GM/c^3 \sim 10^{-6}$ s. No numerical relativity simulations are currently able to simultaneously follow such extremely different timescales. However, general relativistic effects can be considered since the e^+e^- pair creation occurs locally, in the exterior spacetime, and the energy density of pairs is low enough to disregard its feedback onto the spacetime. Therefore, the background metric can be considered as fixed in the estimation of the pair-creation rate and its evolution [119]. The verification of this model, in the analysis of the prompt emission of specific GRB sources, can be found, e.g., in [97, 64, 94, 88] (see also Sec. (2.5) for the connections between the observed radiation from GRBs and the physical processes producing each specific emission in the BdHN model).

These studies have been specialized in the case when the e^+e^- plasma incorporates a limited amount of baryons, characterized by a *baryon load* parameter $B \lesssim 10^{-2}$. The *baryon load* is defined as $B \equiv M_b c^2/E_{e^+e^-}$, namely the ratio between the baryon rest-mass energy respect to the e^+e^- energy. Such low values of B allow the plasma to reach transparency with high Lorentz factor $\Gamma \sim 1/B \gtrsim 10^2$, needed to explain the gamma-ray prompt emission of the GRB. We denote with γ the Lorentz factor of a single particle, and with Γ the one of bulk motion.

In the other directions along the orbital plane, the e^+e^- plasma penetrates inside the SN ejecta at $\sim 10^8$–10^{10} cm, and evolves swallowing up much larger amounts of baryons, finally reaching transparency at 10^{12} cm with $\Gamma \lesssim 4$. The theoretical description and numerical simulations of this evolution in which the e^+e^- plasma engulfs larger amounts of baryons ($B \sim 100$) have been presented in [129]. We recall that, therein, it has been also shown that the transparency of this plasma with such Γ explains the observed flares in the X-rays at nearly 100 s (rest-frame time) in the early GRB afterglow.

3.1.2 Characterizing the pp interactions in a BdHN I

From the above physical and geometrical description, we are ready to set up the properties of the incident and target protons. Therefore, at least two types of pp interactions occur in a BdHN I:

1. Interaction of the protons with $\Gamma < 7$ within the self-accelerated e^+e^-p plasma that penetrates the high baryon density SN ejecta, with the unshocked protons ahead the plasma expansion front, at rest inside the ejecta (see Fig. (3.2)).

2. Interaction of the protons with $\Gamma \sim 10^2$–10^3 loaded in the self-accelerated e^+e^-p plasma in the direction of least baryon density around the newborn BH, with the protons at rest of the interstellar medium (ISM) (see Fig. (3.2)). We adopt that the plasma encounters the ISM clouds at a distance $\sim 10^{16}$ cm from the system, as inferred from the time and value of Γ at transparency, and the agreement of the simulation of the GRB prompt emission with observational data (see, e.g., [64] for details).

The pp interaction between accelerated protons with the target protons, at rest, ahead of them (in both scenarios) is described by the following process:

$$p + p \rightarrow \Delta^{++} \rightarrow \begin{cases} p + n + \pi^+, \quad \pi^+ \rightarrow \mu^+ + \nu_\mu, \quad \mu^+ \rightarrow e^+ + \nu_e + \bar{\nu}_\mu \\ p + p + \pi^0, \quad \pi^0 \rightarrow 2\gamma \\ p + p + \pi^+ + \pi^-, \quad \pi^\pm \rightarrow \mu^\pm + \nu_\mu(\bar{\nu}_\mu), \quad \mu^\pm \rightarrow e^+(e^-) + \nu_e(\bar{\nu}_e) + \bar{\nu}_\mu(\nu_\mu) \\ p + n + \pi^+ + \pi^+ + \pi^-. \end{cases} \tag{3.1}$$

The different decays of the Δ^{++} resonance depend on its energy. If it is a $\Delta^{++}(1232)$, it decays mainly in a nucleon and a pion ($N + \pi$) with branching ratio B.R.=99, 4%; higher Δ decays in a nucleon plus a pion ($N + \pi$) with lower B.R. or in a $\Delta(1232) + \pi$ with the consequent decay of the $\Delta(1232)$ as before.

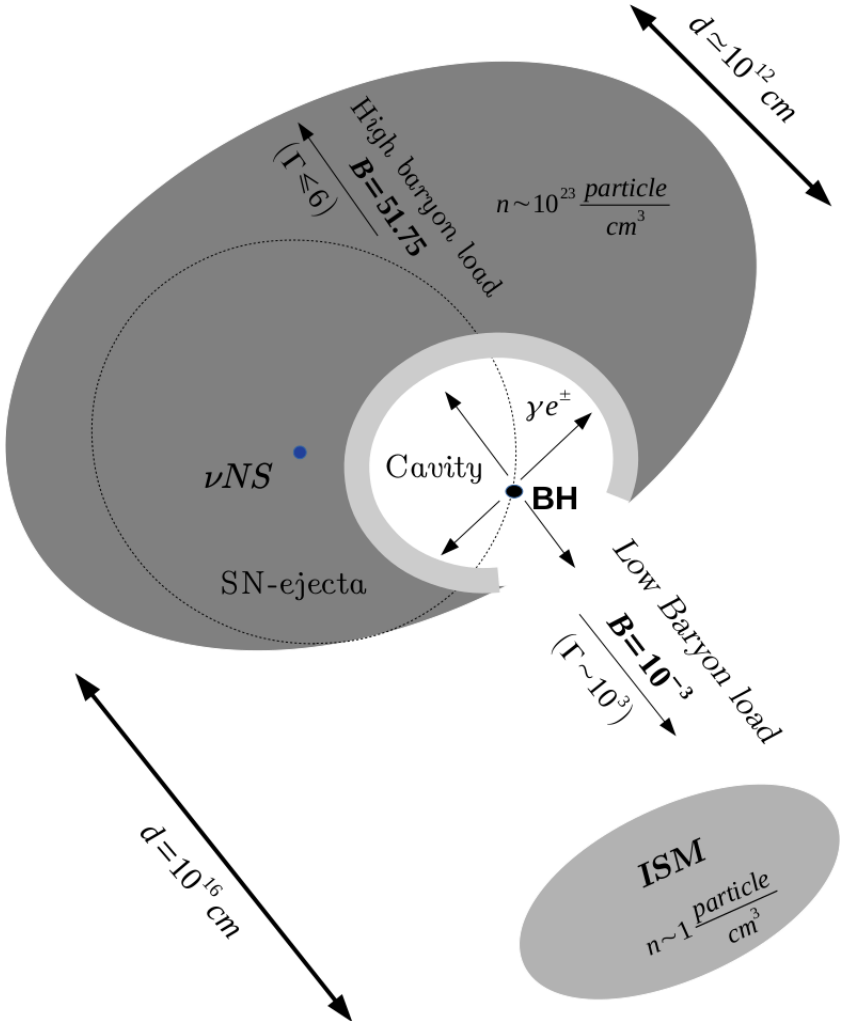

Figure 3.2. Schematic figure of the pp interactions occurring in a BdHN. The interactions 1) and 2) as described in the text: 1) the e^+e^- plasma propagates in the direction of high baryon load, e.g., $B = 51.75$, reaching Lorentz factor of up to $\Gamma \lesssim 7$ in their travel inside the ejecta. The incorporated protons have such Γ and interact with the protons at rest, ahead of the plasma front, and deposited all of their energy. The dotted circular line represents the νNS-BH binary orbit; 2) protons incorporated by the e^+e^-p plasma propagate in the direction where the cavity is open. This plasma is loaded with a relatively low baryon content (e.g., $B \sim 10^{-3}$), so the plasma reaches high Lorentz factor at transparency, $\Gamma \sim 10^2$–10^3. The loaded protons have such Γ factor and interact with the ISM protons at rest.

We shall carry out this analysis in detail in the following sections. In Sec. (3.2), we compute the process of interaction during the initial stages of the expansion of the e^+e^- plasma inside the SN ejecta, namely the interaction 1). We describe how, from the simulations of this expansion/interaction process, we got the physical quantities necessary to compute the particles spectra (Sec. (3.2.1)). We show the different neutrino spectra emerging from the interaction in Sec. (3.2.2). We consider for the cross-section of pp inelastic scattering the parameterization of [25]. We assume a monochromatic protons energy distribution derived from the value of the proton Lorentz factor at every radius of the shell expansion. In Sec. (3.3), we focus on the second type of interaction, the case 2). Since the protons energies are greater than in the case 1), i.e. $E_p \sim 1$ TeV, we use the parameterization by [70], both for the pp cross-section and the emerging particle spectra, that is appropriate for protons energies until 10^5 TeV. Finally, we discuss and summarize in Sec. (3.4) the main results of this work and we try to give an estimate for a direct and indirect detection of the produced neutrinos (and related photons) and, then, a prove for the BdHN model itself.

3.2 pp interactions inside the high-density ejecta

In this section, we analyze here the pp interaction that occurs when the $e^+e^-\gamma$ plasma starts to load the baryons present in the SN ejecta, forming a $e^+e^-\gamma p$ plasma (see Fig. (3.2)). In order to study this phenomenon we have done relativistic hydrodynamic (RHD) simulations of the dynamics of the e^+e^- plasma expanding and swapping baryonic matter in the SN ejecta. The simulations (see [129], for additional details) have been performed with a one-dimensional implementation of the RHD module of the PLUTO code [86]. The equations and the thermodynamical variables, that need to be integrated, are those we have already stated in Sec. (1.2.2): namely Eqs. (1.3), (1.4), (1.5), with Eqs. (1.6), (1.7) and (1.8).

The simulation starts at the moment of BH formation, so the initial conditions are taken from the final configuration of the numerical simulations in [19]:

1. The SN remnant is obtained from the explosion of the CO_{core} evolved from a zero-age main-sequence (ZAMS) star of mass $M_{ZAMS} = 30\ M_\odot$. This CO_{core} has a total mass of $11.15\ M_\odot$, of which $2\ M_\odot$ conform the mass of the νNS (collapsed iron core) and $9.15\ M_\odot$ conform the total ejecta mass (envelope mass). At the SN explosion time, the ejecta profile follows a power-law profile $\rho \propto r^{-2.8}$ (see, e.g., [19]).

2. The orbital period is $P \approx 5$ min, i.e. a binary separation $a \approx 1.5 \times 10^{10}$ cm.

3. The ejecta have negligible pressure and is considered to be in homologous expansion, $v(r) \propto r$, spanning velocities from 10^8 cm s^{-1} of the innermost ejecta layer to 2×10^9 cm s^{-1} of the outermost one. The velocity of the remnant is, however, not relevant in the dynamics of the e^+e^- plasma since its velocity is much higher than the one of the remnant. Therefore, for practical purposes, the remnant can be considered at rest as seen from the plasma.

4. The baryon load of the e^+e^- plasma is not isotropic: the baryon density is different along different directions. This can be appreciated in Figs. (3.1), (3.2) and in Figs. (34) and (35) of [129]). According to the three-dimensional simulations of [19], the density profile of the ejecta, at the BH formation time, decays with distance as a power-law, i.e. $\rho \propto (R_0 - r)^\alpha$. The normalization, the constant R_0 and the parameter $2 < \alpha < 3$ depend on the emission angle, fixing a direction.

5. The total isotropic energy of the e^+e^- plasma is set to $E_{e^+e^-} = 3.16 \times 10^{53}$ erg. This value derives from the values of the initial conditions that have led to the formation of the BH (see [19, 129]) and, consequently, to the formation of the e^+e^+ plasma by vacuum polarization process. Therefore, according to the above ejecta properties, in the high density region the baryon load parameter results equal to [1]

$$B = \frac{M_b\, c^2}{E_{e^+e^-}} = \frac{(9.15\ M_\odot)\ c^2}{3.16 \times 10^{53}\ \text{erg}} = 51.75$$

.

The evolution from these initial conditions leads to the formation of a shock and to its subsequent expansion until reaching the outermost part of the SN. An example of the results of this expansion are shown in Sec. (1.2.2) and, principally, in Figs. (1.3), (1.4). Since throughout this expansion baryons are continuously phagocytosed, the spectrum of the secondary particles, the proton energy distribution, and the baryon number density n_B depend all on the radial position of the shock. Taking snapshots of this process, we obtain the relative spectrum for each secondary particle within a thin shell close to the shock. In the end, we integrate all these spectra over the radius to have an estimate of the released energy through the different channels.

Considering that the protons follow a Maxwell-Boltzmann energy distribution in the comoving frame, it can be seen that the energy distribution in the laboratory frame is peaked enough to be well-approximated

[1] One solar mass is $M_\odot = 1.989 \times 10^{33}$ g; the speed of light is $c = 2.99792458 \times 10^{10}$ cm/s.

by a delta-function. Hence, we consider a monochromatic proton energy distribution $J_p(E_p)$: namely, $J_p(E_p) \propto \delta(E_p - E_p^0)$. The value of E_p^0 depends on the Lorentz factor $\gamma(r)$. Due to the momentum-energy conservation, γ decreases rapidly with time. Therefore, we focus on the first stages of the expansion when protons have enough energy to interact. We estimate the interactions from a radius r_i where the $\gamma e^{\pm}$ plasma with protons has the maximum Lorentz factor, up to a final radius, r_f, over which the proton energy goes down below the interaction energy threshold (see below). Despite the threshold radius is at $r_{th} = 4.79 \times 10^{10}$ cm, in order to have clear spectra with enough points, from our numerical simulation, we find that the interaction region extends from $r_i = 9.59 \times 10^8$ cm to $r_f = 2.98 \times 10^{10}$ cm, so $\Delta r = r_f - r_i = 2.88 \times 10^{10}$ cm. This can be compared with the total extension of the SN ejecta that is of the order of 10^{12} cm [129].

In the following section, we describe how we extract from these simulations the physical quantities, that we use to compute the particles spectra in Sec. (3.2.2): the protons Lorentz factor, the number density of the incident and target protons, each of them considered at every radius of the expansion of the shock inside the ejecta.

3.2.1 Physical quantities for the pp interaction

The baryons of the SN ejecta are incorporated time by time, at every radius, by the $e^{\pm}\gamma$ plasma. Therefore, the incident protons are the ones engulfed on the expanding shock front, which have the maximum $\gamma(r)$ factor. The target protons are the ones of the ejecta that has not been yet loaded by the plasma, and located closely to the shock front. These target protons can be safely assumed to be at rest with respect to the incident protons in the shock front. Having clarified this, we identify the physical quantities needed to calculate the spectra at each radius: the Lorentz factor of the protons in the shock front, γ_p, their energy, their density, $n_{\rm sh}$, and the density of the unshocked protons, n_t. These quantities change at every radius as the plasma expands inside the ejecta. We refer to all quantities in the laboratory frame.

The procedure to compute the above quantities is as follows. First, we obtain the position of the shock front from the simulation, i.e. $r_{\rm front}$. This radius can be estimated as the radius at which the pressure inside the SN ejecta falls off abruptly since it separates the shocked and unshocked regions. It corresponds also to the radius at which the protons of the shock have their maximum Lorentz factor. Although the pressure at $r > r_{\rm front}$ falls down fast, the extension of this region is smaller than the mean-free-path of the front protons, λ_p, defined by $\lambda_p^{-1} = \sigma_{\rm pp}\left(E_p\right) \times n_p$, where $\sigma_{\rm pp}$ is the pp cross-section and n_p their number density. Thus, in order to calculate the density of the incident and target protons, we make an average process to consider all the possible interacting protons at a given time. For the incident protons density, $\langle n_{\rm sh} \rangle$, we average the radial density in the region $r_{\rm front} - \lambda_p < r < r_{\rm front}$. We can consider it as the incident density at an average radius $\langle r_{\rm front} \rangle$. A similar averaging process is applied ahead the front, i.e. in the region $r_{\rm front} < r < r_{\rm front} + \lambda_p$, to obtain the density of the target protons, $\langle n_{\rm t} \rangle$.

Then, we calculate the maximum value of γ_p inside the shell and, correspondingly, the energy of the protons, $E_p(r) = \gamma_p(r) m_p c^2$. The protons Lorentz factor γ_k^p, at the generic radius r_k, is given by the value of the baryons velocity, β_k^p, at the shock front position $\langle r_{\rm front} \rangle$. The profile of the maximum values of the Lorentz factor, at every front radius, is shown in Fig. (3.3). We emphasize that each point in the curve of γ_p in Fig. (3.3) corresponds to the maximum value of the Lorentz factor in the front of the shell. The numerical simulations of the expansion of the plasma inside the ejecta gives us a distribution of the particles velocity (see Fig. (1.4)). From this velocity distribution, we extract the maximum Lorentz factor, consistently with the density average process explained above (see the peaks of the shell front in Fig. (1.4)). From the discussion above, we recognize that the maximum protons Lorentz factor, in Fig. (3.3), corresponds to the Lorentz factor of the shell bulk motion Γ (showed in Fig. (1.4)), namely $\gamma_p = \Gamma(r_{\rm front})$

From the above, we can see that the energy of protons is in the range $1.24 \leq E_p \leq 6.14$ GeV, which is high enough to produce secondary particles. The proton energy threshold to produce pions in the final

state is, for the interaction $pp \to pn\pi^+$, $E_{p,\mathrm{Th}} = 1228$ MeV and, for $pp \to pp\pi^0$, $E_{p,\mathrm{Th}} = 1217$ MeV. The neutrino production at these low energies is dominated by the protons with the highest energy ($\gamma \sim 6$).

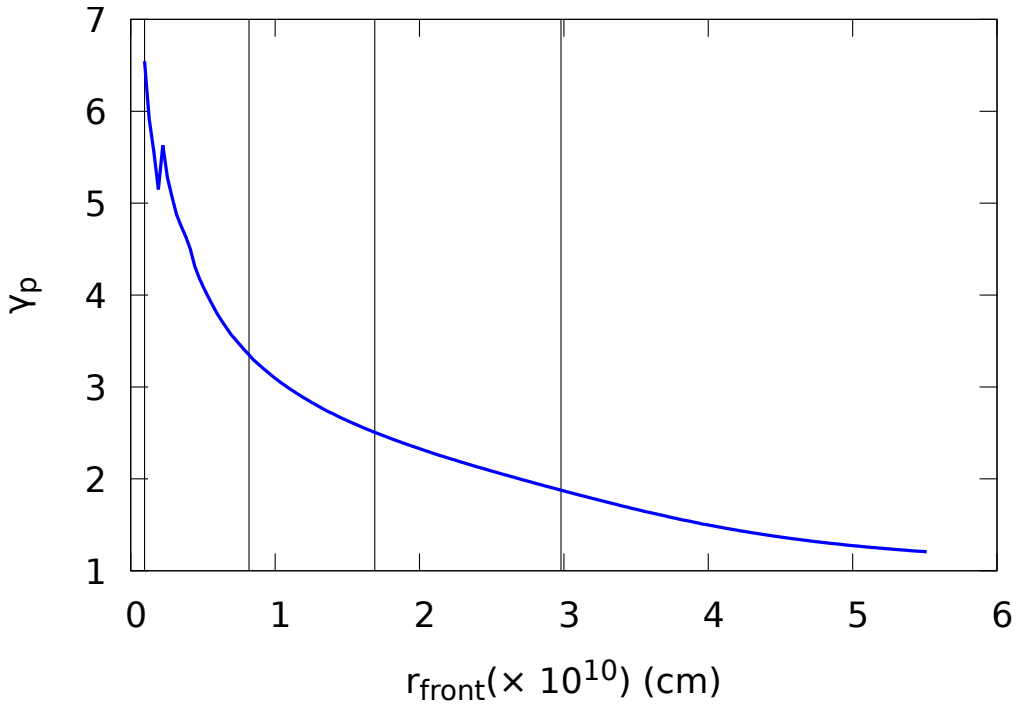

Figure 3.3. Evolution of the Lorentz factor of the protons in the shell front, γ_p, as a function of the front radius position. Clearly, this Lorentz factor of the protons in the shell is the same as the one of the shell bulk motion at the front position, i.e. $\gamma_p = \Gamma(r_{\mathrm{front}})$, since outside the front the protons are roughly at rest with respect to the shell (the velocity of the remnant is much slower). The vertical lines are four selected radii: $r_1 = r_i = 9.59 \times 10^8$ cm, $r_2 = 8.19 \times 10^9$ cm, $r_3 = 1.69 \times 10^{10}$ cm, and $r_f = 2.98 \times 10^{10}$ cm. We recall that at the position $r = r_i$ the protons have the maximum γ factor; for $r = r_f$ see the text.

Fig. (3.3) also shows four vertical lines at fixed radii of reference: the first vertical line corresponds to the radius r_i where the protons have their maximum energy, while the last line corresponds to the radius r_f (there $\gamma_p = 1.878$). The intermediate radii have been chosen only to show the evolution of the particles spectrum during the expansion. In the following, we compute the particles spectra at these four specific radii (different values of the radii will be explicitly indicated).
In the region of the expansion of the shock, at every radius, the average number density of the target protons $\langle n_t \rangle$ in the remnant varies between 8×10^{23} cm^{-3} at r_i to $\sim 5 \times 10^{23}$ cm^{-3} at $r_{\mathrm{end}} = 5.51 \times 10^{10}$ cm (the end point of the simulation). The protons number density at the front of the expanding shell, $\langle n_{\mathrm{sh}} \rangle$, does not vary much either; it is in the range $(0.5\text{–}9) \times 10^{25}$ cm^{-3} (the maximum value occurs in the region close to the initial radius r_i, and the lower value to the final radius r_{end}), as shown in Fig. (3.4). Even in this last figure, the density is plotted as a function of the front radius (consistently with Fig. (3.3)). The decrease of $\langle n_{\mathrm{sh}} \rangle$ can be explained by the following considerations. From the values of n_{t} above, we see that, due to the geometry of the system (see Fig. (3.2)) the target density decreases moving towards the outermost regions (see Fig. (3.1)). Then, during it's expansion, time by time, the plasma incorporates less matter. Moreover, at the beginning of the expansion, since the target density is higher, the Lorentz factor of the protons starts to drop down. Now, remembering how we calculate the front number density (and, then, its definition) as we explained above, namely as a punctual density in a region close to the front of the expanding shell, we understand that the combination of the two factors of a lower plasma expansion

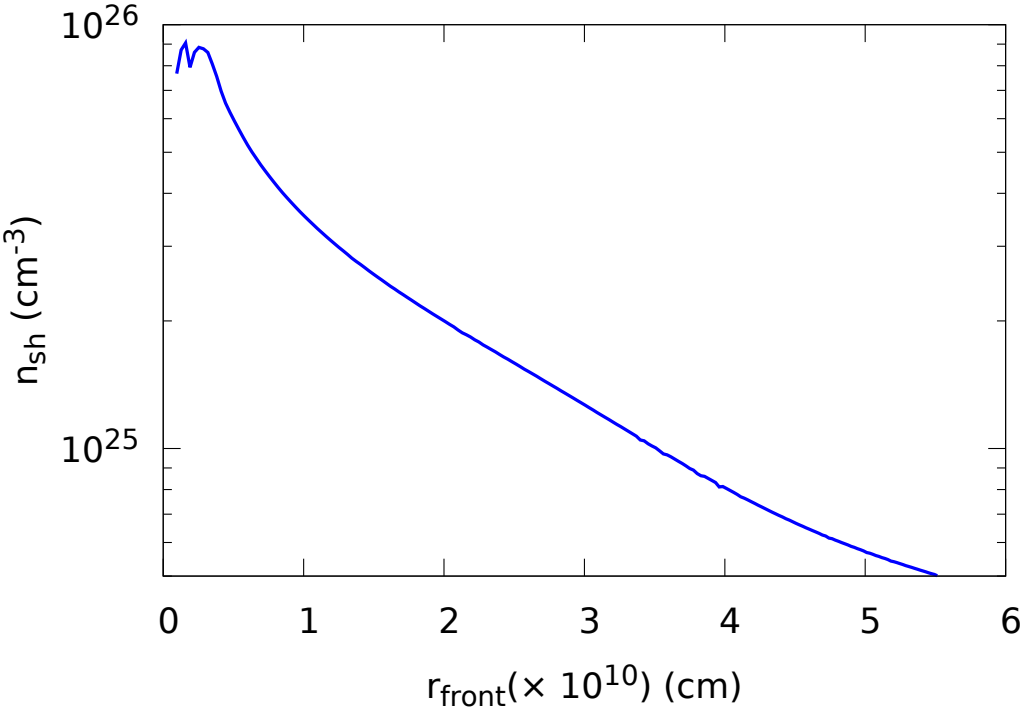

Figure 3.4. Average baryons number density of the expanding shell at the front position $r_{\rm front}$.

rate and lower target density leads to a decrease of shell number density.

Having derived all the necessary physical quantities, we proceed next to the calculation of the spectra of the emerging particles.

3.2.2 Particles spectra

We turn now to the spectra for the emerging particles from the decay of the π and the μ. We need to consider the fact that the μ can be unpolarized and polarized.

In order to obtain the pions production rate, we have used the parameterization for the pion production cross-section presented in [25]. In this work, they provide a useful formula, $d\sigma(E_\pi, E_p)/dE_\pi$, for the production of the three types of pions (π^0, π^+, π^-) as a function of the pion and incident proton energy in two ranges of incident protons kinetic energy in the laboratory frame $T_p^{\rm lab}$: $0.3 \leq T_p^{\rm lab} \leq 2$ GeV and $2 \leq T_p^{\rm lab} \leq 50$ GeV (the parameterization for the differential pion-production cross-section is given in App. (A)). Then, this parameterization of the cross-section in [25] is appropriate for our calculations since it is accurate in the energy region of the present interest, namely $E_p < 7$ GeV.

Then the pions production rate can be computed as

$$Q_\pi(E_\pi) = cn_p \int_{E_\pi}^{E_p^{\rm max}} J_p(E_p) \frac{d\sigma(E_\pi, E_p)}{dE_\pi} dE_p, \tag{3.2}$$

where $J_p(E_p)$ is the proton energy distribution, n_p the number density of the target protons in the remnant,c the speed of light and $E_p^{\rm max}$ is the maximum energy of the protons in the system. Since we consider a fixed value for the proton energy, E_p^0, at the front of each spherical shell, we assume $J_p(E_p) = A\delta(E_p - E_p^0)$, where A is the baryon number density at front of the shell.

With this choice for $J_p\left(E_p\right)$, the equation for the production rate $Q_\pi\left(E_\pi\right)$ becomes

$$Q_\pi\left(E_\pi\right) = cn_p A \frac{d\sigma\left(E_\pi, E_p^0\right)}{dE_\pi}\theta\left(E_p^0 - E_\pi\right)\theta\left(E_p^{\max} - E_p^0\right). \tag{3.3}$$

With Eq. (3.3) for the π production rate, we can compute the spectra for all the particles. Because the cross-section for neutral, negative and positive pions are different, we need to distinguish between emerging particles from π^0 decay in 2 photons, π^- decay: $\pi^- \to \mu^-\,\bar{\nu}_{\mu^{(1)}}$; $\mu^- \to e^- + \bar{\nu}_e + \nu_{\mu^{(2)}}$ and from π^+ decay: $\pi^+ \to \mu^+\,\nu_{\mu^{(1)}}$; $\mu^+ \to e^+ + \nu_e + \bar{\nu}_{\mu^{(2)}}$. In each of the following paragraphs will be shown the spectra for each specific particle from the three mesons.

We denote the spectrum of the produced particle a as $\Phi_a = dN_a/dE_a$, where we indicate with N_a the particle number density per unit time.

Throughout this chapter, we denote as $\nu_{\mu^{(1)}}$ the muonic neutrino/antineutrino from the direct pion decay, $\pi \to \mu\nu_\mu$, and $\nu_{\mu^{(2)}}$ the neutrino/antineutrino from the consequent muon decay, $\mu \to e\nu_\mu\nu_e$.

γ spectrum

The spectrum of photons emerging from π^0 decay is given by

$$\Phi_{\pi^0\to\gamma\gamma}\left(E_\gamma\right) = 2\int_{E^{\min}(E_\gamma)}^{E_\pi^{\max}} \frac{Q_\pi(E_\pi)}{\sqrt{E_\pi^2 - m_\pi^2 c^4}} dE_\pi, \tag{3.4}$$

where $E^{\min}\left(E_\gamma\right) = E_\gamma + m_{\pi^0}^2 c^4/(4E_\gamma)$ can be derived by the kinematics (see App. (B)). The factor 2 is to take into account the two produced photons. $Q_\pi\left(E_\pi\right)$ is given by Eq. (3.3), with the respective pions spectral distribution for π^0 (see App. (A)).

The photons emissivity (in erg/cm^3/s) is shown in Fig. (3.5), while the total energy (in erg), integrated over all photons energies and calculated via Eq. (3.19) (see later Sec. (3.2.3)), in the emissivity region, is given in Tab. (3.1).

$\nu_{\mu^{(1)}}$ spectrum

The spectrum of neutrino from direct pion decay $\pi \to \mu\nu_\mu$ can be calculated as follow

$$\Phi_{\pi\to\mu\nu_\mu}\left(E_{\nu_\mu}\right) = \frac{1}{\lambda}\int_{E^{\min}\left(E_{\nu_\mu}\right)}^{E_\pi^{\max}} \frac{Q_\pi(E_\pi)\theta\left(\lambda - \frac{E_{\nu_\mu}}{E_\pi}\right)}{\sqrt{E_\pi^2 - m_\pi^2 c^4}} dE_\pi, \tag{3.5}$$

where the values of $E_\pi^{\max}$ and $E^{\min}\left(E_{\nu_\mu}\right) = E_{\nu_\mu}/\lambda + (\lambda m_\pi^2 c^4)/(4E_{\nu_\mu})$, are derived from the kinematic of the process (see App. (B)); $\lambda = 1 - r_\pi$, with $r_\pi = (m_\mu/m_\pi)^2$, is the maximum energy fraction that the neutrino emerging from the direct decay can take from the pion.

The spectra derived by Eq. (3.5) must be calculated, via Eq. (3.2), using the parameterization of the cross-section for π^- : $d\sigma_{\pi^-}(E_\pi; E_p)/dE_\pi$, and for π^+ : $d\sigma_{\pi^+}(E_\pi; E_p)/dE_\pi$, given in [25] (see App. (A)). The $\nu_{\mu^{(1)}}$ emissivities (in erg/cm^3/s), for both mesons, are shown in Fig. (3.6). The total energy (erg), integrated over the whole region of emissivity, is given in Tab. (3.1).

$\nu_{\mu^{(2)}}$ and ν_e spectra

The neutrino spectra from the decay chain $\pi \to \mu \to \nu$ can be calculated as:

$$\Phi_{\pi\to\mu\to\nu_\mu/\nu_e}\left(E_\nu\right) = \int_{E^{\min}(E_\nu)}^{E_\pi^{\max}} \frac{Q_\pi(E_\pi)}{\sqrt{E_\pi^2 - m_\pi^2 c^4}}\, g\left(\frac{E_\nu}{E_\pi}\right) dE_\pi. \tag{3.6}$$

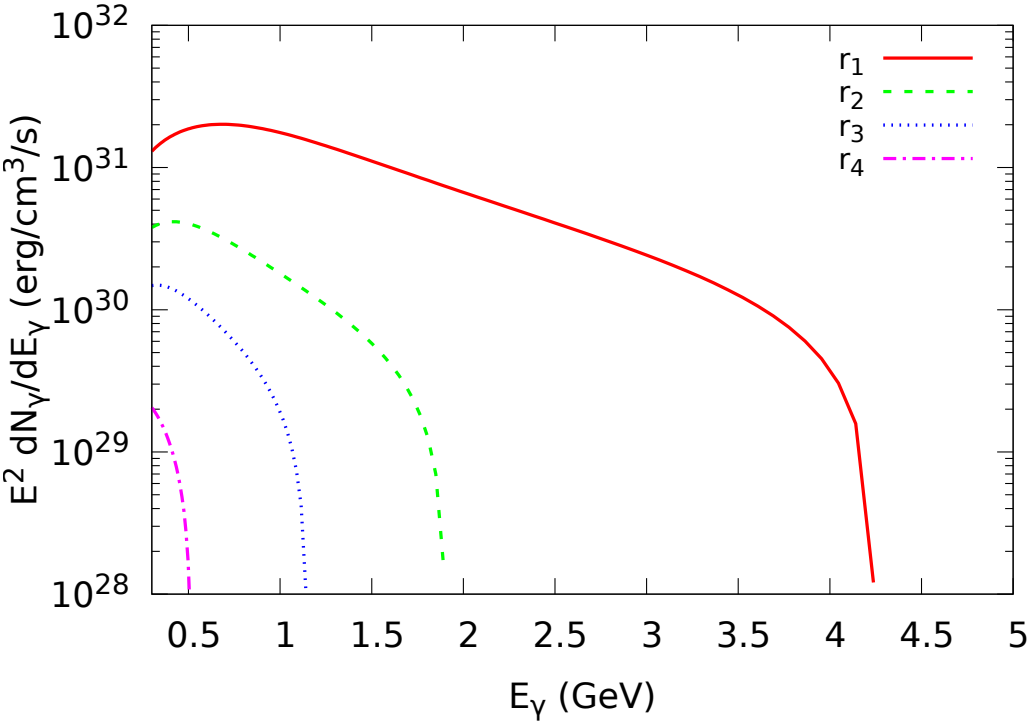

Figure 3.5. Photons spectrum from the decay $\pi^0 \to \gamma\gamma$. The profiles are shown at four selected radii for the expansion of the shell inside the ejecta: the radii $r_{2,3}$ are the same of Fig. (3.3), $r_1 = 1.28 \times 10^9$ cm and$r_4 = 3.287 \times 10^{10}$ cm. At $r \gtrsim r_4$, the proton energy approaches (from higher energies) the interaction threshold energy producing an emission cut-off that makes difficult to draw a spectrum for those positions keeping the same numerical resolution.

Here the pion production rate Q_π is given in Eq. (3.3). The functions $g(z)$ are taken from [78] and represent the ν spectra after the decay chain ($\pi \to \mu \to \nu$) and can be written, in the relativistic and ultrarelativistic limit ($\beta_\pi \to 1$, $\beta_\mu \to 1$), in the following form (see [78])

$$g(z) = \begin{cases} G\left(\frac{z}{r_\pi}\right) - G(z), & \text{for } z \le r_\pi \\ G(1) - G(z), & \text{for } z \ge r_\pi. \end{cases} \tag{3.7}$$

The function $g(z)$ can be decomposed as the sum of an unpolarized spectrum, $g^0(z)$, plus a polarized one, $g^{\rm pol}(z)$, $g(z) = g^0(z) + g^{\rm pol}(z)$. The functions $G(z)$, polarized and unpolarized, can be found in the Appendix of [78] and are reported in the next paragraphs. Here the limit $\beta_\pi \to 1$ is well satisfied. Indeed, from the kinematics, we obtain that the Lorentz factor of the pions lies in the range $4.5 \le \gamma_\pi \le 34.5$.

Without polarization. In order to have an expression for the spectrum of the particles coming from the μ-decay, we have to insert Eq. (3.3) into Eq. (3.6), with $g(z)$ given by Eq. (3.7). The equations for $G(z)$ for $\nu_{\mu^{(2)}}$ and for ν_e (for unpolarized muon) are (see Appendix A in [78]):

$$G^0_{\pi\to\mu\to\nu_\mu}(y) = \frac{1}{1-r_\pi}\left[\frac{5}{3}\ln(y) - \frac{3}{2}y^2 + \frac{4}{9}y^3\right], \tag{3.8a}$$

$$G^0_{\pi\to\mu\to\nu_e}(y) = \frac{1}{1-r_\pi}\left[2\ln(y) - 3y^2 + \frac{4}{3}y^3\right]. \tag{3.8b}$$

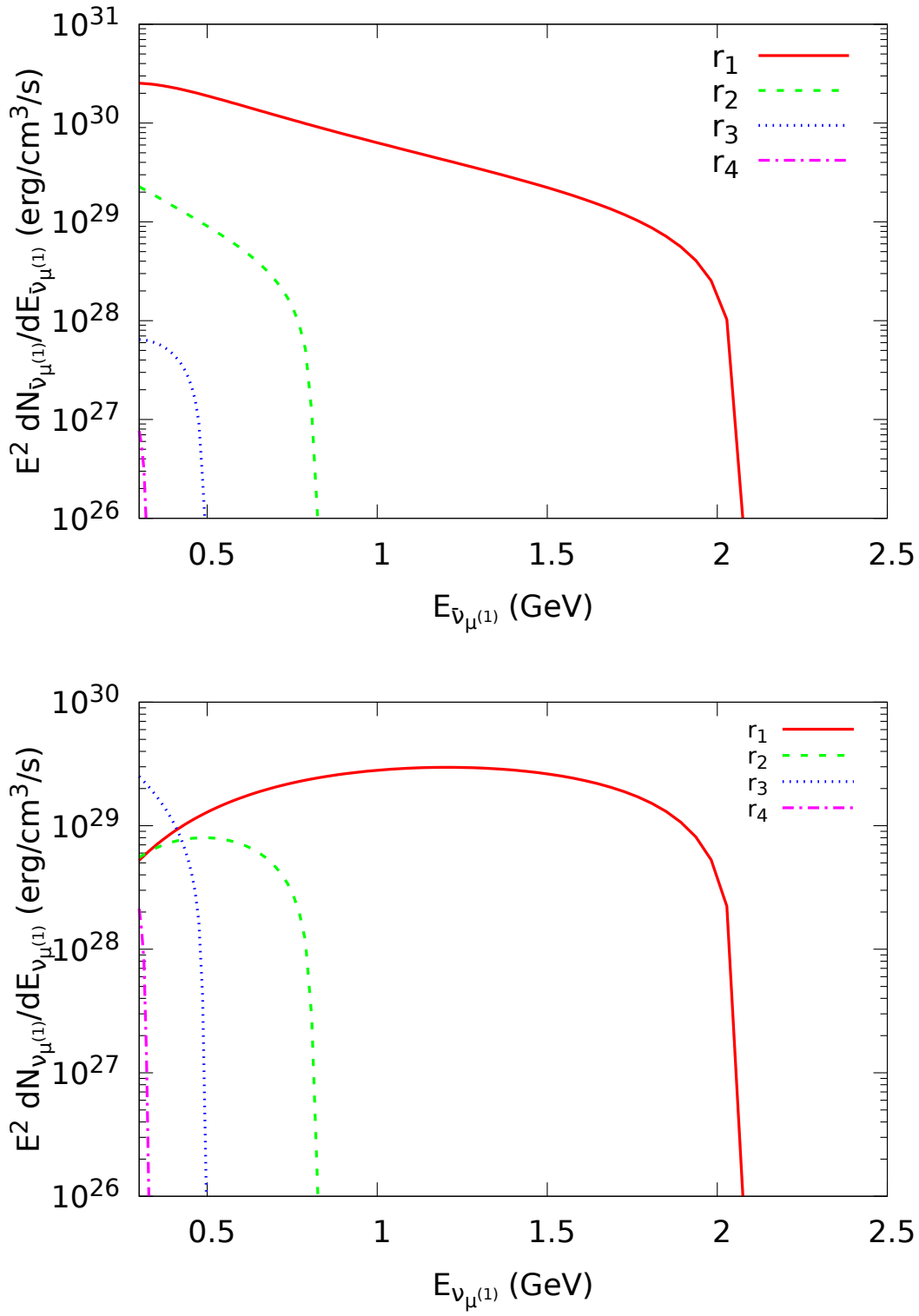

Figure 3.6. Top panel: direct neutrino emissivity from π^--decay. Bottom panel: direct neutrino emissivity from π^+-decay. The different curves in each plot refer to the same radii of Fig. (3.3), but with $r_4 = 2.6 \times 10^{10}$ cm.

Inserting Eqs. (3.8) in Eq. (3.7) and Eq. (3.7) in Eq. (3.6), we can integrate this formula to get the spectra of $\nu_{\mu^{(2)}}$ (with $G(z)$ given by Eq. (3.8a)) and ν_e (with $G(z)$ given by Eq. (3.8b)). The minimum integration value $E^{\rm min}$ derives from the kinematic and is the same for the two particles

$$E^{\rm min}\,(E_\nu) = E_\nu + \frac{m_\mu^2 c^4}{4E_\nu}, \tag{3.9}$$

with $E_\nu = E_{\nu_{\mu^{(2)}}}$ or E_{ν_e} (see App. (B)).

The emissivities for $\nu_{\mu^{(2)}}$ and ν_e are shown, respectively, in Fig. (3.7) (for the particles from π^- decay) and Fig. (3.8) (for the particles from π^+ decay). Let us consider now the case with polarization.

With polarization. Since the muon can be polarized (μ^+ has on average negative helicity and μ^- a positive helicity), the neutrinos produced by these muons depend on this polarization [78]. In order to get the spectrum of emerging particles, in Eq. (3.7), beside to Eq. (3.8a) and (3.8b) (for the unpolarized spectrum), we need to add similar functions for the polarized spectrum. The formula for the polarized spectrum are the following (see [78])

$$G^{\rm pol}_{\pi\to\mu\to\nu_\mu}(y) = \frac{1}{(1-r_\pi)^2}\left\{\frac{1+r_\pi}{3}\ln(y) - \frac{2r_\pi}{3z}y - \frac{3}{2}(1+r_\pi)\,y^2 + \left[\frac{8}{9}(1+r_\pi) + \frac{2r_\pi}{z}\right]y^3 - \frac{4r_\pi}{3z}y^4\right\}, \tag{3.10}$$

$$G^{\rm pol}_{\pi\to\mu\to\nu_e}(y) = \frac{1}{(1-r_\pi)^2}\left\{-2(1+r_\pi)\ln(y) + \left[12(1+r_\pi) + \frac{4r_\pi}{z}\right]y - \left[9(1+r_\pi) + \frac{12r_\pi}{z}\right]y^2 + \right.$$
$$\left. + \left[\frac{8}{3}(1+r_\pi) + \frac{12r_\pi}{z}\right]y^3 - \frac{4r_\pi}{z}y^4\right\}. \tag{3.11}$$

Then the formula for the spectra of νs coming from the decay chain $\pi \to \mu \to \nu$ are given by $g(z) = g^0(z) + g^{\rm pol}(z)$, where $g^0(z)$ is the $g(z)$ for the unpolarized particles (Eqs. (3.8a) and (3.8b)), and $g^{\rm pol}(z)$ the one for polarized particles (Eqs. (3.10) and (3.11)). Inserting $g(z)$ in Eq. (3.6), and integrating in energy, we obtain the spectrum of these emerging neutrinos. The minimum energy to choose for the integral is given by the same Eq. (3.9).

The emissivity of $\nu_{\mu^{(2)}}$ and $\bar{\nu}_e$, from π^- decay, are shown in Fig. (3.9), while the ones for $\bar{\nu}_{\mu^{(2)}}$ and ν_e, from π^+ decay, are shown in Fig. (3.10).

3.2.3 Total luminosity and total energy release

As we have seen from the above formulation we can obtain the particle spectra at every radius r_i, which we denote hereafter as $\Phi^i_a(E_a)$. Thus, the particle emissivity at every radius, ϵ^i_a, is given by

$$\epsilon^i_a = \int_{0.3\,{\rm GeV}}^{E_\pi^{\rm max}} \Phi^i_a(E_a)\,E_a dE_a, \tag{3.12}$$

where $E_\pi^{\rm max}$ is the maximum pion energy derived from the kinematic of the process.
Then, the power ("luminosity") emitted in particles of type a, at the radius r_i, is

$$L^i_a = \int_{V_i} \epsilon^i_a dV, \tag{3.13}$$

where the integration is carried out over the volume V_i of the emitting/interacting shell at the front position r_i.

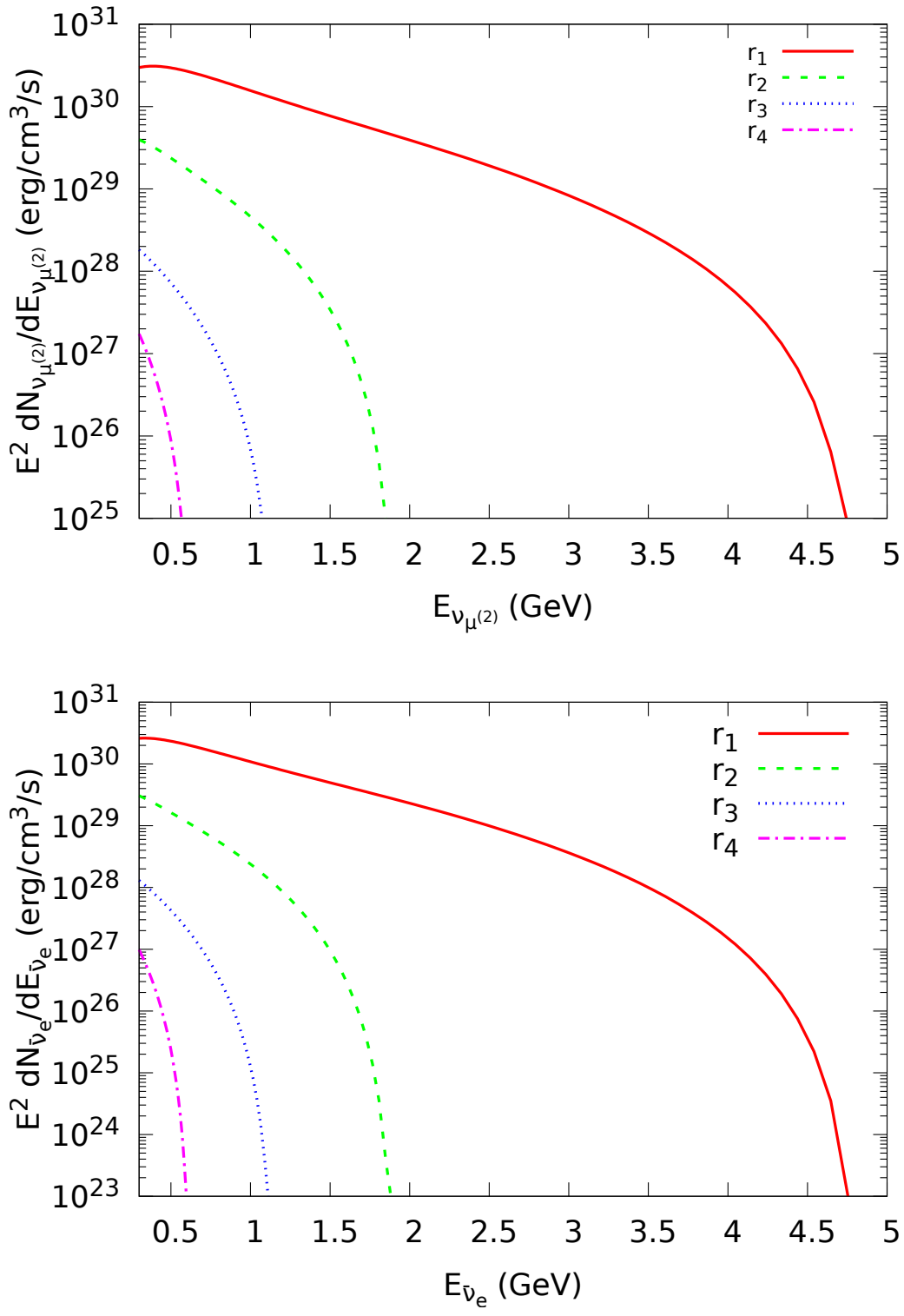

Figure 3.7. Neutrinos from the decay chain $\pi^- \longrightarrow \mu^- \longrightarrow \nu_{\mu^{(2)}} + \bar{\nu}_e$. Top panel: $\nu_{\mu^{(2)}}$ emissivity at the same radii of Fig. (3.5). Bottom panel: $\bar{\nu}_e$ emissivity at the same radii.

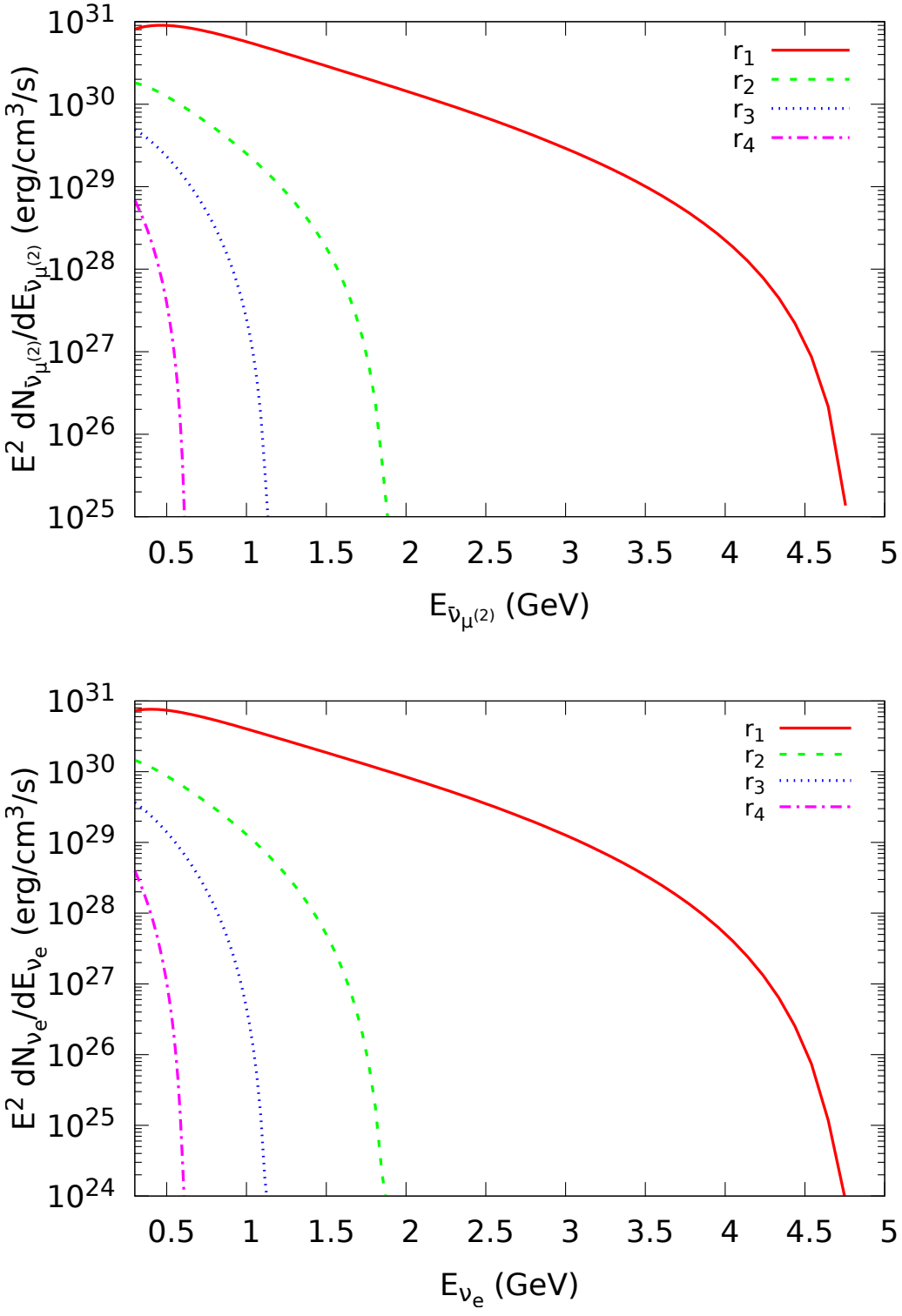

Figure 3.8. Neutrinos from the decay chain $\pi^+ \longrightarrow \mu^+ \longrightarrow \bar{\nu}_{\mu^{(2)}} + \nu_e$.Top panel: emissivity of $\bar{\nu}_{\mu^{(2)}}$ at the same radii of Fig. (3.5). Bottom panel: ν_e emissivity at the same radii.

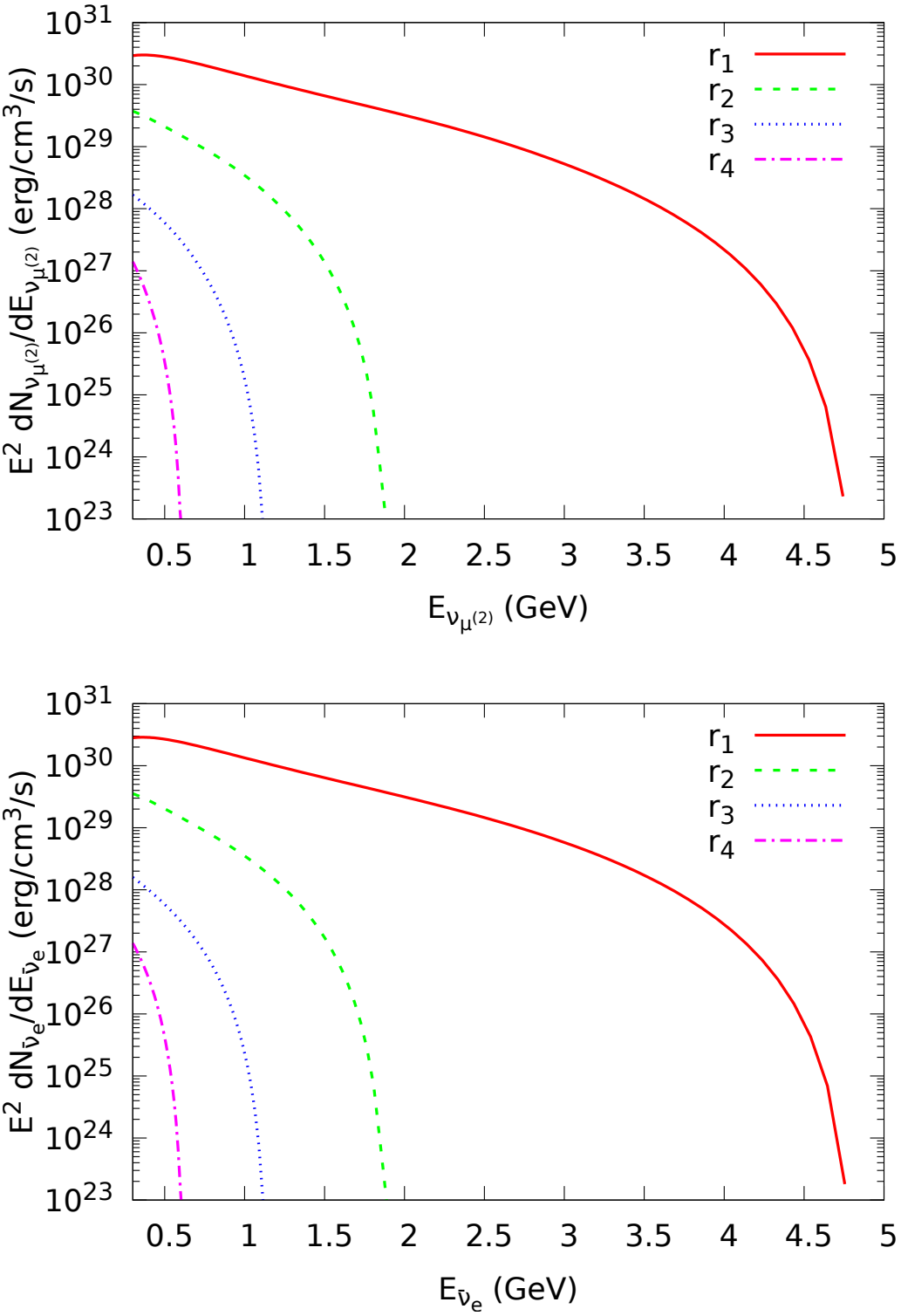

Figure 3.9. $\nu_{\mu^{(2)}}$ (top panel) and $\bar{\nu}_e$ (bottom panel) emissivity from μ^- decay considering the polarization effect.

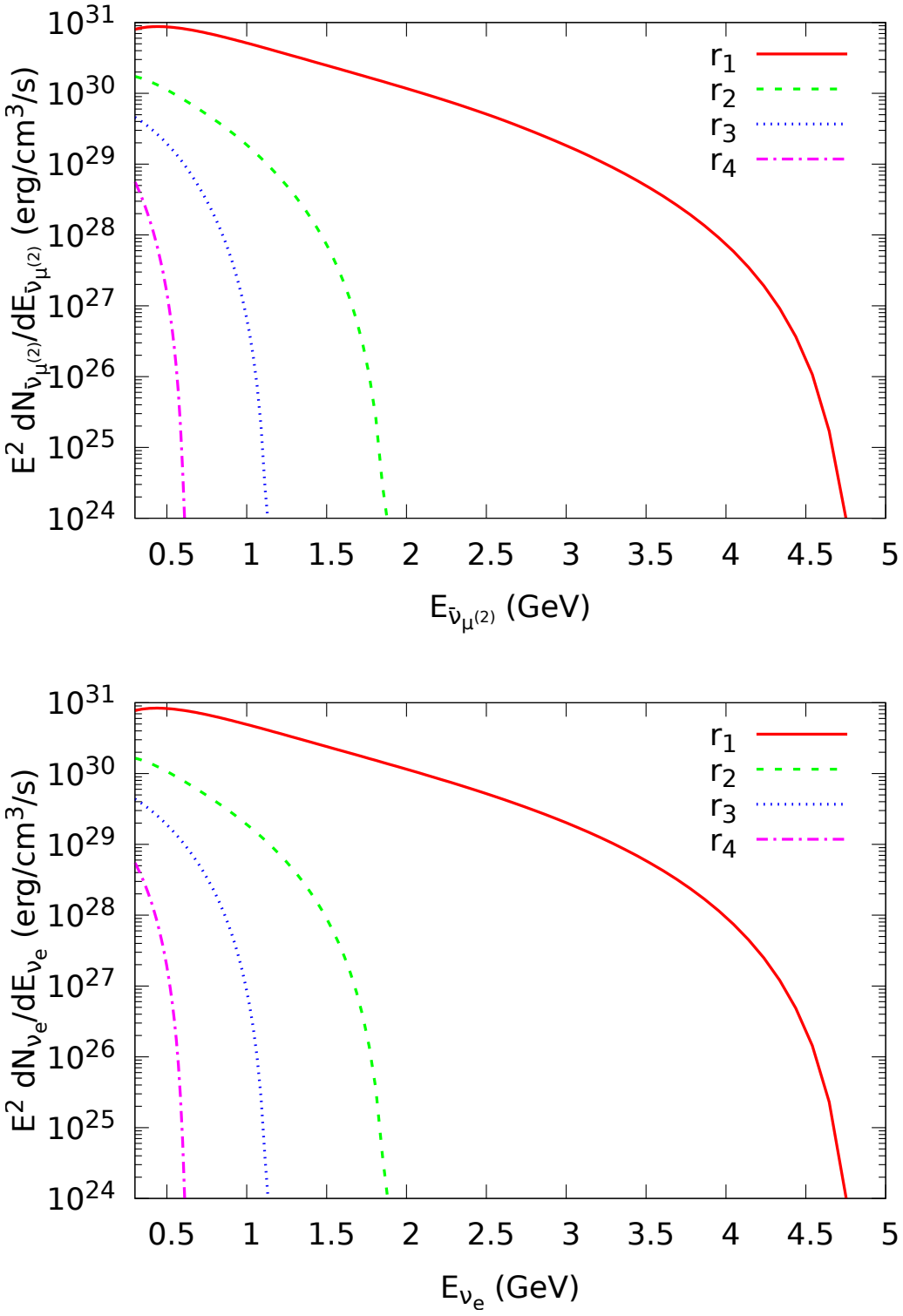

Figure 3.10. $\bar{\nu}_{\mu^{(2)}}$ (top panel) and ν_e (bottom panel) emissivity from μ^+ decay considering the polarization effect.

The total emissivity and luminosity at the radius r_i can be obtained as the sum of the contributions of all particles, i.e.:

$$\epsilon^i_{\rm tot} = \sum_a \epsilon^i_a, \tag{3.14}$$

$$L^i_{\rm tot} = \sum_a L^i_a. \tag{3.15}$$

The energy emitted in a-type particles is given by

$$\mathcal{E}_a = \int L^i_a(t)\, dt, \tag{3.16}$$

where the integration is carried out over all the duration of the emission. Therefore, the total energy emitted in all the emission processes is

$$\mathcal{E} = \sum_a \mathcal{E}_a. \tag{3.17}$$

From the numerical simulation of the expanding shell inside the remnant, we know that the width of the shell is of the order of $\Delta r_{\rm sh} \approx 3 \times 10^8$ cm. Since the mean free path of the interaction is much smaller than the shell width (see below), the interacting volume at the radius i is, approximately, $V_i = 4\pi r_i^2 \lambda_i$, where λ_i is the mean-free path of the protons of energy E^i_p in the shell front. The mean-free path is given by $\lambda_i = (\sigma_{\pi^{\pm,0}} A)^{-1}$, where A (defined before for the protons energy ditribution $J_p\left(E_p\right)$) is the baryon number density at the front, and $\sigma_{\pi^{\pm,0}}$ is the inclusive cross-section for π^-, π^+ and π^0 (see [25] and App. (A)). For π^+: $0.4 \leq \lambda^i_{\pi^+} \leq 11$ cm; for π^-: $1.18 \leq \lambda^i_{\pi^-} \leq 45$ cm; for π^0: $0.65 \leq \lambda^i_{\pi^0} \leq 50.4$ cm [2]. Having defined this volume, we can calculate the luminosity L^i_a at each radius following Eq. (3.13), i.e.

$$L^i_a \approx \epsilon^i_a V_i \approx \epsilon^i_a \times 4\pi r_i^2 \lambda_i. \tag{3.18}$$

Fig. (3.11) shows, as an example, the luminosity L^i_a as a function of time, for $a = \bar{\nu}_{\mu^{(2)}}$, with and without considering the polarization effects.

Clearly, the luminosity is nonzero only in the region of the ejecta where pp interaction leads to a nonzero production of secondary pions. Therefore, the emission occurs till the instant when the shell reaches the radius $r_f = r_4 \approx 4.79 \times 10^{10}$ cm, after which the proton energy is below the process energy threshold. Therefore, the emission time is very quick, from a fraction of a second to ~ 1 s. Indeed, the total precise emission time-interval is ≤ 1.5 s, as it can be seen from Fig. (3.11). The luminosity of each particle is very high (especially for the photons), but this does not violate the energy conservation (as can be seen in Tab. (3.1)) since the majority of the emission occurs in the first fractions of second. For the photons this emission can be recognized as an initial spike in the spectrum (if we have a good resolution at those short times). We can now estimate the total energy emitted for each particle type via Eq. (3.16). The time interval of the emission, Δt_i, is the time the shell spends to cover the distance between r_{i-1} and r_i with the velocity β_i, $\Delta t_i \approx \Delta r_i/(c\beta_i)$, namely

$$\mathcal{E}_a \approx \sum_{i=2}^{n} L^i_a \times \Delta t_i = \sum_{i=2}^{n} L^i_a \times \frac{\Delta r_i}{c\beta_i}, \tag{3.19}$$

where L^i_a is given by Eq. (3.18). The total energy emitted in every particle type, in the whole emitting region, is summarized in Tab. (3.1).

[2] The mean-free path values, for each pion, are calculated at the initial and final radius showed in the several spectra in this section. Note that not all the spectra have the same final radius.

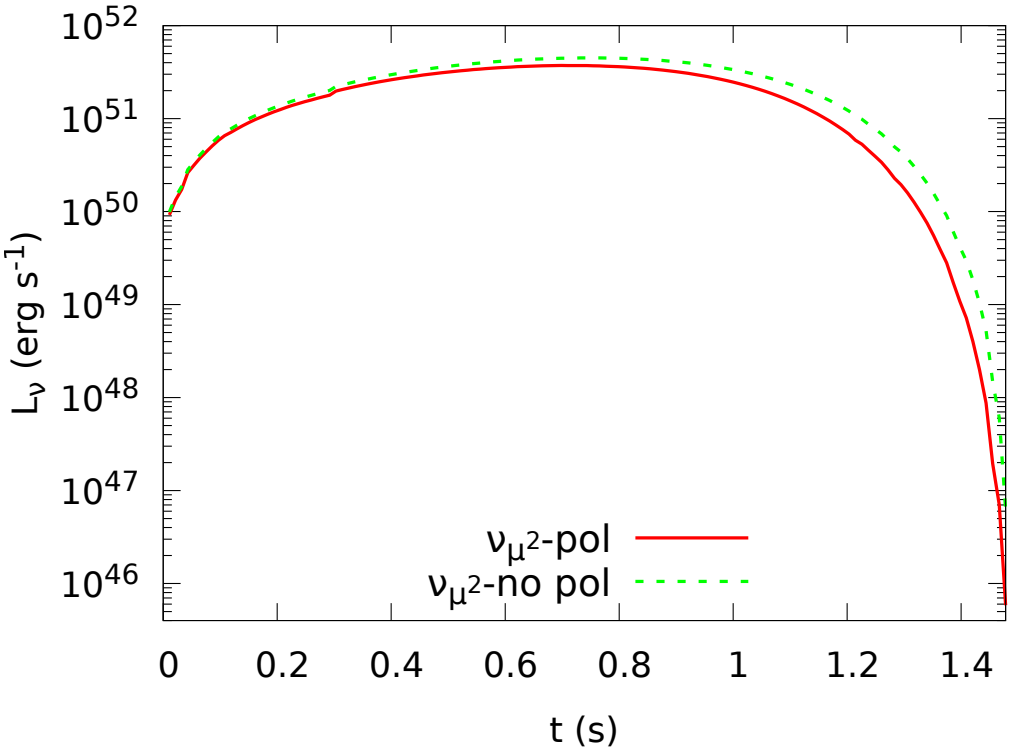

Figure 3.11. $\bar{\nu}_{\mu^{(2)}}$ luminosity, with and without polarization, as a function of time, in the entire time-interval of the emission.

Table 3.1. Total energy, integrated over all the emitting region, via Eqs. (3.19), for γ, $\nu_{\mu^{(1)}}$, $\nu_{\mu^{(2)}}$ and ν_e, with and without considering the polarization (only for $\nu_{\mu^{(2)}}$ and ν_e). If we sum all the energies for all the considered νs, besides the $\nu_{\mu^{(1)}} + \bar{\nu}_{\mu^{(1)}}$, only for the unpolarized or polarized case (in the sum we have considered the polarized case), we obtain a total energy release of 9.11×10^{51} erg, that is $\approx 2.9\%$ of the energy of initial energy of the $\gamma e^{\pm}$ plasma. If you consider in the sum also the energy emitted in photons, we get a total energy of 5.37×10^{52} erg, that corresponds to 17% of $E_{e^+e^-}$.

Particle	Total energy (10^{51} erg)
γ	44.62
$\nu_{\mu^{(1)}}$; $\bar{\nu}_{\mu^{(1)}}$	0.471; 0.155
Without polarization	
$\nu_{\mu^{(2)}}$; $\bar{\nu}_{\mu^{(2)}}$	0.6034; 3.534
ν_e; $\bar{\nu}_e$	2.105; 0.3696
With polarization	
$\nu_{\mu^{(2)}}$; $\bar{\nu}_{\mu^{(2)}}$	2.3067; 2.8536
ν_e; $\bar{\nu}_e$	2.8252 ; 0.4943

3.3 TeV protons interacting with the ISM

We now consider the interaction of incident protons engulfed by plasma of $\gamma e^{\pm}$ in the direction of the circumburst medium (CBM) of low baryon load $B < 10^{-2}$, with target protons of the ISM. Thus, the number density of the target is $n_{\rm ISM} \sim 1$ cm^{-3}. This expanding plasma reaches transparency far away from the BH site, with ultra-relativistic Lorentz factor up to $\gamma_p = \Gamma \sim 10^3$. Therefore, we assume here that the incident protons have energies ~ 1 TeV.

For an isotropic energy of the plasma $E_{e^+e^-} \sim 10^{53}$ erg (see, e.g., Table 7 in [133] for examples of the energy released by BdHNe I), and a baryon load $B = 10^{-3}$, the total number of protons is given by

$$N_p = \frac{BE_{e^+e^-}}{m_p c^2} = 6.65 \times 10^{52}. \tag{3.20}$$

We consider that the interaction with the ISM occurs in a spherical shell that we locate at a distance of between $10^{16} \leq r \leq 10^{17}$ cm from the BH site (see, e.g., [64]). In order to make the computation and obtain the spectra for this new interaction, we have followed another approach that we present below.

3.3.1 Second approach

In this section, since we are going to work now with high-energetic protons ($E_p \geq 1$ TeV), we cannot use the same parameterization for the cross-section of inelastic pp interaction presented in [25] and used here for the high-density case (see Sec. (3.2)). Indeed, the energy range of validity for that parameterization is between (0.3–50) GeV; too low for ours protons.

For these reasons, we now follow the approach described in [70] by Kelner *et al.* (see also App. (C)), for the determination of the interaction cross-section and the spectra of the emerging particles. In this paper, they study the pp interaction using the `SIBYLL` [45] and `QGSJET` [67] codes. They divide their studies in two energy region:

1. for $E_p \geq 0.1$ TeV and $x = E_a/E_p \geq 10^{-3}$ (where E_a is the energy of the secondary product), they construct an analytical parameterization for the spectra of secondary particles, emerging from the decays of the π mesons and the μ leptons, and an analytic formula for the energy distribution of pions (considering different fixed interacting proton energies);

2. for $E_p \leq 0.1$ TeV, they consider a different proton energy distribution, that covers a wide energy range, and develop a method, based on the so called "*δ–functional approximation*" (see [12]), to integrate the equations and obtain the spectrum of the specific particle, until the proton energy threshold for the production of π is reached.

Since we are working with protons energies ≥ 0.1 TeV, we focus only to the first method. Following [70], we denote the energy distribution of protons as $J_p(E_p)$, in units cm^{-3} TeV^{-1}, which gives the number of protons per unit volume in the energy range between E_p and $E_p + dE_p$ (see below Sec. (3.3.2) for the definition of $J_p(E_p)$). The secondary particles production rate in the energy interval $(E_a, E_a + dE_a)$, $\Phi_a(E_a) \equiv dN_a/dE_a$, for $E_p \geq 0.1$ TeV, is given by

$$\Phi_a(E_a) = c\, n_p \int_{E_a}^{\infty} \sigma_{\rm inel}^{pp}(E_p) J_p(E_p) F_a\left(x, E_p\right) \frac{dE_p}{E_p}, \tag{3.21}$$

where n_p is the density of the target protons (we assume it is 1 particle/cm^3), $\sigma_{\rm inel}^{pp}(E_p)$ is the inelastic pp cross-section (see Eq. (3.22)), $x \equiv E_a/E_p$, c the speed of light and F_a is the specific spectrum for the particle a that they derive, (and that we are going to use), with an accuracy better 10% (seen again App. (C)).

The inelastic part of the total pp cross-section is represented, in *Kelner et al.* [70], by the following formula:

$$\sigma_{\text{inel}}^{pp}(E_p) = 34.3 + 1.88\,L + 0.25\,L^2 \text{ mb}, \tag{3.22}$$

with $L = \ln(E_p/1\,\text{TeV})$. For the case $E_p \leq 0.1$ TeV, Eq. (3.22) has to be multiplied by the factor $\left[1 - (E_p^{\text{Th}}/E_p)^4\right]^2$, to take into account the threshold for the pion production. In the parameterization of [70], it is considered both π^+ and π^- derived by pp interaction, without distinguishing between electron and positron, as well as between neutrino and antineutrino. The reason for this is that the production of π^+ exceeds only a little bit that of π^- and this effect is smaller than the accuracy of the approximations made in the analysis. Since now we follow their treatment, this implies that our calculations also include the contribution of antiparticles (e.g π^+ and π^-, μ^+ and μ^- etc.).

3.3.2 Particles spectra

In order to get the emissivity of each specific particle using Eq. (3.21), we need to specify our protons energy distribution $J_p\left(E_p\right)$. We are considering only protons with fixed energy, then we can write it as $J_p\left(E_p\right) = A\delta\left(E_p - E_p^0\right)$, where E_p^0 is our proton fixed energy ($E_p^0 = 1$ TeV). The constant A is the ratio between the number of interacting protons in the considered volume: $A = N_p/\Delta V$ (in particle/cm^3). The volume is calculated as $\Delta V = 4\pi\left(r_2^3 - r_1^3\right)/3$, with $r_1 = 10^{16}$ cm and $r_2 = 10^{17}$ cm, instead the number of protons is derived in Eq. (3.20). Since we are working at high energies, in the lower limit of the integral in Eq. (3.21) we can put easily E_γ, $E_{\nu_{\mu(1)}}$, $E_{\nu_{\mu(2)}}$, E_{ν_e}, instead of the limits used in Sec. (3.2.2). For this interaction, it is meaningless to talk about "*total luminosity*" since the protons spend the time $\Delta t = \Delta r/(c\beta) = 3 \times 10^6$ s (with $\beta \approx 1$ because $\gamma_p = 10^3$) to cross the entire ISM region of width $\Delta r = 9 \times 10^{16}$ cm. Since for the calculation of the horizon distance for neutrino (see Sec. (3.4)) we need the luminosity, this can be obtained considering only the last interaction of the accelerated protons with the target protons of the ISM, namely the ISM shell between $r_* = 10^{17} - \delta s$ cm and $r_2 = 10^{17}$ cm, where $\delta s = 3 \times 10^{10}$ cm is the distance covered by the accelerated protons in 1 second. Thus, the luminosity of the last emitting shell is given by $L_a = \epsilon_a \times \Delta V_{last\ shell}$, with ϵ_a the emissivity of the particle a calculated by Eq. (3.12) and $\Delta V_{last\ shell} = 4/3\pi\left(r_2^3 - r_*^3\right)$.
The total emitted energy, for each particle a, can be calculated as

$$\mathcal{E}_{tot,\,a} = \Delta t \sum_i \epsilon_a^i \times \Delta V_i, \tag{3.23}$$

where $\Delta V_i = 4/3\pi\left(r_i^3 - r_{i-1}^3\right)$, with $r_i = r_{i-1} + \delta s$. Since ϵ_a^i does not depend on the radius, thus $\epsilon_a^i = \epsilon_a$, the total emitted energy can be get easily by

$$\mathcal{E}_{tot,\,a} = \epsilon_a\,\Delta t\,\Delta V, \tag{3.24}$$

with $\Delta V = 4/3\pi\left(r_2^3 - r_1^3\right)$.

γ from π^0

The photon emissivity from π^0 decay is given by Eq. (3.21), with $F_\gamma\left(x, E_p\right)$ derived by [70] (and reported in App. (C)). We need to emphasize that, in the analysis of [70], for the parameterization of the photon spectrum, they consider also the photons produced by the different decay channels of η mesons (see App. (C)).
The photons emissivity is shown in Fig. (3.12). The total energy emitted through photons in all emitting region via Eq. (3.24) is $\mathcal{E}_\gamma = 5.4072 \times 10^{43}$ erg. The luminosity emitted in the last emitting shell of the ISM region, calculated as explained above, is $L_\gamma = 1.0135 \times 10^{43}$ erg/s. Instead, the maximum photon energy corresponding to the maximum value of $E^2\frac{dN_\gamma}{dE}$ is $E_\gamma = 91.62$ GeV.

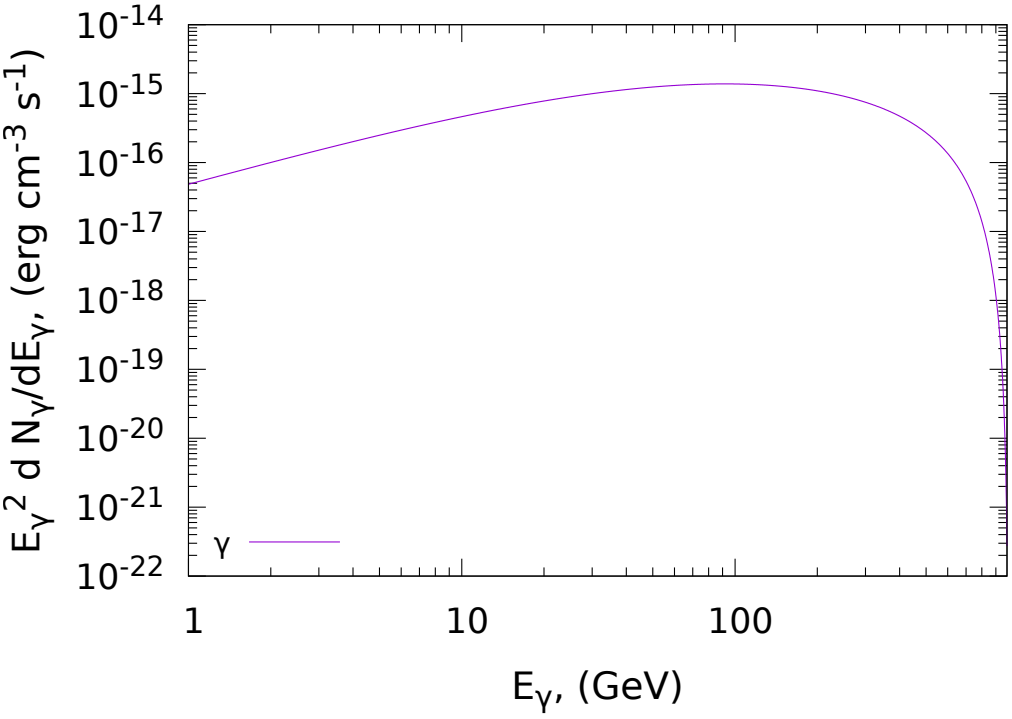

Figure 3.12. High-energy photons emissivity from π^0 (and η) decay, created by the interaction of proton with energy of $E_p = 1$ TeV against proton of the ISM at rest ($n_p^{\rm ISM} = 1$ cm^{-3}).

$\nu_{\mu^{(1)}}$ from direct π decay

The muon neutrino from direct pion decay ($\pi \to \mu\nu_\mu$) is given by the same Eq. (3.21), with $F_{\nu_{\mu^{(1)}}}\left(x, E_p\right)$ given in [70] (and reported in App. (C)). The respective emissivity is shown in Fig. (3.13).

As one can see in Fig. (3.13), the spectrum has a sharp cut-off at $x = 0.427$. This effect is due to the kinematics of the process since, at high energy, this neutrino can take only a factor $\lambda = 1 - r_\pi = 0.427$ of the pion energy.
The total energy emitted in $\nu_{\mu^{(1)}}$ inside the whole emitting region (calculated as before) is $\mathcal{E}_{\nu_{\mu^{(1)}}} = 1.604 \times 10^{43}$ erg, while the luminosity in the last emitting shell is $L_{\nu_{\mu^{(1)}}} = 3.006 \times 10^{42}$ erg/s, whereas, the spectrum reaches its maximum value at the neutrino energy of $E_{\nu_{\mu^{(1)}}} = 44.72$ GeV.

$\nu_{\mu^{(2)}}$ and ν_e from muon decay

The muon neutrino luminosity from muon decay can be calculated from Eq. (3.21), with the specific $F_a\left(x, E_p\right)$ given in [70] (reported in App. (C)). The spectrum of $\nu_{\mu^{(2)}}$ and ν_e can be represented by the same function (with an accuracy less than 5% for ν_e). The emissivity is shown in Fig. (3.14). Differently from the $\nu_{\mu^{(1)}}$, the energy of these neutrinos can reach at maximum the energy of the μ, which can achieve the total pion energy ($E_\mu^{\rm max} \approx E_\pi$).

The total energy emitted in $\nu_{\mu^{(2)}}$ in the whole emitting region results $\mathcal{E}_{\nu_{\mu^{(2)}}} = 1.98 \times 10^{43}$ erg, while the luminosity of the last emitting shell is $L_{\nu_{\mu^{(2)}}} = 3.7115 \times 10^{42}$ erg/s. The maximum of the spectrum is reached at the energy $E_{\nu_{\mu^{(2)}}} = 63.9$ GeV.

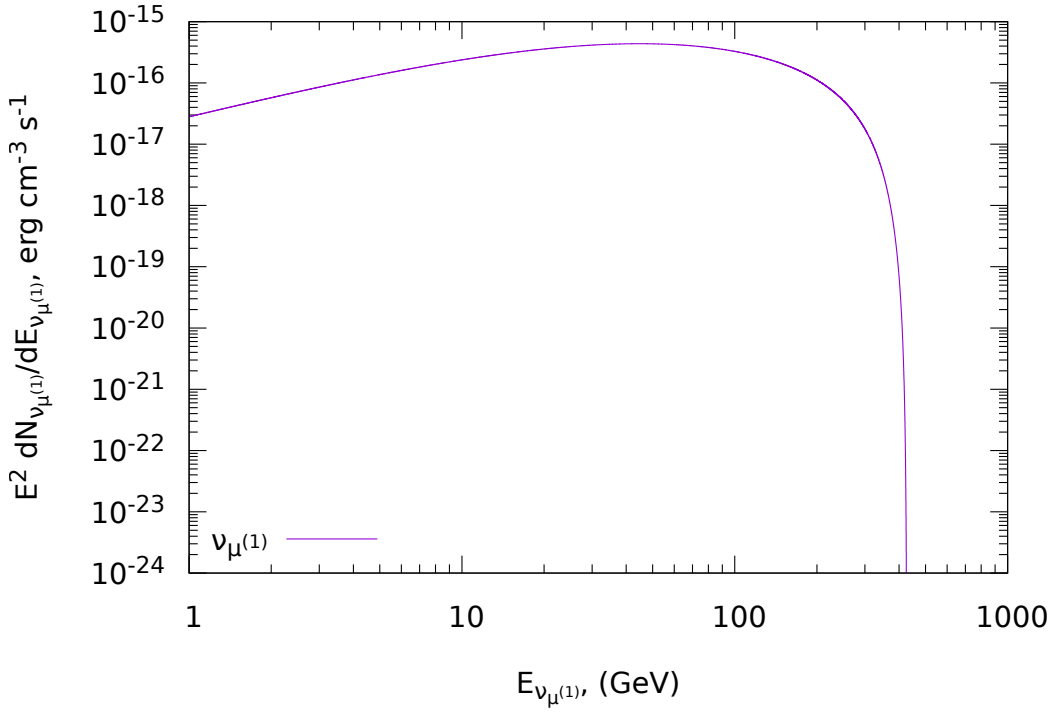

Figure 3.13. High-energy muonic neutrino emissivity from direct pion decay, ($\nu_{\mu^{(1)}}$), produced as in Fig. (3.12).

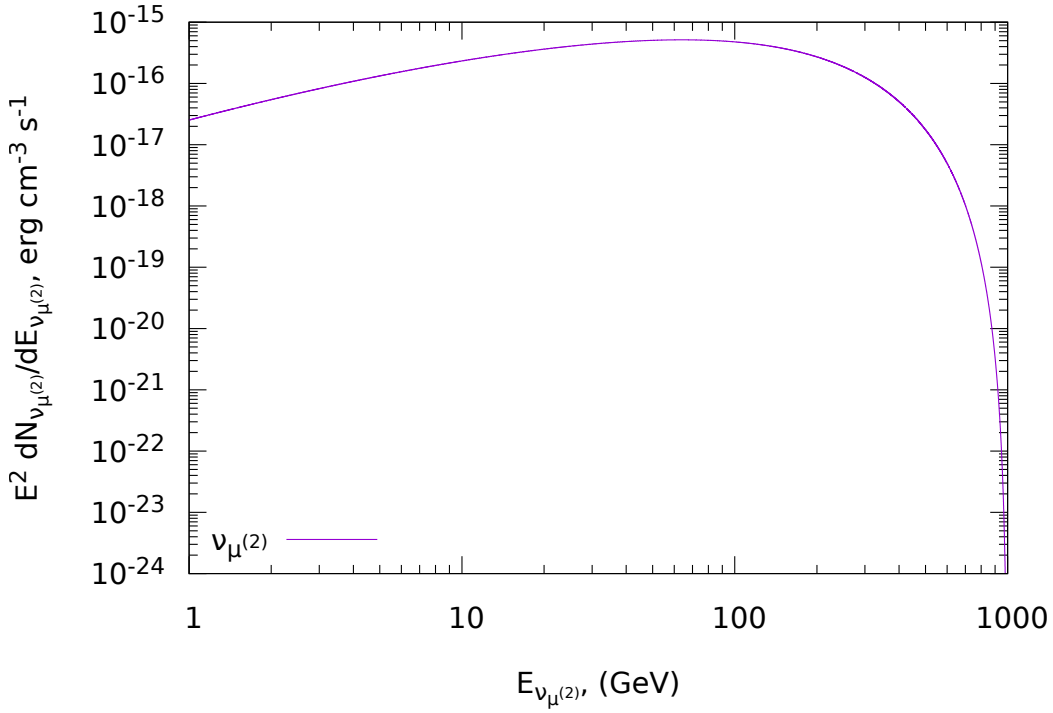

Figure 3.14. $\nu_{\mu^{(2)}}$ (and ν_e) emissivity from μ decay, produced as in Fig. (3.12).

3.4 Summary, Discussion and Conclusions

In this chapter we have computed the photon and neutrino production via pp interaction occurring within the BdHNe I scenario for energetic long GRBs, which we have recalled in Sec. (3.1). From the dynamics of the BdHN I, it follows that the SN ejecta, due to the accretion and to the BH formation, becomes highly asymmetric around the newborn BH site. Therefore, the $e^{\pm}$ plasma created in the BH formation process, during its isotropic expansion and self-acceleration, charges different amounts of matter of the surrounding SN ejecta, depending on the direction (see Fig. (3.2)). This asymmetry leads to a direction-dependent Lorentz factor for the loaded protons in the expanding shell.

From this scheme, we have here studied two different types of physical set-up for pp interactions that cover the generality of the system. In the first part of the chapter, see Sec. (3.2), we studied the pp interactions inside the SN ejecta. For a quantitative estimate, we have adopted numerical values from recent hydrodynamical simulations [129] achieved through an implementation of the PLUTO code [82, 86]. The equations that have been integrated are the same already exposed in Sec. (1.2.2). The initial conditions for the integrations are summarized in Sec. (3.2). The $\gamma e^{\pm}$ expanding plasma incorporates protons of the ejecta with a baryon load parameter $B = 51.75$ and accelerates them up to energies of ~ 7 GeV ($\gamma_p \leq 7$). This region is characterized by a number of target protons (at rest) of $n_{remn} \sim 10^{23}$ cm^{-3}, while the number density of the front of the shell, in the whole considered region, is almost constant, $n_{\rm sh} \simeq 10^{25}$ cm^{-3}.

In order to calculate the emissivity of the emerging particles, and because of the low energetic interacting protons, we have used for this case the parameterization of the differential pion production cross-section presented in [25] (see also App. (A)). The obtained spectra show that, from this high-density region, the photons and neutrinos have energies $E_{\nu_{\mu^{(1)}}} \leq 2$ GeV and E_γ, $E_{\nu_{\mu^{(2)}}}$, $E_{\nu_e} < 5$ GeV, with associated total energy (integrated over the whole emitting region) $\sim 10^{50}$–10^{52} erg (see Tab. (3.1) for the total energy for each particle).

We have calculated that in the high-density region, the particle production occurs in the first ~ 1.5 s of the shell expansion (see Fig. (3.11)). At later times, the energy of the protons in the shell is below the threshold for any pp interaction with the target protons in the remnant.

We have found that the emerging particles from μ decay are not effected by the polarization of the parent muon (compare spectra in Figs. (3.7)–(3.8) with Figs. (3.9)–(3.10)).

In the second part of the chapter, see Sec. (3.3), we have considered the expansion of the shell in the direction of low baryon load, where we adopted $B = 10^{-3}$ (see, e.g., [128, 129]). Here, the expanding $\gamma e^{\pm}$ plasma swallows up a small quantity of baryons in the *cavity* around the BH [118], allowing a self-acceleration that brings the loaded protons to energies of up to $E_p \sim 1$ TeV ($\gamma_p \sim 10^3$). In order to obtain the final emissivity, here we use the parameterization of the cross-section and of the emerging particles spectra presented in [70]. In this case, we obtained a wider range of particles energies $1 \leq E_a \leq 10^3$ GeV (depending on the different particles), with associated total luminosity of $L_\gamma = 1.0135 \times 10^{43}$ erg s^{-1}, $L_{\nu_{\mu^{(1)}}} = 3.006 \times 10^{42}$ erg s^{-1}, and $L_{\nu_{\mu^{(2)}},\nu_e} = 3.7115 \times 10^{42}$ erg s^{-1}.

We found that the secondary particles spectra follow approximately a cut-off power-law function (see, for example, Fig. (3.6) or (3.13)), with spectral index $1 \leq \alpha < 3$ (depending on the considered particle). The power-law term usually derives from the spectral index of the primary interacting protons (see, for example, [54]). But, since we have considered a spherical expansion of the photon-lepton-baryon shell, and a fixed proton energy distribution (at each radius of the expansion), we deduce that the power-law term is intrinsic in the considered process. The exponential decay is explained by the kinematic of the process, since only a fraction of the initial incident proton energy is taken by the secondary neutrino (both from direct pion decay and muon decay). To be more specific, a fraction of the parent proton energy is taken by the pion; for the direct pion decay, the $\nu_{\mu^{(1)}}$ can take, at maximum, a fraction λ of the pion energy, while the muon can take, at maximum, the entire pion energy.

Let's now make a comparison between the results obtained in Sec. (3.2) and Sec. (3.3). Comparing the plots, for the same daughter particles, in Sec. (3.3.2) with the ones obtained in Sec. (3.2), we can

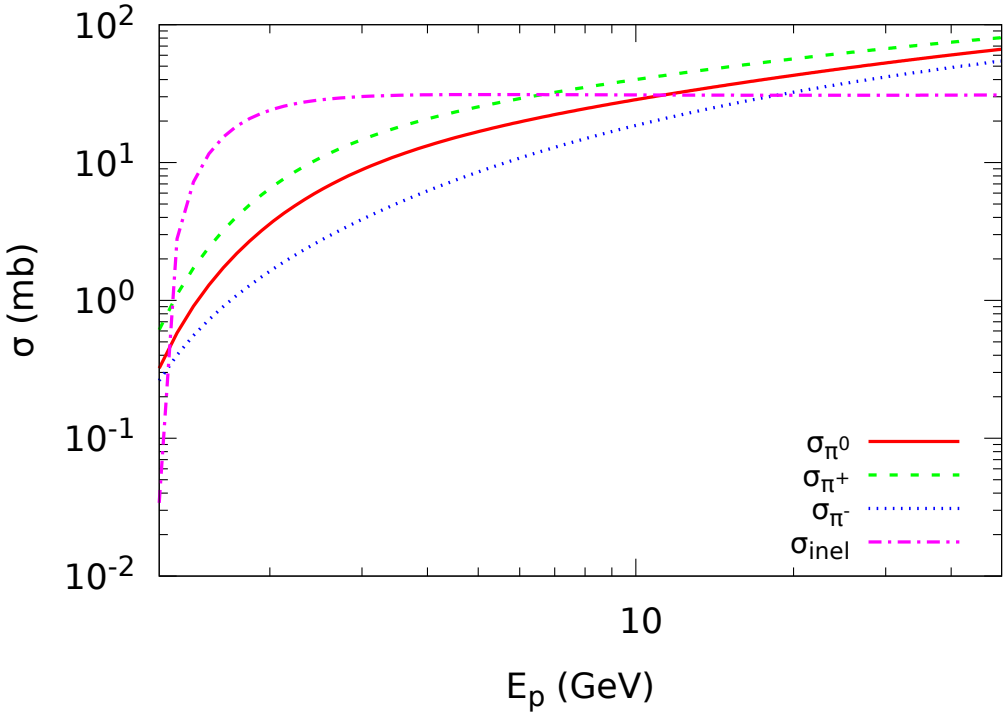

Figure 3.15. Proton-Proton total cross-sections, for production of neutral and charged pions, for the [25] (σ_{π^0} and $\sigma_{\pi^\pm}$, given in App. (A)) and [70] (σ_{inel}) parameterization (by Eq. (3.22)).

deduce some relevant differences. The first is in the emissivity. Between the two approaches there are 46 orders of magnitude of difference. This is principally because of the different values of the involved densities, since the physical conditions of the two interactions are quite different. Indeed we have:

1. for the first interaction inside the high density region, the constants A and n_p (respectively, the number density of the interacting and the target particles) are: $A \sim 10^{25}$ cm^{-3} and $n_p \sim 10^{23}$ cm^{-3}. Then, their product results $\sim 10^{48}$ cm^{-6};

2. for the second interaction in the low density region, the same constants assume the values: $A \approx 16$ cm^{-3} and $n_p = 1$ cm^{-3}. Then their product is of the order of ~ 16 cm^{-6}.

We then deduce that the difference in the emissivity is mainly due to the difference in the density. Another difference between the two cases resides in the two types of cross-sections. Fig. (3.15) shows the total inelastic cross-sections used in this chapter. The cross-sections ($\sigma_{\pi^0}, \sigma_{\pi^+}, \sigma_{\pi^-}$) correspond to the energy integrated differential cross-sections used in the Sec. (3.2), while σ_{inel} to the one used in Sec. (3.3). The order of magnitude of the two types of parameterization is almost the same: the one from [70] dominates at $E_p \leq 10$ GeV, instead the one from [25] dominates at $E_p \geq 6$ GeV. [3] We need also to note that the parameterization of [70] takes into account the polarization effects and they do not distinguish between π^- and π^+ or μ^- and μ^+ (and, consequently, for the other particles and their antiparticles).

Estimate of the ν detection

A precise estimate of the detection probability of these neutrinos is out of the scope of the present work and we plan to addressed it elsewhere. However, on the basis of the present results, we can express some

[3] The plot is made in the validity region for the parameterization in [25]. For larger values of E_p, the σ_{inel}^{pp} from the parameterization in [70] increases sharply.

considerations for the Earth's neutrino detectors.

In general, the cosmological distances at which GRB occurs make the neutrino detection very challenging because of the very low neutrino flux arriving to the Earth. As we shall show below, it is indeed the distance to the source the main problem for the current detection probability.

For the low energy neutrinos ($E_\nu \leq 2$ GeV, at the production site, i.e. in the source frame) coming from the high-density region, there are additional considerations:

- a lower energy neutrino has a lower probability to interact with a nucleon (N) (proton or neutron) in the detector material via the reaction $\nu + N \rightarrow \mu + N'$ (where N' is another nucleon). Indeed, the cross-section for this reaction is $\sigma_{\nu N} \sim 10^{-39}$ cm^2 (see for example [3, 60]), for these low energy neutrinos (see below). In addition, the arrival neutrino energy is redshifted by a factor $1 + z$ with respect its energy in the source frame;

- at such low energies, there is much background noise by atmospheric neutrinos, created in the atmospheric showers by cosmic rays and solar neutrinos.

The high energetic neutrinos coming from the interaction in the low-density region could be, in principle, more easily detected than the previous case. At these energies ($E_\nu \lesssim 10^3$ GeV), there is no background noise from atmospheric neutrinos or solar neutrinos and the cross-section $\sigma_{\nu N}$ is higher, i.e. $\sigma_{\nu N} \sim 10^{-37}$ cm^2 (see, e.g., [3, 60]). The cross-sections considered here are from [3, 60], where are considered total charged current cross-sections including quasi-elastic scattering ($\nu + N \rightarrow l + N'$, with l a lepton), single meson m production ($\nu + N \rightarrow l + N' + m$) and deep-inelastic scattering ($\nu + N \rightarrow l + N'+$ hadrons). However, as we have shown, in the low density interaction the resulting energy released is much less, making the detection of these neutrinos with higher energy even much more difficult than the ones produced in the high density interaction (see below).

We can obtain order-of-magnitude estimate of the probability of detection of these neutrinos. We focus our attention on three detectors: SuperKamiokande, HyperKamiokande and IceCube. The two Kamiokande detectors explore a wide energy range for neutrino (from a few MeV up to 100 PeV). The IceCube detector works principally on high-energy neutrinos ($\gtrsim$ PeV), but the core of the experiment (the *Deep Core Detector*) works down to energies of a few GeV. The only characteristic of these detectors that we need in our estimation is the effective detection volume: 22.5 kton for the SuperKamiokande [143], 560 kton for the HyperKamiokande [61], while for the IceCube effective detection volume we consider 10 Mton for the ν_μ from the high density region, 20 Mton for the $\nu_{\mu^{(1)}}$ from the low density region; 30 Mton for the $\nu_{\mu^{(2)}}$ from the low density region (see [6]), since the energies of these two νs are different and the detector reacts differently depending on the neutrinos energies.

We now estimate the detection horizon for the neutrinos studied here. For this purpose, we use the best experimental conditions, i.e. we use the peak neutrino luminosity and the corresponding neutrino energy. The number of neutrinos per-unit-time and per-unit-area that arrive to the detector can be estimated as

$$\frac{d^2N_\nu}{dS\,dt} = \frac{1}{3}\frac{\mathcal{E}_\nu}{4\pi D^2 E_\nu^*}, \tag{3.25}$$

where $\mathcal{E}_\nu$ is the total energy emitted during 1 s in neutrinos of energy E_ν, D is the luminosity distance to the source, $E_\nu^* = E_\nu/(1+z)$ is the redshifted neutrino energy, and z the source cosmological redshift.The factor $1/3$ is to consider the neutrino oscillations. Indeed, since the source is located at a huge distance, the produced neutrinos have all the necessary time to oscillates between the three neutrino flavors. Then, the ν_μ flux at Earth is $1/3$ of the flux produced at the source.

Therefore, we can obtain the number of detectable neutrino, $N_\nu^{\rm det}$, as the number of neutrino per unit of time and area that arrives to the detector, given by Eq. (3.25), times the cross-section for the neutrino-nucleon interaction, $\sigma_{\nu N}$, times the number of probable total interacting baryons in the detector,

$N_b^{\rm det}$, times the integration time of the detector T_{int}:

$$N_\nu^{\rm det} = \frac{d^2 N_\nu}{dS\, dt} \times T_{int} \times \sigma_{\nu N} \times N_b^{\rm det}. \tag{3.26}$$

$N_b^{\rm det}$ can be estimated as the interacting mass inside the detector multiplied by the Avogadro number N_A. For the present three detectors, we have:

1. for the SuperKamiokande detector $N_b^{\rm det} = (22.5\ \text{kton}) \times 6.022 \times 10^{23} = 1.35 \times 10^{34}$ baryons;
2. for the HyperKamiokande detector $N_b^{\rm det} = (560\ \text{kton}) \times N_A = 3.37 \times 10^{35}$ baryons;
3. for the *Deep Core Detector* of IceCube, the respective effective volume for the different neutrino energies are: $N_b^{\rm det} = (10\ \text{Mton}) \times N_A = 6.022. \times 10^{36}$ baryons (we use this for $E_\nu \lesssim 1$ GeV); $N_b^{\rm det} = (20\ \ \text{Mton}) \times N_A = 1.2044 \times 10^{37}$ baryons (it will be used for $E_\nu \sim 40$ GeV); $N_b^{\rm det} = (30\ \text{Mton}) \times N_A = 1.8066 \times 10^{37}$ baryons (we will use this value for $E_\nu \sim 60$ GeV).

Using the above estimates of $N_b^{\rm det}$, using Eq. (3.26) and the Hubble-Lemaître law, $c\,z = H_0 D_h$ (with $H_0 = 72$ km s^{-1} Mpc^{-1}), we can obtain the neutrino-detection horizon, D_h, i.e. the luminosity distance to the source for which we have $N_\nu^{\rm det} = 1$:

$$D_h = \frac{K H_0}{2c} + \frac{1}{2}\sqrt{\frac{K^2 H_0^2}{c^2} + 4K}, \tag{3.27}$$

where $K = \mathcal{E}_\nu \sigma_{\nu N} T_{\rm int} N_b^{\rm det}/(12\pi E_\nu)$. In Tab. (3.2), we summarize the value of D_h for $\nu_{\mu^{(1)}}$ and $\nu_{\mu^{(2)}}$, in the case of both the high and low density regions, for the three considered detectors. We consider an integration time of the detector of $T_{int} = 1$ s because we are working with transient sources and this value is in agreement with the time-interval of the emission inside the ejecta (see Fig. (3.11)). Then, we can assume that the total emitted luminosity of each specific neutrino L_ν (erg/s) corresponds to the total energy calculated via Eq. (3.19), $\mathcal{E}_\nu$, which are summarized in Tab. (3.1), divided by 1 s. This last assumption is valid only for the neutrino emerging from the **high density case**. For the neutrino emerging from TeV protons (**low density case**), the same assumption is no longer valid since, as we have seen in Sec. (3.3), the protons spend 3×10^6 s to cross the entire emitting region. Thus, in this case we consider the luminosity L_ν emerging from the last emitting shell of the ISM region (as explained in Sec. (3.3.2)), which values are listed, for each specific particle, in Sec. (3.3.2).
We obtain the neutrino energy E_ν by the following considerations:

- for the high density region, considering the neutrino with the higher value of the emissivity at the outer radius r_4. The neutrinos produced at the internal radii ($r_1,\ r_2,\ r_3$) are not considered because the high value of the particles density in the ejecta and the higher value of the neutrino energy enhance the probability of interaction with the baryons in that region;
- for the low density region, we consider the value of E_ν corresponding to the maximum value of the emissivity.

The approximation that we made using the Hubble-Lamaître law is valid. Indeed, we have compared the results from this law with the one obtained from the correct definition of the luminosity distance as a function of the redshift z, $D_L(z)$, which derive from the Friedmann equation (for a flat Universe). Inserting Eq. (3.25) in Eq. (3.26), from the latter deriving D_L and equating it with the right definition of $D_L(z)$, we derived the redshift that practically coincides with the one from the Hubble-Lamaître law.

This analysis suggests that only the IceCube detector might detect the neutrinos here analyzed, i.e. neutrinos produced by pp interactions in the context of BdHNe I, especially the ones coming from the

Table 3.2. Horizon distances D_h for ν's from direct pion decay and μ decay, for the high and low density region cases, for the three considered detectors: SuperKamiokande (SK), HyperKamiokande (HK), Deep Core of IceCube (Deep). We recall that E_ν is the neutrino energy, L_ν is the total energy emitted in those neutrinos in 1 second: 1) in the whole emitting region, for the ones from the high density region; 2) in the last emitting shell, for the low density region one (see Sec. (3.3.2)), and $\sigma_{\nu N}$ is the cross-section relevant for the detection at the specified neutrino energy. For the high density region, the considered $\bar{\nu}$'s come from the π^+ decay since, as one can see from Tab. (3.1), they have the highest energy emitted.

Particle	$D_h^{\rm SK}$	$D_h^{\rm HK}$	$D_h^{\rm Deep}$	E_ν	L_ν	$\sigma_{\nu N}$
High density region	(Mpc)	(Mpc)	(Mpc)	(GeV)	(10^{51} erg s^{-1})	(10^{-39} cm^2)
$\nu_{\mu^{(1)}}$	0.297	1.48	6.28	0.36	0.47	2.88
$\nu_{\mu^{(2)}}$	0.529	2.64	11.12	0.43	3.53	1.45
Low density region	(pc)	(pc)	(pc)	(GeV)	(10^{42} erg s^{-1})	(10^{-37} cm^2)
$\nu_{\mu^{(1)}}$	22.37	111.74	667.97	44.72	3.006	3.17
$\nu_{\mu^{(2)}}$	26.08	130.31	957.13	63.9	3.7115	4.99

high density region, even if all of them have the right energy range of sensibility to detect our neutrinos. We can follow a similar approach searching for the right detector conditions in order to get one detection for our neutrinos. Indeed, if we considers N_b^{det} has the unknown variable, we can get the necessary number of interacting baryons in the detector for one detection using again Eqs. (3.25)-(3.26) and the right expression for the luminosity distance as a function of the redshift:

$$N_b^{det}(E_\nu, \mathcal{E}, z,\ \sigma_{\nu N}) = \frac{4\pi E_\nu}{\mathcal{E}\sigma_{\nu N}}(1+z)\left[\frac{c}{H_0}\int_1^{1+z}\frac{d\tilde{z}}{\sqrt{\Omega_{R0}\tilde{z}^4 + \Omega_{M0}\tilde{z}^3 + (1-\Omega_0)\tilde{z}^2 + \Omega_\Lambda}}\right]^2. \tag{3.28}$$

[4]If we consider all the sources at a distance redshift $z = 1$, we get the results shown in Tab. (3.3). As one can sees from this table, we need a very high mass of the detector in order catch one neutrino: $\sim 10^9$ Pton and $\sim 10^{17}$ Pton for the ν from the high and low density regions, respectively. These are prohibitive conditions! The only detectable events would be neutrinos from a source at a much closer distance and/or several order of magnitude more energetic (both E_ν and $\mathcal{E}_\nu$) than the one analyzed in this work. The latter appears as a feasible possibility from the recent works on the so-called *inner engine* of the high-energy emission occurring in BdHN of type I, which predicts that along (or close to) the rotation axis of the BH, electrons can be accelerated to energies of up to 10^{18} eV, and protons up to 10^{21} eV (see [136, 151], for further details). This is an interesting subject for future research.

Comparison with IceCube low energy neutrino detections and related analysis

Now that we got an estimate of the (im)possibility to detect the neutrinos studied in this chapter, here we have a look on the true detections, and related analysis, of low energy neutrinos by the IceCube-DeepCore detector [5]. We are going to consider the analysis provided in the following three papers [4, 7, 18].

In [18] Bartos *et al.* develop a procedure (in a similar way as we did above in Eqs. (3.25), (3.26), (3.27)) in order to get the detection perspectives, for the IceCube-DeepCore detector, of neutrinos with energies $10 \leq E_\nu \leq 100$ GeV produced by baryons collisions in GRBs. They consider neutrinos, produced by charged pions decay, with energies $E_\nu \sim 0.1\Gamma$ GeV, where $\Gamma = 100 - 1000$ is the baryons Lorentz factor. Their estimate of the mean expectation number of detectable neutrino is given by $\langle n \rangle = A_{eff}\Psi$, where

[4] In Eq. (3.28) we set the density parameters values to: $\Omega_r = 10^{-4}$, $\Omega_m = 0.314$, $\Omega_\Lambda = 0.73$ and $\Omega_0 = 1.02$.

[5] We concentrate only to IceCube detector since it is the best detector among the three considered in our analysis.

Table 3.3. Number of interacting baryons inside a detector in order to have one detection of our νs. The characteristics of the sources and the neutrino are the same of Tab. (3.2).

Particle	N_b^{det}	E_ν	L_ν	$\sigma_{\nu N}$
High density region	(10^{53} baryons)	(GeV)	(10^{51} erg)	(10^{-39} cm^2)
$\nu_{\mu^{(1)}}$	6.646	0.36	0.47	2.88
$\nu_{\mu^{(2)}}$	2.099	0.43	3.53	1.45
Low density region	(10^{62} baryons)	(GeV)	(10^{42} erg s^{-1})	(10^{-37} cm^2)
$\nu_{\mu^{(1)}}$	3.5183	44.72	3.006	3.17
$\nu_{\mu^{(2)}}$	2.5866	63.9	3.7115	4.99

A_{eff} is the detector effective area (in our analysis we used the *effective volume* through the number of interacting baryons in the detector) and $\Psi\left[\text{cm}^{-2}\right]$ is the neutrino fluence (that is related to the GRB gamma-ray fluence $S\ \left[\text{erg cm}^{-2}\right]$). In Fig. (1) of [18] they show the GRB isotropic energy E_{iso} required to produce one neutrino detection by DeepCore, as a function of the luminosity distance D_L and baryons Lorentz factor Γ. We can compare the results we have obtained in this chapter with their estimate of the detection perspectives. We considered as GRB isotropic energy the value $E_{\text{iso}} = 3.16 \times 10^{53}$ erg and the protons Lorentz factor is: 1) $\Gamma \sim 6$ for the interaction studied in Sec. (3.2); 2) $\Gamma = 10^3$ for the interaction studied in Sec. (3.3). From Fig. (1) in [18], we can derive the necessary luminosity distance in order to have one neutrino detection and check if it is in good agreement with our estimate (see Tabs. (3.2), (3.3)). In this way, we may also check if the procedure we developed above, in order to get the luminosity distance D_L, is correct.
For ours two neutrinos, with different energy, (one from the high- and one from the low-density region), we have:

1. For the low energy νs, the scale of the figure is too wide in order to allow us to get a precise estimate of D_L, for our low value of $\Gamma \sim 6$. However, one can see that, for $E_{\text{iso}} = 10^{53}$ erg, $D_L \leq 0.3$ Gpc. This estimate is almost one/two orders of magnitude higher than our estimate in Tab. (3.2).

2. For the higher energetic neutrino (namely the ones produced by interacting protons with $\Gamma = 10^3$), for the same value of E_{iso}, from Fig. (1) in [18] we get a luminosity distance of $D_L \sim 0.9$ Gpc. This result is seven order of magnitude bigger than our estimate for neutrino of this energy (see again Tab. (3.2)).

The discrepancy between our estimates and the ones in [18] is principally due to the different procedure applied to get the luminosity distance D_L and, consequently, the physical variables and parameters used. The principal differences between the two procedures are the followings:

- in our procedure we calculated precisely the total energy emitted in secondary particles γ/νs, while in [18], they assume a fixed value calculated by means of the energy dissipation of photons and neutrinos in the GRB jet motion.

- for our higher energetic neutrinos, the luminosity is very small (also compared to the one in the lower energetic case) because: 1) it comes out from the last emitting shell of the interacting region (the ISM, see Sec. (3.3) and above Eq. (3.23)); 2) due to the very small density of the ISM, there are only few iteractions. Instead, in [18] they consider the energy emitted by the whole burst and the baryons interaction occurs inside the jet. This leads to several order of magnitude difference in the estimation of D_L.

- as temporal variable we used the integration time of the detectos ($T_{int} = 1$ s), while they use the time interval during which the 90% of the burst fluence comes out, T_{em}. The latter time interval varies between $30 - 600$ s and, then, $T_{em} \gg T_{int}$.

- the spatial interacting/emitting region (and, then, the emission time interval) is very small ($T \sim 1$ s), for both our interaction regions, compared to the whole burst emission region considered in [18].

From this analysis, we conclude that: 1) the two procedures are comparable only if one considers the emission in our high density region, because the one in the low density region is not "completely related" to the burst emission; 2) for the neutrinos generated in the high density region, notwithstanding the considerations listed above, the estimate from the two procedures are not totally different. This allow us to state that our estimate of the luminosity distance is honest.

In [4], they present the results of a search for astrophysical sources of transient neutrino emission with IceCube+DeepCore for data acquired in almost one year (between 2012 May 15 and 2013 April 30) and it represents the first searching attempt of IceCube in this energy range. They examined data for muon-neutrino of energy between 30 to 300 GeV and no transient astrophysical source was found. Then, they put an upper limit on the mean number of expected neutrino events and time-integrated flux, at a reference energy of 100 GeV, of the source within the observed period (see Fig. (5) in [4]).

In [7], they present the first all flavor search for transient emission of low energy neutrino, between $1 - 100$ GeV, using three years of data (between 2012 April and 2015 May) of the IceCube+DeepCore detector. Even in this case no astrophysical point sources emitting neutrino were found. Then, they derive the upper limits of $\sim 705 - 2301$ Gpc^{-3} yr^{-1} for the volumetric rate $\dot{\rho}$ of transient neutrino sources, assuming a neutrino spectra consistent with that of subphotospheric emission, with flare time of ~ 600 s, a mean neutrino energy of 100 GeV and a bolometric neutrino energy of $E_{\nu-\mathrm{iso}} = 10^{52}$ erg (see Fig. (8) in [7]). In Fig. (8) of this paper, they show the upper bounds for the volumetric rate as a function of the bolometric neutrino energy, considering a mean neutrino energy of 20 and 100 GeV. The limits stated above correspond to the upper and lower limits (at fixed $E_{\nu-\mathrm{iso}} = 10^{52}$ erg) due to the declination dependence of the discovery potential (see especially Eq. (4.8) of the paper). For the same $E_{\nu-\mathrm{iso}}$ and E_{mean} lower values of $\dot{\rho}$ are available.
From Tab. (3.1), we know that the total (summing on all the secondary neutrinos, $\nu + \bar{\nu}$) energy emitted in muonic and electronic neutrino (and their antiparticles) is 9.11×10^{51} erg$\approx 10^{52}$ erg. Our lower energetic neutrino are the ones produced in the high density region. Their peak energy is around $1 - 2$ GeV. Notwithstanding this value is one order of magnitude lower than the minimum mean neutrino energy used in the analysis in [7] ($E_{\nu,\mathrm{mean}} = 20$ GeV), we can compare the limits they derived for the volumetric rate with the estimate of BdHN occurring rate and, then, decide if these sources could be effectively observable astrophysical low energy neutrino sources. From Fig. (8) in [7], one can see that, for $E_{\nu-\mathrm{iso}} = 10^{52}$ erg and $E_{\nu,\mathrm{mean}} = 20$ GeV, the upper limits for the volumetric rate $\dot{\rho}$ is $(1 - 6) \times 10^3$ Gpc^{-3} yr^{-1}. As stated in Sec. (3.1.1) (see also Tab. (2.1)), the observed occurance rate of BdHN I and II are ~ 1 Gpc^{-3} yr^{-1} and ~ 100 Gpc^{-3} yr^{-1}, respectively. This comparison leads us to conclude that BdHN could be observable low energy neutrino sources. Even if in [7] they have not found any significant source, an improvement of the detector sensibility (PMT-photons sensors) and angular reconstruction algorithm, for low energy neutrino events, may render neutrino emission from high luminosity GRB identifiable.

Related photons emission and detection

We can also seek for an indirect evidence of the presence of these neutrinos, for example through the detection of the associated photons emission. We calculated the photons emission spectra produced by the π^0 decay, and also from η decay (for the low density region), their total energy and luminosity. Since these photons have specific spectrum and peak energies, their possible detection probes, indirectly, this neutrino emission and, moreover, the whole astrophysical scenario for the pp interaction in BdHN. In

Sec. (3.1.1), we recalled previous works in which the photons emission from the transparency of the e^+e^- plasma, loaded with baryons in different amounts, is shown to explain: 1) with $B \lesssim 10^{-2}$, the GRB prompt emission (in $\sim$ MeV) [101, 119, 121, 24]; 2) with $B \sim 100$, (along a different direction of the expansion) the X-ray flares [129]. From our analysis, we obtain the following results:

1. The photons produced by the present mechanism in the region with a high density of baryons have energies of the order of a few GeV. Then, these photons are energetically different from the previously studied ones.

2. The photons produced in the region with a low density of baryons have energies from a few to hundreds of GeV (the peak of the spectrum is reached near 100 GeV). Even in this case, the energy range is different from the one of the GRB prompt emission.

3. The emission studied in Sec. (3.2) occurs in a very small timescale ($\sim$ 1 s) and relatively near the BH site. The other two processes mentioned above are related to the transparency of the photon-lepton-baryon plasma and, then, occur at large distances (and, then, longer time) from the BH site.

From these considerations, we notice that the photons created in the interactions considered in this chapter are temporally and energetically separated from the ones that explain the GRB prompt emission and the X-ray flares. These are dinstinctive features that lead the possible detection of these photons to unambiguous explanation of their producing mechanisms.
Therefore, these photons are in the GeV-TeV regime and, for the ones produced in the high density region, they can be produced with large luminosities of 10^{51}-10^{52} erg s^{-1} (see, e.g., Tab. (3.1)). For a source at $z = 1$ ($D \approx 6.7$ Gpc), it would correspond a flux at Earth of $\sim 10^{-7}$–10^{-6} erg s^{-1} cm^{-2}, a value sufficiently high to be detectable by the Large Area Telescope (LAT) of the *Fermi* satellite. The short timescale of this emission, $\lesssim 1$ s, is challenging both from an observational and a data-analysis viewpoint. On the other hand, the emission radii of $\sim 10^{10}$ cm, together with the aforementioned high photon luminosity, would lead to a high opacity of the $\gamma + \gamma \to e^{\pm}$ process. In such a case, new $e^{\pm}$ pairs are created which could modify the dynamics of the plasma. This effect is studied in App. (E).
The photons coming from the low density region have higher energies (hundreds of GeV, see Sec. (3.3.2)), but low luminosity $\sim 10^{43}$ erg s^{-1} (see again Sec. (3.3.2)). Assuming the same distance of the GRB considered above, for these photons we get a flux on Earth of $\sim 10^{-15}$ erg s^{-1} cm^{-2}, a bit a low value to be detectable by Earth telescopes.
In App. (E) we summarize the principal interaction processes for photons with baryons, electrons/positrons and photons. In this appendix, for each considered process, we calculate the interaction length l_{int} and, comparing it with the extension ΔL of the different interaction/production regions, we deduce if the photons are able to escape from these regions and, then, be detected on Earth, or if they remain trapped inside them.

From the above considerations, we conclude that a detection of photons, principally for the ones coming from the high density region, with the above specified energies, fluxs and timescale, can probe the pp mechanism studied in this work and, in turn, the associated neutrino emission.

Connection with the GWs emission

In connection with the above considerations about the detectability of photons produced via the pp interactions and in order to prove the model by means of another astrophysical messenger, as a final analysis, we would like to consider the gravitational wave (GW) signals. The development in the last years of this new branch of physics is principally due to the construction of new sensible GW-detectors: the gound-based interferometers Advanced LIGO [5] and Advanced Virgo [10], the space-based interferometer eLISA/LISA [37, 14]. This type of cosmic messenger is becoming important in order to have a complete

look on paroxysmally astrophysical events (as GRBs) and, then, to test the feasibility of a particular theoretical model that tries to explain such events.

The occurrence of a GWs emission in short and long GRBs, for the different subclasses introduced in Ch. (2) (see Sec. (2.1)), has been analyzed principally in [107, 132] (see also [104] and [108] [6]). In [107], but in particular in [132], they estimate the GW detection rate for the subclasses from I to VII in Sec. (2.1) and the possibility to detect this emission in different stages of the specific GRB formation. Since the above subclasses of GRBs are all constituted by a binary system, they study the GW emission and possible detection of the "*in-state*", namely the deformation of the space-time due to the orbital motion of the binary components, and the "*out-state*", namely the deformation of the space-time occurring after the merger of the components. We concentrate our attention only on the BdHN class and we refer the reader to [132] for further details on the analysis of the BdHN class and for the other subclasses.

They show that the *in-state* and the inspiral regime of the BdHN cannot be detected by aLIGO (nor by the other detectors), because the minimum GW frequency detectablen by aLIGO is $f_{\rm min}^{\rm aLIGO} \approx 10$ Hz, that corresponds to an orbital period of $P_{orb} \lesssim 0.2$ s (since, during the inspiral regime, the GW frequency is twice the orbital one), while, as explained in Secs. (1.2.2) (2.1) (3.1.1), the orbital period for the BdHN components is $P_{\rm orb} \approx 5$ min $\gg 0.2$ s. The *out-state* of the BdHN, the νNS-BH, could become the "*in-state*" of a new short GRB or leads to U-GRB, because of the merger of that components [51]. In the case of U-GRBs originating from the BdHN out-states, the inspiral regime of the components is detectable for sources located at distances smaller than 253 Mpc for the O1 Advanced LIGO run and smaller than 634 Mpc for the 2022+ run. No U-GRB has yet been electromagnetically identified. The closest distance at which its possible progenitor, namely a BdHN, is located is 805 Mpc. See Tab. 4 in [132] for the expected GW detection rate.

Even if a GW detection of this subsequent stage of the evolution of the original BdHN is possible, it would be difficult to prove the interactions studied in this chapter by means of this particular messenger. Indeed, the two events (neutrino/photons emission and GWs emission) occur in two different temporal ranges of the system evolution: 1) the neutrino/photon emission occurs still during the BdHN phase; 2) the GW emission occurs during the subsequent coalescence and U-GRB phases (see also Sec. (2.1)). In order to match these two probable detections, one needs to know the precise time evolution of the whole BdHN+U-GRB model.

[6] In [108], they compare and contrast the observation of the event GW170817 by LIGO-Virgo collaboration [9], associated with GRB170817A [8, 57] and AT 2017gfo [33, 16, 35, 90], with the subclasses introduced in Sec. (2.1). The negative result emerged from this analisys brought the authors to the introduction of a new, less energetic subclass of GRB formed by WD-WD merger (contrary to the common interpretation of the event by a NS-NS merger) in order to explain the observed gravitational waves and the related electromagnetic waves, in different regions of the spectrum (from optical to infrared and from X-ray to gamma-ray), emission.

Chapter 4

Magnetic field screening near a BH

4.1 Introduction to the screening problem

In this second part of the thesis we start to analyze a totally different problem in comparison to Ch. (3). The main topic of this chapter is to build a simple model to analyze the screening process of a magnetic field, performed by the motion of electrons and positrons inside a region filled by magnetic $\vec{B}$ and electric $\vec{E}$ fields.

The work in this chapter is still based on the BdHN class for GRB. It has been shown that (see [152]) a rotating Black Hole immersed in a test background magnetic field, of initial strength B_0 and aligned parallel to the BH rotation axis, generates an induced electric field, whose strength is proportional to the background magnetic field (see Sec. (2.5.2) and Eq. (4.44) and references therein). In this system, a huge number of e^+e^- pairs can be emitted by means of the vacuum polarization process, start to be accelerated to high energies by the induced electric field and emit photons.

Then, the screening process proceed through the following steps:

1. an initial number of $e^\pm$ pairs are emitted in this region filled by the two fields.

2. these initial electrons/positrons are accelerated by the electric field and emit radiation by means of the curvature, synchrotron or synchro-curvature processes, due to the presence of both electric and magnetic fields.

3. some of these photons create a new pair via the magnetic pair production process (MPP hereafter), $\gamma + B \rightarrow e^- + e^+$.

4. these new pairs start to be accelerated, emitting radiation, and circularize (together with parent particles) around the magnetic field lines generating an induced magnetic field, B_{ind}, oriented in the opposite direction with respect to the background one. This B_{ind} decreases the background magnetic field B_0. Due to the creation of new charged particles and to the proportionality between the strength of the fields, also the electric field decreases via these sequence of processes.

5. the series of the previous processes occurs at every integration time t, will bring to the development a particles shower.

The final purpose of this study is to apply this model in order to study the emission from a region near the BH in GRBs. Indeed, if the screening process occurs and, then, a reduction of the background magnetic field is present, the optical depth for pairs synchrotron emitted photons decreases and photons are free to escape from the region near the BH and could be observed as part of the signal of a GRB.

This is a preliminary study of this problem. The main approximations considered are the following: Minkoskian space-time and one-particle equations. Indeed, as we will show in the next sections, we

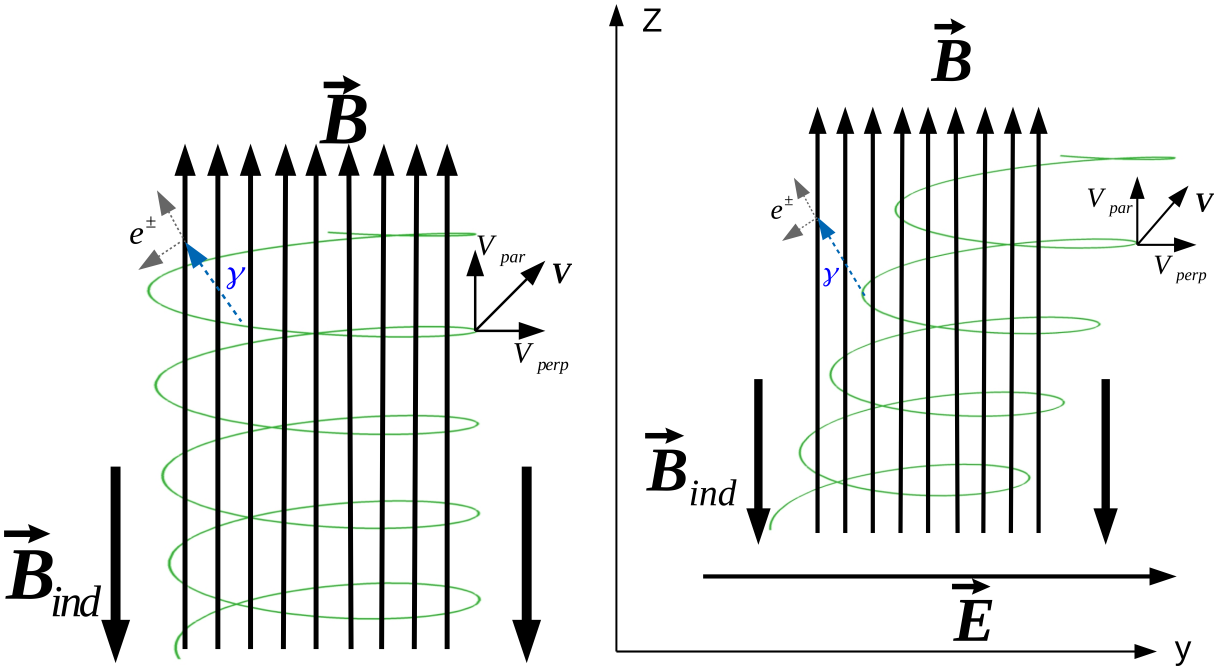

Figure 4.1. Scheme of the particles motion and trajectories around: the magnetic field lines (on the left), the magnetic and electric fields lines (on the right). The particles motion is responsible for the creation of: 1) synchrotron photons, which create new pairs through the MPP process; 2) the opposite induced magnetic field $\vec{B}_{ind}$, which shields both fields.

have built the set of equations which describes the whole mechanism as a one-particle equations. The consequences of this assumption are that all the particles are governed by the same equations and, then, are all emitted in the same directions, have the same energies and velocity, follow the same path. Their path is a helicoidal trajectory around the magnetic field lines (see Fig. (4.1) for a schematic representation of the particles motion and screening process), which leads to the development of a solenoidal structure.

In order to directly apply this model to the GRBs case, one needs to modify both some assumptions and equations of the model. Indeed, at first, since the particles are not all emitted in the same direction and do not have the same energies, one must introduce in the equations the distribution functions for the positions and velocities of the particles.
Secondly, our work is done under the approximation of Minkoskian space-time. In order to apply it to a region near a BH, we must improve the equations using a set of coordinates in agreement with general relativity. However, as we will see in Sec. (4.6), the screening process occurs in a very short time ($10^{-21} \lesssim t \lesssim 10^{-15}$ s, namely of the order of some Compton time $\tau_c \sim 10^{-21}$ s) and, consequently, on a very short space scale (of the order of a Compton length $\lambda_c \sim 10^{-11}$ cm). Since the general relativity effects on the space-time structure (as a proper specific coordinate system) act on macroscopic scales, while we work with very short time/space scales, this ensures us that the approximation of a locally flat space-time is satisfactory for our purposes.

Regarding the work we have developed in this chapter, we have studied the whole screening process for a specific configuration of the electromagnetic field, namely the case of perpendicular fields with electric field oriented along the $\hat{y}$-axis ($\vec{E} = E\,\hat{y}$) and magnetic field oriented along the $\hat{z}$-axis ($\vec{B} = B\,\hat{z}$). We also studied other configurations of the fields: 1) $\vec{E} \times \vec{B} = 0$, namely parallel fields; 2) $\vec{E} \cdot \vec{B} \neq E\,B$, namely with an angle between the two fields, but the works are not finished yet and, then, we put only the mathematical structure of the problem in Appendix (G).

The chapter is structured as follow: in Sec. (4.2), we have built the set of ordinary differential equations (ODEs) which describes the dynamic of the particles and the shower process; in Sec. (4.3), we derive the

ODE for the creation of the induced magnetic field, which will decrease the background one; Sec. (4.4) is devoted to set up the form of the pair-production rate; in Sec. (4.5), we summarize all the necessary equations that we need to integrate; in Sec. (4.6), the results of the integrations of the set of equations are shown; in Sec. (4.7), we discuss about particles number density in our problem and the connection for the applicability of the model to GRBs; Sec. (4.8) is devoted to the conclusions of our study.

4.2 Particles dynamics

Here we build the equations which describe the process of the magnetic field screening. We start to derive the equations of motion for a particle immersed in an electromagnetic field.

Before to start, we remind that in this chapter we use the Gaussian units, where the magnetic and electric field have the same units [Gauss] $= \left[\sqrt{\frac{\mathrm{g}}{\mathrm{cm}}}\frac{1}{\mathrm{s}}\right]$, the electric charge has dimension [statC] $= \left[\mathrm{cm}^{3/2}\ \mathrm{g}^{1/2}\ \mathrm{s}^{-1}\right]$, the mass [m] = [g], the energy $[\varepsilon]$ = [erg] and velocity $[u] = [\frac{\mathrm{cm}}{\mathrm{s}}]$.

Let's start to recall the definition of some variables that we will use in this chapter. The electromagnetic (EM hereafter) tensor is defined as

$$\mathcal{F}_{\alpha\beta} = \begin{pmatrix} 0 & E_x & E_y & E_z \\ -E_x & 0 & -B_z & B_y \\ -E_y & B_z & 0 & -B_x \\ -E_z & -B_y & B_x & 0 \end{pmatrix}, \quad \mathcal{F}^{\alpha\beta} = \begin{pmatrix} 0 & -E_x & -E_y & -E_z \\ E_x & 0 & -B_z & B_y \\ E_y & B_z & 0 & -B_x \\ E_z & -B_y & B_x & 0 \end{pmatrix}. \tag{4.1}$$

The four-momentum, in *covariant* form, of a particle is $p_\alpha = (E/c, -\vec{p})$ (the *controvariant* is $p^\alpha = (E/c, \vec{p})$), the four-velocity $u_\alpha = (\gamma c, -\gamma\vec{u})$, $(u^\alpha = (\gamma c, \gamma\vec{u}))$, and the proper time τ of a particle is defined as $t = \gamma\tau$. The metric is $\eta_{\mu\nu} = (1, -1, -1, -1)$.

After the definition of these variables, we can write the equation of motion of a particle immersed in an EM field as (see [65] or [74])

$$\frac{dp^\alpha}{d\tau} = m\frac{du^\alpha}{d\tau} = \frac{e}{c}\mathcal{F}^{\alpha\beta}u_\beta. \tag{4.2}$$

Now we can make explicit each component of the four-equation. The 0−component is:

$$mc\frac{d\gamma}{d\tau} = \frac{e}{c}\gamma\vec{E}\cdot\vec{u} \Longrightarrow \frac{d\gamma}{dt} = \frac{e}{mc}\vec{E}\cdot\vec{\beta}, \tag{4.3}$$

where $\vec{\beta} = \vec{u}/c$, m the mass of the particle and c the speed of light. The 1−component is

$$m\frac{d(\gamma u_x)}{d\tau} = m\gamma\left(u_x\frac{d\gamma}{dt} + \gamma\frac{du_x}{dt}\right) = \frac{e}{c}\gamma\left[E_x c + (u_y B_z - u_z B_y)\right], \tag{4.4}$$

where we considered also the variation of γ with time because the particle emits radiation and its energy changes. We recognize that the term between the round brackets, inside the square brackets, on the right side of the equation is the x−component of the vector product $\vec{u}\times\vec{B}$. Then, Eq. (4.4) can be rewritten as

$$\gamma\frac{du_x}{dt} = \frac{e}{mc}\left[E_x c + (\vec{u}\times\vec{B})_x\right] - u_x\frac{d\gamma}{dt}. \tag{4.5}$$

The equations for the other components are similar to Eq. (4.5), after operating a rotation of the indexes.

The system of equations, then, becomes

$$\begin{cases} mc\frac{d\gamma}{dt} = \frac{e}{c}\vec{E}\cdot\vec{u}, \\ \gamma\frac{du_x}{dt} = \frac{e}{mc}\left[E_x c + (\vec{u}\times\vec{B})_x\right] - u_x\frac{d\gamma}{dt}, \\ \gamma\frac{du_y}{dt} = \frac{e}{mc}\left[E_y c + (\vec{u}\times\vec{B})_y\right] - u_y\frac{d\gamma}{dt}, \\ \gamma\frac{du_z}{dt} = \frac{e}{mc}\left[E_z c + (\vec{u}\times\vec{B})_z\right] - u_z\frac{d\gamma}{dt}, \end{cases} \tag{4.6}$$

that in vectorial notation can be written as

$$\begin{cases} \frac{d\vec{\beta}}{dt} = \frac{e}{mc\gamma}\left[\vec{E} + \vec{\beta}\times\vec{B}\right] - \frac{\vec{\beta}}{\gamma}\frac{d\gamma}{dt}, \\ \frac{d\gamma}{dt} = \frac{e}{mc}\vec{E}\cdot\vec{\beta}. \end{cases} \tag{4.7}$$

Substituting the second equations into the first, we get that the spatial component of the equation of motion can be written as

$$\frac{d\vec{\beta}}{dt} = \frac{e}{mc\gamma}\left[\vec{E} + \vec{\beta}\times\vec{B} - \vec{\beta}(\vec{E}\cdot\vec{\beta})\right]. \tag{4.8}$$

Now we need to consider the radiation emitted by an accelerated particle in an EM field. From [74] (or [65]) we know that the intensity of the emitted radiation (in the classical form) is given by

$$I \equiv -\frac{2}{3}\frac{e^2}{m^2c^3}\left(\frac{dp_\alpha}{d\tau}\frac{dp^\alpha}{d\tau}\right), \tag{4.9}$$

where $dp_\alpha/d\tau = (e/c)\,F_{\alpha\beta}\,u^\beta$ (and similar for $dp^\alpha/d\tau$). The product between the EM tensor and the four-velocity can be written as

$$\mathcal{F}_{\alpha\beta}\,u^\beta = \begin{pmatrix} \gamma\vec{E}\cdot\vec{u} \\ -\gamma\left(\vec{E}c + \vec{u}\times\vec{B}\right) \end{pmatrix}, \quad \mathcal{F}^{\alpha\beta}\,u_\beta = \begin{pmatrix} \gamma\vec{E}\cdot\vec{u} \\ \gamma\left(\vec{E}c + \vec{u}\times\vec{B}\right) \end{pmatrix}. \tag{4.10}$$

Then, the product between the two four-vectors in Eq. (4.9) becomes

$$\frac{dp_\alpha}{d\tau}\frac{dp^\alpha}{d\tau} = \frac{e^2}{c^2}\left(\mathcal{F}_{\alpha\beta}u^\beta\right)\left(\mathcal{F}^{\alpha\beta}u_\beta\right) = e^2\gamma^2\left[\left(\vec{E}\cdot\vec{\beta}\right)^2 - \left(\vec{E} + \vec{\beta}\times\vec{B}\right)^2\right], \tag{4.11}$$

and, then, the emitted intensity becomes

$$I \equiv \left|-\frac{dE}{dt}\right| = \frac{2}{3}\frac{e^4\gamma^2}{m^2c^3}\left[\left(\vec{E} + \vec{\beta}\times\vec{B}\right)^2 - \left(\vec{E}\cdot\vec{\beta}\right)^2\right]. \tag{4.12}$$

We are now able to write the set of equations that describe the motion of the particle and its energy loss:

$$\begin{cases} \frac{d\vec{r}}{dt} = c\vec{\beta}, \\ \frac{d\vec{\beta}}{dt} = \frac{e}{mc\gamma}\left[\vec{E} + \vec{\beta}\times\vec{B} - \vec{\beta}(\vec{E}\cdot\vec{\beta})\right], \\ \frac{d\gamma}{dt} = \frac{e}{mc}\left(\vec{E}\cdot\vec{\beta}\right) - \frac{I}{mc^2}, \end{cases} \tag{4.13}$$

with I given by Eq. (4.12). For what concerns the energy emitted by the particle one needs to be careful on which expression to use. Indeed, the previous expression for the emitted intensity is valid only when

the emission occurs in classical regime. If the particle radiates in quantum regime the expression for I is different. In order to determine the right expression to use, we need to introduce the parameter χ, defined as (see [71])

$$\chi = \frac{\varepsilon_*}{2\,\varepsilon_e}, \tag{4.14}$$

where $\varepsilon_* = \hbar\omega_*$ is the energy of the photons emitted by the particle, and is given by,

$$\omega_* = \frac{3e\gamma^2}{2mc}\sqrt{\left(\vec{E}+\vec{\beta}\times\vec{B}\right)^2 - \left(\vec{\beta}\cdot\vec{E}\right)^2}. \tag{4.15}$$

Instead, $\varepsilon_e = \gamma m_e c^2$ is the electron/positron energy. The expression in Eq. (4.14) is the generalization for the χ parameter, for magnetic and electric field orientated in any direction, of the well known result presented in [38], where they give the expression for χ only in the case of $\vec{E}\cdot\vec{B} = 0$, namely perpendicular fields. We will use this parameter to discriminate the region where we can apply the classical or the quantistic expression for the emitted intensity I. Indeed, when $\chi \geq 1$ the particle radiates in the quantistic regime, while for $\chi < 1$ the particle radiates in the classical regime.

The energy loss in the quantistic regime is given by (see [71]):

$$I \equiv \left|-\frac{dE}{dt}\right| = \frac{e^2\,m^2\,c^3}{\sqrt{3}\,\pi\,\hbar^2}\overline{H}(x), \tag{4.16}$$

where

$$\overline{H}(x) \approx \frac{8\pi\sqrt{3}}{27}\frac{\chi^2}{\left(1+\frac{3}{4}\frac{(2\chi)^{2/3}}{\sqrt{\Gamma\left(\frac{2}{3}\right)}}\right)^2}\left[1+\frac{0.52\,\sqrt{\chi}\left(1+3\,\sqrt{\chi}-3.2\chi\right)}{1+0.3\,\sqrt{\chi}+17\chi+11\chi^2}\right]. \tag{4.17}$$

In our simulations, we use the last expression for the emitted intensity, Eq. (4.17), since (see [71]) the first part (before the square brackets) gives the right asymptotes at $\chi \ll 1$ and $\chi \gg 1$ and provides an accuracy better than 10% for other values of χ, whereas the term in the square brackets improves the accuracy to 0.1% for any value of χ. Then, Eqs. (4.16) and (4.17) can be used both for classical and quantistic emission.

Now that we have derived the equations for the motions of the particles, we need to derive the equations which describe their production. The evolution with time of the number of created photons can be written as

$$\frac{dN_\gamma}{dt}(t,\phi) = N_\pm(t,\phi)\,\frac{I(t)}{\varepsilon_\gamma^e(t)}, \tag{4.18}$$

where I is the emitted intensity and $N_\pm$ is the number of created pairs via the MPP process. Then, the quantity I/ε_γ gives the rate of photon production. Since the particles that we are considering are relativistic or ultra-relativistic, the photons are emitted principally in a straight angle along the direction of the emitting particle. We call ϕ as the angle between the particle moving direction and the magnetic field.

The equation describing the evolution of the number of pairs is strictly related to the one for the number of photons. Then, the equation for the evolution of the number of created pairs $N_\pm$ can be written as

$$\frac{dN_\pm}{dt}(t,\phi) = N_\gamma(t)\,R_A^e(t,\phi)\,c. \tag{4.19}$$

In the last equation the term $R_A^e \times c$ is the attenuation coefficient for the MPP process that, practically, gives us informations about the efficiency of the pair-production process. The MPP rate will be analyzed in Sec. (4.4).

Finally, we only want to clarify that the number of pairs $N_\pm$ here is not related to any density of particles; $N_\pm$ is only the number of particles inserted in the process as an initial condition that, successively, increases its number due to the MPP process. In order to give to $N_\pm$ a more "physical applicability" to our specific problem for GRBs, we will come back to this point in Sec. (4.7), where we will discuss about the particles number density and, thanks to it, to the applicability of our model to real astrophysical systems.

4.3 Magnetic field equation

Before to derive the equation of the magnetic field, let's define an important quantity useful to understand the motion of the particles: the curvature radius of the trajectory of the particle, which is defined as (see [71])

$$R_c = \frac{\gamma\, m\, c^2}{e}\left[\left(\vec{E}_{tot} + \vec{\beta}\times\vec{B}_{tot}\right)^2 - \left(\vec{\beta}\cdot\vec{E}_{tot}\right)^2\right]^{-\frac{1}{2}} \quad \text{cm}, \tag{4.20}$$

(B_{tot} and E_{tot} are the total magnetic and electric fields, respectively, defined below). The curvature radius is, by definition, the radius of the circular arc which better approximates the trajectory of the particle path at any time step of the motion.

The motion of a particle in an EM field can be considered as the combination between the motion along the $z-$direction and in a series of coils around the magnetic field lines, in the $x-y$ plane. The linear number density of the particles on a path dl is defined as $n_\lambda = dN_\pm/dl$ (#/cm), while the current density (in statC/s) in the two directions perpendicular and parallel to B are

$$\vec{J}_\perp = e\,\vec{\beta}_\perp\, n_\lambda\, c \tag{4.21a}$$

$$\vec{J}_\parallel = e\,\vec{\beta}_\parallel\, n_\lambda\, c, \tag{4.21b}$$

where $\beta_\perp = \sqrt{\beta_x^2+\beta_y^2}$, while $\beta_\parallel = \beta_z$.

From the well known Biot-Savart law, the infinitesimal element $d\vec{B}_{ind}$ generated by a current on an element of a coil dl is given by [1]

$$d\vec{B}_{ind} = \frac{J_\perp}{c}\frac{dl\times\Delta\vec{r}}{|\Delta\vec{r}|^3} = \frac{J_\perp}{c}\frac{dl}{|\Delta\vec{r}|^2} = e\,\beta_\perp\frac{dN_\pm}{dl}\frac{dl}{|\Delta\vec{r}|^2}, \tag{4.22}$$

where the subscript *ind* means "*induced*" magnetic field, $\Delta\vec{r}$ is the vector connecting an element of the coil, in the $x-y$ plane, with an element of the coil axes. Note that the element of the coil dl is always perpendicular to $|\Delta\vec{r}|$. The only non-zero component of the magnetic field vector is the one parallel to the coil axes. Then, we only have $dB_z = d\vec{B}\sin(\theta)$, where $\sin(\theta) = R_c(t)/\Delta\vec{r}$ and $|\Delta\vec{r}| = \sqrt{z^2+R_c(t)^2}$ (with z the height on the coil axes and $R_c(t)$ defined in Eq. (4.20)).
If we calculate the contribution at the center of the coil ($z=0$) and write the coil element dl as $dl = c\,dt$, we get the time evolution of the magnetic field as a function of the time evolution of the number of particles:

$$\frac{dB_{z,ind}}{dt} = e\frac{\beta_\perp(t)}{R_c(t)^2}\frac{dN_\pm}{dt}, \tag{4.23}$$

with $R_c(t)$ given in Eq. (4.20). Here B_{tot} is the total magnetic field (updated at each steps of the integration time) defined as $B_{tot}(t) = B_0 - B_{ind}(t)$; B_0 is the background magnetic field. Then, the equation describing the evolution of the magnetic field is $\dot{B}_{tot}(t) = -\dot{B}_{ind}(t)$.

In order to complete the set of the necessary equations for our problem, in the following section, we need to derive the photons induced pair production rate for the orthogonal configuration of the magnetic and electric fields ($\vec{B} = B\,\hat{z}$ and $\vec{E} = E\,\hat{y}$). As we stated in the introduction of this chapter, the set of equations for the configurations of parallel fields and for $\vec{E}$ and $\vec{B}$ in arbitrary direction, still need to be completed, but we show the set of equations that needs to be considered for these cases in Appendix (G). In our model, we consider the strength of the electric field proportional to the one of the magnetic field: $E(t) = (1/2)\,\Upsilon B(t)$, with Υ a constant that, for the application of our model to the case of black hole in

[1] The use of the Biov-Savart law is not restrictive in this case. Indeed, the background magnetic field can be considered constant if the time the particles spends to complete an "*orbit*" around the magnetic field lines (t_{circ}) is shorter than the screening time scale t_{screen}, namely the time that the magnetic field takes to decrease considerably. For almost all the considered cases, $t_{circ} < t_{screen}$ or $\ll t_{screen}$. We compare the two times scales in Sec. (4.6).

GRB, it corresponds to the BH spin. Since the BH spin can assume values in the range between $0 < \Upsilon \leq 1$, we have chosen to integrate our equations with three different values for the spin ($\Upsilon = 1,\ 1/5,\ 1/50$), in order to see how the model and the screening process react to a change of the fields strength. This is equivalent to look at the screening efficiency at different distances from the central BH (see [105, 136]).

In the following sections, all the variables and the equations are written in a dimensionless way, normalized with these criteria: the temporal variables, as t and $1/\omega_0$, becomes $\tilde{t} = t/\tau_c$ and $\tilde{\omega}_0 = \omega_0\ \tau_c$, with τ_c the Compton time $\tau_c = \hbar/m\ c^2 = 1.288 \times 10^{-21}$ s; the lengths become $(\tilde{x}, \tilde{y}, \tilde{z}) = (x, y, z)/\lambda\!\!\!^{-}_c$, with $\lambda\!\!\!^{-}_c$ the Compton length $\lambda\!\!\!^{-}_c = \hbar/m\ c = 3.862 \times 10^{-11}$ cm and, defining the critical electric/magnetic field as $E_{cr} = B_{cr} = m_e^2 c^3/e\hbar = 4.414 \times 10^{13}$ Gauss, we can normalize the magnetic field as $\tilde{B} = B/B_{cr}$ and the electric field as $\tilde{E} = E/E_{cr}$. All the energies are normalized to the electrons rest mass energy $m_e c^2 = 0.511$ MeV: for example the photon energy ε_γ becomes $\tilde{\varepsilon}_\gamma = \varepsilon_\gamma/m_e c^2$.

4.4 Pair production rate

In Eq. (4.19) we have introduced the attenuation coefficient for the magnetic pair production (MPP) R^e_A (the dimension of R^e_A is cm^{-1}). $R^e_A \times c$ gives the MPP rate (in s^{-1}), that, from now on, we call it $\zeta \equiv R^e_A c$. In [38] and [39], Daugherty & Lerche have found the expression for the pair production rate in strong electric and magnetic fields in two different cases for the orientation of the fields. In the first paper, they study the rate in the observer frame at rest with $\vec{E} \cdot \vec{B} = 0$, namely the electric and magnetic field are perpendicular, while in the second one they consider the case for $\vec{E}$ and $\vec{B}$ oriented in the same direction, namely parallel fields. The results of this second case can be generalized to the case where $\vec{E} \cdot \vec{B} \neq 0$ (namely $\vec{E}$ and $\vec{B}$ could be in any relative direction) through a proper Lorentz transformation.

In the next section, we study the pair production rate for the case of perpendicular fields, where we apply the results of [38]. The cases with other configurations of the field will be treated in App. (G).

4.4.1 Production rate for $\vec{E} \perp \vec{B}$

In this section we consider $B = (0, 0, B_z)$ and $E = \left(0, E_y, 0\right)$ and we study the pair production for a general direction propagation of photons. Let's consider a photon with energy ε_γ and momentum vector $\hbar\vec{k}$, with director cosines $\left(\eta_x,\ \eta_y,\ \eta_z\right)$. With the same configuration of the system, in [38] they give the pair production rate as a function of the magnitude of the fields and $\vec{\eta}$. Following [38], we make a Lorentz transformation in the $x-$direction which brings us to a new frame, $K^{'}$, where the electric field becomes 0. The velocity (and the correspondent Lorentz factor of the transformation) is

$$\vec{\beta^*} = \frac{\vec{E} \times \vec{B}}{B^2} = \frac{E_y}{B_z}\ \hat{x} \Longrightarrow \gamma^* = \frac{1}{\sqrt{1 - \left(\frac{E_y}{B_z}\right)^2}}. \tag{4.24}$$

The Lorentz transformation of all the variables (for generic vectors A^μ and tensors $C^{\alpha\beta}$) can be derived with the Lorentz boost in the x direction described by the matrix:

$$\Lambda^\mu_\nu = \begin{pmatrix} \gamma^* & -\gamma^*\,\beta^* & 0 & 0 \\ -\gamma^*\,\beta^* & \gamma^* & 0 & 0 \\ 0 & 0 & 1 & 0 \\ 0 & 0 & 0 & 1 \end{pmatrix}, \quad \begin{cases} A^{'\mu} = \Lambda^\mu_\nu\ A^\nu, \\ C^{'\alpha\beta} = \Lambda^\alpha_\sigma\ \Lambda^\beta_\delta\ C^{\sigma\delta}. \end{cases} \tag{4.25}$$

In the $K^{'}$ frame, the electromagnetic tensor becomes

$$\mathcal{F}^{'\alpha\beta} = \begin{pmatrix} 0 & 0 & 0 & 0 \\ 0 & 0 & -\frac{B_z}{\gamma^*} & 0 \\ 0 & \frac{B_z}{\gamma^*} & 0 & 0 \\ 0 & 0 & 0 & 0 \end{pmatrix}. \tag{4.26}$$

Defining the photon four-momentum as $k^{\mu} = \begin{pmatrix} \omega/c \\ \vec{k} \end{pmatrix}$ and the four-vector for the photon direction, *director cosines*, as $\eta^{\mu} = \begin{pmatrix} 1 \\ \vec{k}/k^0 \end{pmatrix}$, with k^0 the 0-component of k^{μ} (namely the photon energy). From Eq. (4.25), we get the photon energy and director cosines (where the numeric indices represents the Cartesian spatial directions, $1 \rightarrow x$, $2 \rightarrow y$, $3 \rightarrow z$)

$$\begin{cases} \varepsilon^{'}{}_{\gamma} = \gamma^* \left(1 - \beta^* \eta^1\right) \varepsilon_{\gamma} \\ \eta^{'1} = \frac{k^0}{k^{'}_0} \Lambda^1_{\nu} \eta^{\nu} = \frac{\varepsilon_{\gamma}}{\varepsilon^{'}_{\gamma}} \gamma^* \left(\eta^1 - \beta^*\right) \\ \eta^{'2} = \frac{\varepsilon_{\gamma}}{\varepsilon^{'}_{\gamma}} \eta^2 \\ \eta^{'3} = \frac{\varepsilon_{\gamma}}{\varepsilon^{'}_{\gamma}} \eta^3, \end{cases} \tag{4.27}$$

with $\varepsilon_{\gamma} = \hbar k^0$. We now need to derive the component of the magnetic field, in the $K^{'}$ frame, perpendicular to the direction of the propagation of the photons, which is given by

$$\vec{B^{'}} \times \vec{\eta^{'}} = \left(B^{'}_{\parallel} \hat{e^{'}}_{\parallel} + B^{'}_{\perp} \hat{e^{'}}_{\perp}\right) \times \hat{e^{'}}_{\parallel} = B^{'}_{\perp} \left(\hat{e^{'}}_{\perp} \times \hat{e^{'}}_{\parallel}\right) = B^{'}_{\perp}, \tag{4.28}$$

where $\hat{e^{'}}$ are the basic versors of the $K^{'}$ system relative to the photon propagation direction. The vector $\vec{B^{'}}_{\perp}$ assumes the form $\vec{B^{'}}_{\perp} = \left(-B^{'}_z \eta^{'}_y, B^{'}_z \eta^{'}_x\right)$ and then, from Eq. (4.27), we get the magnitude of $B^{'}_{\perp}$ as a function of the fields, the photon director cosines and energy in the laboratory frame:

$$B^{'}_{\perp} = B_z \sqrt{1 - \frac{E_y^2}{B_z^2}} \frac{\varepsilon_{\gamma}}{\varepsilon^{'}_{\gamma}} \sqrt{\eta_y^2 + \gamma^{*2} (\eta_x - \beta^*)^2}. \tag{4.29}$$

Now that we have derived the form of the necessary variables, we can write the pair production rate (in s^{-1}), in the $K^{'}$ frame, which is given by (see [38]):

$$\zeta^{'} = 0.23 \frac{\alpha_f c}{\lambda\!\!\!^{-}_c} \frac{B^{'}_{\perp}}{B_{cr}} \exp\left[-\frac{8}{3} \frac{mc^2}{\varepsilon^{'}_{\gamma}} \frac{B_{cr}}{B^{'}_{\perp}}\right]. \tag{4.30}$$

This form of the pair production rate is valid as long as the following condition is satisfied

$$\Psi = \frac{1}{2} \left(\frac{\varepsilon^{'}_{\gamma}}{mc^2}\right) \left(\frac{B^{'}_{\perp}}{B_{cr}}\right) \ll 1. \tag{4.31}$$

We will come back to this condition in Sec. (4.6) and we will see that it implies constraints of the values of initial parameters for the integrations of ours set of equations.
The pair production rate in the laboratory frame (observer at infinity) is given by $\zeta = \zeta^{'}/\gamma^*$, that can be rewritten as a function of the variables in the K frame as

$$\zeta = 0.23 \frac{\alpha_f c}{\lambda\!\!\!^{-}_c} \frac{B_z}{B_{cr}} \left(1 - \frac{E_y^2}{B_z^2}\right) \frac{\sqrt{\eta_y^2 \left(1 - \frac{E_y^2}{B_z^2}\right) + \left(\eta_x - \frac{E_y}{B_z}\right)^2}}{1 - \frac{E_y}{B_z} \eta_x} \exp\left\{-\frac{8}{3} \frac{mc^2}{\varepsilon_{\gamma}} \frac{B_{cr}}{B_z} \left[\eta_y^2 \left(1 - \frac{E_y^2}{B_z^2}\right) + \left(\eta_x - \frac{E_y}{B_z}\right)^2\right]^{-1/2}\right\}. \tag{4.32}$$

Eq. (4.32) can be rewritten in normalized form, namely multiplying by the Compton time τ_c, as

$$\tilde{\zeta} = 0.23\ \alpha_f\ \tilde{B}_z \left(1 - \frac{\tilde{E}_y^2}{\tilde{B}_z^2}\right) \frac{\sqrt{\eta_y^2\left(1 - \frac{\tilde{E}_y^2}{\tilde{B}_z^2}\right) + \left(\eta_x - \frac{\tilde{E}_y}{\tilde{B}_z}\right)^2}}{1 - \frac{\tilde{E}_y}{\tilde{B}_z}\eta_x} \exp\left\{-\frac{8}{3}\frac{\left[\eta_y^2\left(1 - \frac{\tilde{E}_y^2}{\tilde{B}_z^2}\right) + \left(\eta_x - \frac{\tilde{E}_y}{\tilde{B}_z}\right)^2\right]^{-1/2}}{\tilde{\varepsilon}_\gamma \tilde{B}_z}\right\}. \quad (4.33)$$

Now that we have derived the expression for the pair production rate for the case of $\vec{E} \perp \vec{B}$, we would like to relate the photons momentum directors cosines $\vec{\eta}$ with the electron velocity $\vec{\beta}$. This procedure can be done making a Lorentz transformation in the particles comoving frame, deriving the relation in this frame and coming back to the K frame. The general procedure to get this result is done in App. (F). Here we write the result of transformation that gives $\vec{\eta}\left(\vec{\beta}, \Theta, \Phi\right)$, where Θ and Φ are the polar and azimuthal angles, respectively, of emission in the comoving frame:

$$\begin{cases} \eta_x = \frac{\sin(\Theta)\cos(\Phi) + \beta_x\left[\gamma + \frac{(\gamma-1)}{\beta^2}\nu\right]}{\gamma(1+\nu)} \\ \eta_y = \frac{\sin(\Theta)\sin(\Phi) + \beta_y\left[\gamma + \frac{(\gamma-1)}{\beta^2}\nu\right]}{\gamma(1+\nu)} \\ \eta_z = \frac{\cos(\Theta) + \beta_z\left[\gamma + \frac{(\gamma-1)}{\beta^2}\nu\right]}{\gamma(1+\nu)}, \end{cases} \quad (4.34)$$

where

$$\nu = \beta_x \sin(\Theta)\cos(\Phi) + \beta_y \sin(\Theta)\sin(\Phi) + \beta_z \cos(\Theta). \quad (4.35)$$

Here γ and β are the Lorentz factor and the velocity of the particle. Selecting specific emission angles of the photon in the comoving frame (e.g., $\Theta = \Phi = \pi/2$), we can integrate our set of equations for the necessary variables (see next section, Sec. (4.5)).

4.5 Set of equations for the case $\vec{E} \perp \vec{B}$

In this configuration the electric field is along the $\hat{y}-$axis ($\vec{E} = E\,\hat{y}$), while the magnetic field still lying along the $\hat{z}-$axis ($\vec{B} = B\,\hat{z}$). Here the definition of B_{tot} and E_{tot} is the same stated above.

With this configuration of the fields, the equations for the particle velocity become:

$$\begin{cases} \frac{d\beta_x}{d\tilde{t}} = \frac{\beta_y}{\gamma}\left[\tilde{B}_{tot} - \beta_x \tilde{E}_{tot}\right] \\ \frac{d\beta_y}{d\tilde{t}} = \frac{\left[\tilde{E}_{tot}\left(1-\beta_y^2\right) - \beta_x \tilde{B}_{tot}\right]}{\gamma} \\ \frac{d\beta_z}{d\tilde{t}} = -\frac{\tilde{E}_{tot}\beta_z\beta_y}{\gamma}. \end{cases} \quad (4.36)$$

The equations for the positions of the particles are

$$\begin{cases} \frac{d\tilde{x}}{d\tilde{t}} = \beta_x(t) \\ \frac{d\tilde{y}}{d\tilde{t}} = \beta_y(t) \\ \frac{d\tilde{z}}{d\tilde{t}} = \beta_z(t). \end{cases} \quad (4.37)$$

The equation for the particle Lorentz factor is

$$\frac{d\gamma}{d\tilde{t}} = \beta_y \, \tilde{E}_{tot} - \frac{1}{\sqrt{3}\,\pi}\alpha_f \overline{H}(\tilde{\chi}), \tag{4.38}$$

with $\overline{H}(\chi)$ given by Eq. (4.17) and $\chi = \tilde{\varepsilon}_\gamma/2\gamma$ given by Eq. (4.14), with the photon energy given by

$$\tilde{\varepsilon}_\gamma = \frac{3}{2}\gamma^2 \sqrt{\beta_y^2\left(\tilde{B}_{tot}^2 - \tilde{E}_{tot}^2\right) + \left(\tilde{E}_{tot} - \beta_x \tilde{B}_{tot}\right)^2}. \tag{4.39}$$

The equation for the number of photons becomes

$$\frac{dN_\gamma(\tilde{t})}{d\tilde{t}} = \frac{2}{3\pi\sqrt{3}}\alpha_f \frac{N_\pm(\tilde{t})}{\gamma^2} \frac{\overline{H}(\tilde{\chi})}{\sqrt{\beta_y^2\left(\tilde{B}_{tot}^2 - \tilde{E}_{tot}^2\right) + \left(\tilde{E}_{tot} - \beta_x \tilde{B}_{tot}\right)^2}}. \tag{4.40}$$

The equation for the number of pairs is

$$\frac{dN_\pm(\tilde{t})}{d\tilde{t}} = N_\gamma(\tilde{t})\,\tilde{\zeta}(\tilde{t}), \tag{4.41}$$

with $\tilde{\zeta}$ given by Eq. (4.33), together with Eq. (4.34). The curvature radius $\tilde{R}_c$ becomes

$$\tilde{R}_c = \frac{\gamma}{\sqrt{\beta_y^2\left(\tilde{B}_{tot}^2 - \tilde{E}_{tot}^2\right) + \left(\tilde{E}_{tot} - \beta_x \tilde{B}_{tot}\right)^2}}. \tag{4.42}$$

Finally, we can write the equation for the magnetic field as

$$\frac{d\tilde{B}_{tot}}{d\tilde{t}} = -\alpha_f \frac{\sqrt{\beta_x^2 + \beta_y^2}}{\gamma^2} \frac{dN_\pm}{d\tilde{t}} \left[\beta_y^2\left(\tilde{B}_{tot}^2 - \tilde{E}_{tot}^2\right) + \left(\tilde{E}_{tot} - \beta_x \tilde{B}_{tot}\right)^2\right]. \tag{4.43}$$

4.6 Results

In this section we report the results obtained by the integrations of the set of equations described in Sec. (4.5), for the configuration of perpendicular fields ($\vec{E} = E\,\hat{y}$ and $\vec{B} = B\,\hat{z}$). In Sec. (4.6.1), we explain how we derived the initial conditions for our set of equations, which conditions we selected and the plots of the pair production rate. In Sec. (4.6.2), we show the results of the integrations for the magnetic field screening. In Sec. (4.6.3) the results for the emitted photons (energy and number) and the trajectories of the particles are shown. Sec. (4.6.4) is devoted to the comparison between the circularization and the screening times scale. Finally, in Sec. (4.6.5), we give further conditions (besides the one stated in Sec. (4.6.1)) that ensure us the occurrence of the pair production. In this last section, we also explain the results for the rate obtained in Sec. (4.6.1).
We remind that in our calculations and, then, in the following results, we assume the proportionality between the electric and magnetic field ([130, 136, 105])

$$E(t) = \frac{1}{2}\,\Upsilon\, B(t), \tag{4.44}$$

where the parameter Υ should be $\Upsilon \leq 1$. We made integrations selecting three values $\Upsilon = 1,\ 1/5$ and $1/50$. This proportionality, then, implies that when $B(t)$ changes, also the electric field changes consistently. This is an important effect, since the decrease of the electric field affects the motion of particles themselves and, consequently, all the successive processes that give rise to the screening effect.

4.6.1 Initial conditions and MPP rate

In order to apply the specific formula for the rate of pair-production, as already stated in Sec. (4.4), the condition in Eq. (4.31) on the parameter Ψ needs to be satisfied. In Eq. (4.31) the condition for Ψ is expressed in the frame where there is no perpendicular electric field but only magnetic field, the $K^{'}$ frame. Now, we need to transform back to the original frame (K frame), where the two fields are perpendicular. The photon energy transforms with the usual formula for the relativistic Doppler effect

$$\varepsilon_{\gamma}^{'} = \gamma^{*}\,(1 - \beta^{*}\eta_{x})\,\varepsilon_{\gamma}, \tag{4.45}$$

while the perpendicular component of the magnetic field transforms like

$$B_{\perp}^{'} = B\sqrt{1 - \frac{E^2}{B^2}}\frac{\varepsilon_{\gamma}}{\varepsilon_{\gamma}^{'}}\sqrt{\eta_{y}^{2} + \gamma^{*2}\,(\eta_{x} - \beta^{*})^{2}}, \tag{4.46}$$

where $\beta^{*} = E/B$, and $\gamma^{*} = 1/\sqrt{1 - E^2/B^2}$, is the velocity, and the respective Lorentz factor, of the transformation between the two systems and $\vec{\eta}$ is the photon momentum director cosines. Inserting Eq. (4.45) and Eq. (4.46) and the expression for the photon energy

$$\varepsilon_{\gamma} = \frac{3}{2}\frac{e\hbar}{m^2\,c^3}B\,\gamma^{2}\sqrt{\beta_{y}^{2}\left(1 - \frac{E^2}{B^2}\right) + \left(\frac{E}{B} - \beta_{x}\right)^{2}}, \tag{4.47}$$

in Eq. (4.31), we get

$$\Psi = \frac{3}{4}\frac{e\hbar}{m\,c}\frac{B^2}{B_{cr}}\gamma^{2}\sqrt{\beta_{y}^{2}\left(1 - \frac{E^2}{B^2}\right) + \left(\frac{E}{B} - \beta_{x}\right)^{2}}\sqrt{\eta_{y}^{2}\left(1 - \frac{E^2}{B^2}\right) + \left(\eta_{x} - \frac{E}{B}\right)^{2}} \ll 1. \tag{4.48}$$

This condition brings with it three conditions for the values of the parameters in our calculations, namely the magnetic field strength B_0, the initial value of the Lorentz factor of the particle γ_0 (which derives from ε_{γ}) and the initial direction of emission of the particle (contained in the particles initial velocities ($\beta_{x,0}$, $\beta_{y,0}$, $\beta_{z,0}$) and, then, in the director cosines of the photons $\vec{\eta}$). Then, we need to choose the right values of the three parameters in order to apply the formula for the rate in Eq. (4.33).

We proceeded firstly choosing a specific emission direction of the particles. We selected three directions: 1) along the $\hat{y}-$axis; 2) along the $\hat{z}-$axis; 3) with a polar and azimuthal angle of $\theta = 75°$ and $\phi = 30°$, respectively (from now on, we call this last direction of emission as "*generic*"). For each direction of emission, we chose the initial value of the magnetic field B_0 and, consequently, the maximum value of particle Lorentz factor γ_0.

In Tab. (4.1), we list the respective values of B_0 and γ_0 for each emission direction and for the three values of the parameter Υ. The values of B_0 and γ_0 for which particles can be emitted in the three selected directions and satisfy, at the same time, the condition in Eq. (4.48) are

- $\Upsilon = 1 \rightarrow B_0 = 0.1\ B_{cr}$ and $\gamma_0 = 3.66$;
- $\Upsilon = \frac{1}{5} \rightarrow B_0 = 0.1\ B_{cr}$ and $\gamma_0 = 3.71$;
- $\Upsilon = \frac{1}{50} \rightarrow B_0 = 0.1\ B_{cr}$ and $\gamma_0 = 3.71$.

For some of the conditions listed in Tab. (4.1), we have integrated the system of equations given in Sec. (4.5) varying the initial number of emitted particles, $N_{\pm,0}$ and photons, $N_{\gamma,0}$. We have chosen the following values:

- $N_{\pm,0} = 1,\ 10^3,\ 10^6,\ 10^{10}$, with $N_{\gamma,0} = 0$;

Table 4.1. Maximum initial upper values for B_0 (in unit of the critical field B_{cr}) and γ_0, for initial emission directions of the particles along the directions (y, z, *generic*), for the three selected values of the BH spin Υ, necessary in order to satisfy the condition given in Eq. (4.48).

Υ	Direction	$B_0(B_{cr})$	γ_0
1	y	0.1	3.66
	z	0.1	7.098
		0.3	2.14
	Generic	0.1	6.48
		0.3	2.27
$\frac{1}{5}$	y	0.1	3.71
	z	0.1	22.66
		0.3	10.04
		0.5	4.79
		0.7	2.63
	Generic	0.1	4.18
$\frac{1}{50}$	y	0.1	3.71
	z	0.1	22.66
		0.3	22.66
		0.5	22.66
		0.7	22.66
		0.9	15.92
		1.1	10.04
		1.3	7.48
		1.5	5.8
		1.7	4.59
		1.9	3.66
		2.1	3
		2.3	2.51
		2.5	2.13
	Generic	0.1	3.81

- $N_{\gamma,0} = 10^3$, with $N_{\pm,0} = 1$.

We are looking for a significant variation for the value of the magnetic field. We expect that the integration made with the initial condition $N_{\pm,0} = 1$ does not affect much the magnetic field. Indeed, for all the specific set of conditions listed in Tab. (4.1) (with fixed $N_{\pm,0} = 1$ and $N_{\gamma,0} = 0$), we found that the number of pairs remains practically constant $\gtrsim 1$, while very a few of photons are created [2]. Then, since practically no other particles are created, for this case the particle current is not sufficient to decrease significantly B_0. Indeed, for this case, the percentage variation of the magnetic field spans between $10^{-5}\%$ and $10^{-10}\%$ (see Tab. (4.2) (4.3) (4.4)). Increasing the initial number of pairs $N_{\pm,0}$, we got a consistently percentage variation of the magnetic field.
In Tabs. (4.2) (4.3) (4.4) we report, for all the studied initial conditions (emission direction, B_0, γ_0, $N_{\pm,0}$, $N_{\gamma,0}$), the percentage variation of the magnetic field $\Delta B(\%)$, the final number of created pairs $N_{\pm,f}$ and photons $N_{\gamma,f}$. In Tab. (4.2) we report the results for $\Upsilon = 1$, Tab. (4.3) for $\Upsilon = 1/5$ and Tab. (4.4) for $\Upsilon = 1/50$. From Tabs. (4.2) (4.3) (4.4), we can get some interesting results. Firstly, we see that the

[2] All the numerical integrations stop when the Lorentz factor of the particle becomes equal to 1, namely when the particle loses all of its energy because of the emitted radiation. We start the integrations at $t_0 = 10^{-21}$ s and the previous condition is reached at $t_f \sim 10^{-18} - 10^{-15}$ s, depending on the specific initial conditions.

Table 4.2. Results for the integrations of the set of equations given in Sec. (4.5) for each case in Tab. (4.1) and for the different initial conditions. The BH spin parameter is setted to $\Upsilon = 1$. **Column (1):** initial emission direction for particles; **Column (2):** initial value of the magnetic field strength; **Column (3):** initial value of the Lorentz factor; **Column (4):** percentage variation of the magnetic field (calculated as $\frac{B(t_0)-B(t_f)}{B(t_0)} \times 100$); **Column (5):** initial number of emitted particles; **Column (6):** final number of created particles; **Column (7):** initial number of emitted photons; **Column (8):** final number of emitted photons. In column (6), in some cases $N_{\pm,0} \simeq N_{\pm,f}$. This could be misleading. When $N_{\pm,0}$ has a low value, the number of particles remain almost the same; when $N_{\pm,0}$ is high, the final number of particles increases, but remain still lower than $N_{\pm,0}$.

Direction	$B_0(B_{cr})$	γ_0	$\Delta B(\%)$	$N_{\pm,0}$	$N_{\pm,f}$	$N_{\gamma,0}$	$N_{\gamma,f}$
Generic	0.1	6.48	$-4.7 \times 10^{-12}\%$	1	1	0	3.5
			$-4.7 \times 10^{-9}\%$	10^3	10^3	0	3500
			$-4.7 \times 10^{-6}\%$	10^6	$\gtrsim 10^6$	0	3.5×10^6
			$-4.66 \times 10^{-2}\%$	10^{10}	$\gtrsim 10^{10}$	0	3.5×10^{10}
			$-6.3 \times 10^{-8}\%$	1	1	10^3	1003
	0.3	2.27	$-1.34 \times 10^{-10}\%$	1	1	0	0.45
			$-1.34 \times 10^{-7}\%$	10^3	10^3	0	447
			$-1.34 \times 10^{-4}\%$	10^6	10^6	0	4.48×10^5
			-1.09%	10^{10}	$\gtrsim 10^{10}$	0	4.46×10^9
			$-1.46 \times 10^{-6}\%$	1	1	10^3	1000.4
Along y	0.1	3.66	$-2.25 \times 10^{-10}\%$	1	1	0	2.79
			$-2.25 \times 10^{-7}\%$	10^3	10^3	0	2798
			$-2.2 \times 10^{-4}\%$	10^6	10^6	0	2.8×10^6
			-1.72%	10^{10}	$\gtrsim 10^{10}$	0	2.84×10^{10}
			$-1.7 \times 10^{-6}\%$	1	1	10^{-3}	1002
Along z	0.1	7.098	$-1 \times 10^{-12}\%$	1	1	0	11.3
			$-1 \times 10^{-9}\%$	10^3	10^3	0	1.13×10^4
			$-1 \times 10^{-6}\%$	10^6	10^6	0	1.13×10^7
			-0.01%	10^{10}	$\gtrsim 10^{10}$	0	1.13×10^{11}
			$-1.5 \times 10^{-8}\%$	1	1	10^3	1011
	0.3	2.14	$-1.06 \times 10^{-10}\%$	1	1	0	2.33
			$-1.6 \times 10^{-7}\%$	10^3	10^3	0	2333
			$-1.6 \times 10^{-4}\%$	10^6	10^6	0	2.3×10^6
			-1.27%	10^{10}	$\gtrsim 10^{10}$	0	2.4×10^{10}
			$-1.5 \times 10^{-6}\%$	1	1	10^3	1002

model is strictly correlated to the direction of emission of particles and to the strength of the background magnetic field. A sufficient decrease of $\vec{B}$ is operated principally when we start the integration with a high initial number of particles $N_{\pm,0}$. For particles emitted along the $\hat{z}-$axis and along the *generic* direction, we notice that the stronger the background field, the higher the reduction of the field itself is, and lower (with respect to the number of emitted particles) is the final number of photons. This means that not all the particles emit photons, but they "prefer" to circularize along the field lines. Even when they are emitted along the $\hat{y}-$axis, there is a significant reduction of $\vec{B}$, but this occurs with a lower strength of the field (contrary with the behaviour on the other directions of emission). These characteristics can be understood by looking the dependence of the rate $\zeta(t)$ in Eq. (4.33) on $B(t)$ and $\vec{\eta}$.

We have to point out that, in all the tables for the initial condition $N_{\pm,0} \geq 10^6$, the number of final particles $N_{\pm,f}$ seems not to increase. Actually it increases, but the variation is some orders of magnitude less than $N_{\pm,0}$ and cannot be completely represented in the tables. For example, for $N_{\pm,0} = 10^{10}$, hundreds to thousands new particles are created. For $N_{\pm,0} = 10^6$, only a few particles are created.

This result tells us that the MPP process is not so efficient almost for all the cases, in the range of time necessary for the particles to lose all of their energy. When $N_{\pm,0}$ is high ($\gtrsim 10^{10}$), the increment of the number of particles seems bigger mainly due to the higher number of photons rather than a greater value of the pair-production rate. Indeed, as one can see from Figs. (4.2) (4.3) where the MPP rate as a function of time is shown for the case $\Upsilon = 1$, $B_0 = 0.3\ B_{cr}$ and for different $N_{\pm,0}$, the rate is practically the same for $N_{\pm,0} = 10^3,\ 10^6,\ 10^{10}$, whereas it's value decreases if one inserts a higher number of particles. From Figs. (4.2) (4.3), one can also notice that $\zeta(t)$ decreases with time. This is mainly due to the decrease of the strength of the magnetic field, because of the greater number of particles, and to the decrease of the photon energy (see Eq. (4.32)). Even the several oscillations of the curves are related to ε_γ and position $\vec{\eta}$.

Table 4.3. Same results of Tab. (4.2), but for $\Upsilon = 1/5$.

Direction	$B_0(B_{cr})$	γ_0	$\Delta B(\%)$	$N_{\pm,0}$	$N_{\pm,f}$	$N_{\gamma,0}$	$N_{\gamma,f}$
Generic	0.1	4.18	$-3.2\times10^{-11}\%$	1	1	0	4.63
			$-3.2\times10^{-8}\%$	1000	10^3	0	4633
			$-3.2\times10^{-5}\%$	10^6	10^6	0	4.63×10^6
			-0.308%	10^{10}	$\gtrsim 10^{10}$	0	4.62×10^{10}
			$-4.35\times10^{-7}\%$	1	1	10^3	1004
Along y	0.1	3.71	$-9.14\times10^{-11}\%$	1	1	0	4.45
			$-9.14\times10^{-8}\%$	10^3	10^3	0	4457
			$-9.14\times10^{-5}\%$	10^6	10^6	0	4.46×10^6
			-0.798%	10^{10}	$\gtrsim 10^{10}$	0	4.42×10^{10}
			$-9.49\times10^{-7}\%$	1	1	10^{-3}	1004
Along z	0.1	22.66	0%	1	1	0	64
			0%	10^3	10^3	0	6.4×10^4
			$-2.2\times10^{-14}\%$	10^6	10^6	0	6.4×10^7
			$-4.2\times10^{-11}\%$	10^{10}	10^{10}	0	6.4×10^{11}
			0%	1	1	10^3	1063
	0.3	10.04	$-1.13\times10^{-12}\%$	1	1	0	19.6
			$-1.15\times10^{-9}\%$	10^3	10^3	0	1.96×10^4
			$-1.15\times10^{-6}\%$	10^6	10^6	0	1.96×10^7
			$-1.15\times10^{-2}\%$	10^{10}	$> 10^{10}$	0	1.96×10^{11}
			$-8\times10^{-9}\%$	1	1.0025	10^3	1019
	0.5	4.8	$-1.75\times10^{-11}\%$	1	1	0	10.6
			$-1.75\times10^{-8}\%$	10^3	10^3	0	1.05×10^4
			$-1.75\times10^{-5}\%$	10^6	10^6	0	1.05×10^7
			-0.171%	10^{10}	$> 10^{10}$	0	1.05×10^{11}
			$-8.3\times10^{-8}\%$	1	1.0036	10^3	1010
	0.7	2.63	$-8.3\times10^{-11}\%$	1	1	0	5.8
			$-8.3\times10^{-8}\%$	10^3	10^3	0	5811
			$-8.3\times10^{-5}\%$	10^6	10^6	0	5.81×10^6
			-0.734%	10^{10}	$> 10^{10}$	0	5.93×10^{10}
			$-2.87\times10^{-7}\%$	1	1.0027	10^3	1005

Table 4.4. Same results of Tab. (4.2), but for $\Upsilon = 1/50$.

Direction	$B_0(B_{cr})$	γ_0	$\Delta B(\%)$	$N_{\pm,0}$	$N_{\pm,f}$	$N_{\gamma,0}$	$N_{\gamma,f}$
Generic	0.1	3.81	$-2.5\times10^{-11}\%$	1	1	0	5.15
			$-2.5\times10^{-8}\%$	10^3	10^3	0	5153
			$-2.5\times10^{-5}\%$	10^6	10^6	0	5.15×10^6
			-0.237%	10^{10}	$\gtrsim 10^{10}$	0	5.14×10^{10}
			$-3.4\times10^{-7}\%$	1	1	10^3	1005
Along y	0.1	3.71	$-8\times10^{-11}\%$	1	1	0	4.91
			$-8\times10^{-8}\%$	10^3	10^3	0	4912
			$-8\times10^{-5}\%$	10^6	10^6	0	4.91×10^6
			-0.711%	10^{10}	$\gtrsim 10^{10}$	0	5.02×10^{10}
			$-8.8\times10^{-7}\%$	1	1	10^{-3}	1004
Along z	0.1	22.66	0%	1	1	0	22.23
			0%	10^3	10^3	0	2.22×10^4
			0%	10^6	10^6	0	2.22×10^7
			0%	10^{10}	10^{10}	0	2.22×10^{11}
			0%	1	1	10^3	1022
	1.1	10.04	$-1.6\times10^{-14}\%$	1	1	0	26.8
			$-7.8\times10^{-12}\%$	10^3	10^3	0	1.49×10^4
			$-7.8\times10^{-9}\%$	10^6	10^6	0	1.77×10^7
			$-7.5\times10^{-5}\%$	10^{10}	$\gtrsim 10^{10}$	0	1.75×10^{11}
			$-2.7\times10^{-11}\%$	1	1.0022	10^3	1026
	2.5	2.13	$-5.7\times10^{-12}\%$	1	1	0	35.3
			$-5.4\times10^{-9}\%$	10^3	10^3	0	3.53×10^4
			$-5.6\times10^{-6}\%$	10^6	$\gtrsim 10^6$	0	3.53×10^7
			$-5.5\times10^{-2}\%$	10^{10}	$> 10^{10}$	0	3.52×10^{11}
			$-1.3\times10^{-8}\%$	1	1.025	10^3	1036

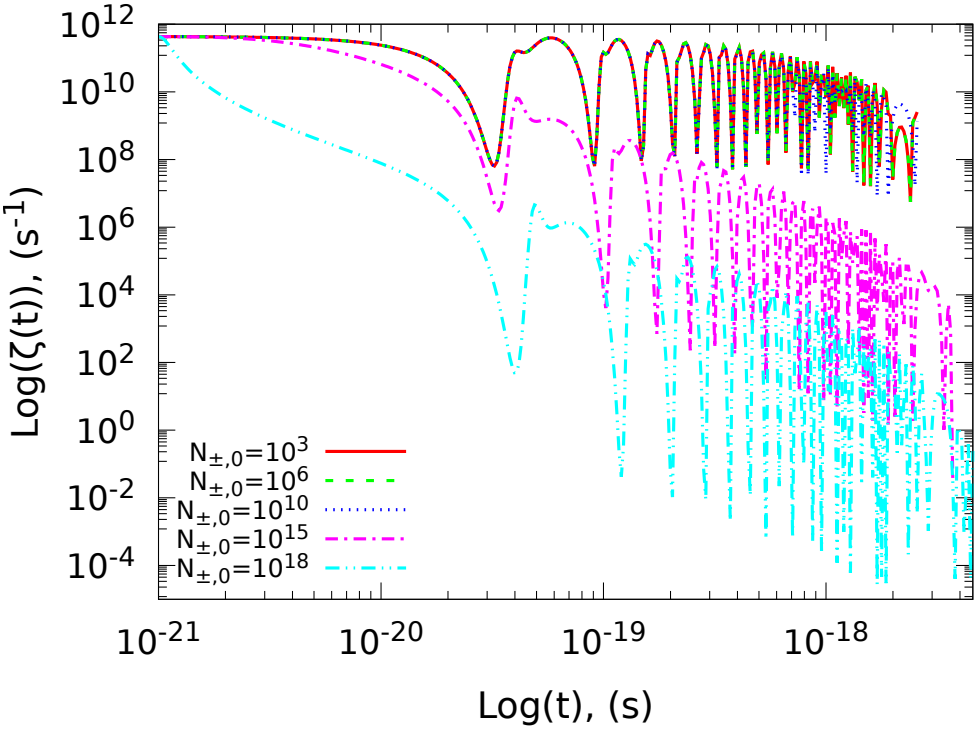

Figure 4.2. Magnetic pair-production rate (in s^{-1}), given by Eq. (4.32), with initial conditions: $\Upsilon = 1$, $N_{\pm,0} = 10^3,\ 10^6,\ 10^{10},\ 10^{15},\ 10^{18}$, $B_0 = 0.3\ B_{cr}$, $\gamma_0 = 2.27$ and particles emitted along the *generic* direction.

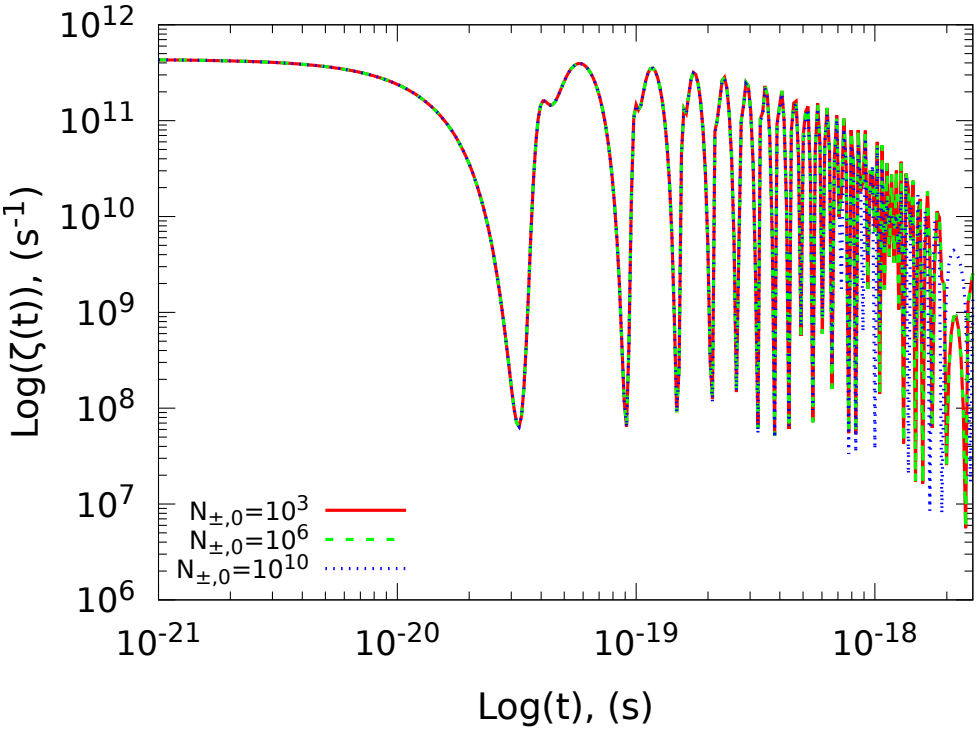

Figure 4.3. Same as Fig. (4.2), for $N_{\pm,0} = 10^3,\ 10^6,\ 10^{10}$ and with the same initial conditions.

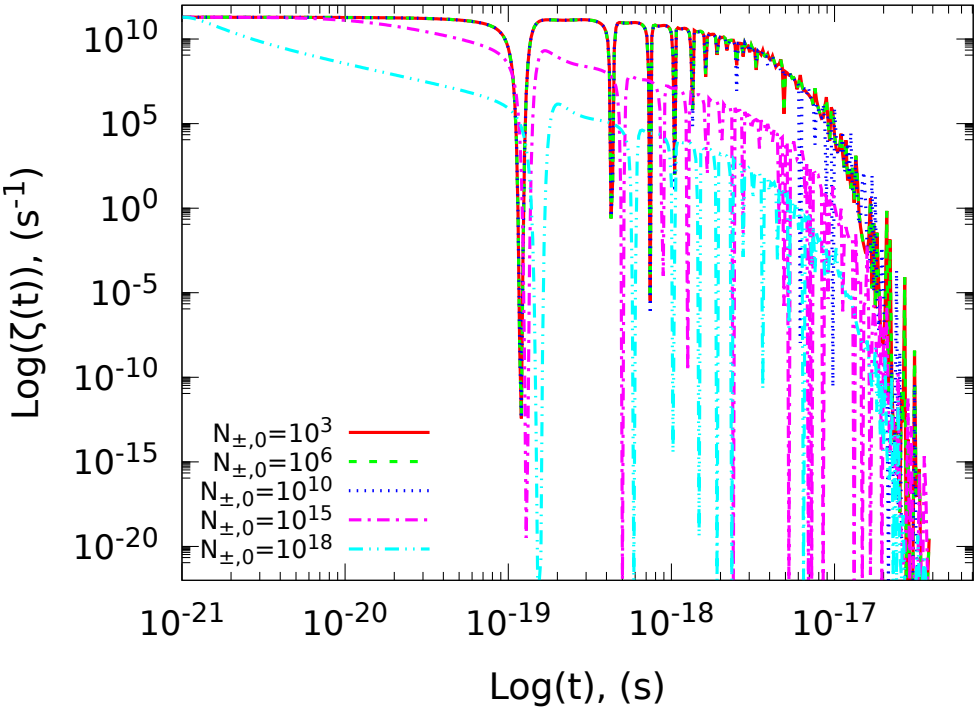

Figure 4.4. Same as Fig. (4.2), for the case with $\Upsilon = 1/5$, $B_0 = 0.1\ B_{cr}$, $\gamma_0 = 4.18$ and particles emitted along the *generic* direction.

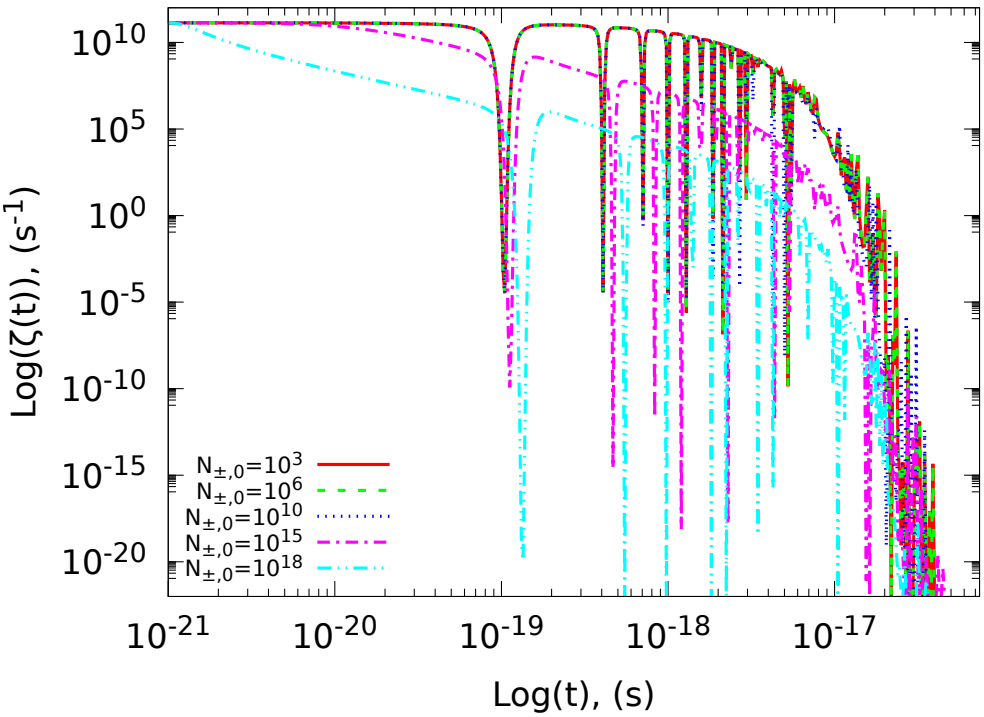

Figure 4.5. Same as Fig. (4.2), for the case with $\Upsilon = 1/50$, $B_0 = 0.1\ B_{cr}$, $\gamma_0 = 3.81$ and, again, particles emitted along the *generic* direction.

In Figs. (4.4) and (4.5), the rate $\zeta(t)$ is shown for $\Upsilon = 1/5$ (Fig. (4.4)) and $\Upsilon = 1/50$ (Fig. (4.5)). Here $B_0 = 0.1\ B_{cr}$. Also for these last two plots, we notice the same features for the rate present in Fig. (4.2) and (4.3), namely that:

- the curves for the rate practically coincide for $N_{\pm,0} = 10^3,\ 10^6,\ 10^{10}$, while the one for $N_{\pm,0} = 10^{15},\ 10^{18}$ the rate tends to decrease its efficiency;
- together with Fig. (4.2), we notice a small increase of the rate if we decrease the parameter Υ (see below Fig. (4.13)). Decreasing Υ, the curves also present more deep and narrow peaks.

In Fig. (4.6) is shown the variation of the parameter Ψ in Eq. (4.48), for the case with $\Upsilon = 1$ and for the three directions of emission (**generic**, **y** and **z**), with $B_0 = 0.1\ B_{cr}$. It is evident that the condition in Eq. (4.48) is satisfied, for all the analyzed cases and for all the integration time. Fig. (4.7) and Fig. (4.8) show the behaviour of $\Psi(t)$ for $\Upsilon = 1/5$ and $\Upsilon = 1/50$, respectively.

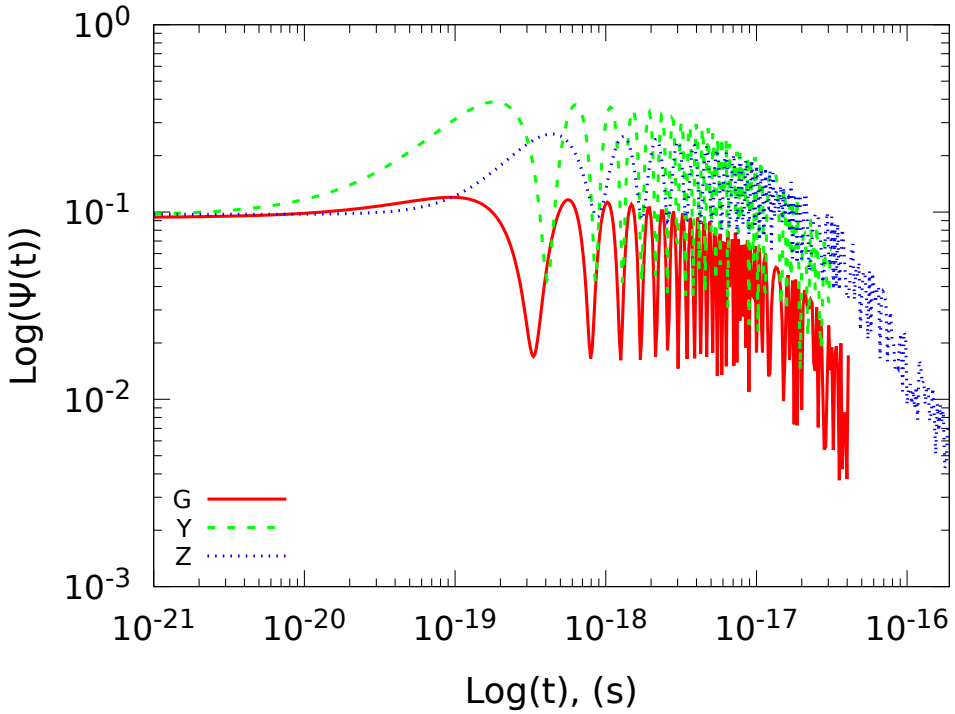

Figure 4.6. Variation of the Ψ parameter, calculated for the case $\Upsilon = 1$, for the three directions of emission (**generic**, **y** and **z**) and for an initial magnetic field of strength $B_0 = 0.1\ B_{cr}$. The plot is made with the results of integrations considering $N_{\pm,0} = 10^6$, even if the parameter Ψ is not affected by the initial number of particles.

4.6.2 Magnetic field screening

From Fig. (4.9) to Fig. (4.14), we report the results for the magnetic field screening, for different set of initial conditions (in accordance with Tab. (4.2)). In Figs. (4.9) and (4.10), we show the decrease of the magnetic field, with different initial conditions for B_0 and γ_0 (with $N_{\pm,0} = 10^{10}$), operated by the motion of the particles emitted initially along the three directions *generic*, *y* and *z* (Fig. (4.9), with $B_0 = 0.1\ B_{cr}$), along the *generic* direction and $\hat{z}$ axis (Fig. (4.10), with $B_0 = 0.3\ B_{cr}$). [3] In these two plots, the parameter Υ is fixed to $\Upsilon = 1$.

[3] Since not all the integrations end at the same time, we have extended the solutions, for these cases, with the last constant value until the end time of the longer solution. We apply the same procedure for the other plots of the magnetic field.

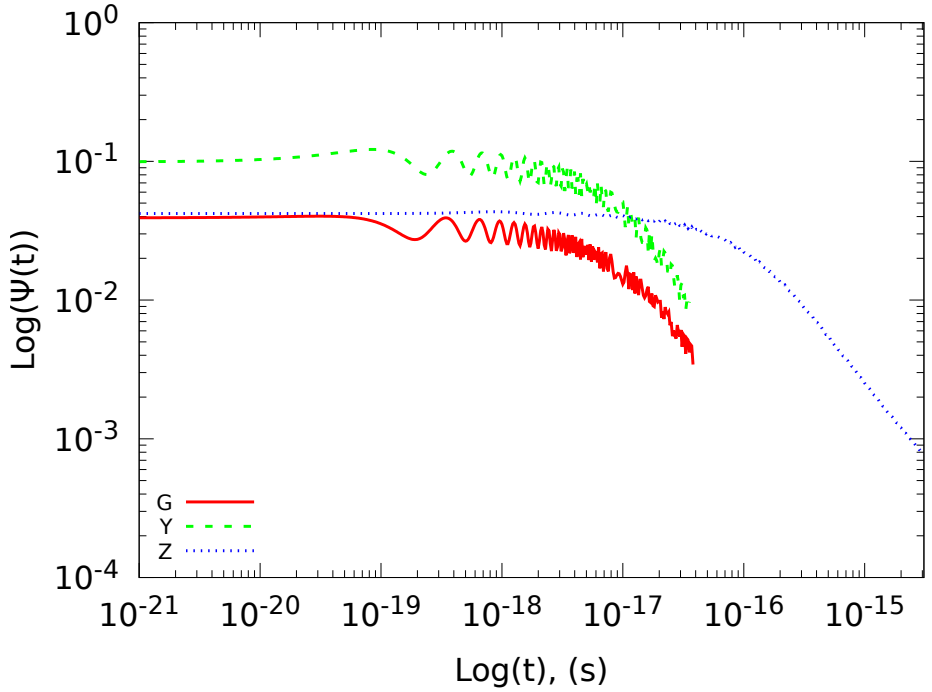

Figure 4.7. The Ψ parameter, calculated for $\Upsilon = 1/5$, for the same values of B_0 and $N_{\pm,0}$ as in Fig. (4.6).

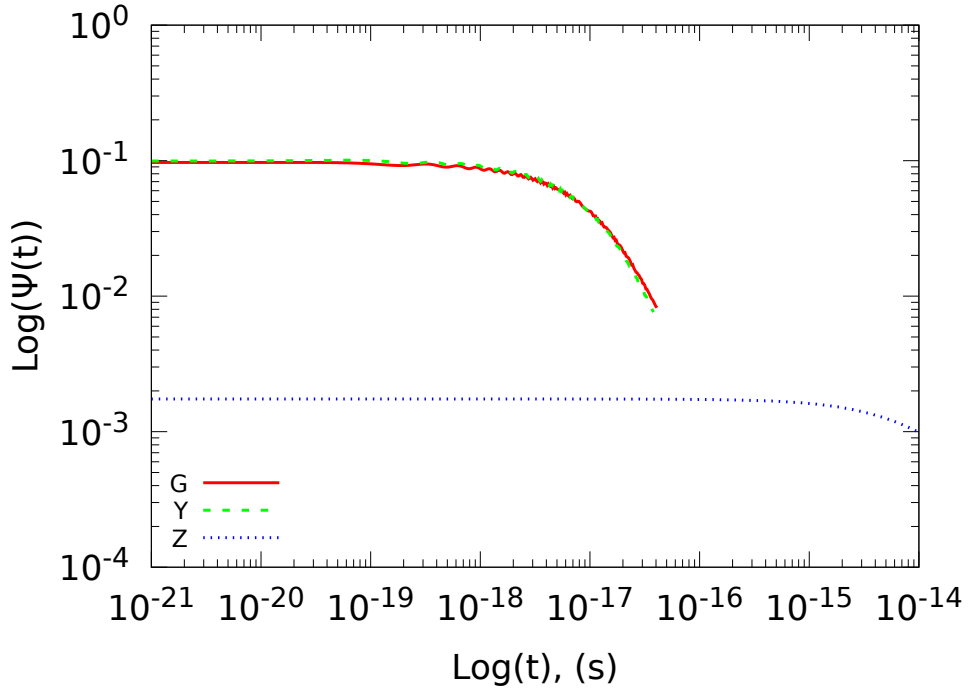

Figure 4.8. The Ψ parameter, calculated for the case $\Upsilon = 1/50$, for the same values of B_0 and $N_{\pm,0}$ as in Fig. (4.6).

In Fig. (4.11) and Fig. (4.12), the magnetic field decrease is shown for the case with $\Upsilon = 1/5$ (Fig. (4.11)) and $\Upsilon = 1/50$ (Fig. (4.12)). In both cases, we have chosen $B_0 = 0.1\ B_{cr}$ and $N_{\pm,0} = 10^{10}$. For the first plot, all the considered three directions of emission are shown, while in the second case (consistently with Tab. (4.4)) only the emission along the *generic* and $\hat{y}$ directions are shown.

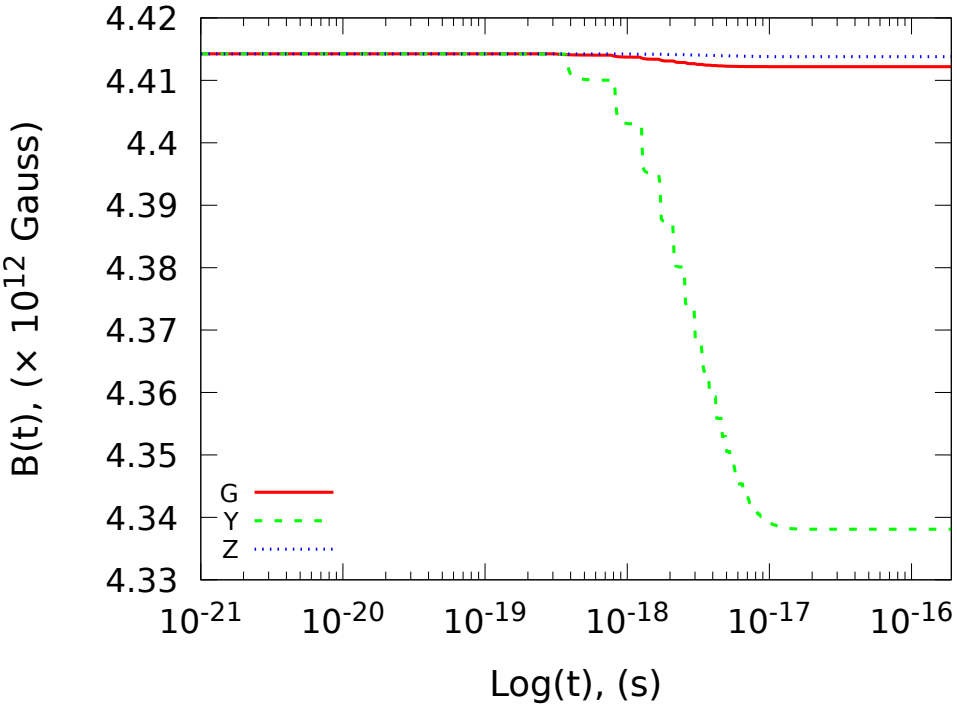

Figure 4.9. Magnetic field decrease, as a function of time, due to an initial number of particles $N_{\pm,0} = 10^{10}$, emitted initially along the directions "*generic*" (with $\gamma_0 = 6.48$), $\hat{y}$ (with $\gamma_0 = 3.66$) and $\hat{z}$ (with $\gamma_0 = 7.098$). In this case $\Upsilon = 1$ and the initial magnetic field is $B_0 = 0.1\ B_{cr}$. For all the three cases, the magnetic field presents a decrease, even if for the case of emission in the $\hat{z}$ direction it cannot be appreciated because of the small magnitude of the decrease itself.

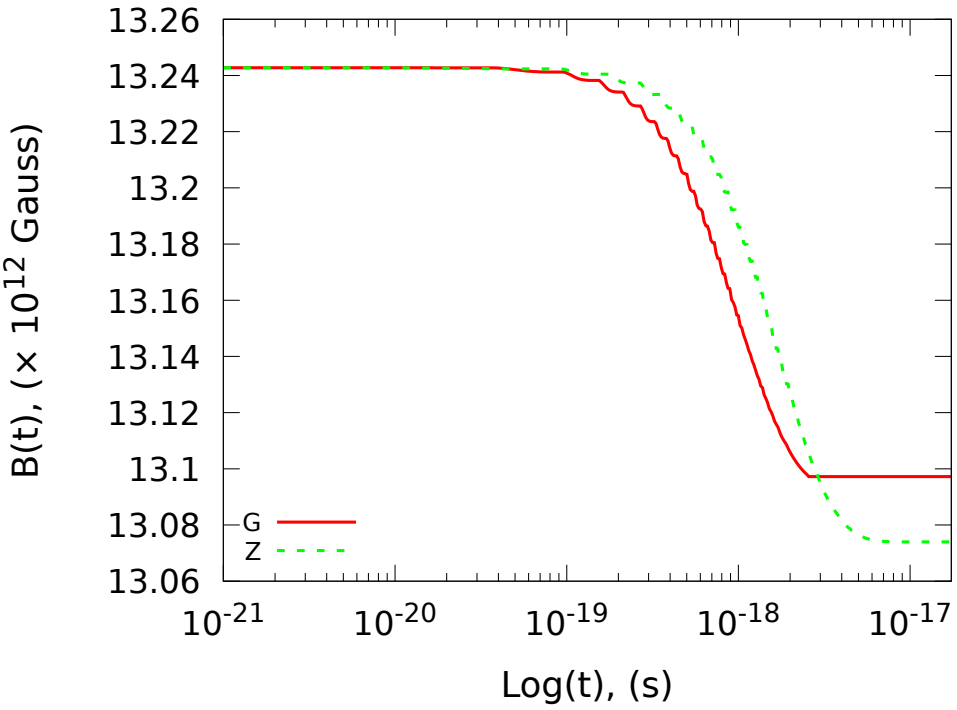

Figure 4.10. Magnetic field decrease due to an initial number of particles, $N_{\pm,0} = 10^{10}$, emitted initially along the *generic* direction (with $\gamma_0 = 2.27$) and along the $\hat{z}$ axis (with $\gamma_0 = 2.14$). Here $\Upsilon = 1$ and $B_0 = 0.3\ B_{cr}$.

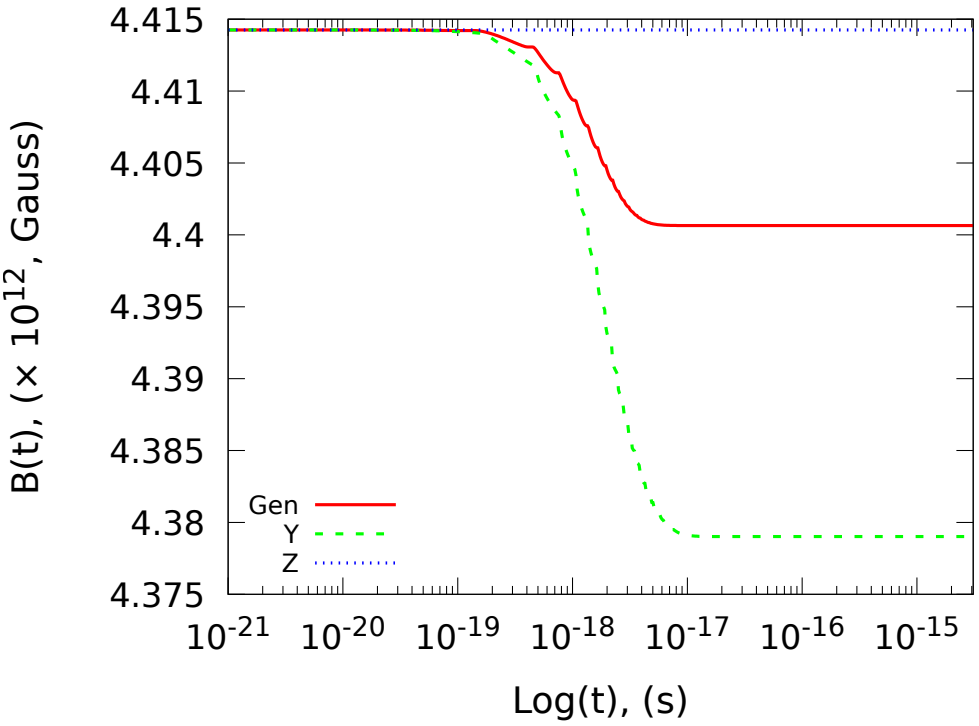

Figure 4.11. Magnetic field decrease (with $\Upsilon = 1/5$ and $B_0 = 0.1\ B_{cr}$) operated by an initial number of particles, $N_{\pm,0} = 10^{10}$, emitted initially along the directions "*generic*" ($\gamma_0 = 4.18$), $\hat{y}$ ($\gamma_0 = 3.71$) and $\hat{z}$ ($\gamma_0 = 22.66$).

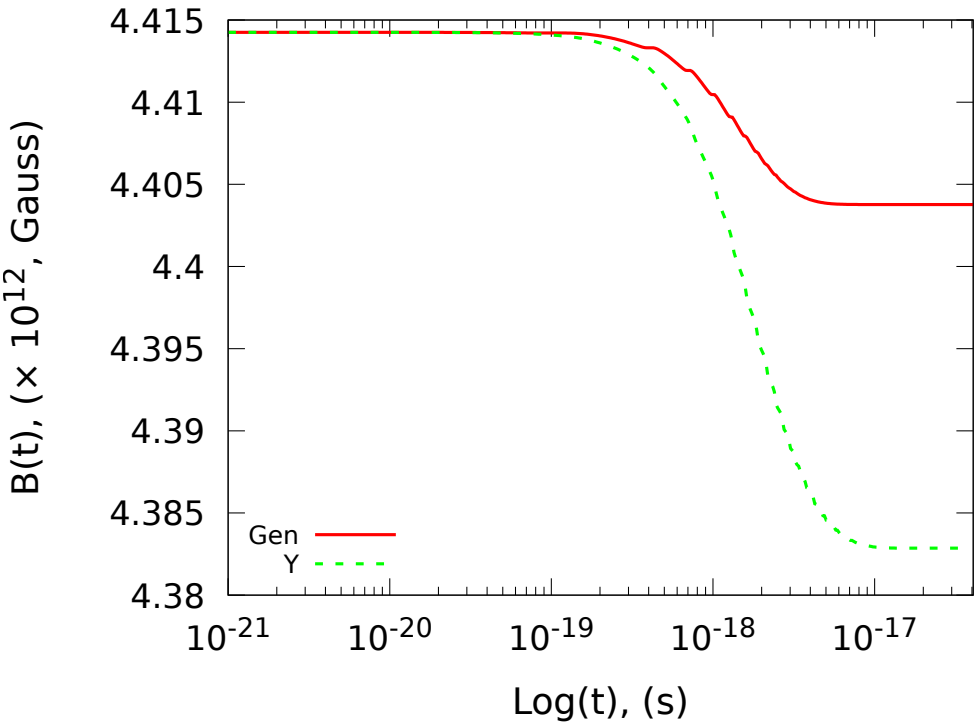

Figure 4.12. Magnetic field decrease (with $\Upsilon = 1/50$ and $B_0 = 0.1\ B_{cr}$) with $N_{\pm,0} = 10^{10}$ emitted initially along the *generic* direction ($\gamma_0 = 3.81$) and along $\hat{y}$ axis ($\gamma_0 = 3.71$).

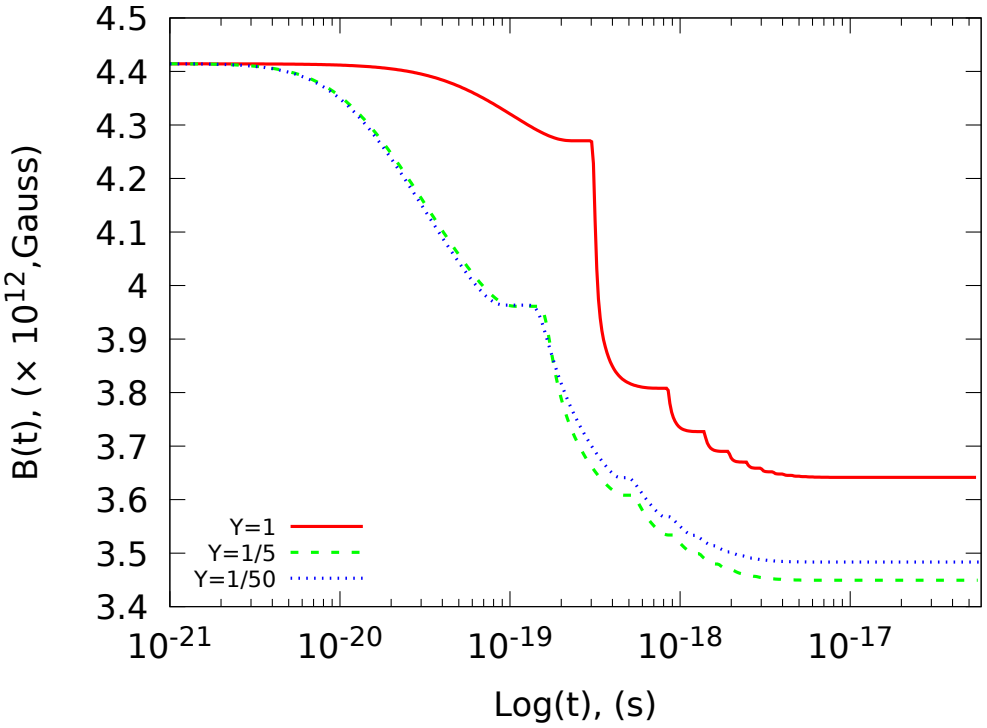

Figure 4.13. Magnetic field decrease, with $N_{\pm,0} = 10^{15}$ and $B_0 = 0.1\ B_{cr}$, emitted initially along the *generic* direction, for $\Upsilon = 1,\ 1/5,\ 1/50$, with Lorentz factor $\gamma_0 = 6.48,\ 4.18,\ 3.81$, respectively.

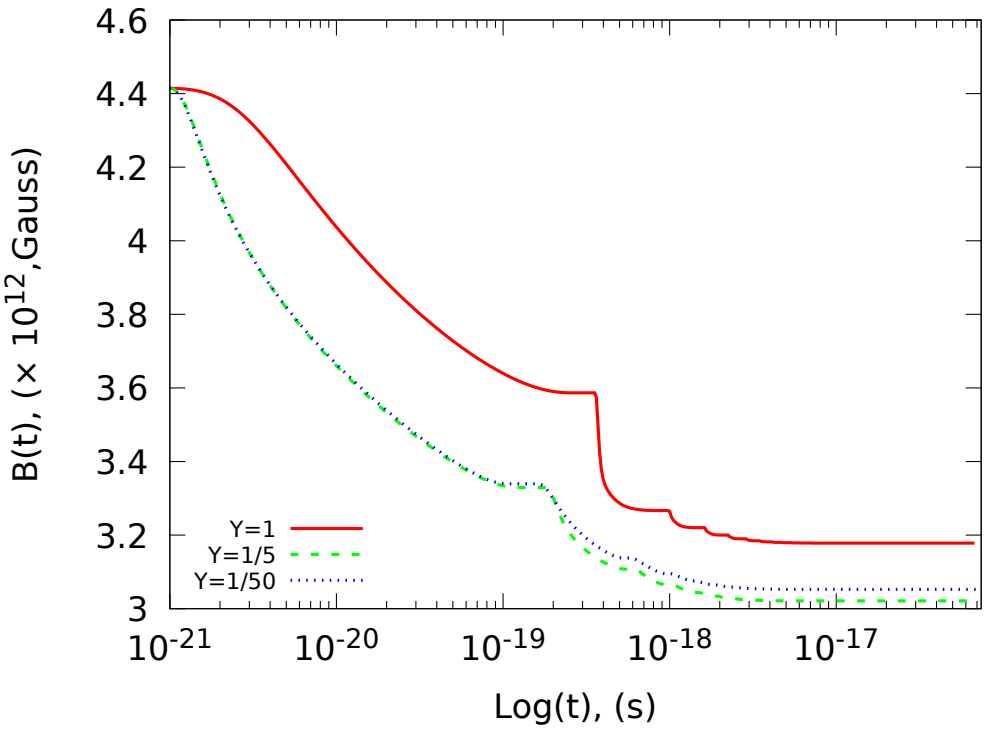

Figure 4.14. Same as Fig. (4.13), but with $N_{\pm,0} = 10^{18}$.

In Fig. (4.13) and Fig. (4.14), the decrease of the magnetic field is shown when a number of initial

particles equal to $N_{\pm,0} = 10^{15}$ and $N_{\pm,0} = 10^{18}$, respectively, is inserted in the system. In both cases, we choose particles emitted in the *generic* direction with $B_0 = 0.1\ B_{cr}$. The three curves correspond to the chosen value for the black hole spin $\Upsilon = 1,\ 1/5,\ 1/50$.

In Tabs. (4.2) (4.3) (4.4), we do not put the results for the integrations with $N_{\pm,0} > 10^{10}$ because the behaviour of the variables is similar to the one already shown for other values of the initial conditions. From Figs. (4.13) and (4.14) an useful information can be get looking at the shape of the curves for the magnetic field. Indeed, we can see that enhancing the number of initial particles inserted in the system (for $N_{\pm,0} > 10^{10}$), the magnetic field decrease is faster and presents a different shape than the other analyzed cases. Indeed, for example in Figs. (4.10) or (4.11), the reduction has a smooth behaviour. While in Figs. (4.13) and (4.14), it is evident the presence of a more sharp decay, characterized by several steps, which decrease their height enhancing the initial number of particles $N_{\pm,0}$. A closer look to all the plots for the magnetic field (from Fig. (4.9) to Fig. (4.14)) reveal the presence of the steps behaviour in the decrease of the magnetic field for all the studied conditions. This feature can be understood looking at the equation for the magnetic field reduction (Eq. (4.43)). From this equation we see that the decreasing rate mainly depends on the Lorentz factor and the velocity components $\left(\beta_x,\ \beta_y\right)$ of the particle. As we will see in the next section, Sec. (4.6.3), these two variables have an oscillatory behaviour due to the motion of the particles and to the transformation between energy gained and energy lost. In Eq. (4.43), the components of the particles velocity does not affect much the $\vec{B}$ decreasing rate, while a variation of the particle γ factor leads to a stronger/lower impact of the reduction (in this equation, the dependence by γ is quadratic, $\frac{dB}{dt} \propto \gamma^{-2}$). A plot of the Lorentz factor is shown in Fig. (4.15) (for the same initial conditions in Fig. (4.9)). Then, comparing Fig. (4.15) and Fig. (4.9) [4], it is easily to see that when γ reaches its minimum value, this corresponds to a stronger induced magnetic field and, consequently, to a reduction of B; on the contrary, when γ reaches its maximum, the B decreasing rate reduces its intensity and this is represented by the constancy of the magnetic field. Then, each step in the plots of the magnetic field represents the oscillatory behaviour of the particle Lorentz factor.

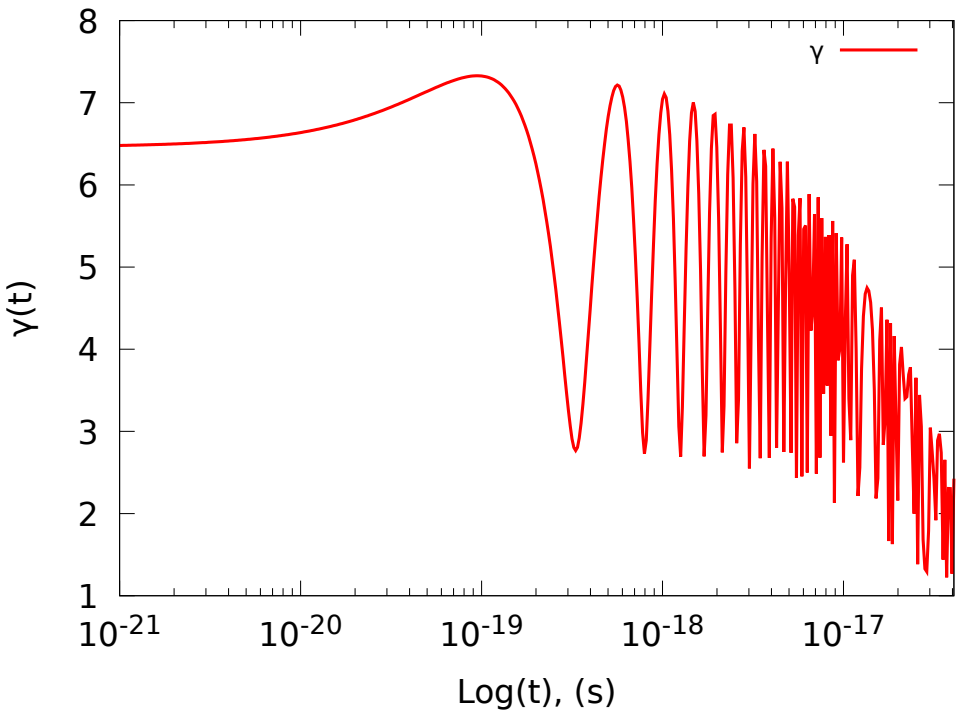

Figure 4.15. γ factor for particles emitted along the generic direction, with $\Upsilon = 1,\ B_0 = 0.1\ B_{cr}$ and $N_{\pm,0} = 10^{10}$.

[4] Comparing the other plots for the magnetic field and γ, with the same initial conditions, we get the same characteristics.

4.6.3 Emitted photons and particles trajectories

Photons energy

In this section, we show the results for the photons (their energy and number) and the trajectories of the particles immersed in a region with crossed magnetic and electric fields. We will notice that the two quantities are strictly correlated. Indeed, if we look at Fig. (4.16), where the photons energy $\varepsilon_\gamma(t)$ is shown, for initial conditions $\Upsilon = 1$, $B_0 = 0.1\ B_{cr}$, $N_{\pm,0} = 10^{10}$ and particles emitted in the three considered directions (same as in Fig. (4.9)), it is evident the oscillatory behaviour of the energy. This feature can be understood looking at Eqs. (4.38) and (4.39). Eq. (4.38) is the ODE that describes the evolution with time of the particle Lorentz factor, which is drove by the electric field and by the energy loss due to the emission of radiation. As we noticed in the end of the previous section, from Fig. (4.15), we can see that also $\gamma(t)$ presents an oscillatory behaviour. This implies that there is a competition between the acceleration of the particle (due to the electric field) and the emission of radiation, and, then, a continuous transformation between the two type of energies (gained and lost). Instead from Eq. (4.39), we learn that the photon energy depends by the particle γ factor, the magnetic (and electric) field, the particle velocity components $\left(\beta_x,\ \beta_y\right)$. Since the magnetic field does not present an oscillatory behaviour, this feature of $\varepsilon_\gamma(t)$ depends only by $\gamma(t)$ and $\left(\beta_x(t),\ \beta_y(t)\right)$. A plot of the particle velocity components is shown in Fig. (4.17). Then, from Figs. (4.15) and (4.17), we learn that the characteristic oscillatory behaviour of $\varepsilon_\gamma(t)$, it is due to: 1) the circular motion of the particles $\left(\beta_x,\ \beta_y\right)$; 2) and the continuous transformation between energy gained and energy lost of the particle (γ).
In Fig. (4.18), we show the evolution of $\varepsilon_\gamma(t)$, for the three values of $\Upsilon = 1,\ \frac{1}{5},\ \frac{1}{50}$, with a number of initial particles $N_{\pm,0} = 10^{10}$ emitted along the *generic* direction. The related particles Lorentz factors are shown in Fig. (4.19). From these plots we notice that a decrease of Υ leads to a decrease of $\varepsilon_\gamma(t)$, since it corresponds to a decrease of the particle γ factor (see Fig. (4.19) and Tab. (4.1)). This can be understood looking at the Eq. (4.47): notwithstanding the terms under square root increase if one decreases Υ, the Lorentz factor decreases and, since $\varepsilon_\gamma \propto \gamma^2$, it results the dominant terms for the photon energy.

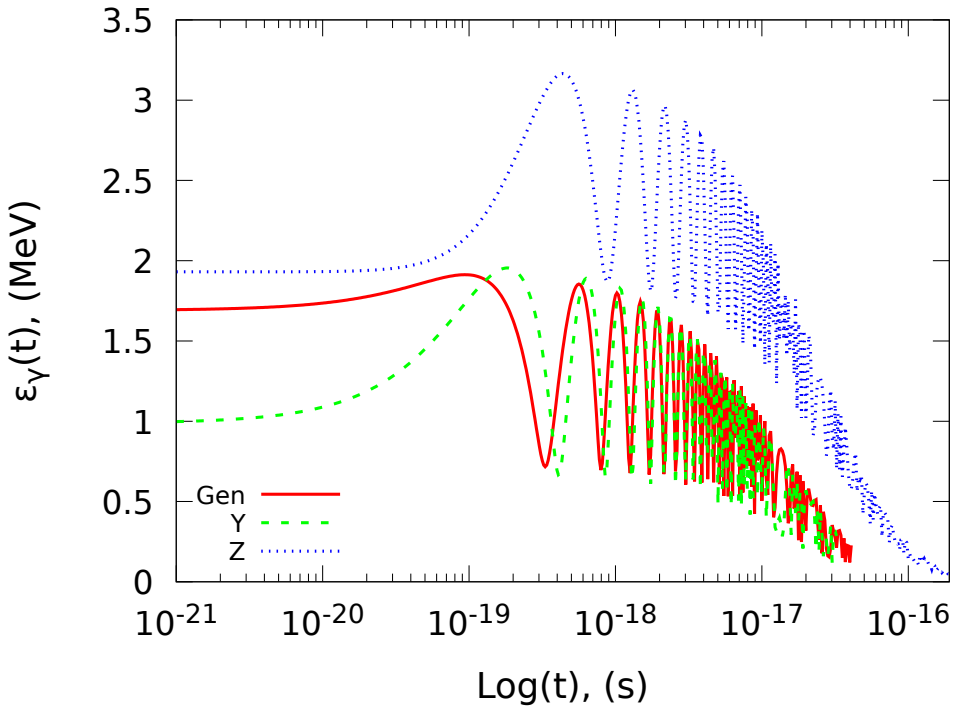

Figure 4.16. Emitted photons energy in (MeV), with the same conditions of Fig. (4.9), as a function of time.

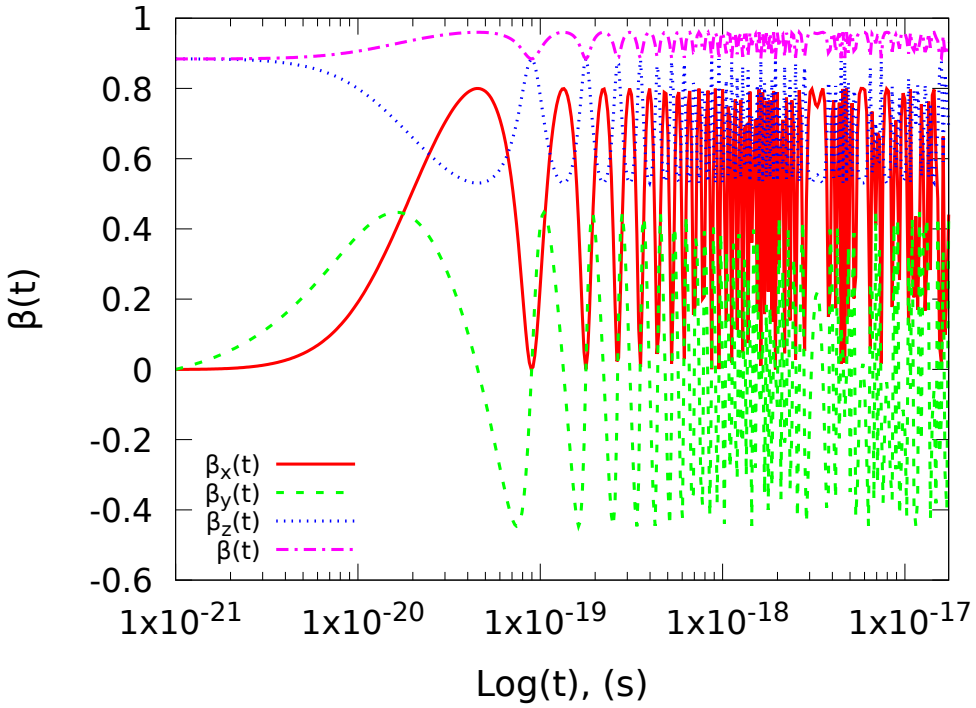

Figure 4.17. All the three components of the particles velocity (β_x, β_y, β_z) and the total β (as a function of time), for a number of particles $N_{\pm,0} = 10^{10}$ emitted along the z direction, with $B_0 = 0.3\ B_{cr}$, $\Upsilon = 1$ and $\gamma_0 = 2.14$.

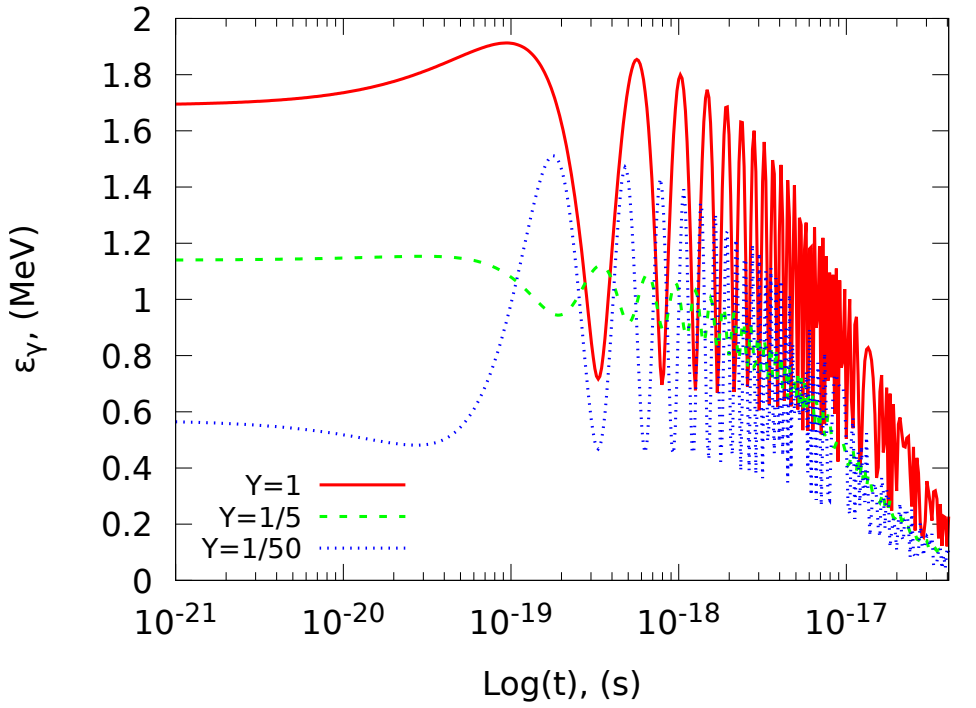

Figure 4.18. Emitted photons energy, as a function of time, for $N_{\pm,0} = 10^{10}$ emitted along the *generic* direction, with $B_0 = 0.1\ B_{cr}$, for the three values of the parameter $\Upsilon = 1,\ 1/5,\ 1/50$. The related evolution of the Lorentz factors for the emitting particles are shown in Fig. (4.19).

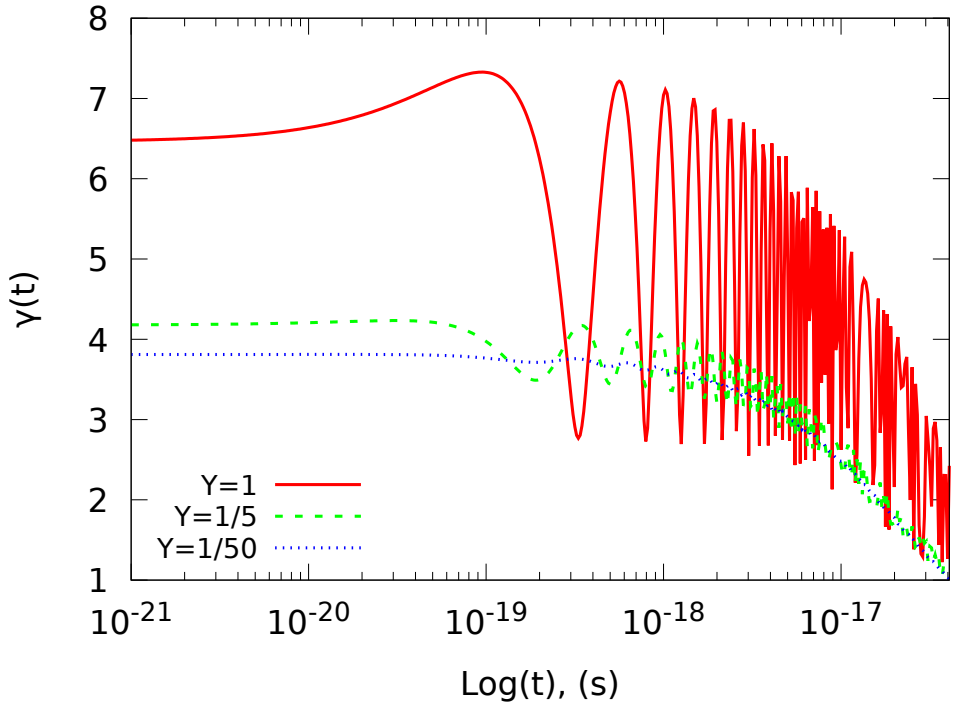

Figure 4.19. Particles Lorentz factor for the same initial conditions of Fig. (4.18).

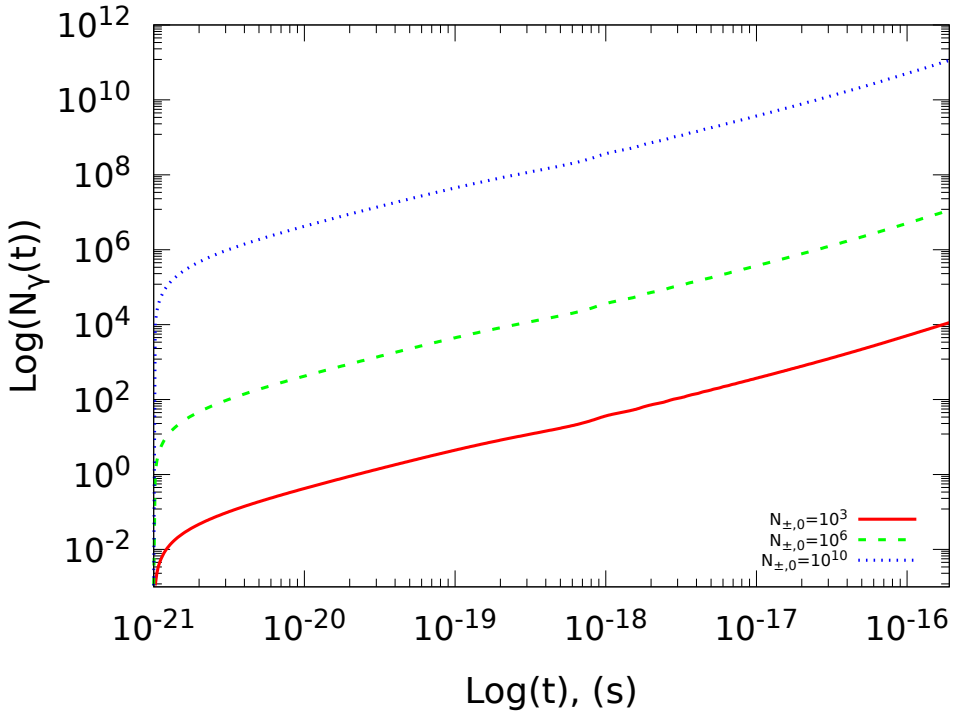

Figure 4.20. Number of photons created by different values of the initial number of emitted particles $N_{\pm,0} = 10^3,\ 10^6,\ 10^{10}$. This result coming out from the integration of the equations setting the emission direction along the $\hat{z}$-axis, with $B_0 = 0.1\ B_{cr}$, $\gamma_0 = 7.098$ and $\Upsilon = 1$.

In Fig. (4.20), we show the increase of the number of photons, for different initial number of particles (for particles emitted along the $\hat{z}$ axis, with $B_0 = 0.1\ B_{cr}$). From this plot we see that there is an exponential growth of the number of photons and that, consistently with Tab. (4.2), the corresponding final value $N_{\gamma,f}$ (for this particular set of initial conditions) is always one order of magnitude greater than the initial and final number of pairs. In Fig. (4.21) the number of synchrotron photons, created by different initial numbers of pairs $N_{\pm,0} = 10^3,\ 10^6,\ 10^{10}$ emitted along the *generic* direction, is shown for the three values of the parameter $\Upsilon = 1,\ \frac{1}{5},\ \frac{1}{50}$. We notice that, for each specific $N_{\pm,0}$, a decrease of Υ leads to the creation of a greater number photons. This derives from Eq. (4.44). Indeed a decrease of Υ corresponds to a decrease of the electric field respect to the magnetic field. This implies that the particles emit more synchrotron photons and, consequently, a greater number of secondary pairs is created.

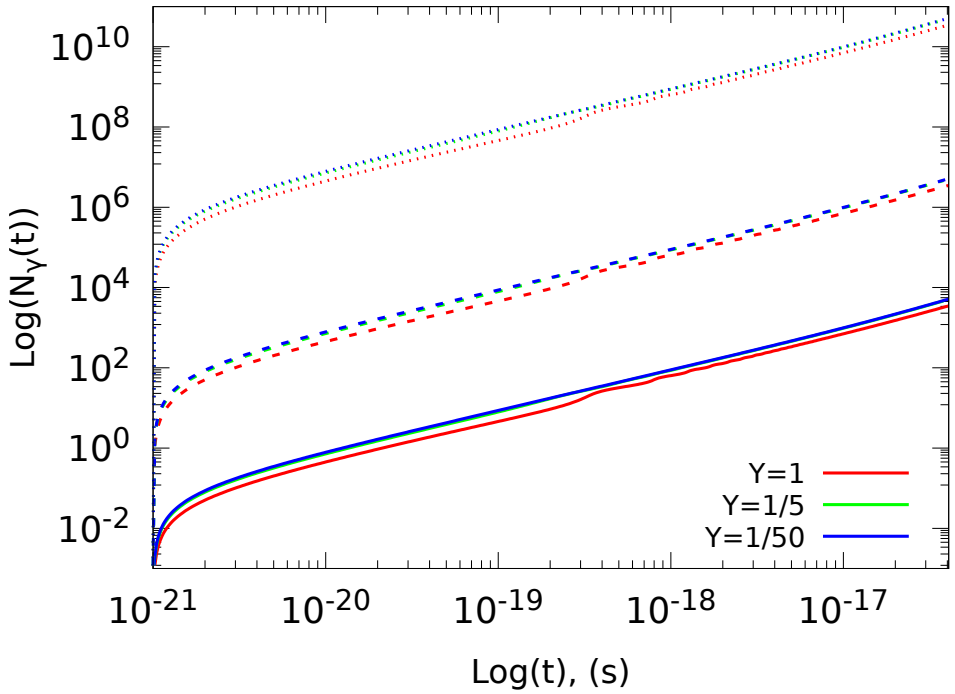

Figure 4.21. Number of photons created by different values of the initial number of emitted particles $N_{\pm,0} = 10^3$ (continuous lines), 10^6 (dashed lines), 10^{10} (dotted lines). Here we consider particles emitted along the *generic* direction, with $B_0 = 0.1\ B_{cr}$, for $\Upsilon = 1$ (red lines), $\frac{1}{5}$ (green lines), $\frac{1}{50}$ (blue lines). The curves for $\Upsilon = \frac{1}{5}$ and $\frac{1}{50}$ are almost overlapped.

Particles helicoidal trajectories

The oscillatory behaviour of the particles energy and velocity showed, for example, in Figs. (4.16) (4.17), respectively, is the representation of the motion of the particles drove by the electric and magnetic fields and described by Eq. (4.36). As already stated, the motion of the particles is a composition of a series of coils around the magnetic field lines (in the $x - y$ plane) and an accelerated motion drove by the electric field (in the $y - z$ plane). The shape of the coils and their lying planes depend by the particles initial emission direction. In Figs. (4.22) (4.23) (4.24) we show a few examples of these coils, for different initial conditions. In Fig. (4.22), the particles are emitted along the $\hat{z}$ direction, with $B_0 = 0.1\ B_{cr}$, $N_{\pm,0} = 10^6$ and $\Upsilon = 1$. In Fig. (4.23), the particles are emitted along the *generic* direction, for the case with $\Upsilon = 1/5$, $B_0 = 0.1\ B_{cr}$ and $N_{\pm,0} = 10^6$. In Fig. (4.24) the particles are emitted along the $\hat{y}-$axis, for the case with $\Upsilon = 1/50$, '$B_0 = 0.1\ B_{cr}$ and $N_{\pm,0} = 10^6$. In this last case, we note that if the particles are

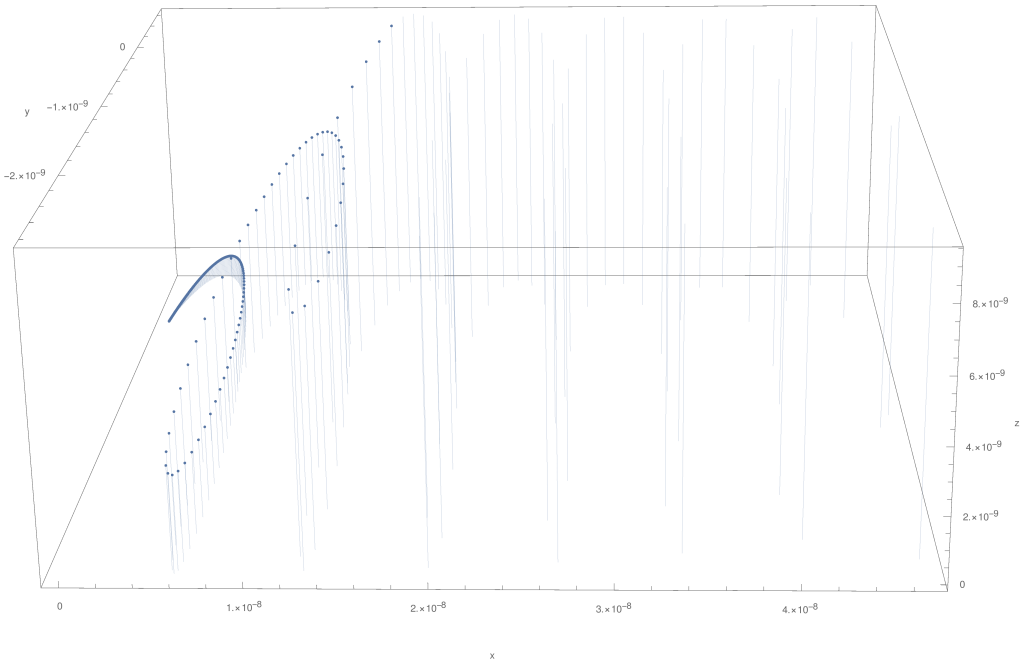

Figure 4.22. Particles positions, as a function of times, when they are emitted in the $\hat{z}$ direction, with $B_0 = 0.1\ B_{cr}$ and $N_{\pm,0} = 10^6$, for the case $\Upsilon = 1$. It is evident that the motion of the particles along the B lines generates coils which follow the drift velocity, due to the presence of the electric field on the $y-$axis.

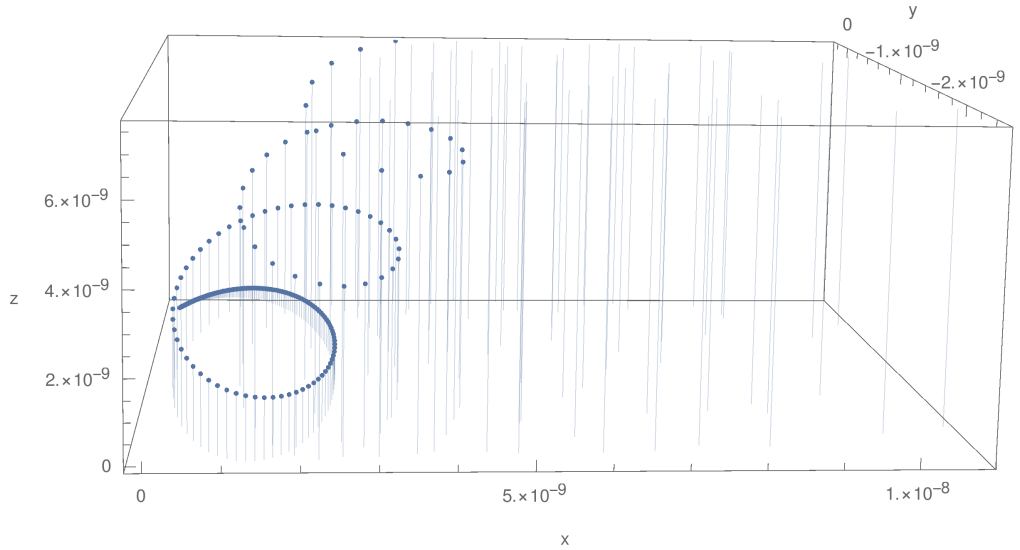

Figure 4.23. Coils produced by particles emitted initially along the *generic* direction, with $B_0 = 0.1\ B_{cr}$, $N_{\pm,0} = 10^6$ and $\Upsilon = 1/5$.

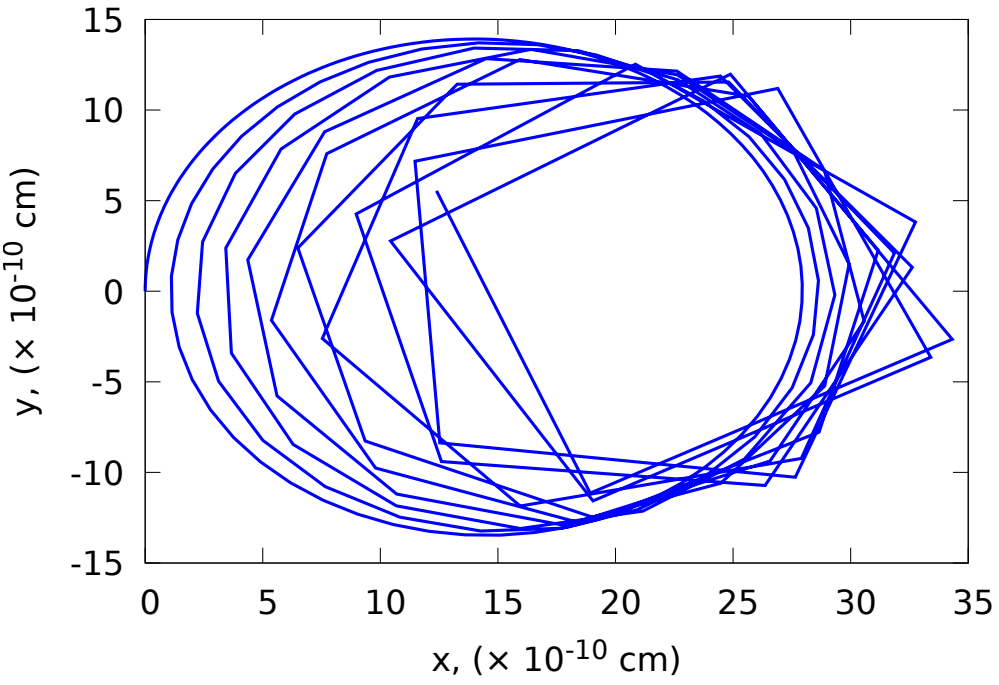

Figure 4.24. Coils produced by particles emitted initially along the $\hat{y}-$axis, with $B_0 = 0.1\ B_{cr}$, $N_{\pm,0} = 10^6$ and $\Upsilon = 1/50$. In this case, the particles move only in the $x - y$ plane and follow the direction of the drift velocity.

emitted initially along the $\hat{y}-$axis, they continue their motion in the azimuthal $x - y$ plane, with coils that follow the direction of the drift velocity and move along the $x-$direction. [5]

For completeness and consistently with Fig. (4.23), in Fig. (4.25) we show the three components of the particles positions (for the same conditions considered in Fig. (4.23)) as a function of time. From this plot, it is clear the oscillatory behaviour of the particle motion, principally due to the y (and x) coordinate, which is affected by the electric field oriented in that direction.

4.6.4 Screening time scale vs Circularization time scale

In Sec. (4.3) we stated that, in order to apply the derivation and the final form of the induced magnetic field (see Eq. (4.23)), the condition $t_c < t_{screen}$ or $\ll t_{screen}$ needs to be satisfied, in such a way that one can consider the magnetic field stationary for a specific small time interval. We define the circularization time as

$$t_c(t) = \frac{2\pi R_c(t)}{\beta(t)c}, \tag{4.49}$$

namely the time the particle spends to complete one "*orbit*" around the $\vec{B}$ lines. Here we approximate the coil as perfectly circular. As we have seen in Sec. (4.6.3) and we will return in Sec. (4.7), this is not completely true because the projection of the orbit on the azimuthal plane is more similar to an ellipse than a circle. Since we are interested to in the order of magnitude of the time scales, we can consider, as a first order approximation, that this assumption is right.

[5] As one can see in Fig. (4.24), after some time, the integration loses precision, with a consequent decrease of the number of points. The circular motion is already present, even if the trajectory is represented by polygonal segments.

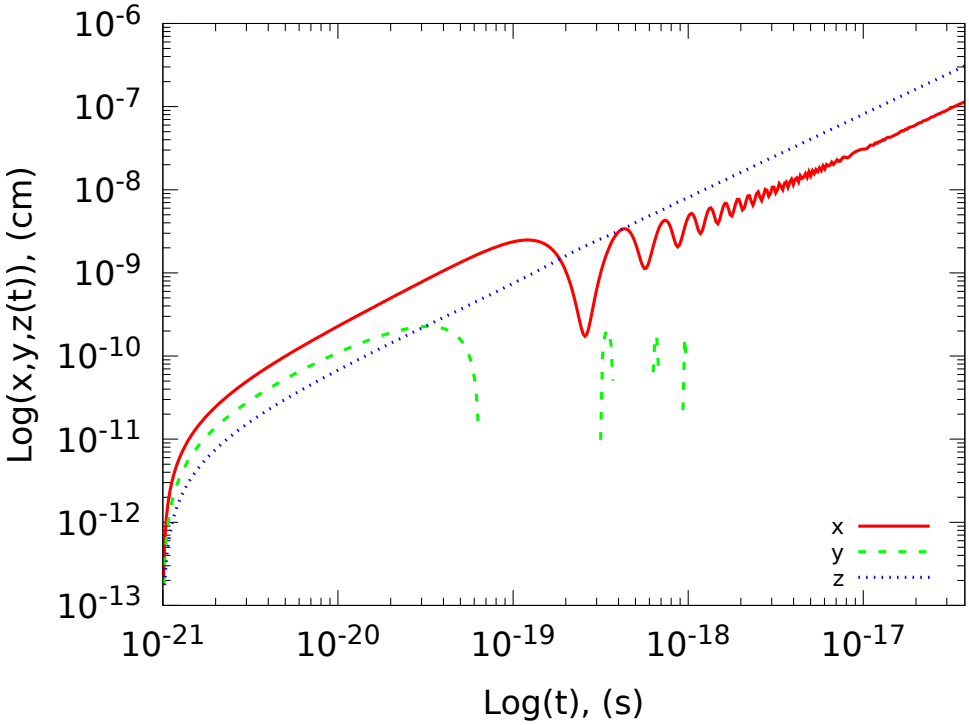

Figure 4.25. The three components of the particles positions, for the same initial conditions of Fig. (4.23). It is evident the oscillatory behaviour in the **y** direction due to the presence of the electric field. Because in some temporal ranges $y < 0$, we have a lack of points on the y curve, due to the logarithmic scale of the plot.

By definition, the screening time scale can be written as

$$t_{screen}(t) = \left| \frac{B(t)}{\frac{dB}{dt}} \right|. \tag{4.50}$$

Then, if $t_c < t_{screen}$ we can assume the magnetic field stationary, for the time interval under consideration, and then, use the Eq. (4.43) to study the magnetic field variation with time. Instead, if $t_{screen} \lesssim t_c$, the assumptions of stationary field is no longer valid and Eq. (4.43) cannot be applied. In the last case, we need to derive another equation for the variation of the magnetic field directly from the Maxwell equations.

In Figs. (4.26) (4.27) (4.28) (4.29), we compare the two time scales (t_c, t_{screen}) for different values of the initial conditions. In all of these plots, the particles are emitted along the *generic* direction and $B_0 = 0.1\ B_{cr}$. In Figs. (4.26) (4.27), we show the curves for the case with $\Upsilon = 1$, $\gamma_0 = 6.48$ and $N_{\pm,0} = 10^6,\ 10^{10}$ (Fig. (4.26)), $N_{\pm,0} = 10^{15},\ 10^{18}$ (Fig. (4.27)).

In Fig. (4.28), we set $\Upsilon = 1/5$, $\gamma_0 = 4.18$ and $N_{\pm,0} = 10^6,\ 10^{10},\ 10^{15}$, whereas in Fig. (4.29), $\Upsilon = 1/50$, $\gamma_0 = 3.81$ and still $N_{\pm,0} = 10^6,\ 10^{10},\ 10^{15}$.

From these comparisons between the circularization time scale and the screening time scale, we see that for almost all the considered cases, the condition $t_c < t_{screen}$ or $\ll t_{screen}$ is satisfied. From Fig. (4.27), we see that if one inserts, as initial condition, a number of pairs $N_{\pm,0} = 10^{18}$, t_{screen} becomes smaller than t_c (even if for not all the integration time of the simulation). In Sec. (4.7) we will give another argument in favor to exclude the results from the simulations setting $N_{\pm,0} = 10^{18}$. Indeed, we will see that the results, for this initial condition, violate the physical applicability of our model to GRBs, since it gives rise to a volumetric particles number density much greater than the usual one adopted for these systems. These two considerations lead us to exclude the solutions with $N_{\pm,0} = 10^{18}$ since, at least in the beginning of the integration, this conditions does not satisfy our physical conditions for the problem. In all of these plots,

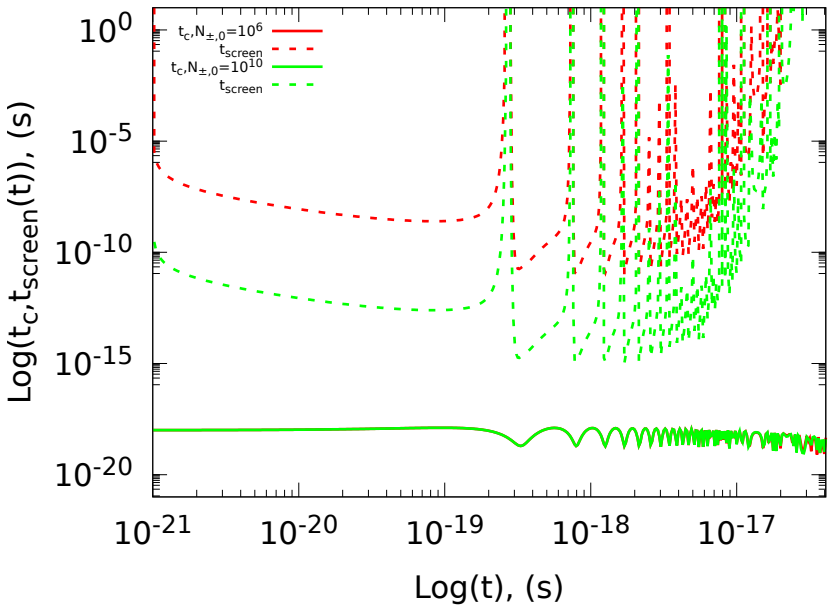

Figure 4.26. Comparison between the circularization time scale t_c (defined in Eq. (4.49)) and the screening time scale (defined in Eq. (4.50)), for $\Upsilon = 1$ and $B_0 = 0.1\ B_{cr}$, when a number of particles $N_{\pm,0} = 10^6,\ 10^{10}$ are emitted along the "*generic*" direction with $\gamma_0 = 6.48$. The full lines refer to t_c; the dashed lines refer to t_{screen}. Since $t_c(t)$ does not depend on $N_{\pm,0}$ all the curves practically coincide and are overlapped. Instead, t_{screen} reaches lower values enhancing $N_{\pm,0}$.

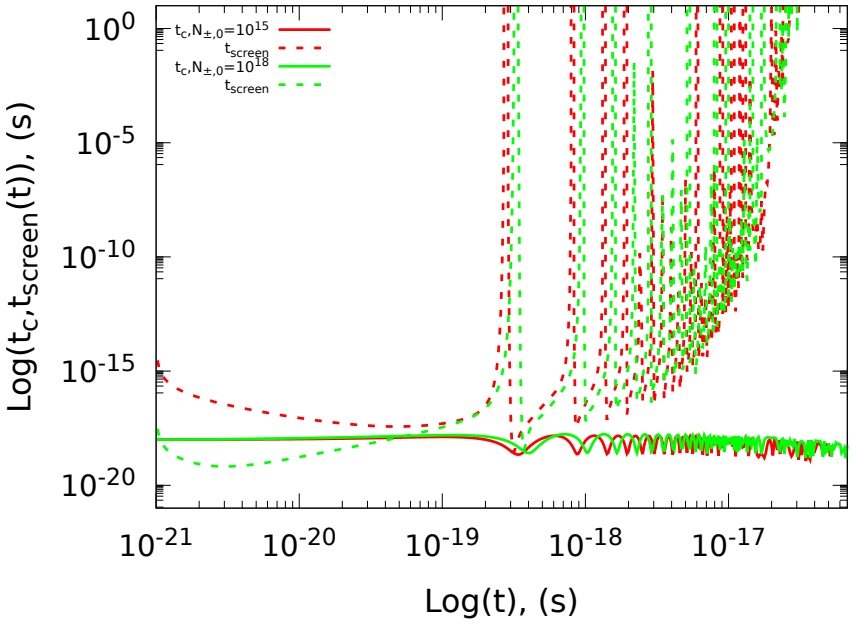

Figure 4.27. Same as in Fig. (4.26), with the same conditions, but with $N_{\pm,0} = 10^{15},\ 10^{18}$. One can sees that for $N_{\pm,0} = 10^{15}$, t_{screen} is still greater than t_{circ}, but for $N_{\pm,0} = 10^{18}$, $t_{screen} < t_c$. Then, choosing $N_{\pm,0} = 10^{18}$, the assumption of a stationary field is not longer valid (at least in the beginning of the integration). As we will see in Sec. (4.7), this value of $N_{\pm,0}$ will be excluded from ours results since it also does not respect the physical condition of the particles number density for the applicability to GRBs.

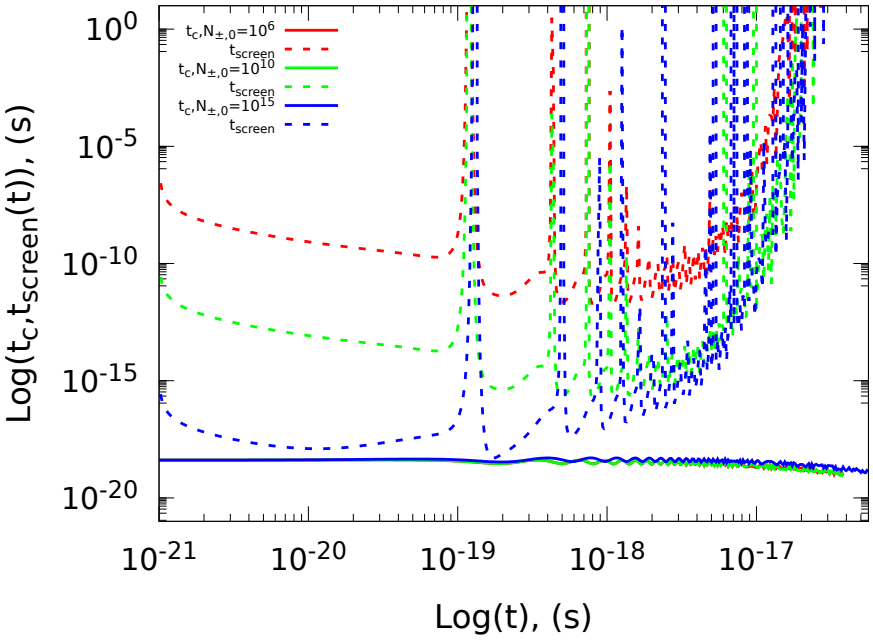

Figure 4.28. Same as in Fig. (4.26), with $\Upsilon = 1/5$, $B_0 = 0.1\ B_{cr}$, $\gamma_0 = 4.18$, $N_{\pm,0} = 10^6,\ 10^{10},\ 10^{15}$, since from Fig. (4.27), we have seen that the curve with $N_{\pm,0} = 10^{18}$ cannot represent our problem.

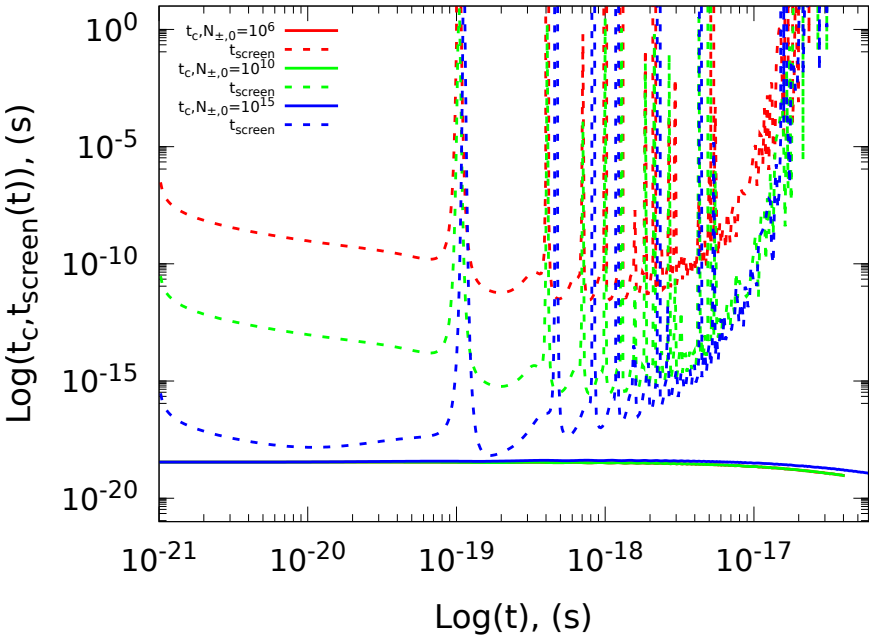

Figure 4.29. Same as in Fig. (4.28), with $\Upsilon = 1/50$ and $\gamma_0 = 3.81$.

we also note that the circularization time scale does not change if we choose different values of $N_{\pm,0}$. This is trivial since $R_c(t)$ does not depend, at least directly, by $N_{\pm,0}$. Whereas, a small variation on the values of t_c is present if we vary the parameter Υ and this is due to the dependence of $R_c(t)$ by Υ.
As stated in the beginning of the section, since t_c depends on the curvature radius, this creates an oscillatory behaviour of the t_c, proper of $R_c(t)$. Even the oscillatory behaviour of t_{screen} can be traced back to $R_c(t)$

(see Eq. (4.43)). Due to this dependence, the oscillations of t_{screen} are related to the oscillatory behaviour of: the particles velocity components $\beta_x(t)$ and $\beta_y(t)$, the particle Lorentz factor $\gamma(t)$ and, principally, by the pair-production rate $\zeta(t)$ (through $dN_{\pm}/dt$) (see Figs. (4.2) (4.4) (4.5)) [6]. Indeed, comparing the plots of the rate and the one of t_{screen}, the similar behaviour of the curves, characterized by high and narrow peaks, is evident. Then, for t_{screen}, the oscillations of the velocity and the curvature radius $R_c(t)$ have lower impact than the rate $\zeta(t)$ on the total behaviour of the screening time scale.
A final comment concerns the dependence of the two times scales by the parameter Υ. Comparing Figs. (4.26) (4.27) (4.28) (4.29), it comes out that, a variation of Υ seems not to have a strong effect on the shape of t_c and t_{screen}. But, from a closer look, one can see that a small variation of the shape of the curves is present and, also, they are principally affected by the rate $\zeta(t)$. Indeed, comparing Figs. (4.26) (4.27) (4.28) (4.29) with Figs. (4.2) (4.4) (4.5), it is evident the correlation between the two variables $t_{screen}(t)$ and $\zeta(t)$.

4.6.5 Further conditions for the magnetic pair production

From Figs. (4.6)-(4.8) we have seen that the condition in Eq. (4.48) for the applicability of the pair production rate formula, Eq. (4.33), is satisfied. In Eq. (4.14) we defined the parameter χ as the fraction between the photon energy and the pairs energy. This parameter has two important interpretations: 1) tells us the energy of the emerging pairs; 2) sets a threshold for the efficiency of the MPP process. The first interpretation derives directly from the definition of χ. If $0.01 \lesssim \chi \leq 1$, the emerging pairs share equally the photon energy. Instead, if $\chi > 1$ or $\gg 1$, the photon energy is not equally shared between the two emerging leptons: one component of the pairs tends to absorb almost all the energy of the photon, while the other component takes the remaining part of the photon energy (see [40]). The second interpretation derives from calculations already made about pair production in strong magnetic field (see again [40] and references therein). It has been shown that the pair production is not expected to occur with significant probability unless $\chi \gtrsim 0.1$. In Fig. (4.30), it is shown the parameter $\chi(t)$ for the three considered values of the parameter Υ, for the integrations started with particles emitted in the *generic* and z direction (the curves for the case of particles emitted in the y-direction coincide with the one emitted in the *generic* direction).

As we can see from Fig. (4.30), χ is always greater than 0.1, except for the case with $\Upsilon = 1/50$ and particles emitted initially along the z-direction. Then, a production of pairs via MPP process is expected for almost all the analyzed cases and the emerging pairs share almost equally the parent photons energy. A further condition, that is a rule-of-thumb condition for pair production by photons in magnetic field, was derived by Sturrock (see [147] and [38, 59]). This condition imposes that the magnetic pair production occurs whenever

$$\varepsilon_\gamma \times B_\perp \gtrsim 10^{18.6} = 3.98 \times 10^{18},$$

where ε_γ is the photon energy (in eV) and $B_\perp$ (in Gauss) the component of the magnetic field perpendicular to the photon propagation direction. This condition is valid if only the magnetic field is present. It can be modified as follow when a perpendicular (to the magnetic field) electric field is also present (consistently with Eq. (4.33)):

$$\varepsilon_\gamma \times B \left[\left(\eta_x - \frac{E}{B} \right)^2 + \eta_y^2 \left(1 - \frac{E^2}{B^2} \right) \right]^{1/2} \gtrsim 10^{18.6}. \tag{4.51}$$

For all the analyzed cases (and even for others cases that we did not show the results in this chapter), the condition in Eq. (4.51) is satisfied, even if for not the total integration time. Indeed the values of Eq. (4.51) span between 10^{18} and 10^{23} (depending on the different initial conditions).

These results contrast with what we have shown in Figs. (4.2)-(4.5) for the rate of pair production. In these plots we have seen that the rate $\zeta(t)$ is not so efficient as we expected. From a quick look to the

[6] We emphasize that also the rate $\zeta(t)$ depends by $(\beta_x, \beta_y, \gamma)$ (see Eq. (4.33))

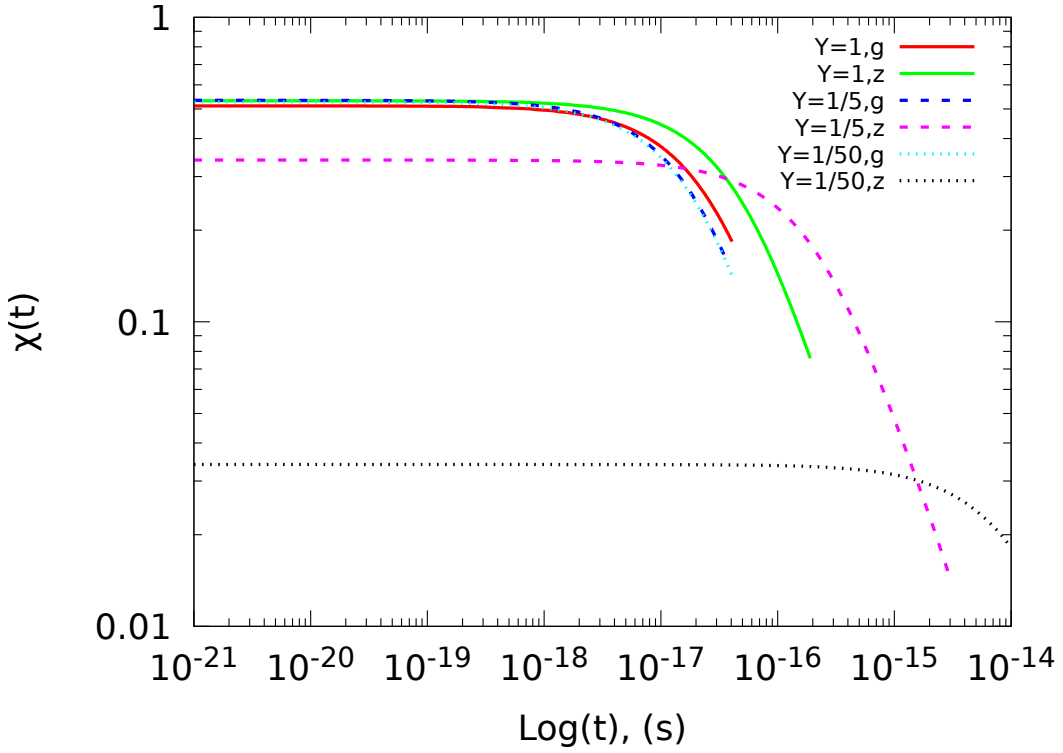

Figure 4.30. $\chi(t)$ for particles emitted in the *generic* and z directions and with $\Upsilon = 1,\ 1/5,\ 1/50$.

structure of $\zeta(t)$ in Eq. (4.33), and comparing our results with the one in [38] (where, for $B = 10^{12}$ Gauss and $\varepsilon_\gamma = 1$ GeV, a value for the rate around $\sim 10^{15} - 10^{16}$ s^{-1} is expected), we deduce that the lower value of our rate is due, principally, to the low value of the photon energy ε_γ. From what we have learnt before by the definition of the parameter $\chi(t)$, this implies that the emerging pairs have very low energy. Indeed, see Figs. (4.16)-(4.18), the energy of our photons is of the order of a few MeVs or lower and, then, the electron/positron pairs gain energy just a bit higher than their rest mass energy. As a consequence, the pairs do not make many "*loops*" around the $\vec{B}$ lines and emit photons with almost the same energy. This is a crucial point to understand why we did not obtain also a strong decrease of the magnetic field.
A higher values of the photon energy can be obtained varying the initial conditions in the integrations of the set of equations. The specific choice that we have made for the considered initial conditions, at least for $\left(\gamma_0,\ \beta_{x,0},\ \beta_{y,0},\ \beta_{z,0},\ \theta,\ \phi\right)$, was guided by the curiosity to see: how the system reacts to different conditions (principally to the different emission angles of the particles), if it is able to accelerate particles (produced at rest, since we are in a region close to the BH horizon) to high energy. In the nearly future we have in mind to change the initial conditions consistently with higher values for the photon energy.

Notwithstanding our low energy photons, in our results we saw that the magnetic field screening is present. Then, from the discussion above, we expect that, enhancing the initial particles Lorentz factor γ_0 (and, then, the photon energy), the impact of the screening effect on the system will be stronger.

4.7 Particles volumetric number density and applicability to GRBs

The model we have built in this chapter is a generic model and can be applied to different physical systems. As we already stated in the introduction, we would like to apply it for the study of GRBs. To this purpose, we need to put some inputs derived from the model adopted to describe these type of systems. One of these inputs is the initial number density of particles in the system. In this section, we show how to

calculate the number density of the particles in our model and contrast it with the one derived from a specific model for GRBs. This procedure will put constraints on the initial number of particles $N_{\pm,0}$ that we can insert as initial condition in our model.

As is shown in the plots in Figs. (4.22) (4.23) (4.24), particles make a series of continuous coils, which build a solenoidal structure around the field lines. We emphasize that, in our representation, all the particles have the same dynamic and, then, they follow the same coils (generating a current which creates the induced magnetic field), with the same curvature radius.
By this representation, we can define the number density of the particles, which is the number of particles inside the solenoidal structure [7]. Since it is not so easy to calculate the volume of this structure, because its section is not a perfect circle, we proceed in the following way. The particles volumetric number density is defined as

$$n_{\pm} = \frac{dN_{\pm}}{dV}. \tag{4.52}$$

We can write the volume element as $dV = dx\, dy\, dz$, namely as we are approximating, at any time of the integration, the particle's path with a parallelepipeds of dimensions $\Delta x_i = x_i - x_{i-1}$, $\Delta y_i = y_i - y_{i-1}$, $\Delta z_i = z_i - z_{i-1}$, where the subscript i refers to each step of the integration. Then, the volumetric number density can be evaluated numerically step by step as (with $\Delta N_{\pm,i} = N_{\pm,i} - N_{\pm,i-1}$)

$$n_{\pm,i} = \frac{\Delta N_{\pm,i}}{\Delta x_i\, \Delta y_i\, \Delta z_i}. \tag{4.53}$$

We want to emphasize that the particles density defined in Eq. (4.52) and the one we have used in Sec. (4.3) n_λ (for the derivation of the induced magnetic field equation) are two different types of density. Firstly, n_λ is a linear number density, whereas $n_\pm$ is a volumetric number density. The linear density n_λ corresponds to the number of particles on the coil, which will generates the current density $\vec{J}$ (see Eq. (4.21)) that, flowing on this coil, creates the induced magnetic field. Instead the volumetric number density $n_\pm$ analyzed in this section is the density inside the solenoidal structure, with lateral surface created by the coils themselves.

In the following figures, we report $n_\pm$, evaluated using Eq. (4.53), for the three values of the parameter Υ already analyzed: $\Upsilon = 1$ (Fig. (4.31)), $\Upsilon = 1/5$ (Fig. (4.32)), $\Upsilon = 1/50$ (Fig. (4.33)). In each plot, the curves refer to a different number of initial particles inserted in the problem: $N_{\pm,0} = 10^6,\ 10^{10},\ 10^{15}$. In these plots, we have considered particles emitted in the *generic* direction, with $B_0 = 0.1\ B_{cr}$.

The evident oscillatory behaviour of $n_\pm$ is just the result of the oscillatory motion of the particles, during their path, and principally of the y coordinate. This behaviour has no other physical meanings, but it is just a numerical artifact related to how we calculate the density. We can approximate the behaviour of the density, for the different curves, with the expressions in Eqs. (4.54) (4.55) (4.56).
For the case with $\Upsilon = 1$:

$$\begin{cases} \mathbf{N_{\pm,0} = 10^6} : f(t) = A_1 \exp\left[-B_1 \left(\frac{t}{C_1}\right)\right]; \\ \mathbf{N_{\pm,0} = 10^{10}} : f(t) = A_2 \exp\left[-B_2 \left(\frac{t}{C_2}\right)\right]; \\ \mathbf{N_{\pm,0} = 10^{15}} : \begin{cases} f(t) = A_3 \exp\left[-B_3 \left(\frac{t}{C_3}\right)\right] & t < 10^{-18}\ s \\ f(t) = A_4 \exp\left[-B_4 \left(\frac{t}{C_4}\right)\right] & t \geq 10^{-18}\ s \end{cases}. \end{cases} \tag{4.54}$$

[7] Which shape can be represented as a tube.

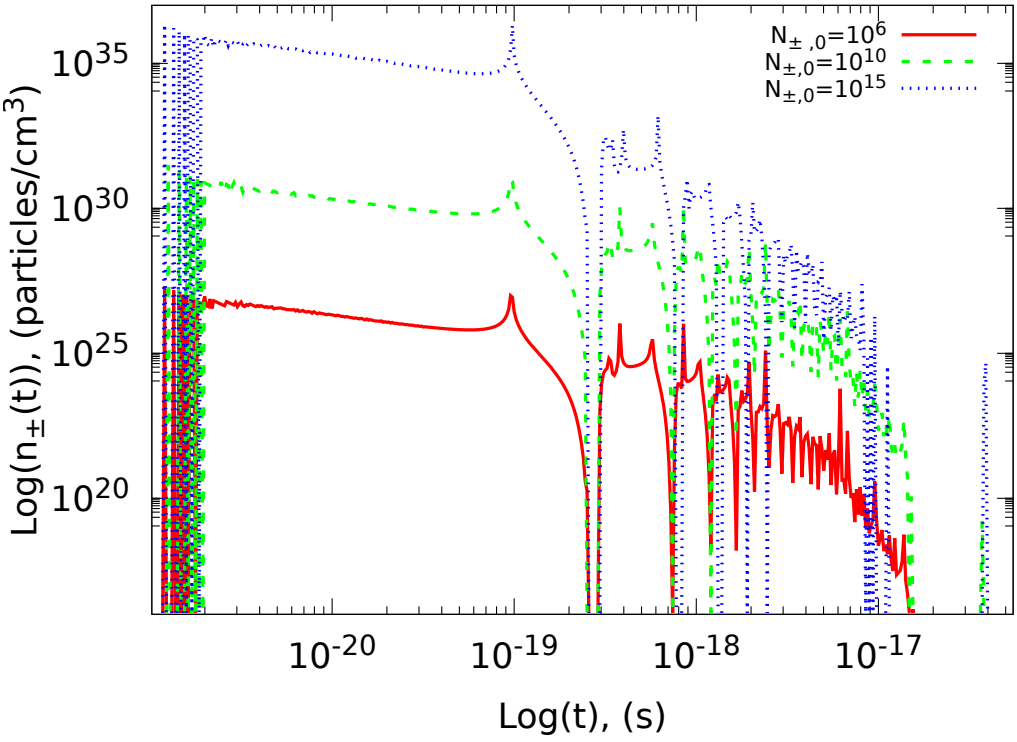

Figure 4.31. Particles volumetric number density, evaluated using Eq. (4.53), for $\Upsilon = 1$. The particles are emitted along the *generic* direction, with a value for the initial background magnetic field of $B_0 = 0.1\ B_{cr}$.

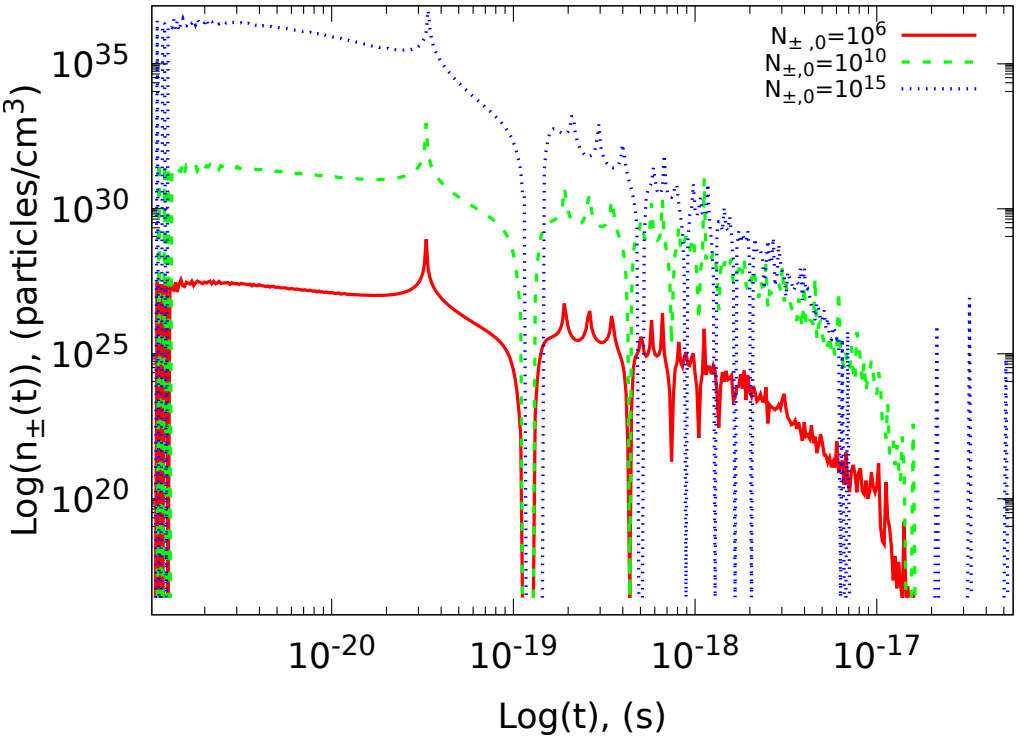

Figure 4.32. Same as in Fig. (4.31), with $\Upsilon = 1/5$

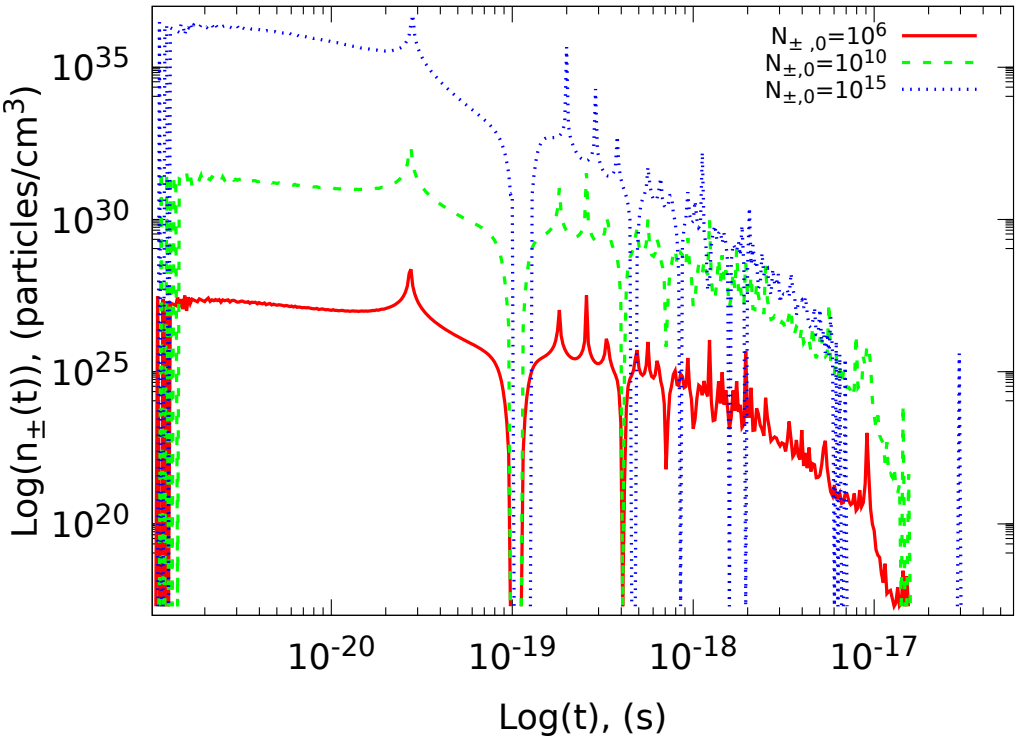

Figure 4.33. Same as Fig. (4.31), with $\Upsilon = 1/50$.

For $\Upsilon = 1/5$:

$$\begin{cases} \mathbf{N_{\pm,0} = 10^6} : \begin{cases} f(t) = A_1 \exp\left[-B_1\left(\frac{t}{C_1}\right)\right] & t < 10^{-18}\ s \\ f(t) = A_2 \exp\left[-B_2\left(\frac{t}{C_2}\right)\right] & t \geq 10^{-18}\ s \end{cases}; \\ \mathbf{N_{\pm,0} = 10^{10}} : \begin{cases} f(t) = A_3 \exp\left[-B_3\left(\frac{t}{C_3}\right)\right] & t < 10^{-18}\ s \\ f(t) = A_4 \exp\left[-B_4\left(\frac{t}{C_4}\right)\right] & t \geq 10^{-18}\ s \end{cases}; \\ \mathbf{N_{\pm,0} = 10^{15}} : \begin{cases} f(t) = A_5 \exp\left[-B_5\left(\frac{t}{C_5}\right)\right] & t < 10^{-18}\ s \\ f(t) = A_6 \exp\left[-B_6\left(\frac{t}{C_6}\right)\right] & t \geq 10^{-18}\ s \end{cases}. \end{cases} \tag{4.55}$$

For $\Upsilon = 1/50$:

$$\begin{cases} \mathbf{N_{\pm,0} = 10^6} : \begin{cases} f(t) = A_1 \exp\left[-B_1\left(\frac{t}{C_1}\right)\right] & t < 10^{-18}\ s \\ f(t) = A_2 \exp\left[-B_2\left(\frac{t}{C_2}\right)\right] & t \geq 10^{-18}\ s \end{cases}; \\ \mathbf{N_{\pm,0} = 10^{10}} : \begin{cases} f(t) = A_3 \exp\left[-B_3\left(\frac{t}{C_3}\right)\right] & t < 10^{-18}\ s \\ f(t) = A_4 \exp\left[-B_4\left(\frac{t}{C_4}\right)\right] & t \geq 10^{-18}\ s \end{cases}; \\ \mathbf{N_{\pm,0} = 10^{15}} : \begin{cases} f(t) = A_5 \exp\left[-B_5\left(\frac{t}{C_5}\right)\right] & t < 10^{-18}\ s \\ f(t) = A_6 \exp\left[-B_6\left(\frac{t}{C_6}\right)\right] & t \geq 10^{-18}\ s \end{cases}. \end{cases} \tag{4.56}$$

The values of all the parameters in the formulae in Eqs. (4.54) (4.55) (4.56) are tabulated in Tab. (4.5). An example of these fits, for the case with $\Upsilon = 1$, is shown in Fig. (4.34). From these plots we can get useful informations about the applicability of our model to different astrophysical systems. These systems have several parameters and values of physical variables that need to be satisfied in order to apply

Table 4.5. Parameter values in Eqs. (4.54) (4.55) (4.56)

Υ	A_1	A_2	A_3	A_4	A_5	A_6	B_1	B_2	B_3	B_4	B_5	B_6	C_1	C_2	C_3	C_4	C_5	C_6
1	10^{25}	10^{29}	6×10^{34}	10^{31}			$\frac{3}{2}$	$\frac{3}{2}$	1	1.7			10^{-18}	10^{-18}	10^{-19}	10^{-18}		
$\frac{1}{5}$	10^{26}	10^{25}	10^{30}	10^{29}	10^{35}	10^{31}	4	$\frac{3}{2}$	4	$\frac{3}{2}$	2	2.4	10^{-18}	10^{-18}	10^{-18}	10^{-18}	10^{-19}	10^{-18}
$\frac{1}{50}$	10^{26}	10^{25}	10^{30}	10^{29}	10^{34}	10^{30}	2.7	$\frac{3}{2}$	2.8	$\frac{3}{2}$	1	1.7	10^{-18}	10^{-18}	10^{-18}	10^{-18}	10^{-19}	10^{-18}

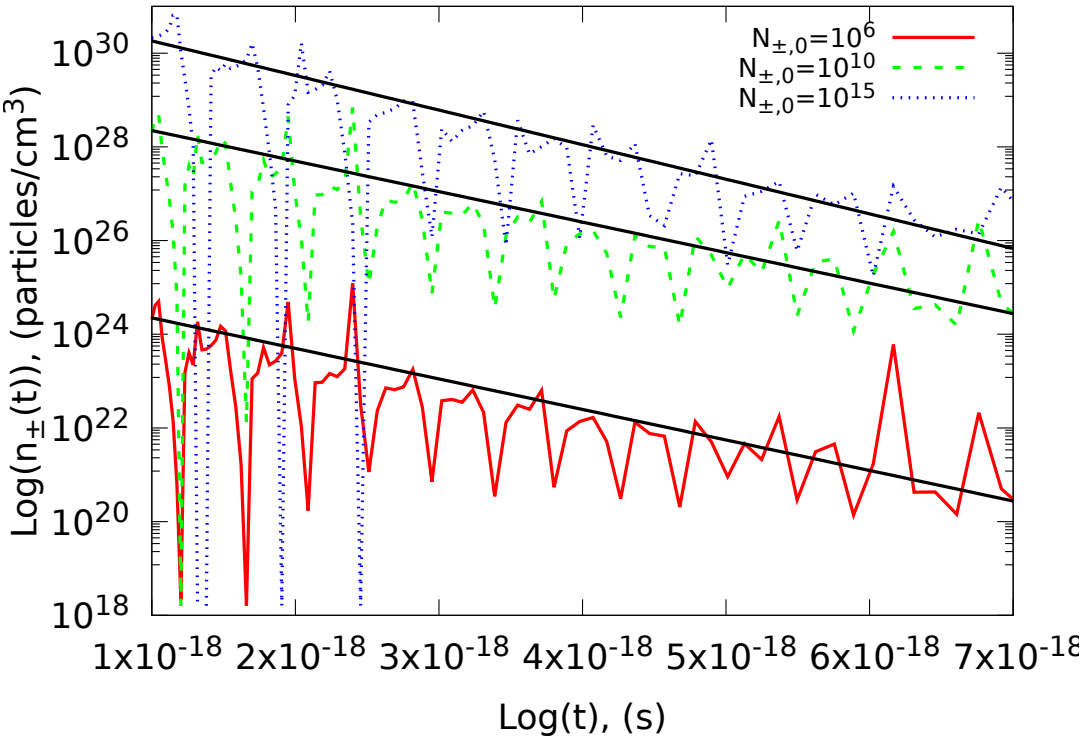

Figure 4.34. Same as Fig. (4.31), with the fit (black lines) given by Eq. (4.54).

a particular model to them, trying to explain and reproduce a particular physical event. The particles number density, spread it in a specific region of the considered system, is one of these parameters.
For GRBs, usual values for the number density of particles, emitted near a BH, is $10^{30} \lesssim n_{\pm,0} \lesssim 10^{35}$ particle/cm^3. With this numeric value for $n_\pm$, we can now select specific inputs for our model. In our calculations we set the following initial conditions (consistently with the set of equations that need to be integrated): particles positions (x_0, y_0, z_0), the particles velocities $\left(\beta_{x,0}, \beta_{y,0}, \beta_{z,0}\right)$ (and, then, γ_0), the number of photons $N_{\gamma,0}$, the number of injected pairs $N_{\pm,0}$, the background magnetic field B_0 and the direction of the emission of the particles. The initial position, the velocities and the direction of emission are almost arbitrary parameters; the initial values of the background field B_0 is setted by the model assumed to study the black hole behind the GRB; the number of initial photons is strictly correlated to the initial number of particles emitted. Then, $N_{\pm,0}$ is a fundamental parameter that needs to be setted consistently with the physics of the problem.

From the plots of $n_{\pm,0}$ in Figs. (4.31) (4.32) (4.33), one can see that, in order to satisfy the magnitude of $n_{\pm,0}$ that we gave above, we should set, as an initial conditions for our problem, a number of pairs $10^{10} \leq N_{\pm,0} \leq 10^{15}$. This result tells us that we cannot insert a bigger number of particles in the system, in order to fulfil the real value of the particles number density for our case.
In ours computations, we have also integrated the set of equations with initial conditions $N_{\pm,0} \geq 10^{15}$. The only result that we have shown is the decrease of the magnetic field, for $N_{\pm,0} = 10^{15}$ and 10^{18}, in

Figs. (4.13) (4.14), respectively. Then, from the last result of this section, we conclude that only if we set $N_{\pm,0} \leq 10^{15}$ (see Fig. (4.13)), we can have a real and useful interpretation and applicability of our screening model to the particular type of GRBs that we considered in this chapter and in the whole thesis.

4.8 Conclusions

In this chapter we have built a schematic model for the study and the description of the magnetic field screening effect. The basic idea of this model is that, when an initial number of particles is injected in a region where both magnetic and electric field are presents (perpendicular to each other), the oscillatory motion of these particles creates, from the well known Biot-Savart law, an induced magnetic field, oriented in opposite direction with respect to the background one, which decreases the background magnetic field.

The Wald mechanism, that leads to the formation of the induced electric field on the BH when it is immersed inside a region where a background magnetic field is present (see [152]), fixes the analytical structure for the electromagnetic field. In [130, 136, 105] the complete expression of the electromagnetic field, when the background magnetic field is considered parallel to the BH spin, is given using Boyer-Lindquist coordinates with Carter's orthonormal tetrad. Since, as we explained in the introduction of this chapter, we work on an honest locally Minkoskian frame, we decided to start the study of the screening process, firstly, considering the configuration of crossed fields: with $\vec{B}$ along the $\hat{z}$-axis and $\vec{E}$ along the $\hat{y}$-axis. In order to have a complete view of the process and to see how it reacts to other configurations of the magnetic and electric fields, in future works we will study the cases of $\vec{E} \times \vec{B} = 0$ (parallel fields) and $\vec{E} \times \vec{B} < EB$ [8] (when an angle between the two fields is present). In App. (G), we give a brief introduction on the pair production rate and on the set of equations to use for these cases.

Before to resume the results of our study, three important comments need to be considered about the model and the results obtained in this chapter by the integration of the set of equations which governs the process:

1. In this chapter, we already stated the assumption we made for the schematization of the particles motion. Indeed, we constructed the equations of the model treating the huge number of particles as a single particle. Then, the resultant set of equations become one-particle equations. At a first sight, this assumption could seems restrictive, but can be argued by some considerations. Firstly, one needs to keep in mind that this is only a first schematization of the screening problem, in order to see if this effect could really occurs and if it would be efficient. Some of the assumptions of the model needs to be relaxed, in order to have a complete real description of the process. We will have a closer look on this problem in the nearly future. Secondly, since the strength of the fields is too high, the particles are bounded to follow almost the same trajectory, without much freedom to vary their motion. The third comment is that a flux of particles, with the same velocity and governed by such strong fields, can be treated as a fluid, since it obeys to the continuity equation. Indeed, in Eq. (4.53), we have calculated the volume as an instantaneous volume around the position of the particles, at each time. Consequently, the volume can be treated as with constant dimensions (at each step of the integration time). Then, the variation with time of the particles density inside the tube volume (calculated via Eq. (4.53)) is due to the flux of outgoing particles through the boundary surface of the volume itself. The flux through the lateral surface can be approximated to 0 since the majority of the particles follow the same path described by the coils. Instead, the upper and lower surfaces are crossed by the electrons and positrons, respectively, since their movement is oriented in opposite directions. Because the two particles are created with the same multiplicity, the two surfaces experience the same flux of particles. From these arguments, we can conclude that the charge conservation and, then, the continuity equation are satisfied and, then, as a first order approximation, we can consider the particles flux as a fluid.

[8] Where E and B are the strength of the two fields.

2. In our calculations, we set a proportionality between the electric and magnetic field. Then, a magnetic field reduction, due to the screening, leads to the reduction of the electric field too. The screening of also the electric field can be justified by the following arguments. Firstly, even if we did not write an equation for the reduction of the electric field, as we have done for $\vec{B}$, the structure of the problem itself brings with it the creation of an induced electric field too. Indeed, the emission and the creation of new particles leads to the formation of a charged current, which screens the electric field. This is only a qualitative argument about $\vec{E}$ screening and more quantitative approach needs to be developed, but it is just to justify that our assumption of $\vec{E}$ screening, due to the proportionality relation, it is not so wrong. The second argument to support our choice is related to the applicability of the model to GRBs. The geometric structure of the EM field near a rotating BH is described in [136, 105], where it is shown that it exists between the two fields the same type of proportionality that we have set for our problem, at least inside a region close to the BH horizon. The results obtained from the integration of our equations tell us that the screening effect acts in a temporal range between $10^{-21} \lesssim t \lesssim \left(10^{-17} - 10^{-15}\right)$ s. Since this corresponds to a region of radius $r_s \approx c \times t$ of $10^{-11} \lesssim r_s \lesssim \left(10^{-7} - 10^{-5}\right)$ cm, namely a region very close to the BH horizon, then, we can conclude that the assumption of proportionality between the two fields is well satisfied in our problem.

3. The basic idea of our approach to the problem was the creation of showers of pairs and photons due to the magnetic pair-production process. The results we obtained (see Tabs. (4.1) (4.2) (4.3)) tell us that the principal process that gives the major contribution to the creation of new particles is the photons emission via the synchrotron or synchro-curvature processes from charged particles. Indeed, from these tables we can see that when we insert an arbitrary value for $N_{\pm,0}$, the final number of photons N_γ reaches a value similar or, at most, greater than one order of magnitude than the initial number of particles $N_\pm$. The energy of these photons is of the order of MeV (see Figs. (4.16) (4.18)).
   What we expected, in the beginning, was that there would have been a balance between the pairs creation (via the MPP process) and the emission of radiation, and also that there would have been an exponential growth of $N_\pm$ too. Whereas, from the plots of the rate in Figs. (4.2) (4.3) (4.4) (4.5), we can see that the rate of the process is not so efficient for the limited time-scales under consideration. From these arguments, we deduce that, for the chosen set of initial conditions, the screening is principally operated by the number of initial particles inserted in the system. From the discussion in Sec. (4.6.5), we understood that the low value of the rate $\zeta(t)$ is due principally to the low energy of the photons that produce, consequently, less energetic $e^\pm$. Higher energetic photons energy would produce higher energetic pairs, with consequent higher number of loops around the magnetic field lines and, then, a stronger screening effect. These calculations will be done in the nearly future.

4. We verified that the applicability of Biot-Savart law for the calculation of the induced magnetic field is not restrictive. In order to apply this formulation, it is necessary that the background magnetic field can be considered as stationary. This occurs when the circularization time scale $t_c(t)$ (the time the particle spends to complete one "orbit" around the magnetic field lines) is faster than the screening time scale t_{screen} (the time necessary for the magnetic field to reduce its strength). In Sec. (4.6.4), we have verified that, for almost all the analyzed initial conditions, $t_c < t_{screen}$ or $\ll t_{screen}$ and, then, the assumption that the field can be considered stationary, at least for the specific temporal range under consideration, is valid. The only case when this condition is no longer valid, is when a number of particles greater than $N_{\pm,0} = 10^{15}$ is inserted in the problem. From this consideration and from the consideration for the number density in Sec. (4.7), we can exclude this initial condition from the results of our problem since it does not verify the physical applicability of our model to the considered astrophysical systems of GRBs.

Now that we have fixed in mind the above considerations, we can resume the results we have obtained.

The principal result is that the screening of the magnetic field can occur, but with different efficiency depending on the set of initial conditions. Indeed, firstly a conspicuous decrease of $\vec{B}$ is obtained if we increase the number of initial pairs inserted in the problem $N_{\pm,0}$. With $10^6 < N_{\pm,0} \leq 10^{15}$, we got a strong effect of the screening.
Secondly, this effect is also dependent from the initial direction of emission of the particles. Indeed, we note that the major effect is operated when the particles are emitted in the *generic* and $\hat{y}$ direction. This is a natural consequence of the nature itself of the effect. Indeed, as we stated in Sec. (4.3), the screening is produced by the particle velocity orthogonal component (with respect to the $\hat{z}-$axis), that is dominant if the particles are emitted in the *generic* or $\hat{y}$ direction. We should also note that a small decrease of the field occurs also when the particles are launched along the $\hat{z}$ direction, since a little component of the velocity in the azimuthal plane is present (due to the different orientation of the fields).
A further dependence of the effect is the one related to the parameter Υ. The dependence of the screening effect (namely the reduction of the magnetic field) by Υ is not linear or easily identifiable. Indeed, comparing the plots in Figs. (4.9)-(4.14) (in particular Fig. (4.13)) and the results in Tabs. (4.2) (4.3) (4.4), we can notice the following features:

1. **Fixing Υ:** the screening is larger if the particles are emitted initially along the $\hat{y}$-axis; it is lower if they are emitted along the *generic* direction;

2. **Fixing the $\hat{y}$ direction:** the screening increases if we increase the value of Υ;

3. **Fixing the *generic* direction:** the screening increases if we decrease Υ.

The first characteristic is related to the dynamics of the process. Indeed, the particles emitted along the $\hat{y}$-axis have only the perpendicular component of their velocity $\beta_\perp$ (the only necessary for the screening effect). Instead, the particles emitted along the *generic* direction have both $\beta_\perp$ and $\beta_\parallel$. The other two points are related to the dependence of the equation for the magnetic field Eq. (4.43) and, in particular, of the rate $\zeta(t)$, by the particle velocity $\vec{\beta}$, the photon director cosines $\vec{\eta}$ and the parameter Υ. Indeed, for the third point, analyzing Eq. (4.43), together with Eqs. (4.33)-(4.35), one can derive analytically (after some arithmetic passages) that a decrease of the value of Υ leads to a stronger MPP rate $\zeta(t)$ (see Figs. (4.2) (4.4) (4.5)). Moreover, a decrease of Υ implies a lower value for the particle Lorentz factor, as we have shown in Fig. (4.19). In Fig. (4.21), we have also shown that a decrease of Υ leads to a stronger synchrotron emission, with the related increase of the number of produced photons. Then, since $\frac{dN_\pm}{d\tilde{t}} = N_\gamma(\tilde{t})\,\tilde{\zeta}(\tilde{t})$ and $\frac{d\tilde{B}_{tot}}{d\tilde{t}} \propto \gamma^{-2} \times \frac{dN_\pm}{d\tilde{t}} = \gamma^{-2} \times N_\gamma(\tilde{t}) \times \tilde{\zeta}(\tilde{t})$, the discussions above imply that lower values of Υ leads to a stronger screening effect. Concerning the second point, it can be explained by the following arguments. Firstly, considering also the discussion in the introduction of this paragraph, we have verified that: 1) the velocity component $\beta_\perp$, for particles emitted along the $\hat{y}$ direction, is always larger than the one for particles emitted along the *generic* direction; 2) an increase of Υ leads to an increase of $\beta_\perp$. Secondly, the rate $\zeta(t)$ for $\Upsilon = \frac{1}{5}$ and $\frac{1}{50}$ is higher than the one for $\Upsilon = 1$ only between $10^{-21} \leq t \lesssim t^* = 5 \times 10^{-18}$ s[9]. For $t > t^*$, $\zeta(t)_{\Upsilon=1}$ is always higher than $\zeta(t)_{\Upsilon=\frac{1}{5}}$, $\zeta(t)_{\Upsilon=\frac{1}{50}}$, as shown in Fig. (4.35), where the rate is plotted for a number of particles $N_{\pm,0} = 10^{10}$ emitted along the $\hat{y}$ direction and with $B_0 = 0.1\ B_{cr}$. This implies also a higher value for the respective $dN_\pm/dt$ (see Fig. (4.36)). Notwithstanding the values of these variables (for $\Upsilon = 1$) seem just a little bit higher than their values for $\Upsilon = \frac{1}{5}$, $\frac{1}{50}$, such amount, together with the related increase of $\beta_\perp$ described above, is enough to explain a wider decrease of the magnetic field when we enhance Υ, for particles emitted along the $\hat{y}$ direction.

We conclude that the screening effect due to the motion of a high number of particles occurs and it is necessary to take it into account in the study of physical systems with the same characteristics of the one we have considered.

[9]The time t^* represents the point when the curves for the magnetic field start to drop down and the screening effect starts to act.

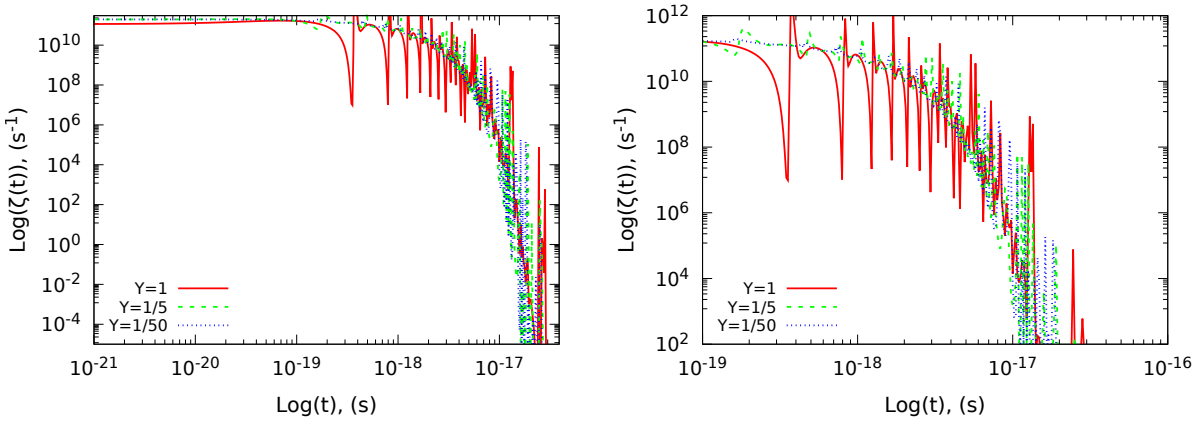

Figure 4.35. MPP rate for a number of particles $N_{\pm,0} = 10^{10}$ emitted along the $\hat{y}$ direction, for the three values of $\Upsilon = 1,\ \frac{1}{5},\ \frac{1}{50}$.

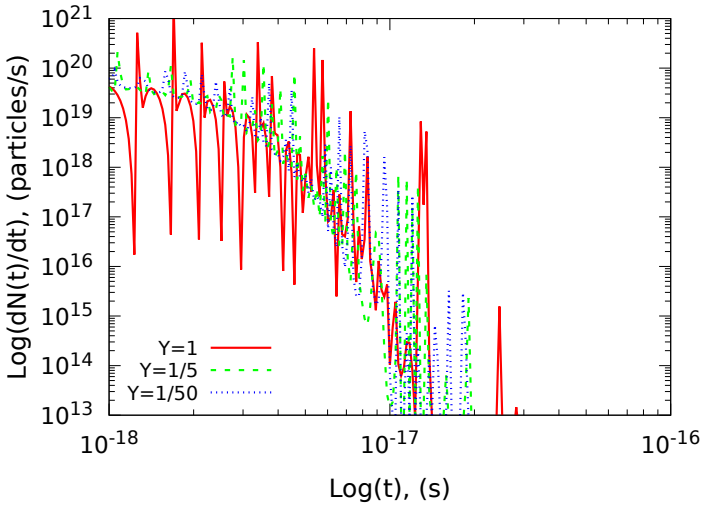

Figure 4.36. The evolution with time of the number of produced pairs $\frac{dN_{\pm}}{dt}$, for the three values of $\Upsilon = 1,\ \frac{1}{5},\ \frac{1}{50}$, for $N_{\pm,0} = 10^{10}$ emitted along the $\hat{y}$ direction and with $B_0 = 0.1\ B_{cr}$.

Photons mean-free-path and their detectability

Here we study briefly the probability to detect synchrotron photons emitted by the e^+e^- pairs during their motion inside the EM field. Firstly, we need to make a general comment on this subject. The effect studied in this chapter is based on the magnetic pair production process carried out by these synchrotron photons. Then, for the effectiveness of the screening process, we expect/hope that no photons escape from the system. However, from our results (see Tabs. (4.2) (4.3) (4.4) and Fig. (4.20)), we obtained that, for the considered small time scale, not all the created photons produce new pairs via the MPP process. Indeed, if it would not have been like this, a higher number of pairs would have been created, consistently with the number of new photons. Then, some of these photons do not interact with the background magnetic field and, at first, are able to escape from the system.

In order to study this escape probability, we calculate the photons mean free path by $\lambda_\gamma(t) = c/\zeta(t)$, with $\zeta(t)$ the MPP production rate given in Eq. (4.32). We can justify the choice to consider only the MPP process for the calculation of the mean free path as follow. As stated in the beginning of the chapter, we have built a set of one-particle equations, assuming that all the particles follow the same path because the strength of the fields is very high. This assumption implies that there will not be any scattering (Compton,

Inverse Compton, Pairs Compton) between the emitting e^+e^- and the emitted γs. This can be understood if one looks at the plots of the particles trajectroy (see Figs. (4.22) (4.23)). The synchrotorn photons are emitted tangentially to the particle trajectrory and along its specific direction. Then, since all the particles are assumed to follow the same path, those photons never interact with these particles. Anyway, this is only an approximation due to the assumptions of our model. In the real physical system, due to the high density of pairs, photons will surely interact with e^+e^-, but we expect that the MPP still results the dominant process. We will calculate the complete (considering all the possible interactions) photons opacity in a future work.

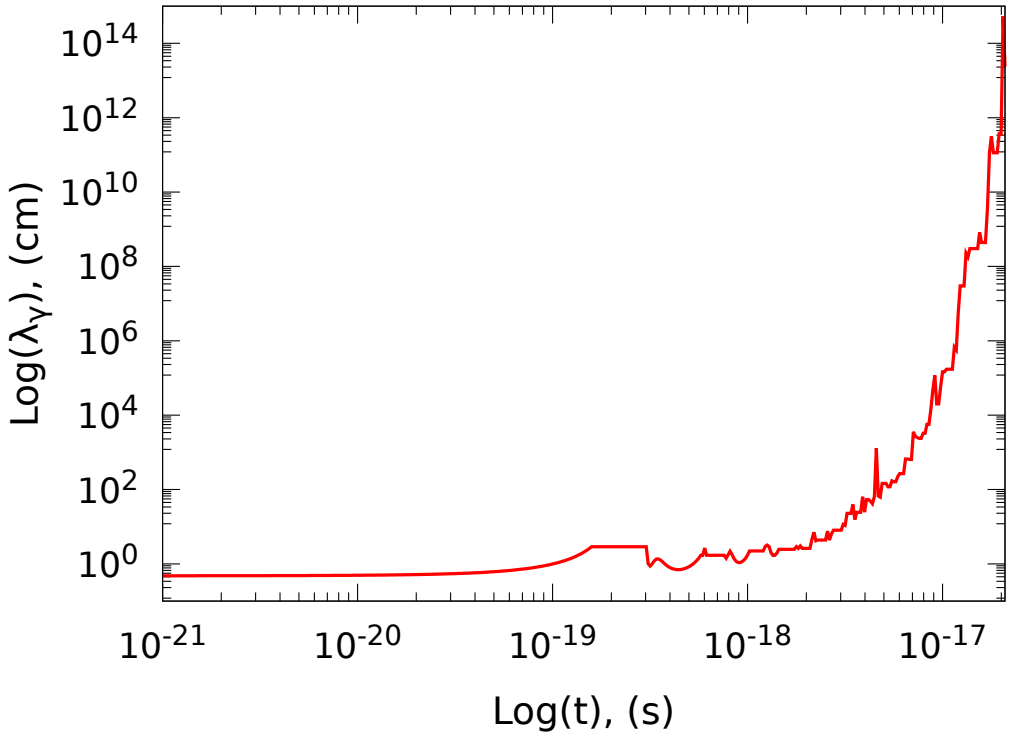

Figure 4.37. Mean free path for synchrotron photons, λ_γ, emitted by the accelerated e^+e^- pairs. The mean free path is calculated by $\lambda_\gamma = c/\zeta$, with ζ the MPP production rate given in Eq. (4.32). We consider only the MPP process because, under the assumptions of the model and for our set of equations, it is the dominant process in this configuration. The purely arithmetical oscillations of λ_γ, due to its dependence by ζ, have been smoothed out since they do not have any physical meaning for the mean free path. The value of the parameters considered for this plot are: $\Upsilon = 1$, $B_0 = 0.1\ B_{cr}$, $N_{\pm,0} = 10^6$ and particles emitted along the *generic* direction.

In Fig. (4.37) the photons mean free path, calculated as described above, is shown considering the following initial conditions: particles emitted along the *generic* direction, $\Upsilon = 1$, $B_0 = 0.1\ B_{cr}$ and $N_{\pm,0} = 10^6$. For the other analyzed initial conditions, the behaviour and the values of the mean free path are very similar or overlapped to the one shown in Fig. (4.37). From this plot we see that the mean free path is, for almost all the integration time, $0.1 < \lambda_\gamma \leq 1$ cm or of the order of a few centimeters. Only at longer times, the mean free path starts to increase of several orders of magnitude, specularly with the decrease of the magnetic pair-production rate (see, e.g., Fig. (4.2) or the other rate plots). In this figure we show only the values of λ_γ necessary for the photons to escape from the BH site; we have cut out larger values of λ_γ. Thus, since the size of the whole BdHN system is of the order of $\sim 10^{12}$ cm, we deduce that only the photons emitted at longer time can, in principle, escape from the system ad reach the Earth.

Screening process in alternative fields configurations

In the beginning of this chapter and this section, we stated that, in order to have a more precise description of the process, we need to relax some assumptions and apply another approach in the study of this the problem. Before to apply these changes to the model, we need to analyze the cases with different configurations of the fields: 1) with $\vec{E}$ and $\vec{B}$ parallel; 2) when an angle between the two fields is present. We want to study the screening process in these other configurations for two reasons: 1) in order to understand how the model reacts if one changes the fields structure; 2) because we do not know the microscopic structure of the electromagnetic field (the complete analytical structure of the filed in [130, 136, 105] is written in macroscopic Boyer-Lindquist coordinates). To justify the reasons for these further studies and to show that the screening process may occurs, we propose the following considerations:

- **Pair production rate and particle trajectory**
  - The pair production rate via the MPP process for strong, constant and parallel magnetic and electric fields has been derived by *Daugherty & Lerche* in [39]. They show that the pair production rate is 0 only when the photons propagate parallel to the direction of the fields. For all other photons directions, the rate $\zeta \neq 0$. In this configuration of the fields, the particle moves with a helicoidal trajectory (for the same time interval considered), with the coil axis oriented parallel to the direction of the fields [10]. From the theory of synchrotron emission, it is known that the emission is confined in a cone along the velocty direction of the particle. This suggests that there will be no (or only a few) photons propagating parallel to the fields and, then, a production rate different from 0 is expected. We report the prodution rate for this configuration in Eq. (G.8) (expressed in the frame $K^{'}$ where the photon momentum is perpendicular to the parallel fields).
  - For the second case of not parallel nor perpendicular fields, we can use the pair production rate used in this chapter (Eq. (4.30)), after have carried out the proper Lorentz transformations in order to set the fields and the photons propagation vector in the right conditions to apply that formula (see App. (G.2)). Since we have demonstrated that, both in the case analyzed in this chapter (with $\vec{E} \perp \vec{B}$) and the case with $\vec{E} \parallel \vec{B}$ (see the discussion above), the emitting particle is accelerated in the direction of the electric field, while is keeping circularizing around the magnetic field lines, in the case with $0 < |\vec{E} \cdot \vec{B}| < EB$ we expect that the particle follows the same type of trajectory, with wider coils oriented closely to the BH rotation axis. Thus, since the radiation is emitted along the direction of the particle velocity, the perpendicular components of the photon director cosines ($\eta_x,\ \eta_y$) are not null and then, from Eq. (4.32), the production rate is different from zero. We should note that, for the considered configuration of the fields, Eq. (4.32) is not the right expression for the pair production rate. The right expression of ζ can be derived by Eq. (4.30), after have carried out two Lorentz transformations (the first one to move into a frame where the two fields are perpendicular; the second one to move into a frame where only the magnetic field is present and the photon momentum vector is perpendicular to the new magnetic field), transforming $\zeta^{''}$ back to the original frame. However, the structure of the equation is similar to Eq. (4.30).

- **Magnetic field equation**
  - For the configuration of parallel fields, the equation for the magnetic field screening is given in Eq. (G.11). Comparing the latter with Eq. (4.43) (for perpendicular fields), we notice that the structure of the two equations is similar (only the composition of the terms inside the square brackets is different). They depend on the same variables $\left(\tilde{B}_{tot}, \tilde{E}_{tot}, \beta_x, \beta_y, \gamma, \dot{N}_{\pm}\right)$ (in

[10] We have already verified this phenomenon, even if we will not show the results because we still need to improve the model.

Eq. (G.11), $\dot{\tilde{B}}_{ind}$ depends also on β_z) and, then, on the components that lead to the screening process, namely the perpendicular components of the velocity vector $\left(\beta_x, \beta_y\right)$ (related to the "*geometry*" of the process), γ and $\dot{N}_{\pm}$ (related to the intensity of the proccess).

- For the case of not parallel nor perpendicular fields, we still need to finish to write all the equations that describe the system and we address the problem to a future paper. However the procedure to derive the equation for the magnetic field is the same we followed in Sec. (4.3) (and in App. (G.1)) and $\dot{\tilde{B}}_{ind}$ will depend on the same variables cited above. Only the combination between the field and the velocity components is different due to the different configuration of the fields.

In App. (G) we just lay the foundation for the structure of the problem for these two cases, even if we did not finish to write all the equations yet, but we are keep on working on these other configurations.
One of the assumptions of the model we have built is to consider a Minkoskian space-time. This assumption might seem restrictive since we are working with BH and, then, a general relativity analytical formulation of the problem might seems mandatory. But, as we already stated in the beginning of this chapter (and corroborated by the results shown in Sec. (4.6)), the assumption of a locally flat space-time is not restrictive, since the screening process occurs in very short time/space scales and, then, the particles do not feel the general relativity effects.

Finally, we want to emphasize that the model we have built can be applied to other physical or astrophysical objects which satisfy the assumptions of our model (as a rotating BH or NS or the proportionality between the electric and magnetic field).

Chapter 5

Conclusions

This thesis is based on the work I have developed during the almost four years of the Ph. D. program inside *"ICRANeT" center* and *"Sapienza" University of Rome*. The work focus on two different aspects of astroparticles physics applied to Gamma-Ray Bursts (GRBs), on which *"ICRANeT"* institution is specialized.
In the first two chapters of the thesis, Chs. (1) and (2), I have introduced the reader to:

1. the physics of GRBs, with their characteristics and their interpretation within the *fireshell* model (Ch. (1)) developed by Prof. Ruffini, R. and his group during the last 20 years;

2. the framework of the long GRB class (Ch. (2)). I have differentiated all the GRB classes and concentrated my attention principally on the GRB subclass of BdHNe, listing all of its different physical features and its observable counterparts, since it represents the basic astrophysical system on which I have developed the rest of the thesis.

In the second half of the thesis, Chs. (3) and (4), the two works that I have developed during the Ph. D. program are presented. These works are based on the BdHN model for long GRB and could provide, at least, two ways to check the feasibility of the model.

In Ch. (3) I have studied the production of neutrinos from the *proton-proton* interaction between accelerated protons (with different orders of magnitude difference of their Lorentz factor γ_p depending on their emission direction) and protons at rest inside two regions which characterize the GRB: 1) a denser one (with particles number density $n_t \sim 10^{23}$ particle/cm^3) near the central BH, where resides all the material expelled by the SN companion, the SN-ejecta (see Chs. (1) and (2)); 2) a less dense one corresponding to the interstellar medium ISM (with particles number density $n_{ISM} = 1$ particle/cm^3). The neutrinos emerge from the pion decay $\pi \to \mu\, \nu_{\mu^{(1)}}$ and muon decay $\mu \to e\, \nu_e\, \nu_{\mu^{(2)}}$, while the pions come out from the creation of the Δ resonance in the pp interaction.
I have studied the spectrum of all the particles created by this hadronic interaction, namely photons (by π^0 decay), electrons, electronic neutrinos and double muonic neutrinos (by $\pi^\pm$ and $\mu^\pm$-decay), for different physical setups:

1. In the first case, I have analyzed the expansion of a plasma of $\gamma e^\pm$, emitted by the BH, inside the SN-ejecta (with number density n_t and baryon load of $B = 51.75$), lying in the azimuthal plane defined by the BH and the νNS (which emerges from the SN explosion). This plasma shell starts to acquire protons from the ejecta and accelerates them up to a Lorentz factor $\gamma_p \leq 6$. The particles number density of the front of the shell varies between $10^{25} \leq n_{sh} \leq 10^{26}$ particle/cm^3, inside all the emitting region of the ejecta. These accelerated protons interact with the protons (at rest) ahead of the shell front (at every radius of the expansion). The γ and νs, created in this physical setup, have energies of the order of ~GeV and emissivity that varies between $10^{29} \leq E^2\,(dN/dE) \leq 10^{31}$ erg/cm^3/s, depending on their creation point inside the ejecta.

2. Since the SN-ejecta is not symmetric, there is an open region where the emitted plasma is let free to escape without interaction with matter (see Fig. (3.2)). Even in this case, ejecta protons are loaded (with a baryon load of $B \simeq 10^{-3}$) and accelerated by the plasma up to a Lorentz factor of $\gamma_p = 10^3$. Since they are free to escape from the creation site, the first dense region they can find on their path is the ISM, at a distance of $r \sim 10^{16}$ cm from the BH site. The interaction between the accelerated protons and the one at rest of the ISM produce secondary particles with energies between $1 \leq E_a \leq 10^3$ GeV, but with a maximum on their spectrum around $\sim$ 100 GeV. The emissivity is lower in comparison with the previous case: $10^{-17} \leq E^2\,(dN/dE) \leq 10^{-15}$ erg/cm^3/s. This is principally due to the difference in the target protons density.

3. In App. (D.1), I will analyze an interaction similar to the previous case, but when the protons are emitted along the BH axis and can reach energies of $E_p = 10^{21}$ eV ($\gamma_p = 10^{12}$), since they are free to escape from the BH site without interacting with matter. The interaction of these protons with the ISM protons leads to secondary particles with energies of the order of $\sim 10^4$ PeV and luminosity of 10^{21} erg/s.

In the conclusion of Ch. (3), I have tried to give an estimate of the possibility to detect these neutrinos using three detectors: SuperKamiokande, HyperKamiokande and IceCube. We derived the horizon distance inside which these neutrinos can be seen. Unfortunately, for cosmological GRBs, with redshift $z \sim 1$, the derived horizon distance is not enough to reach the Earth. In order to be able to see these neutrinos, we need to have sources with higher energy or higher detector interactive mass and improvements of its sensibility. Indeed, in the same section, I have made a few comparisons of the obtained results with IceCube observations and expectations. Even if no low energy neutrino sources have been found in the collected data, the expectation rate for BdHNe sources is still in the available range for a neutrino detection. I have also provided an indirect way to test the occurrence of the considered neutrino production, analyzing the photons produced in the same interaction by π^0 decay. These photons are energetically and temporally separated from the other GRB radiation emissions and, then, may be easy to detect. The flux of photons produced inside the high density region have the right value to be detected on Earth but, as explained in App. (E), the several interactions between photons and matter decrease the possibility to detect these photons. However, a more complete and precise description of the opacity inside this region will be the subject of further future studies.
Also the connection with the gravitation wave signals from BdHN is considered in the conclusion of Ch. (3). The formation of the BdHN system can lead to the emission of gravitational waves, but the signal is to weak to be detected by any Earth detector since the orbital period of the BdHN components is too long respect to the minimum orbital period necessary for a signal to be detected ($P_{\rm orb}^{\rm BdHN} \approx 5$ min$\gg P_{det} \lesssim 0.2$ s). Instead, a GW signal can be detected if the BdHN becomes the *in-state* of a new class of short GRB, called Ultra-Short GRB (U-GRB), forming from the coalescence of the BdHN components (NS+BH). The GW signals from this type of source can be detected by our Earth detectors if it is loaceted between 253 and 634 Mpc. However this GRB class still needs to be electromagnetically identified.

In Ch. (4), I have developed the second topic of this thesis, concerning the screening of the BH magnetic field due to the motion of electron-positron pairs. The considered configuration of the electromagnetic field is the one of crossed fields ($\vec{E} \perp \vec{B}$), with their strengths related by the proportionality relation $E(t) = \frac{1}{2}\Upsilon B(t)$, with Υ the BH spin parameter. This configuration is valid, at least, in a region close to the BH horizon. In this physical setup, e^+e^- pairs are launched in different directions and I have studied their motion inside the EM field. During their motion the pairs emit synchrotron photons, which interact with virtual photons of the background magnetic field generating a new pair via the *magnetic pair-production* process, $\gamma + B \rightarrow e^+e^-$. These new pairs emit other photons that start again the series of processes describes above, creating a particles shower. The motion of all the pairs creates an induced magnetic field oriented in the opposite direction to the background one and, then, reducing it. All of these processes are described by the set of equations I derived and showed in Sec. (4.5).

Integrating the set of these ordinary differential equations, which describe all the above processes, results that the screening of a magnetic field is present in these type of systems and needs to be taken into account for a precise study of the emission process of the GRBs emissions. The strength of the decrease depends, principally, by three factors:

1. The number of initial pairs inserted in the problem $N_{\pm,0}$. Higher the number of $N_{\pm,0}$ ($10^6 < N_{\pm,0} \leq 10^{15}$) stronger is the effect of the screening. Indeed, it seems to be dominated by $N_{\pm,0}$ instead of the particles emerging from the cascade process, at least for the considered very short time scale. This is due to the low value of the pair production rate $\zeta(t)$, because of the low value of the photons energy, for the considered set of initial conditions.

2. The initial direction of emission of the particles. The major effect is operated when the particles are emitted along the *generic* and $\hat{y}$ direction. A small decrease of the field occurs also when the particles are launched along the $\hat{z}$ direction, since the particles have always a perpendicular component of their velocity.

3. The parameter Υ. A decrease of Υ leads to a higher efficiency of the screening effect. This effect is explained if we note that a decrease of Υ corresponds to a decrease of the electric field. This implies that the synchrotron process is more efficient, with a consequent increase of the number of produced photons and of the MPP rate $\zeta(t)$.

Even this screening process can provide a possibility to check the BdHN model. Indeed the purpose of this study has been to check if this decrease of the magnetic field, due to the screening process, can occur in order to enhance the transparency for the synchrotron photons emitted in the inner regions of the system. In this way, the photons will be no longer trapped inside the emission region, can leave the source and be detected. I have discussed this topic in the conclusion of Ch. (4) (see Sec. (4.8)), where I have calculated the photons mean free path considering only the MPP process (since, under the assumptions of the model, it results the dominant process). It has turned out that synchrotron photons are free to escape from their creation point and BH site at longer integration time, namely when: the mangetic pair production rate decreases its efficiency and the total magnetic field reaches a constant value.

The two processes studied in Chs. (3) (4) are, in some way, connected. Indeed, in Ch. (3) the protons responsible of the neutrino production are accelerated by the expansion of the e^+e^- plasma, created via the vacuum polarization process. The same e^+e^- pairs are responsible for the magnetic field screening analyzed in Ch. (4). Then, in the evolution history of the particles mechanisms occurring in the BdHN system, the magnetic field screening process happens before that the leptonic plasma starts to expand, to load baryons of the ejecta and, then, to produce neutrino by means of the pp interaction. As we have emphasized in Ch. (4) (see the time scale of all the plots in that chapter), the screening process occurs in a very short time scale ($10^{-21} \leq t \leq 10^{-15}$ s), while the expansion of the e^+e^--baryons plasma inside the ejecta (at least in the region energetically available for a secondary pions production) occurs on a time scale of the order of ~ 1 s. Then, from this consideration, even the two emission processes of photons and neutrinos are temporally separated.

However, a check of the whole BdHN model by means of the combined detection of these particles messenger, generated by the considered processes, is hard to obtain. In fact, even if the screening process will allow the photons to escape from the system and be detected (as discussed in Sec. (4.8)) and if we would be able to detect the photons and neutrinos emerging form the pp interaction (principally the ones generated by the interaction inside the SN-ejecta) and if we have the right detectors time resolution that allows us to discriminate between the different detections, the two events occur on different emission planes. Indeed, the ν/γ production by pp interaction happens on the equatorial plane of the BH+NS system (as described in Fig. (3.2)). Obviously the matter around the BH is not distributed only in the equatorial plane of the system, but has a 3D-distribution (see, e.g., Fig. (2) in [134]). However, the majority

of SN expelled material resides on the BdHN components orbital plane. Whereas, the acceleration of the pairs producing the screening effect, and the related photons emission occurring during their motion, is principally concentrated on the perpendicular or leaned planes respect to the equatorial plane (depending on the initial direction of emission of the e^+e^- pairs). Only if the particles are emitted initially along the y-axis (namely parallel to the electric field), they continue to move in the equatorial plane (see Fig. (4.24)). But, in this last case, also the emitted photons lie in the $x-y$ plane and will not be able to escape from the system due to the presence of the SN-ejecta. For the other emission directions, since the photons are emitted tangentially to the particle trajectory and, due to the relativistic helicoidal motion of the particles around the magnetic field lines (parallel to the $\hat{z}$-axis), oriented along the paritcle direction at the moment of the photons production (see, for example, Fig. (6.11) in [138]). Then, the radiation is principally concentrated along the initial emission direction of the e^+e^-, on a plane leaned with an angle $\delta = 90^\circ - \theta$ respect to the equatorial plane (with θ the initial polar angle of the emission).
Thus, from the considerations above, we deduce that it would be hard to detect both paritcle messengers from the two processes studeid in this Thesis, and correlate the two detections, because of the different emission and observable planes.

We discuss now the future improvements for the works developed in this Thesis. About the neutrino production, a further and more detailed study concerns the pp interaction with protons of energy $E_p \sim 10^{21}$ eV, as I will describe in App. (D) (see below). The analysis presented in this appendix is only a preliminary study principally because the parameterization of the pp corss-section, or differential cross-section, for these high energies is not available yet. As described above and in Ch. (3), very-high-energy protons and sources with higher energy than those analyzed here will increase the horizon distance within which the neutrino produced via the pp mechanism may be seen and, then, enhance the probability to detect them.
About the magnetic field screening work, I have already discussed the future improvements of the model in Sec. (4.1). The principal improvement concerns in the rearrangement of the set of one-particle equations introducing a distribution function for the position and velocity of the particles. This will allow to release some assumtpions of the mdoel. I will also try to build up an integration method in order to follow the particles motion for longer time. This will impose to re-write the set of equations considering also the effects of General Relativity on the structure of the space-time near the BH, which act on macroscopic scales (greather than those analyzed here). A more precise description of the particles motion, consequence of these improvements, will help to understand which further scattering processes need to be considered in the calculation of the photons mean free path and, then, to get the detection probability for these synchrotron photons emitted by the e^+e^- pairs, that come out from the system due to the screening process.

A final general comment on my two works have to be made. The analysis of the neutrino production developed in Ch. (3) is specific of the BdHN model and is based on the relative geometry of the various components. I developed this study in order to see if we can have a test of the model also through this astrophysical messenger. The physics behind the process is already well known, as one can see from the references I implemented in my calculations. However, my study can be applied to other extreme astrophysical systems with similar characteristics and same actors on scene.
Instead the study concerning the magnetic field screening is the new and "*original*" part of the Thesis. This is also evident from the literature I used for my calculations. Indeed, I only took, from one paper, the magnetic pair production rate ζ and, from another paper, the expression for the intensity of the radiation emitted by the accelerating particles. Moreover, it is a more general study, respect to the previous one, since the components of the system (magnetic field, electron/positrons, photons) and even the processes considered (synchrotron emission, magnetic pair production, particles dynamic in an electromagnetic field) are common to all the astrophysical sources. From these considerations, we deduce that this study can be applied to many other systems (not necessarily an astrophysical one) that share the same physics

and physical background (as, e.g., AGN or NS).
From this discussion follows that a direct application of the results I have obtained in this Thesis to differents GRBs models is not immediate. Indeed, as already stated in Sec. (3.1), for example, even the fireball model considers the neutrino production through baryons interaction but both the dynamic of the interaction and the conditions to satisfy are differents than the one analyzed in Ch. (3). Also the magnetic field screening effect may occur in the fireball model but, even in this case, the reuslts of Ch. (4) cannot be applied directly to this model due to the different dynamic of the expanding plasma and physical background conditions. In order to fit the effect with the structure of the fireball other theroretical modifications of the equations describing the model have to be done.

The several appendices of the thesis contain all the formula and calculations I have done and used to get the results shown in Chs. (3) and (4) and further results. Appendices from "**A**" to "**E**" are related to the study of neutrino production in Ch. (3), while appendices from "**F**" to "**H**" are related to the study of the screening process in Ch. (4).

In App. (A) the differential and total cross-sections for the γ and νs productions by pp interactions, for the case of low energy protons, are shown.

App. (B) is devoted to the derivation of the kinematic limits of the secondary particles emerging from the pp interaction.

In App. (C), I report the parameterizations for the spectra of the secondary particles of the interaction studied in [70], for the case of high energy interacting protons.

In App. (D), I study the spectrum of secondary particles emerging from the interaction between UHE-protons and protons of the ISM, using the parameterization for the spectra exposed in App. (C).

In App. (E), I study the probability to detect the photons from the π^0-decay, emerging from the pp interaction. For the different physical conditions analyzed in Ch. (3), I calculate the interaction lengths for the most probable interactions between photons and matter, in order to provide another source of particles messenger to test the BdHN model and the νs emission.

In App. (F) are reported all the calculations I have done in order to derive the relation between the momentum of a photon in the *rest frame* of the emitting electrons (which is moving in an external electromagnetic field), with the photon momentum received by an observer at rest at infinity, *laboratory frame*.

In App. (G), I write the same set of equations I have derived in Ch. (4), but for other configurations of the electric and magnetic fields: parallel fields and $\vec{E} \cdot \vec{B} \neq 0$, namely when the fields vectors form an angle $0 < \theta < \frac{\pi}{2}$.

Finally, in App. (H), I want also to show the preliminary work I have done about the magnetic field screening process [1]. The principal differences between the approach in this appendix and the correct one in Ch. (4) are that in this early work: 1) I did not study the entire motion of the particles and I set a fixed *pitch angles* for the particles; 2) because of the point 1), I considered only high energy photons; 3) the considered pair production rate does not take into account the presence of the electric field and the different director cosines of the photons (this assumption is still related to the point 1)); 4) the equation for the magnetic field screening has a different form compared to the one derived in Ch. (4), since it does not take into account the different components of the particles velocity and it is based on the assumption that the induced magnetic field should depends by the total magnetic field itself.
Notwithstanding the analytical formulation for the screening process described in Ch. (4) (and related appendices) is the correct one, since it is more precise and complete than the one analyzed in this appendix, this early approach has been useful even to study this mechanism, to a better comprehension of it and its feasibility.

[1] Presented at the "SIF Congress" in L'Aquila (September 2019) and at the "30th Texas Symposium" in Portsmouth (December 2019)

Appendix A

Pions production cross sections at low protons energy

In this appendix we describe the differential cross sections for pions production $(d\sigma/dE)_{lab}$ (where the subscript *lab* refers to the laboratory frame) for the prodution of the three types of mesons $\left(\pi^0,\ \pi^+,\ \pi^-\right)$ proposed in [25]. In this paper, they give a parameterization for the production of the three mesons for different laboratory kinetic energy of the protons T_{lab}. They consider two regions of T_{lab}: $0.3 \leq T_{lab} \leq 2$ GeV and $2 \leq T_{lab} \leq 50$ GeV. We use this parameterization of the differential cross-section for π^0, π^+ and π^- in Sec. (3.2.2) for the derivation of the neutrinos and photons spectra.

A.1 Differential cross-section for π^0

For the laboratory kinetic energy of protons in the range $0.3 \leq T_{lab} \leq 2$ GeV, the neutral pion spectral distribution can be represented by

$$F_2 = A_1\ T_\pi^{A_2} + A_3\ T_{lab}^{A_4}, \tag{A.1}$$

$$F_1 = \exp\left(A_5 + \frac{A_6}{\sqrt{T_{lab}}} + A_7\ T_{lab}^{A_8} + A_9\ T_\pi^{A_{10}} + A_{11}\ T_\pi^{A_{12}}\right), \tag{A.2}$$

$$\left(\frac{d\sigma}{dE}\right)_{lab} = \left[A_{13}\ \frac{F_1}{F_2} + A_{14}\ \exp\left(A_{16}\ \sqrt{T_\pi} + A_{17}\ T_\pi^{A_{18}}\ T_{lab}^{A_{19}}\right)\right]\ T_\pi^{A_{15}}, \tag{A.3}$$

where the constants A_i are given in Tab. (A.1).
For $2 \leq T_{lab} \leq 50$ GeV, it assumes the form

$$F_2 = B_1\ T_\pi^{B_2} + B_3\ T_{lab}^{B_4}, \tag{A.4}$$

$$F_1 = \exp\left[B_5 + \frac{B_6}{\sqrt{T_{lab}}} + B_7\ T_{lab}^{B_8} + B_9\ T_\pi^{B_{10}} + B_{11}\ T_\pi^{B_{12}}\right], \tag{A.5}$$

$$\left(\frac{d\sigma}{dE}\right)_{lab} = B_{13}\ T_\pi^{B_{14}} \frac{F_1}{F_2} + B_{15}\ T_\pi^{B_{16}}\ \exp\left(B_{17}\ \sqrt{T_\pi}\right), \tag{A.6}$$

where the constants B_i are given in Tab. (A.2).

Table A.1. Constants for Eq. (A.1).

$A_1 = 6.78 \times 10^{-10}$	$A_8 = -1.75$	$A_{15} = 0.25$
$A_2 = -2.86$	$A_9 = -32.1$	$A_{16} = -39.4$
$A_3 = 1.82 \times 10^{-8}$	$A_{10} = 0.0938$	$A_{17} = 2.88$
$A_4 = -1.92$	$A_{11} = -23.7$	$A_{18} = 0.025$
$A_5 = 22.3$	$A_{12} = 0.0313$	$A_{19} = 0.75$
$A_6 = 0.226$	$A_{13} = 2.5 \times 10^6$	
$A_7 = -0.33$	$A_{14} = 1.38$	

Table A.2. Constants for Eq. (A.4).

$B_1 = 1.3 \times 10^{-10}$	$B_8 = -1.25$	$B_{15} = 60322$
$B_2 = -2.86$	$B_9 = -33.2$	$B_{16} = 1.07$
$B_3 = 4.27 \times 10^{-9}$	$B_{10} = 0.0938$	$B_{17} = -67.5$
$B_4 = -2.4$	$B_{11} = -23.6$	
$B_5 = 22.3$	$B_{12} = 0.0313$	
$B_6 = -1.87$	$B_{13} = 2.5 \times 10^6$	
$B_7 = 1.28$	$B_{14} = 0.25$	

A.2 Differential cross-section for π^+

In this section we give a parameterization for the positive charged pion spectral distribution. In the range of proton kinetic energy $0.3 \leq T_{lab} \leq 2$ GeV, it can be written as

$$F_2 = C_1\, T_\pi^{C_2} + C_3\, T_{lab}^{C_4}, \tag{A.7}$$

$$F_1 = \exp\left[C_5 + \frac{C_6}{\sqrt{T_{lab}}} + C_7\, T_{lab}^{C_8} + C_9\, T_\pi^{C_{10}} + C_{11}\, T_\pi^{C_{12}}\, T_{lab}^{C_{13}} + C_{14}\, \ln(T_{lab})\right], \tag{A.8}$$

$$\left(\frac{d\sigma}{dE}\right)_{lab} = C_{15}\, T_\pi^{C_{16}} \frac{F_1}{F_2} + C_{17} T_\pi^{C_{18}} \exp\left(C_{19}\sqrt{T_\pi} + C_{20}\sqrt{T_{lab}}\right), \tag{A.9}$$

where the constants C_i are given in Tab. (A.3).
For the range $2 \leq T_{lab} \leq 50$ GeV, it assumes the following form

$$F_2 = D_1\, T_\pi^{D_2} + D_3\, T_{lab}^{D_4}, \tag{A.10}$$

$$F_1 = \exp\left(D_5 + \frac{D_6}{\sqrt{T_{lab}}} + D_7\, T_\pi^{D_8} + D_9\, T_\pi^{D_{10}}\right), \tag{A.11}$$

$$\left(\frac{d\sigma}{dE}\right)_{lab} = D_{11}\, T_\pi^{D_{12}} \frac{F_1}{F_2} + D_{13}\, T_\pi^{D_{14}} \exp\left(D_{15}\sqrt{T_\pi} + D_{16}\, T_{lab}^{D_{17}}\right), \tag{A.12}$$

where the constants D_i are given in Tab. (A.4).

Table A.3. Constants for Eq. (A.7).

$C_1 = 2.2 \times 10^{-8}$	$C_8 = -1.75$	$C_{15} = 2.5 \times 10^6$
$C_2 = -2.7$	$C_9 = -29.4$	$C_{16} = 0.25$
$C_3 = 4.22 \times 10^{-7}$	$C_{10} = 0.0938$	$C_{17} = 976$
$C_4 = -1.88$	$C_{11} = -24.4$	$C_{18} = 2.3$
$C_5 = 22.3$	$C_{12} = 0.0312$	$C_{19} = -46$
$C_6 = 1.98$	$C_{13} = 0.0389$	$C_{20} = -0.989$
$C_7 = -0.28$	$C_{14} = 1.78$	

Table A.4. Constants for Eq. (A.10).

$D_1 = 4.5 \times 10^{-11}$	$D_7 = -35.3$	$D_{13} = 60322$
$D_2 = -2.98$	$D_8 = 0.0938$	$D_{14} = 1.18$
$D_3 = 1.18 \times 10^{-9}$	$D_9 = -22.5$	$D_{15} = -72.2$
$D_4 = -2.55$	$D_{10} = 0.0313$	$D_{16} = 0.941$
$D_5 = 22.3$	$D_{11} = 2.5 \times 10^6$	$D_{17} = 0.1$
$D_6 = -0.765$	$D_{12} = 0.25$	

A.3 Differential cross-section for π^-

Finally, here we report the parameterization for the negative charged pion spectral distribution. In the range $0.3 \leq T_{lab} \leq 2$ GeV it can be written as

$$F_2 = G_1\, T_\pi^{G_2} + G_3\, T_{lab}^{G_4}, \tag{A.13}$$

$$F_1 = \exp\left(G_5 + \frac{G_6}{\sqrt{T_{lab}}} + G_7\, T_\pi^{G_8} + G_9\, T_\pi^{G_{10}}\right), \tag{A.14}$$

$$\left(\frac{d\sigma}{dE}\right)_{lab} = T_\pi^{G_{11}} \left[G_{12}\frac{F_1}{F_2} + G_{13} \exp\left(G_{14}\ \sqrt{T_\pi}\right)\right], \tag{A.15}$$

where the constants G_i are printed in Tab. (A.5).
While in the range $2 \leq T_{lab} \leq 50$ GeV, it can be written as

$$F_2 = H_1\, T_\pi^{H_2} + H_3\, T_{lab}^{H_4} \tag{A.16}$$

$$F_1 = \exp\left(H_5 + \frac{H_6}{\sqrt{T_{lab}}} + H_7\, T_\pi^{H_8} + H_9\, T_\pi^{H_{10}}\right), \tag{A.17}$$

$$\left(\frac{d\sigma}{dE}\right)_{lab} = H_{11}\, T_\pi^{H_{12}}\, \frac{F_1}{F_2} + H_{13}\, T_\pi^{H_{14}} \exp\left(H_{15}\ \sqrt{T_\pi} + H_{16}\, T_{lab}^{H_{17}}\right), \tag{A.18}$$

where the constants H_i are printed in Tab. (A.6).

Table A.5. Constants for Eq. (A.13).

$G_1 = 1.06 \times 10^{-9}$	$G_6 = -1.5$	$G_{11} = 0.25$
$G_2 = -2.8$	$G_7 = -30.5$	$G_{12} = 2.5 \times 10^6$
$G_3 = 3.7 \times 10^{-8}$	$G_8 = 0.0938$	$G_{13} = 7.96$
$G_4 = -1.89$	$G_9 = -24.6$	$G_{14} = -49.5$
$G_5 = 22.3$	$G_{10} = 0.0313$	

Table A.6. Constants for Eq. (A.16).

$H_1 = 2.39 \times 10^{-10}$	$H_7 = -31.3$	$H_{13} = 60322$
$H_2 = -2.8$	$H_8 = 0.0938$	$H_{14} = 1.1$
$H_3 = 1.14 \times 10^{-8}$	$H_9 = -24.9$	$H_{15} = -65.9$
$H_4 = -2.3$	$H_{10} = 0.0313$	$H_{16} = -9.39$
$H_5 = 22.3$	$H_{11} = 2.5 \times 10^{6}$	$H_{17} = -1.25$
$H_6 = -2.23$	$H_{12} = 0.25$	

A.4 Total inclusive cross-sections

From the previous sections can be derived the total inclusive cross-sections, which assume the following form:

$$\sigma_{\pi^0} = \left(0.007 + 0.1\frac{\ln\left(T_{lab}\right)}{T_{lab}} + \frac{0.3}{T_{lab}^2}\right)^{-1}, \tag{A.19}$$

for the neutral pion;

$$\sigma_{\pi^+} = \left(0.00717 + 0.0652\frac{\ln\left(T_{lab}\right)}{T_{lab}} + \frac{0.162}{T_{lab}^2}\right)^{-1}, \tag{A.20}$$

for positive charged pions;

$$\sigma_{\pi^-} = \left(0.00456 + \frac{0.0846}{T_{lab}^{0.5}} + \frac{0.577}{T_{lab}^{1.5}}\right)^{-1}, \tag{A.21}$$

for negative charged pions.

Appendix B

Kinematics limits for particles spectra

In this chapter we derive the kinematic limits that appear in the extremes of the formula for the calculations of the particles spectra emerging from the pp interaction analyzed in Ch. (3) (see Sec. (3.2.2)). We need to derive the maximum and minimum pion energy, $E_\pi^{max}(E_a)$ and $E_\pi^{min}(E_a)$ (as a function of the specific particle energy E_a), for the three type of particles created in the process, namely γ, $\nu_{\mu^{(1)}}$ and $\nu_{\mu^{(2)}}$ (since the limits for $\nu_{\mu^{(2)}}$ and ν_e can be assumed as equal).

The pp interaction that we are considering occurs (in the laboratory frame "*lab*") between an accelerated proton (with energy E_1 and momentum $\vec{p}_1$) and a proton at rest (with energy $E_2 = m_p c^2$ and momentum $\vec{p}_2 = 0$), which produces a pion and another particles: $p + p \longrightarrow \pi + X$, where X it's a combination of two protons or one proton and one neutron [1]. We take into consideration only the pion, which decay in $\pi \to \mu\nu_{\mu^{(1)}}$, and, consequently, $\mu \to e\nu_{\mu^{(2)}}\nu_e$.

In the next section we derive the pion energy limits as a function of the interacting proton energy E_p, while in the successive sections, we derive the lower limit of the pion energy as a function of the different daughter particles energy.

B.1 Pion energy limits

In order to derive the energy limits of the pion, we move from the *lab* frame (where one of the proton is at rest) to the C.M. frame [2]. The *invariant mass* of the process is (1 and 2 are the two colliding protons; 3 and 4 the two emerging particles)

$$s = \left(E_1^* + E_2^*\right)^2 = \left(E_1 + m_2c^2\right)^2 - |\vec{p}_1|^2c^2 = 2m_2c^2E_1 + m_1^2c^4 + m_2^2c^4. \tag{B.1}$$

The momentum conservation $\vec{p_1^*} + \vec{p_2^*} = 0 \Longrightarrow p_1^* = p_2^* \equiv p^*$. Expressing E_1^* and E_2^* as $\sqrt{m_1^2c^4 + p*^2c^2}$ (since $m_1 = m_2$), replacing in Eq. (B.1) and solving for p^* as a function of s, one obtains the momentum in the C.M frame for the interacting particles

$$p_i^*c = \frac{1}{2\sqrt{s}}\sqrt{\left[s - (m_1c^2 - m_2c^2)^2\right]\left[s - (m_1c^2 + m_2c^2)^2\right]}. \tag{B.2}$$

From the conservation of momentum of the emerging particles, $\vec{p_3^*} + \vec{p_4^*} = 0$ and from the *invariant mass* $s = \left(E_3^* + E_4^*\right)^2$, one obtains the final momentum, in the C.M. frame, for the emerging particles

$$p_f^*c = \frac{1}{2\sqrt{s}}\sqrt{\left[s - (m_3c^2 - m_4c^2)^2\right]\left[s - (m_3c^2 + m_4c^2)^2\right]}. \tag{B.3}$$

[1] For simplicity, here we consider that the proton and the neutron has the same mass.
[2] The quantities in the C.M. frame are denoted with an asterisk or with the subscript *C.M.*

[3] At this point, we express the energy of one daughter particle in the laboratory frame performing the Lorentz transformation:

$$E_3 = \gamma_{CM}\left(E_3^* + \beta_{CM}|\vec{p}_3^*|\cos(\theta^*)\right), \tag{B.4}$$

where θ^* is the angle between the particle 3 and the direction of the collision (that we assume occurs in the $z-$direction). The value of the gamma factor of the C.M. can be derived from the conservation of energy and the Lorentz transformation between the *lab* frame and the C.M. frame

$$E_1 + E_2 = E_1 + m_2c^2 = \gamma_{CM}\left(E_1^* + E_2^* + \beta_{CM}\left(p_{1,z} + p_{2,z}\right)\right) = \gamma_{CM}\left(E_1^* + E_2^*\right) = \gamma_{CM}\sqrt{s}, \tag{B.5}$$

where $p_{1,z}$ ($p_{2,z}$) is the absolute value of $\vec{p}_{1,z}$ ($\vec{p}_{2,z}$). The particles momentum disappear since $\vec{p}_{1,z} = -\vec{p}_{2,z}$, namely they are emitted in opposite direction in the C.M. frame. Then

$$\gamma_{CM} = \frac{E_1 + m_2c^2}{\sqrt{s}}; \tag{B.6a}$$

$$\beta_{CM} = \sqrt{1 - \frac{1}{\gamma_{CM}^2}} = \frac{\sqrt{(E_1 + m_2c^2)^2 - s}}{E_1 + m_2c^2}. \tag{B.6b}$$

If we assume that the particle 3 is the pion, we have that the maximum and minimum value of the pion energy, in the *lab* frame, are given by

$$E_\pi^{max}(E_p) = \gamma_{CM}(E_p)\left[E_\pi^*(E_p) + \beta_{CM}(E_p)\, p_\pi^*(E_p)\right] \tag{B.7a}$$

$$E_\pi^{min}(E_p) = \gamma_{CM}(E_p)\left[E_\pi^*(E_p) - \beta_{CM}(E_p)p_\pi^*(E_p)\right], \tag{B.7b}$$

with γ_{CM} and β_{CM} from Eqs. (B.6), p_π^* from Eq. (B.3) and $E_\pi^*(E_p) = \sqrt{m_\pi^2c^4 + p_\pi^*(E_p)^2c^2}$.

B.2 Kinematic limits for γ

In this section we consider the neutral pion decay $\pi^0 \to \gamma\gamma$. In order to derive the kinematic limits for the pion energy as a function of the photon energy, we move to the pion rest frame (where the pion is at rest). The Lorentz factor of the transformation is

$$\gamma_{CM} = \frac{E_{\pi^0}}{m_{\pi^0}c^2}, \quad \beta_{CM} = \sqrt{1 - \frac{m_{\pi^0}^2c^4}{E_{\pi^0}^2}}. \tag{B.8}$$

From the conservation of energy we have

$$\begin{cases} E_{\pi^0}^* = m_{\pi^0}c^2 = E_1^* + E_2^* \\ 0 = \vec{p}_1^* + \vec{p}_2^*, \end{cases} \tag{B.9}$$

(where the subscripts 1 and 2 refer to the emerging photons) from which we derive that

$$E_\gamma^* \equiv E_1^* = E_2^* = \frac{m_{\pi^0}c^2}{2}, \tag{B.10}$$

since the two photons share the pion energy, and $\vec{p}_1^* = -\vec{p}_2^*$.
The photon energy in the *lab* frame is given by the Lorentz transformation

$$E_\gamma = \gamma_{CM}\left(E_\gamma^* + \beta_{CM}\left|\vec{p}_\gamma^*\right|c\,\cos\left(\theta^*\right)\right), \tag{B.11}$$

[3] Looking at the scheme of the interaction in Eq. (3.1), we see that the emerging particles from the pp interaction is a combination of nucleons plus a pion. We write the finale state as $\pi + X$, where X refers to the combination of baryons. Since we have assumed the same mass for proton and neutron, in the calculations, we consider $m_X = 2m_pc^2$.

where θ^* is the angle between the two photons in the C.M. frame, that is $\theta^* = \pi$. Then, inserting these relations in Eq. (B.11), we get

$$E_\gamma = \frac{E_{\pi^0}}{2}\left(1 \mp \sqrt{1 - \frac{m_{\pi^0}^2 c^4}{E_{\pi^0}^2}}\right). \tag{B.12}$$

From Eq. (B.12), we can derive the pion energy as a function of the photon energy $E_{\pi^0}\left(E_\gamma\right)$:

$$E_{\pi^0}\left(E_\gamma\right) = \left(2E_\gamma + \frac{m_{\pi^0}^2 c^4}{2E_\gamma}\right) \times \frac{1}{2} = E_\gamma + \frac{m_{\pi^0}^2 c^4}{4E_\gamma}, \tag{B.13}$$

where we inserted the factor $\frac{1}{2}$ since the pion energy is shared between the two photons.
The same results can be obtained writing the *invariant mass* before and after the decay

$$\sqrt{s_i} = m_{\pi^0} = \sqrt{s_f} = \sqrt{(E_1 + E_2)^2 - \left|\vec{p}_1 + \vec{p}_2\right|^2 c^2} = \sqrt{2E_1 E_2\,(1 - \cos(\theta))}, \tag{B.14}$$

where E_1 and E_2 are the energies of the two photons in the final state and θ is the angle between the two photons. Using the relation $\sin^2(\frac{\theta}{2}) = \frac{1-\cos(\theta)}{2}$ and considering that $E_\pi = E_1 + E_2$, we can solve Eq. (B.14) for E_{π^0} as a function of the photon energy

$$E_{\pi^0}\left(E_\gamma\right) = E_\gamma + \frac{m_{\pi^0}^2 c^4}{4E_\gamma \sin^2\left(\frac{\theta}{2}\right)}. \tag{B.15}$$

The minimum value of Eq. (B.15) is obtained when $\theta = \pi$. The we get

$$E_{\pi^0}^{min}\left(E_\gamma\right) = E_\gamma + \frac{m_{\pi^0}^2 c^4}{4E_\gamma}. \tag{B.16}$$

B.3 Kinematic limits for $\nu_{\mu^{(1)}}$ and μ

B.3.1 For $E_\pi\left(E_{\nu_{\mu^{(1)}}}\right)$

Let's now derive the minimum limit for the pion energy as a function of $E_{\nu_{\mu^{(1)}}}$ (the muonic neutrino from direct pion decay $\pi \longrightarrow \mu\nu_{\mu^{(1)}}$). From the conservation of momentum we get

$$0 = \vec{p_\mu^*} + \vec{p_\nu^*} \Longrightarrow \vec{p_\mu^*} = -\vec{p_\nu^*} \Longrightarrow p_\mu^*\, c = p_\nu^*\, c \equiv p^*\, c = E_\nu^*. \tag{B.17}$$

The equation for the *invariant mass* says that (where the quantities with an asterisk refer to C.M. frame)

$$m_\pi c^2 = \sqrt{s} = E_\mu^* + E_\nu^* = \sqrt{m_\mu^2 c^4 + p^{*2} c^2} + p^* c. \tag{B.18}$$

Solving this equation for p^*c, we get the muon and neutrino energies in the pion rest frame

$$E_\mu^* = \frac{m_\mu^2 c^4 + m_\pi^2 c^4}{2\, m_\pi c^2}, \tag{B.19a}$$

$$E_\nu^* = \frac{m_\pi^2 c^4 - m_\mu^2 c^4}{2\, m_\pi c^2} = \frac{m_\pi c^2}{2}\,(1 - r_\pi) = \frac{\lambda\, m_\pi c^2}{2}, \tag{B.19b}$$

where $r_\pi = m_\mu^2 c^4 / m_\pi^2 c^4$ and $\lambda = 1 - r_\pi$. The Lorentz factor of the C.M. here is

$$\gamma_{CM} = \frac{E_\pi}{m_\pi c^2}, \quad \beta_{CM} = \frac{|\vec{p}_\pi| c}{E_\pi}. \tag{B.20}$$

Then, the neutrino energy in the *lab* frame is given by the Lorentz transformation

$$E_{\nu_\mu} = \gamma_{CM}\left[E_\nu^* + \beta_{CM} p_\nu^* c\cos(\theta^*)\right] = \frac{\lambda}{2}\left[E_\pi + \sqrt{E_\pi^2 - m_\pi^2 c^4}\cos(\theta^*)\right]. \tag{B.21}$$

The maximum value for the neutrino energy, E_ν^{max}, is given by Eq. (B.21), with $\theta^* = 0$. Solving Eq. (B.21) for E_π, one gets

$$E_\pi^{min}\left(E_{\nu_{\mu(1)}}\right) = \frac{E_{\nu_{\mu(1)}}}{\lambda} + \frac{m_\pi^2 c^4}{E_{\nu_{\mu(1)}}}\frac{\lambda}{4}. \tag{B.22}$$

Then, the energetic limits for the pion (as a function of the neutrino energy), for the calculation of the spectrum of the direct muonic neutrino $\Phi_{\pi\to\mu\nu_\mu}$, are $E_\pi^{min}\left(E_{\nu_{\mu(1)}}\right) \le E_\pi \le E_\pi^{max}(E_p)$, with E_π^{min} given by Eq. (B.22), while E_π^{max} by Eq. (B.7a).

B.3.2 For $E_\pi\left(E_\mu\right)$

Following the same procedure applied for $E_{\nu_{\mu(1)}}$ in the previous section, one gets the following expression for the minimum energy of the pion as a function of the muon energy:

$$E_\pi^{1,2} = \frac{E_\mu\,(2-\lambda) \pm \sqrt{E_\mu^2 - m_\pi^2 c^4 + m_\pi^2 c^4 \lambda}}{2\,(1-\lambda)}. \tag{B.23}$$

From this expression, we derive that E_μ should be greater than $m_\pi c^2\sqrt{1-\lambda} \approx 105$ MeV, namely the muon mass. This condition is satisfied since the muon is not produced at rest.
We need to choose the right solution in Eq. (B.23). If we consider the numerator of Eq. (B.23), we have the condition

$$E_\mu\,(2-\lambda) \pm \sqrt{E_\mu^2 - m_\pi^2\,c^4\,(1-\lambda)} \lesseqgtr 0. \tag{B.24}$$

After some simple analytical passages, we get

$$E_\mu^2 > -\frac{m_\pi^2\,c^4}{4}\frac{1-\lambda}{(2-\lambda)^2 - 1}, \tag{B.25}$$

and, then, since we are looking for the lower energetic limit, the right solution is

$$E_\mu\,(2-\lambda) > \sqrt{E_\mu^2 - m_\pi^2\,c^4\,(1-\lambda)}. \tag{B.26}$$

Thus, $E_\pi^{min}(E_\mu)$ is

$$E_\pi^{min}\left(E_\mu\right) = \frac{E_\mu\,(2-\lambda) - \sqrt{E_\mu^2 - m_\pi^2 c^4 + m_\pi^2 c^4 \lambda}}{2\,(1-\lambda)}. \tag{B.27}$$

Then, in this case, $E_\pi^{min}\left(E_\mu\right) \le E_\pi \le E_\pi^{max}(E_p)$, with E_π^{min} given by Eq. (B.27) and, again, $E_\pi^{max}\left(E_p\right)$ by Eq. (B.7a).

B.4 Muon energy limits

The procedure to get the expression for the minimum energy of the muon as a function of the particle energy emerging from its decay (e, ν_μ, ν_e) $E_\mu\,(E_a)$ is a little bit longer than the previous cases.

We start from the conservation of moments: $p_\mu = p_e + p_{\nu_\mu} + p_{\nu_e}$. Let's define the four variables

$$s = P_\mu^2 = m_\mu^2 c^4, \tag{B.28a}$$

$$s_1 = \left(P_\mu - P_e\right)^2 = \left(P_{\nu_\mu} + P_{\nu_e}\right)^2, \tag{B.28b}$$

$$s_2 = \left(P_\mu - P_{\nu_\mu}\right)^2 = \left(P_{\nu_e} + P_e\right)^2, \tag{B.28c}$$

$$s_3 = \left(P_\mu - P_{\nu_e}\right)^2 = \left(P_e + P_{\nu_\mu}\right)^2, \tag{B.28d}$$

where the P_a are the four-momentum of each particle.
The four variables are related as follow:

$$p_1 + p_2 + p_3 = s + m_e^2 c^4. \tag{B.29}$$

In the frame of the muon $\left(P_\mu = \left(m_\mu c^2, 0, 0, 0\right)\right)$, we can write

$$s_1 = P_\mu^2 + P_e^2 - 2P_\mu \cdot P_e = m_\mu^2 c^4 + m_e^2 c^4 - 2m_\mu c^2 E_e^*. \tag{B.30}$$

Since $E_e^* \geq m_e c^2$, the maximum of s_1 is $\left(m_\mu c^2 - m_e c^2\right)^2$. In order to get the minimum of s_1, since the four s_i are invariant, we evaluate s_1 in the rest frame of the system $\left(\nu_\mu, \nu_e\right)$:

$$s_1 = \left(P_{\nu_\mu} + P_{\nu_e}\right)^2 = \left(\hat{E}_{\nu_\mu} + \hat{E}_{\nu_e}\right)^2 \geq \left(m_{\nu_\mu} c^2 + m_{\nu_e} c^2\right)^2 = 0, \tag{B.31}$$

and similarly for the other variables. In the end, we get the following limits

$$s_1 \in \left[0; \left(m_\mu c^2 - m_e c^2\right)^2\right], \tag{B.32a}$$

$$s_2 \in \left[m_e c^2; m_\mu c^2\right], \tag{B.32b}$$

$$s_3 \in \left[m_e c^2; m_\mu c^2\right]. \tag{B.32c}$$

Now we find the limits for s_2 at a fixed s_1. Let's move in the rest frame of the two neutrinos (we indicate the variables in this frame with an hat). In the rest frame of ν_μ and ν_e (defined as $\vec{\hat{p}}_{\nu_\mu} = -\vec{\hat{p}}_{\nu_e} \implies \hat{p}_{\nu_\mu} = \hat{p}_e$), we have

$$s_1 = \left(P_\mu - P_e\right)^2 = \left(\hat{E}_\mu - \hat{E}_e\right)^2 = \left(\sqrt{m_\mu^2 c^4 + \hat{p}_e^2 c^2} - \sqrt{m_e^2 c^4 + \hat{p}_e^2 c^2}\right)^2. \tag{B.33}$$

Solving Eq. (B.33) for $\hat{p}_e c$, one gets

$$\hat{p}_e c = \frac{1}{2\sqrt{s_1}} \lambda^{1/2}\left(s_1; m_\mu^2 c^4; m_e^2 c^4\right), \tag{B.34}$$

with $\lambda(x; y; z) = x^2 + y^2 + z^2 - 2xy - 2yz - 2xz$. From $s_1 = \left(P_{\nu_\mu} + P_{\nu_e}\right)^2 = \left(\hat{E}_{\nu_\mu} - \hat{E}_{\nu_e}\right)^2$ we obtain

$$\hat{p}_{\nu_\mu} c = \hat{p}_{\nu_e} c = \frac{1}{2\sqrt{s_1}} \lambda^{1/2}\left(s_1; m_{\nu_\mu}^2 c^4; m_{\nu_e}^2 c^4\right) = \frac{1}{2\sqrt{s_1}} \lambda^{1/2}(s_1; 0; 0) = \frac{\sqrt{s_1}}{2}. \tag{B.35}$$

The same procedure can be applied to get the maximum and minimum value of s_2. From the definition we have:

$$s_2 = \left(P_e + P_{\nu_e}\right)^2 = P_e^2 + P_{\nu_e}^2 + 2P_e \cdot P_{\nu_e} = m_e^2 c^4 + 2\left(\hat{E}_e \hat{E}_{\nu_e} - \hat{p}_e \hat{p}_{\nu_e} \cos(\alpha)\right). \tag{B.36}$$

Using the value of $\hat{p}_e$ and $\hat{p}_{\nu_e}$ derived in Eq. (B.34) and Eq. (B.35), respectively, we can derive the formula for $\hat{E}_e$ and $\hat{E}_{\nu_e}$. Substituting in Eq. (B.36), we get the expression for the maximum and minimum value of s_2:

$$s_{2,\pm} = m_e^2 c^4 + \frac{1}{2}\left[\left(s - s_1 - m_e^2 c^4\right) \pm \lambda^{1/2}\left(s_1, s, m_e^2 c^4\right)\right]. \tag{B.37}$$

The same procedure can be applied to s_3, in order to find its maximum and minimum value. The series of these maximum and minimum values of the three variables s_1, s_2 and s_3, constitutes the *Dalitz plot*, namely the energy range available for the daughter particles from the analyzed process.

B.4.1 Kinematic limits for daughter particles of muon decay

From the results of the previous section, we have

$$s_1 = m_\mu^2 c^4 + m_e^2 c^4 - 2 m_\mu c^2 E_e^*,$$

and then we get

$$E_e^* = \frac{m_\mu^2 c^4 + m_e^2 c^4 - s_1}{2\, m_\mu c^2}. \tag{B.38}$$

The maximum value of E_e^* occurs when s_1 is minimum, namely $s_1 = 0$. Then we have

$$E_e^{*max} = \frac{m_\mu^2 c^4 + m_e^2 c^4}{2\, m_\mu c^2} = \frac{m_\mu c^2}{2}\left(1 + r_\mu\right), \tag{B.39}$$

with $r_\mu = m_e^2 c^4 / m_\mu^2 c^4$, and

$$p_e^{*max} = \frac{m_\mu c^2}{2}\left(1 - r_\mu\right). \tag{B.40}$$

We also have that $p^{*max}_{\nu_\mu} c = p^{*max}_{\nu_e} c = E^{*max}_{\nu_\mu} = E^{*max}_{\nu_e} = m_\mu c^2/2$.
Let's derive the minimum energy of the muon as a function of the daughter particles energy. Being $\gamma_{CM} = E_\mu / m_\mu c^2$ and $\beta_{CM} = |\vec{p}_\mu| c / E_\mu$ and from the expression of the electron energy in the *lab* frame

$$E_e = \gamma_{CM}\left[E_e^* + \beta_{CM} |\vec{p}_e| \cos(\theta^*)\right], \tag{B.41}$$

as we already done before, we can derive $E_\mu\,(E_e)$ (considering again $\theta^* = 0$):

$$E_\mu^{min}\,(E_e) = \frac{E_e\left(1 + r_\mu\right) - \left(1 - r_\mu\right)\sqrt{E_e^2 - m_e^2 c^4}}{2\, r_\mu}. \tag{B.42}$$

Applying the same procedure for the ν_μ and ν_e, we get

$$E_\mu^{min}\left(E_{\nu_\mu}\right) = E_{\nu_\mu} + \frac{m_\mu^2 c^4}{4\, E_{\nu_\mu}}, \tag{B.43a}$$

$$E_\mu^{min}\,(E_{\nu_e}) = E_{\nu_e} + \frac{m_\mu^2 c^4}{4\, E_{\nu_e}}. \tag{B.43b}$$

A this point, we need the expression of E_π as a function of the energy of the three daughter particles. The energy range of E_μ is: $E_{min}\,(E_a) \leq E_\mu \leq E_\mu^{\max}\,(E_\pi) = E_\pi^{max}\left(E_p\right)$ (since the maximum energy the muon can take is the pion energy itself); instead for the pion: $E_\pi^{min}\left(E_p\right) \leq E_\pi \leq E_\pi^{max}\left(E_p\right)$. Then, we can extend (see Fig. (B.1)) the minimum limit of E_π, as a function of the daughter particles energy from μ-decay, as $E^{min}\,(E_a) \leq E_\pi \leq E_\pi^{max}\left(E_p\right)$, with $E^{min}(E_a)$ given by Eq. (B.42) or Eq. (B.43a) or Eq. (B.43b).

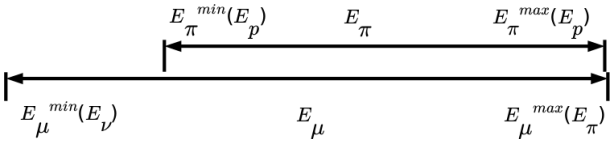

Figure B.1. Extension of the pion and muon energy ranges. The pion energy range depends on the proton energy. The maximum value of the muon is the pion energy, while the minimum is written as a function of the daughter particles from μ-decay (see Eqs. (B.42) (B.43)). Since we are looking for a relation between the pion energy and the daughter particles energies from μ-decay, we can extend the E_π^{min} to $E_\mu^{min}\,(E_a)$.

Appendix C

Kelner *et al.* particles spectra for high energy protons

In this chapter we report the analytical parameterization of the particles spectra, emerging from pp interaction via the decay of the mesons π (for γ and νs) and η (for γ), derived in [70], that we use for the case of high energy interacting protons in Sec. (3.3) and App. (D).
In order to calculate the spectra of the particles emerging from our physical setup, we need to use Eq. (3.21), where the function $F_a\left(x,\ E_p\right)$ (where a refers to each specific particle and $x = E_a/E_p$) are given by [70] and we report them here. These functions represent the number of the specific particles in the interval $(x,\ x + dx)$ and they derive them as the results of the simulations, for the energy distributions of π and η mesons, by the `SIBYLL` code.

C.1 Analytical parameterization for photons

The total spectrum of photons calculated from the decay of π^0 and η mesons in two γ can be represents by the following analytical formula

$$\begin{aligned} F_\gamma\left(x,\ E_p\right) &= B_\gamma \frac{d}{dx}\left[\ln(x)\left(\frac{1-x^{\beta_\gamma}}{1+k_\gamma x^{\beta_\gamma}\left(1-x^{\beta_\gamma}\right)}\right)^4\right] \\ &= B_\gamma \frac{\ln(x)}{x}\left(\frac{1-x^{\beta_\gamma}}{1+k_\gamma x^{\beta_\gamma}\left(1-x^{\beta_\gamma}\right)}\right)^4\left[\frac{1}{\ln(x)} - \frac{4\,\beta_\gamma\, x^{\beta_\gamma}}{1-x^{\beta_\gamma}} - \frac{4\,k_\gamma\,\beta_\gamma x^{\beta_\gamma}\left(1-2\,x^{\beta_\gamma}\right)}{1+k_\gamma x^{\beta_\gamma}\left(1-x^{\beta_\gamma}\right)}\right], \end{aligned} \tag{C.1}$$

where the parameters $B_\gamma,\ \beta_\gamma,\ k_\gamma$ (which depend on the proton energy) are well represented, in the proton energy range 0.1 TeV$\leq E_p \leq 10^5$ TeV, by

$$B_\gamma = 1.30 + 0.14\ L + 0.011\ L^2, \tag{C.2}$$

$$\beta_\gamma = \frac{1}{1.79 + 0.11\ L + 0.008\ L^2}, \tag{C.3}$$

$$k_\gamma = \frac{1}{0.801 + 0.04\ L + 0.014\ L^2}, \tag{C.4}$$

where $L = \ln(E_p/1\ \text{TeV})$.
This formula represents the decay of $\pi^0 \longrightarrow 2\gamma$ and the different decays of the η meson in $\eta \longrightarrow 2\gamma$ (with probability 39.4%), $\eta \longrightarrow 3\pi^0 \longrightarrow 6\gamma$ (32.5%), $\eta \longrightarrow \pi^+\pi^-\pi^0 \longrightarrow 2\gamma$ (22.6%), and $\eta \longrightarrow \pi^+\pi^-\gamma$ (5%).

C.2 Analytical parameterization for $\nu_{\mu^{(1)}}$ from direct pion decay

The spectrum of muonic neutrino from direct pion decay $\pi \longrightarrow \mu\nu_\mu$ can be described by

$$F_{\nu_{\mu^{(1)}}}\left(x,\ E_p\right) = B^{'}\frac{\ln(y)}{y}\left(\frac{1-y^{\beta^{'}}}{1+k^{'}\,y^{\beta^{'}}\left(1-y^{\beta^{'}}\right)}\right)^4\left[\frac{1}{\ln(y)}-\frac{4\,\beta^{'}\,y^{\beta^{'}}}{1-y^{\beta^{'}}}-\frac{4\,k^{'}\,\beta^{'}\,y^{\beta^{'}}\left(1-2\,y^{\beta^{'}}\right)}{1+k^{'}\,y^{\beta^{'}}\,\left(1-y^{\beta^{'}}\right)}\right], \quad \text{(C.5)}$$

where $x = E_{\nu_\mu}/E_p$, $y = x/0.427$ and

$$B^{'} = 1.75 + 0.204\,L + 0.010\,L^2, \quad \text{(C.6)}$$

$$\beta^{'} = \frac{1}{1.67 + 0.111\,L + 0.0038\,L^2}, \quad \text{(C.7)}$$

$$k^{'} = 1.07 + 0.086\,L + 0.002\,L^2, \quad \text{(C.8)}$$

where $L = \ln(E_p/1\ \text{TeV})$. Because of the kinematic limits of the interaction (see Sec. (3.3.2)), the spectrum has a sharply cut-off at $x = 0.427$.

C.3 Analytical parameterization for $e,\ \nu_e,\ \nu_{\mu^{(2)}}$

The formula from [70] for the description of the spectra of electrons, electronic neutrino and muonic neutrino (all of them from muon decay) are well represented by the following formula (where x is, respectively, $E_e/E_p,\ E_{\nu_e}/E_p,\ E_{\nu_{\mu^{(2)}}}/E_p$):

$$F_e(x,\ E_p) = B_e\frac{\left(1+k_e\ (\ln(x))^2\right)^3}{x\,(1+0.3/x^{\beta_e})}\,(-\ln(x))^5\,, \quad \text{(C.9)}$$

where the parameters $B_e,\ \beta_e,\ k_e$ are given by (where $L = \ln(E_p/1\ \text{TeV})$)

$$B_e = \frac{1}{69.5 + 2.65\,L + 0.3\,L^2}, \quad \text{(C.10)}$$

$$\beta_e = \frac{1}{(0.201 + 0.062\,L + 0.00042\,L^2)^{1/4}}, \quad \text{(C.11)}$$

$$k_e = \frac{0.279 + 0.141\,L + 0.0172\,L^2}{0.3 + (2.3+L)^2}. \quad \text{(C.12)}$$

Appendix D

Neutrinos from Ultra-High-Energy protons

In this chapter we derive the spectra of the daughter particles emerging from pp interaction, as we have done in Ch. (3), when the interacting protons are ultra-relativistics (Ultra-High-Energy protons, UHEps). We consider protons emitted along the BH $\hat{z}-$axis, which are accelerated by the electric field ([135, 136]) to energies $E_p = 10^{21}$ eV (see Fig. (D.1)). In this scheme, the magnetic and the electric field are both oriented along the $\hat{z}-$axis of the BH, but in opposite directions (*anti-parallel* fields). This allow to accelerates protons instead of electrons.

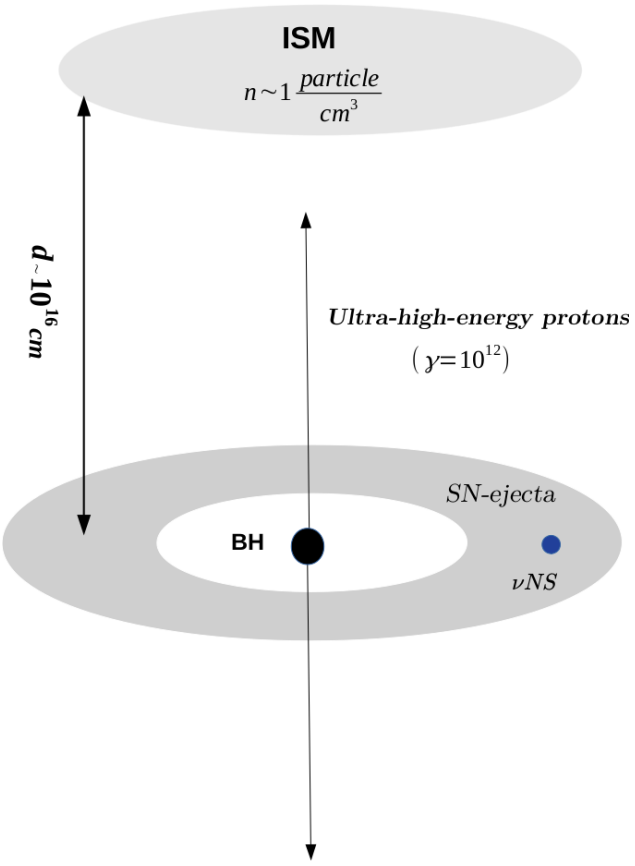

Figure D.1. Interaction scheme for the case of protons emitted along the BH $\hat{z}-$axis, with very small aperture angle, and they are accelerated to energies $E_p = 10^{21}$ eV ($\gamma_p \simeq 10^{12}$), which interact with protons of the ISM (at rest) at a distance of $d = 10^{16}$ cm.

This interaction scheme complete the one analyzed in Ch. (3). There, we have analyzed only the interactions, by accelerated protons, in the equatorial plane of the binary system characteristic of the BdHNe model. Since the protons are emitted in all the directions, here we analyze the case when they are emitted along the BH axis. Since the polar cap of the BH is empty, these protons can escape freely from the BH site without interact with any matter and maintaining their initial energy. The first region of target matter that they find on their path is the interstellar medium (ISM), with an extension of $\Delta L = 10^{17} - 10^{16} = 9 \times 10^{16}$ cm (with respect to the laboratory frame centered on the BH) and volumetric particles number density $n_{ISM} = 1$ particle/cm^3.

The scheme of the process suggests to assume as energy distribution of the interacting protons a δ fucntion, $J_p(E_p) = A\delta\left(E_p - E_p^0\right)$, where $E_p^0 = 10^{21}$ eV. The normalization constant A is chosen in such a way to contain all of these protons and their linear spatially extension in the interaction. The *inner engine* of the BH can accelerates a number of protons $N_p = 1.94 \times 10^{34}$ in a timescale $\tau_{\rm el} \approx 10^{-6}$ s, hence $dN_p/dt \equiv \dot{N}_p \sim N_p/\tau_{\rm el} \approx 2 \times 10^{40}$ particles/s [135, 136].
We consider a single impulsive emission, hence the total number of emitted protons are $N_p = 1.94 \times 10^{34}$. Since the protons can reach that ultra-high-energy E_p^0 only if they are emitted exactly along the $\hat{z}-$axis or with a very small aperture angle, we can assume as negligible the section of the tube (or cone) where the protons are emitted. Consequently, the volume where the interaction occurs can be considered as linear and equal to the extension of the interacting region, namely $\Delta L = 9 \times 10^{16}$ cm. Then, the normalization constant A (which have the dimensions of a linear number density) of $J_p\left(E_p\right)$ can be calculated as

$$A = \frac{N_p}{\Delta L} = \frac{1.94 \times 10^{34}}{9 \times 10^{16}} \approx 2.16 \times 10^{17} \quad \text{cm}^{-1}. \tag{D.1}$$

Then the interacting protons energy distribution $J_p\left(E_p\right)$ has the dimension of cm^{-1}eV^{-1}.

Since the proton energy is $E_p \geq 0.1$ TeV, we can use the parameterization of the spectra of the emerging particles from pp interaction that we used in Sec. (3.3) for the TeV protons (see [70] and App. (C)). But we need to emphasize that we are not sure about the validity of the analytical parameterization for the spectra for interacting protons of this energy, since those formula have been studied under the conditions $0.1 \leq E_p \leq 10^5$ TeV and $x = E_a/E_p \geq 10^{-3}$ (with E_a the energy of the secondary particles). In our case, the second condition is satisfied but not the first one. Then, the results of this chapter can be assumed only as indicative.
In this case, the spectrum $\Phi_a\left(E_a\right)$ given by Eq. (3.21) has the dimension of $[\Phi_a] = \left[\frac{\text{particles}}{\text{cm s erg}}\right]$ and is shown in Fig. (D.2) for γ, $\nu_{\mu^{(1)}}$, $\nu_{\mu^{(2)}}$. For each neutrino, calculating the emissivity integrated over the energy by means of Eq. (3.12), multiplying by: 1) the extension of the ISM region $\Delta L = 9 \times 10^{16}$ cm; 2) the time necessary for the protons to cross ΔL, $\Delta t \simeq \Delta L/c = 3 \times 10^6$ s, we get the total energy emitted in neutrinos, $\mathcal{E}_\nu$, by UHEps interaction through the entire ISM region, which values are shown in Tab. (D.1). In Tab. (D.1) we report also the neutrino luminosity for the last emitting shell of the ISM (see Sec. (3.3.2)), the neutrino maximum energy E_ν (the energy corresponding to the peak of the emissivity) and the neutrino-nucleon cross-section $\sigma_{\nu N}$ for these specific energies (see [32]). Also the maximum energy, the total energy emitted and the luminosity of the last emitting shell for the photons are shown in Tab. (D.1).

As we have done in Sec. (3.4), even in this case we have tried to calculate the horizon distance for each neutrino. We have considered only the IceCube detector, since it is the most efficient and bigger detector (we have adopted the complete mass of the detector, namely 1 Gigaton= 6.022×10^{38} baryons), for these ultra-high-energy neutrino. Due to the very low value of the neutrino luminosity (L_ν in Tab. (D.1)), we got a very low short horizon distance, notwithstanding the neutrino energy and the cross-section are orders of magnitude greater than the cases analyzed in Ch. (3). This lack of efficiency is principally due to the small value of the target particles number density (as happended for the TeV protons in Sec. (3.3)). This suggest that, for these cases, the calculation of the horizon distance (in the way of Eq. (3.27)) maybe is not the proper technique in order to have an estimate for the detectability of these high energy neutrinos.

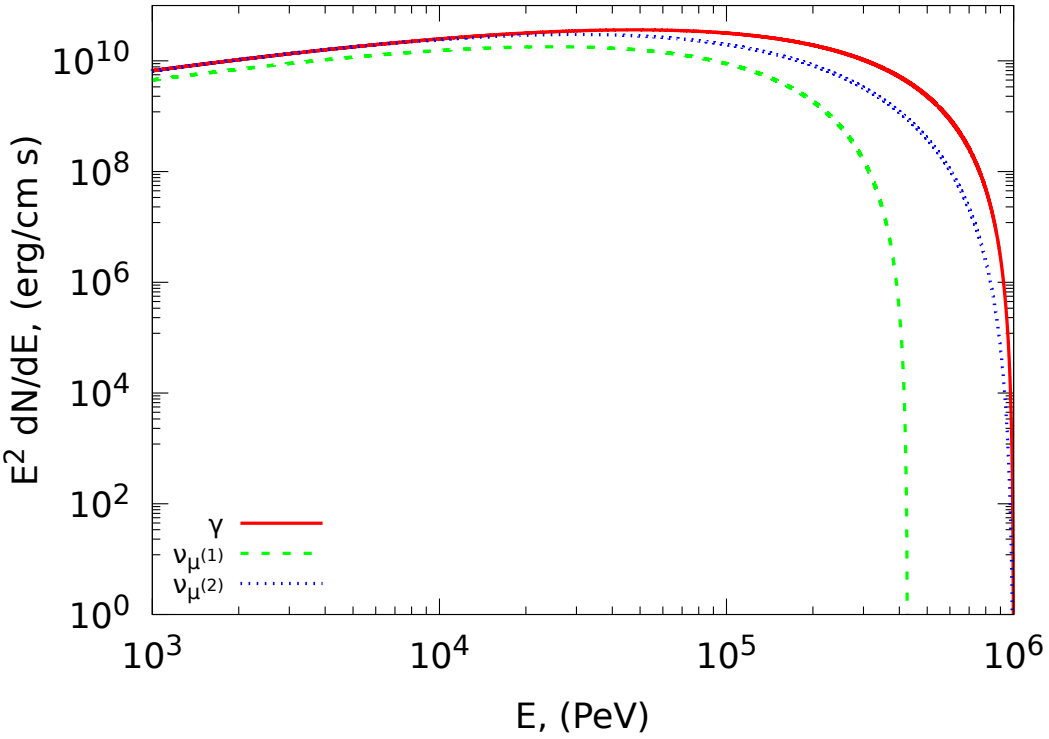

Figure D.2. Spectra of the daughter particles from π^0, $\pi^{\pm}$, $\mu^{\pm}$-decay, created by the interaction between ultra-high-energy protons ($E_p = 10^{21}$ eV) emitted along the BH $\hat{z}$−axis and protons (at rest) of the ISM (with density $n_{ISM} = 1$ particle/cm^3) located at a distance between $10^{16} \leq r \leq 10^{17}$ cm far from the BH site.

Table D.1. Characteristic values for νs and γ from direct pion decay and μ decay, for UHE-protons interacting with the low density region cases of the ISM ($n_{ISM} = 1$ particle/cm^3). For each particle we show: the proper maximum energy $E_{\nu,\gamma}$ (corresponding to the peak of their spectrum), the complete energy emitted in the whole emitting region $\mathcal{E}_{\nu,\gamma}$, the luminosity of the last ISM emitting shell $L_{\nu,\gamma}$ and, only for ν, the values of the neutrino-nucleon cross-section. The values of the cross-section have been kept by [32].

Particle	E_ν	$\mathcal{E}_\nu$	L_ν	$\sigma_{\nu N}$
	(PeV)	(10^{34} erg)	(10^{21} erg/s)	(10^{-31} cm^2)
γ	4.786×10^4	3.687	4.097	
$\nu_{\mu^{(1)}}$	2.478×10^4	1.676	1.862	0.41
$\nu_{\mu^{(2)}}$	3.005×10^4	2.932	3.258	0.41

Appendix E

Photons scattering interaction length

In this appendix we weigh up the possibility to detect photons, by π^0-decay, for the three considered physical setups studied in Sec. (3.2), Sec. (3.3) and App. (D).
The kernel of this chapter concerns the study of the possibility to detect the photons emerging from the pp interaction inside the SN-ejecta (Sec. (3.2)). Since the particles density inside the ejecta is high, the photons can interact with matter and are not free to escape from the creation site. About the other two cases, when the photons are created in the interaction with the ISM by protons with energy $E_p = 10^3,\ 10^{21}$ eV (Sec. (3.3) and App. (D), respectively), the ISM particles number density is too low and, thus, photons are free to escape without interaction and can be detected on Earth.

The possible photon-matter interactions that we consider are: 1) *Photo-meson production*: $\gamma + p \rightarrow h + n\pi$ (where h is an hadron and n the number of produced pions); 2) *Photon pair-production*: $\gamma + p \rightarrow p\ e^+\ e^-$ (Bethe-Heitler process); 3) *Compton scattering*: $\gamma + p \rightarrow \gamma'\ p$ (where γ' is the photon emerging with different energy in comparison with to the interacting one); 4) *Pairs Compton scattering*: $\gamma + e^{\pm} \rightarrow \gamma' + e^{\pm}$. For these interactions, we calculate the interaction length l_{int} defined as $l_{int} = \left(\sigma_{int}\, n_{targ}\right)^{-1}$, where σ_{int} is the cross-section for the specific considered interaction and n_{targ} the number density of the target particles of the medium. Comparing l_{int} with the extension of the specific region of interaction (ejecta or ISM) ΔL, if $l_{int} > \Delta L$ the photon are free to escape and vice versa. In Sec. (E.3) we analyze also the process $\gamma + \gamma \rightarrow e^- e^+$.
For the three setups we have different photons energies:

- for the interaction inside the SN-ejecta, the photon energy decreases during the expansion of the protons shell inside the ejecta, because the protons energy decreases too. We consider the photons emitted at the first radius of the expansion, r_1. At r_1, the maximum photon energy [1] is $E_\gamma^{\max}(r = r_1) = 0.69$ GeV. At greater radii, the maximum photon energy varies between $0.3 \leq E_\gamma < 0.69$ GeV;

- for the case of interacting protons with energy $E_p = 1$ TeV, the maximum value of the photons energy is $E_\gamma^{\max} = 91.62$ GeV;

- for interacting protons of energy $E_p = 10^{21}$ eV, the maximum value of the photons energy is $E_\gamma^{\max} = 47.86$ EeV.

Let's now analyze separately the interactions by photons with protons and pairs.

[1] corresponding to the maximum value of the flux.

E.1 $\gamma - p$ interactions

In this section we analyze the $\gamma - p$ interactions. The *photon pair-production* and the *photomeson production* occur when the energy of the photon (in the proton rest frame) is greater than the threshold energy: $\gtrsim 2m_e c^2 \simeq 1$ MeV and $m_\pi c^2(1+m_\pi/2m_p) = 145$ MeV, respectively. While the *Compton scattering* always occurs but, when E_γ exceeds the threshold for pair-production and photomeson production, the Compton scattering is negligible compared to these processes. Moreover, the pair-production can be neglected when $E_\gamma \geqslant 145$ MeV. Indeed, in spite of the pair-production cross-section is large, the fraction of photon energy transferred to the secondary electrons is smaller than the one transferred to secondary particles in the photomeson production. Then, the photomeson production results the predominant process at high energies (see [69]). For this reason, we start to consider the photomeson production process and after we analyze the pair-production process, because our photons energies (in the proton rest frame) are in the range (0.7; 100) GeV.

E.1.1 Photomeson production

For the $\gamma - p$ photomeson production, we consider the interaction between the γ produced by π^0 decay and the protons of the remnant at greater radius than the γ production point. We got the $\gamma - p$ cross-section values from [1], where the total cross-section is plotted as a function of the total momentum in the laboratory frame. In the considered interaction, this momentum coincides with the photon energy in the proton rest frame (that is our laboratory frame). The values of the cross-sections $\sigma_{\gamma p}$ for the three photons energies are:

- $E_\gamma = 0.69$ GeV, $\sigma_{\gamma p} = 0.2646$ mb;
- $E_\gamma = 91.62$ GeV, $\sigma_{\gamma p} = 0.11559$ mb;
- $E_\gamma = 47.86$ EeV, $\sigma_{\gamma p} = 0.7$ mb.

From these values for the cross-sections and the protons number density of the remnant, we can calculate the interaction length by $l_{int} = (\sigma_{\gamma p} n_{targ})^{-1}$. For photons energies between $0.2 \leq E_\gamma \leq 10^4$ GeV, the cross-section does not vary much. Indeed, as it is shown in Fig. (E.1), for a wide range of energies, the order of magnitude is practically constant. In the whole extension of the remnant, the target particles number density varies between $5 \times 10^{23} \leq n_{targ} \leq 8 \times 10^{23}$ particle/cm^3 and, then, we can assume it as constant and equal to the mean value $n_{targ} = 6.5 \times 10^{23}$ particle/cm^3. Instead in the ISM region the target protons have a particles number density equal to $n_{targ} = 1$ particle/cm^3. The interaction length for the three cases is:

- 1) $l_{int} = 5.793 \times 10^3$ cm;
- 2) $l_{int} = 8.65 \times 10^{27}$ cm;
- 3) $l_{int} = 1.43 \times 10^{27}$ cm,

respectively. The thickness of the ejecta is $\Delta L = 5.513 \times 10^{10} - 9.616 \times 10^8 = 5.417 \times 10^{10}$ cm, while the thickness of the ISM region is $\Delta L = 10^{17} - 10^{16} = 9 \times 10^{16}$ cm. From these results, we see that: 1) $l_{int} < \Delta L$ for the first case and, then, the remnant is not transparent to photo-meson interaction and photons are not free to escape from this region (at least considering this interaction); 2) for photon energy $E_\gamma = 91.62$ GeV and 47.86 EeV and interaction with the ISM region, the interaction length is $l_{int} \gg \Delta L$ and, then, the photon are free to escape and can be detected on Earth. Then, we got that only the interaction with the ISM is not affected by photomeson production.

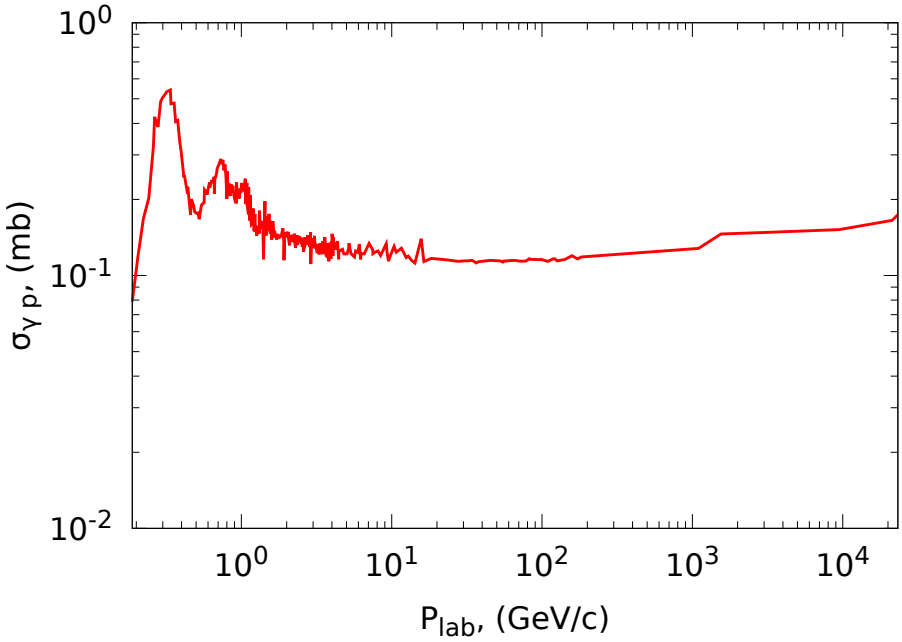

Figure E.1. $\gamma - p$ total cross section (in mbarn= 10^{-27} cm^2) as a function of the laboratory momentum, that, in this case, coincides with the photon energy.

E.1.2 Photon pair-production

At photons energies $1 \leq E_\gamma \leq 145$ MeV, the principal interaction that occurs for photons is the pair-production process, $\gamma p \rightarrow p e^+ e^-$. Since the spectra of our photons start to acquire importance at $E_\gamma \geq 10$ MeV, in this range of energies the pair-production cross-section is almost constant (it has a fast increase between $1 \lesssim E_\gamma \leq 10$ MeV and after it remains almost constant also at high energy $\simeq 10^5$ MeV, (see Fig. (33.15) in [2]). In order to obtain this cross-section, we have to introduce the *radiation length* X_0, that has two interpretations: 1) as the mean distance over which a high-energy electron loses about $1/e$ of its energy by bremsstrahlung processes; 2) as 7/9 of the mean free path for pair-production by high-energy photon. The interaction length is defined as:

$$\frac{1}{X_0} = 4\alpha r_e^2 \frac{N_A}{A}\{Z^2\left[L_{rad} - f(Z)\right] + ZL'_{rad}\}, \tag{E.1}$$

where α is the fine structure constant, r_e is the classical electron radius, N_A the Avogadro's number, Z the atomic number of the atom where the interaction occurs and A its molar mass. $f(Z)$ is given by

$$f(Z) = a^2\left[\left(1 + a^2\right)^{-1} + 0.20206 - 0.0369a^2 + 0.0083a^4 - 0.002a^6\right], \tag{E.2}$$

with $a = Z\alpha$. For H atoms $L_{rad} = 5.31$ and $L'_{rad} = 6.144$ (see [2]). The cross-section is given by

$$\frac{d\sigma_{pp}}{dx} = \frac{A}{X_0 N_A}\left[1 - \frac{4}{3}x(1-x)\right], \tag{E.3}$$

where $x = E/E_\gamma$ is the fraction of energy transferred to the secondary particles by the photon. Integrating Eq. (E.3) and considering the high-energy limit $x \ll 1$, the cross section assumes the constant value

$$\sigma_{pp} \simeq \frac{7}{9}\left(\frac{A}{X_0 N_A}\right), \tag{E.4}$$

that, using the definition of the *radiation length*, can be written as

$$\sigma_{pp} = 4\alpha r_e^2 \frac{7}{9}\left(L_{rad} - f(Z) + L'_{rad}\right) = 20.66 \quad \text{mb}. \tag{E.5}$$

Here we have considered hydrogen atom as the nucleus that absorbs the recoil momentum of the interaction. At this point one can calculate the interaction length $l_{int}(r) = (\sigma_{pp} \times \rho(r))^{-1}$:

- 1) $l_{int} = 74.21$ cm;
- 2) $l_{int} = 4.84 \times 10^{25}$ cm;
- 3) $l_{int} \sim 10^{25}$ cm,

respectively. Also here, we see that the photons are trapped inside the ejecta for pair-production process, while they are free to leave the ISM region [2].

E.2 $\gamma - e^{\pm}$ interaction

E.2.1 Compton scattering

In this section, we analyze the Compton scattering between $\gamma - e^{\pm} \rightarrow \gamma' - e^{\pm}$. The electron number density is related to the baryon mass density by the formula $n_{e^-} = \rho\Gamma/m_p$ and, since this is also equal to the procedure we had applied to calculate the baryon number density (neglecting the mass of electron/positron) and assuming one electron per nucleon in average, we can conclude that the pair number density is equal to the one of protons (respectively, for the two considered regions) [3].
The $\gamma - e^-$ cross-section is given by the Klein-Nishina formula:

$$\sigma_{K-N} = \pi r_e^2 \frac{1}{x}\left\{\left[1 - \frac{2(x+1)}{x^2}\right]\ln(2x+1) + \frac{1}{2} + \frac{4}{x} - \frac{1}{2(2x+1)^2}\right\}, \tag{E.6}$$

that, in the case of high energy photons, becomes

$$\sigma_{K-N} = \pi r_e^2 \frac{1}{x}\left(\ln(2x) + \frac{1}{2}\right). \tag{E.7}$$

Here r_e is the classical electron radius $r_e = e^2/4\pi\epsilon_0 m_e c^2 = 2.818 \times 10^{-13}$ cm and $x = h\nu/m_e c^2$, namely the photon energy normalized to the electron mass.

For the three photon energies and the different number density of target particles, we get

- 1) $E_\gamma = 0.69$ GeV, $\sigma_{KN} = 1.55$ mb, $l_{int} = 987.55$ cm;
- 2) $E_\gamma = 91.62$ GeV, $\sigma_{KN} = 1.84 \times 10^{-2}$ mb, $l_{int} = 5.4 \times 10^{28}$ cm;
- 3) $E_\gamma = 47.86$ EeV, $\sigma_{KN} = 88.87$ fb, $l_{int} = 1.13 \times 10^{37}$ cm.

As we expected, even in this case, the photons are affected by Compton scattering when they expand inside the SN-ejecta, while they remain unperturbed when they are produced inside the ISM region.
At the considered photons energies, the Klein-Nishina cross section is very low since at $E_\gamma \gg m_e c^2$, the principal process for photons is the pair production that we are going to analyze in the next section.

[2] The value of l_{int} for the interaction of photons $E_\gamma \geq$ EeV is only approximated since it is not clear if Eq. (E.5) is valid at these energies.

[3] Here we had considered only electrons because, from the already done calculations in [129], one can infer that the number of positrons is negligible than the electrons.

E.2.2 Pair production

For high energy photons, $E_\gamma \gg m_e c^2$, the threshold for pair production, $E_\gamma^{th} = 4\, m_e c^2$, is open. Since we have high energy photons, this results as the principal process. For the estimate of the interaction length for different photons energies, we use the cross-section σ_{pp} of the process developed in [66], where they give better formula for σ_{pp} for *free* and *bound* electrons (and also for bremsstrahlung) compared to Bethe-Heitler one, both near the threshold of pair production and for high-energy photons. The high-energy limit of the pair-production cross-section assumes the following form

$$\sigma_{pp}^{hl} = \alpha_f r_e^2 \left(\frac{28}{9} \ln\left(\frac{E_\gamma}{m_e c^2} \right) - \frac{100}{9} \right). \tag{E.8}$$

With this formulation for σ_{pp}, we get the interaction length for the three photons energies and the two density regime analyzed until now:

- 1) $E_\gamma = 0.69$ GeV, $\sigma_{pp} = 7.808$ mb, $l_{int} = 196.32$ cm;
- 2) $E_\gamma = 91.62$ GeV, $\sigma_{pp} = 16.62$ mb, $l_{int} = 6.015 \times 10^{25}$ cm;
- 3) $E_\gamma = 47.86$ EeV, $\sigma_{KN} = 5.28$ mb, $l_{int} = 1.893 \times 10^{25}$ cm.

Eq. (E.8) is surely valid for photons energies until 1 or tens of GeV, but in [66] it is not explicitly stated the validity at ultra-high-energies (even if the order of magnitude should be the same).
As we can see, only GeV photons created in the SN-ejecta are much affected by pair-production due to the high density of matter of the region.

E.3 Photon-Photon Pair Production

Concerning the pair production via photon-photon interaction, $\gamma + \gamma \rightarrow e^+ + e^-$, since we guessed that this process could be relevant for the calculation of the photon detection probability, instead of using mean values for the photon energy and for the density (as we have done for the previous interactions), in this case we calculate the interaction length at each step of the plasma expansion inside the ejecta. In this analysis, we consider only the photons produced by the interaction inside the ejecta because: 1) in Sec. (3.4) we derived that are the ones with major detection probability due to their higher flux; 2) due to the creation of new $e^\pm$ pair, this could affect the others interacting processes analyzed in this appendix.

We can get the interaction length $l_{\gamma\gamma}$ at the radius i by mean of:

$$l_{\gamma\gamma}^i = \left(\sigma_{\gamma\gamma}^i n_\gamma^i \right)^{-1}, \tag{E.9}$$

with n_γ^i the photon number density, while $\sigma_{\gamma\gamma}^i$ the pair production cross-section (both calculated at the specific radius i):

$$\sigma_{\gamma\gamma} = \frac{3}{16} \sigma_T \left(1 - \zeta^2\right) \left[2\zeta \left(\zeta^2 - 2\right) + \left(3 - \zeta^4\right) \ln\left(\frac{1+\zeta}{1-\zeta} \right) \right], \tag{E.10}$$

with $\sigma_T = (8\pi/3)\, e^4 / \left(m_e c^2\right)^2 = 6.65 \times 10^{-25}$ cm^2 the Thomson cross-section, $\zeta = \sqrt{1 - 2\left(m_e c^2\right)^2 / \left(\varepsilon_{\gamma,1} \varepsilon_{\gamma,2}\right)}$ the velocity of the particle in the center of momentum frame[4], $\varepsilon_{\gamma,1}$ the interacting photon energy and $\varepsilon_{\gamma,2}$ the target photon energy. We need to note that we assume $\varepsilon_{\gamma,1} = \varepsilon_{\gamma,2}$ since, at every radius, the photons are produced with the same energy by the same mechanism. Moreover, this energy, at each radius, is the

[4] An isotropic radiation field is adopted

photon energy corresponding to the maximum point of the spectrum (see Fig. (3.5)). The photons number density is given by:

$$n_\gamma^i = \frac{L_\gamma^i}{4\pi r_i^2 c \varepsilon_\gamma^i} \tag{E.11}$$

where L_γ^i is the photon luminosity, calculated at every radius as explained in Sec. (3.2.3). The result of these calculations is shown in Fig. (E.2). From this plot we understood that also the pair production is a

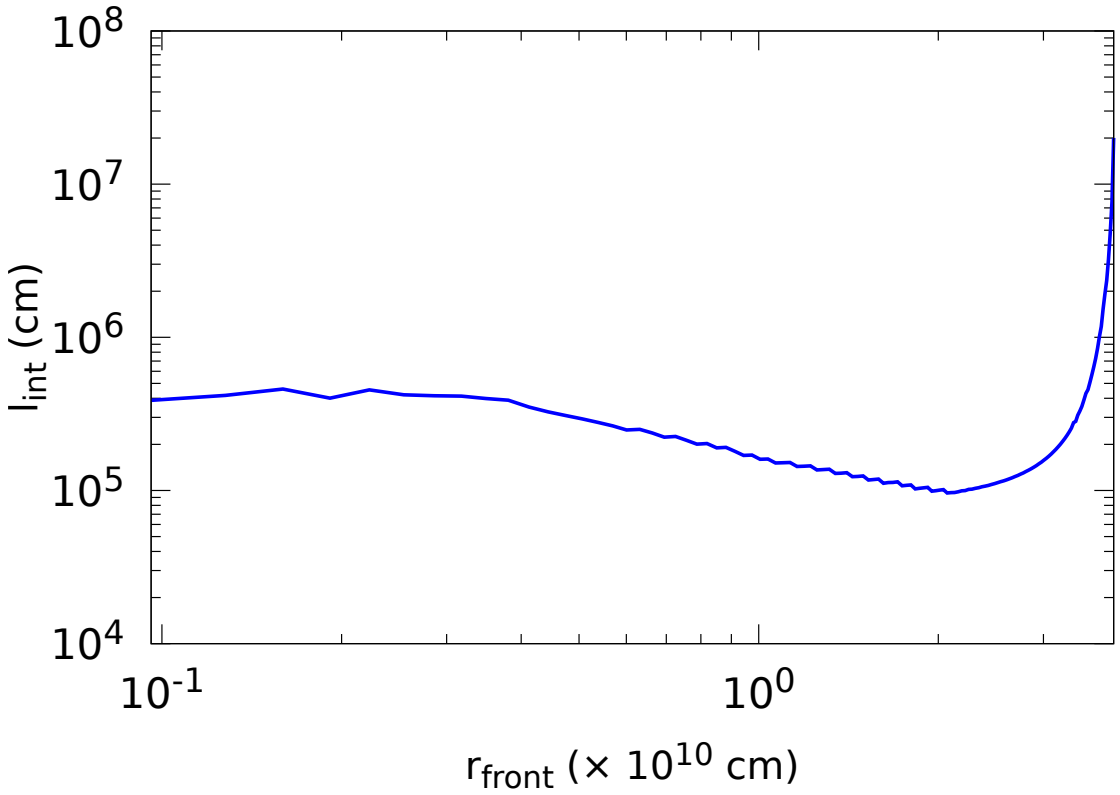

Figure E.2. Interaction length for $\gamma\gamma$ pair production, for photons produced and interacting inside the ejecta.

very efficient process and, then (together with the other processes studied in this appendix), the photons can hardly leave unperturbed the system and arrive at Earth.

From all the interactions considered in this appendix, we deduce that it can be difficult to detect photons created inside the SN-ejecta region since they are affected by all the considered interactions with baryonic and leptonic matter, even if their luminosity and the related flux on Earth can be detected by the Earth telescopes (see Sec. (3.4)) and they are higher than the ones for photons coming out the interaction in the ISM region. Whereas, photons produced by pp interaction inside the ISM are not affected by those interactions (due to the low particle number density in the region) and can reach the Earth, with only a variation of their energy by a factor $1/1+z$ (where z is the redshift of the ISM region) due to the cosmological expansion of the Universe.

Appendix F

Appendix on the transformations of the photon momentum

In this chapter, we would like to write the relation between the momentum of a photon in the *rest frame* of the emitting electrons, with the photon momentum received by an observer at rest at infinity, *laboratory frame*. The electron moves in an external electromagnetic field.
Let's denote with a prime sign $'$ the variable in the particle rest frame and without any sign the variables in the *laboratory frame*.
In the calculations we use the metric $\eta_{\mu\nu} = (1, -1, -1, -1)$. With this metric, the *controvariant components* of a four-vectors are $A^{\mu\nu} = \left(A^0, \vec{A}\right)$, while the *covariant components* are $A_{\mu\nu} = \left(A^0, -\vec{A}\right)$. Let's call, measured in the laboratory frame, the electron momentum $p^{\mu} = m\, c\, \gamma\left(1, \vec{\beta}\right)$, with γ and β the electron Lorentz factor and velocity, respectively; $k^{\mu} = \left(\omega/c, \vec{k}\right)$ the photon momentum.

The Lorentz transformation for a four-vector from the laboratory frame to the particle rest frame is given by

$$A'^{\mu} = \Lambda^{\mu}{}_{\nu}\, A^{\nu}, \tag{F.1}$$

while the inverse transformation is

$$A^{\alpha} = \tilde{\Lambda}_{\mu}{}^{\alpha}\, A'^{\mu}. \tag{F.2}$$

The matrix Λ^{μ}_{ν}, and the inverse $\tilde{\Lambda}^{\alpha}_{\mu}$, is the direct and inverse boost between the two frames, respectively:

$$\Lambda^{\mu}{}_{\nu} = \begin{pmatrix} \gamma & -\gamma\,\beta_x & -\gamma\,\beta_y & -\gamma\,\beta_z \\ -\gamma\,\beta_x & 1+(\gamma-1)\frac{\beta_x^2}{\beta^2} & (\gamma-1)\frac{\beta_x\,\beta_y}{\beta^2} & (\gamma-1)\frac{\beta_x\,\beta_z}{\beta^2} \\ -\gamma\,\beta_y & (\gamma-1)\frac{\beta_x\,\beta_y}{\beta^2} & 1+(\gamma-1)\frac{\beta_y^2}{\beta^2} & (\gamma-1)\frac{\beta_y\,\beta_z}{\beta^2} \\ -\gamma\,\beta_z & (\gamma-1)\frac{\beta_x\,\beta_z}{\beta^2} & (\gamma-1)\frac{\beta_y\,\beta_z}{\beta^2} & 1+(\gamma-1)\frac{\beta_z^2}{\beta^2} \end{pmatrix}, \quad \tilde{\Lambda}_{\mu}{}^{\alpha} = \begin{pmatrix} \gamma & \gamma\,\beta_x & \gamma\,\beta_y & \gamma\,\beta_z \\ \gamma\,\beta_x & 1+(\gamma-1)\frac{\beta_x^2}{\beta^2} & (\gamma-1)\frac{\beta_x\,\beta_y}{\beta^2} & (\gamma-1)\frac{\beta_x\,\beta_z}{\beta^2} \\ \gamma\,\beta_y & (\gamma-1)\frac{\beta_x\,\beta_y}{\beta^2} & 1+(\gamma-1)\frac{\beta_y^2}{\beta^2} & (\gamma-1)\frac{\beta_y\,\beta_z}{\beta^2} \\ \gamma\,\beta_z & (\gamma-1)\frac{\beta_x\,\beta_z}{\beta^2} & (\gamma-1)\frac{\beta_y\,\beta_z}{\beta^2} & 1+(\gamma-1)\frac{\beta_z^2}{\beta^2} \end{pmatrix}. \tag{F.3}$$

Here γ and the β components are the electron Lorentz factor and velocity, respectively.
The inverse matrix is given by

$$\tilde{\Lambda}_{\mu}{}^{\alpha} = \eta_{\mu\tau}\, \Lambda^{\tau}{}_{\sigma}\, \eta^{\sigma\alpha}. \tag{F.4}$$

From the definition, the electron momentum in the rest frame is $p'^{\mu} = \left(mc, \vec{0}\right)$.
The acceleration of the particle is defined by the equation of motion

$$a^{\alpha} = \frac{1}{m}\frac{dp^{\alpha}}{d\tau} = \frac{e}{mc}\, \mathcal{F}^{\alpha\beta}\, u_{\beta}, \tag{F.5}$$

where u_{β} is the covariant component of the particle velocity $u_{\beta} = (\gamma c, -\gamma\vec{u})$, τ the proper time ($d\tau = dt/\gamma$)

and $\mathcal{F}^{\alpha\beta}$ is the electromagnetic tensor

$$\mathcal{F}_{\alpha\beta} = \begin{pmatrix} 0 & E_x & E_y & E_z \\ -E_x & 0 & -B_z & B_y \\ -E_y & B_z & 0 & -B_x \\ -E_z & -B_y & B_x & 0 \end{pmatrix}, \quad \mathcal{F}^{\alpha\beta} = \begin{pmatrix} 0 & -E_x & -E_y & -E_z \\ E_x & 0 & -B_z & B_y \\ E_y & B_z & 0 & -B_x \\ E_z & -B_y & B_x & 0 \end{pmatrix}. \tag{F.6}$$

From Eq. (F.5), the four-acceleration takes the following form

$$a^{\alpha} = \frac{e}{m}\gamma \begin{pmatrix} \vec{E}\cdot\vec{\beta} \\ \vec{E} + \vec{\beta}\times\vec{B} \end{pmatrix}. \tag{F.7}$$

The four acceleration transform as

$$a'^{\alpha} = \Lambda^{\alpha}{}_{\beta}\, a^{\beta}. \tag{F.8}$$

The transformation gives the following components

$$a'^{0} = \gamma^2 \left[\left(\vec{E}\cdot\vec{\beta}\right) - \vec{\beta}\cdot\left(\vec{E} + \vec{\beta}\times\vec{B}\right)\right], \tag{F.9a}$$

$$a'^{1} = -\gamma^2 \beta_x \left(\vec{E}\cdot\vec{\beta}\right) + \gamma\left(\vec{E} + \vec{\beta}\times\vec{B}\right)_x + (\gamma - 1)\frac{\gamma\beta_x}{\beta^2}\left[\vec{\beta}\cdot\left(\vec{E} + \vec{\beta}\times\vec{B}\right)\right], \tag{F.9b}$$

$$a'^{2} = -\gamma^2 \beta_y \left(\vec{E}\cdot\vec{\beta}\right) + \gamma\left(\vec{E} + \vec{\beta}\times\vec{B}\right)_y + (\gamma - 1)\frac{\gamma\beta_y}{\beta^2}\left[\vec{\beta}\cdot\left(\vec{E} + \vec{\beta}\times\vec{B}\right)\right], \tag{F.9c}$$

$$a'^{3} = -\gamma^2 \beta_z \left(\vec{E}\cdot\vec{\beta}\right) + \gamma\left(\vec{E} + \vec{\beta}\times\vec{B}\right)_z + (\gamma - 1)\frac{\gamma\beta_z}{\beta^2}\left[\vec{\beta}\cdot\left(\vec{E} + \vec{\beta}\times\vec{B}\right)\right]. \tag{F.9d}$$

The inverse transformation is

$$a^{\alpha} = \tilde{\Lambda}_{\beta}^{\alpha} a'^{\beta},$$

and gives the components

$$a^0 = \gamma\left[a'^{0} + \left(\vec{\beta}\cdot\vec{a'}\right)\right], \tag{F.10a}$$

$$a^1 = a'^{1} + \beta_x\left[\gamma\, a'^{0} + \frac{(\gamma-1)}{\beta^2}\left(\vec{\beta}\cdot\vec{a'}\right)\right], \tag{F.10b}$$

$$a^2 = a'^{2} + \beta_y\left[\gamma\, a'^{0} + \frac{(\gamma-1)}{\beta^2}\left(\vec{\beta}\cdot\vec{a'}\right)\right], \tag{F.10c}$$

$$a^3 = a'^{3} + \beta_z\left[\gamma\, a'^{0} + \frac{(\gamma-1)}{\beta^2}\left(\vec{\beta}\cdot\vec{a'}\right)\right]. \tag{F.10d}$$

Let's see now how the components of the photon momentum transform. In the particle rest frame, by the following transformation

$$k'^{\mu} = \Lambda^{\mu}{}_{\nu}\, k^{\nu},$$

the four momentum components become

$$k'^{0} = \gamma\left[k^0 - \left(\vec{\beta}\cdot\vec{k}\right)\right], \tag{F.11a}$$

$$k'^{1} = k^1 - \beta_x\left[\gamma\, k^0 - \frac{(\gamma-1)}{\beta^2}\left(\vec{\beta}\cdot\vec{k}\right)\right], \tag{F.11b}$$

$$k'^{2} = k^2 - \beta_y\left[\gamma\, k^0 - \frac{(\gamma-1)}{\beta^2}\left(\vec{\beta}\cdot\vec{k}\right)\right], \tag{F.11c}$$

$$k'^{3} = k^3 - \beta_z\left[\gamma\, k^0 - \frac{(\gamma-1)}{\beta^2}\left(\vec{\beta}\cdot\vec{k}\right)\right], \tag{F.11d}$$

while the inverse are

$$k^0 = \gamma\left[k^{'0} + \left(\vec{\beta}\cdot\vec{k'}\right)\right], \tag{F.12a}$$

$$k^1 = k^{'1} + \beta_x\left[\gamma k^{'0} + \frac{(\gamma-1)}{\beta^2}\left(\vec{\beta}\cdot\vec{k'}\right)\right], \tag{F.12b}$$

$$k^2 = k^{'2} + \beta_y\left[\gamma k^{'0} + \frac{(\gamma-1)}{\beta^2}\left(\vec{\beta}\cdot\vec{k'}\right)\right], \tag{F.12c}$$

$$k^3 = k^{'3} + \beta_z\left[\gamma k^{'0} + \frac{(\gamma-1)}{\beta^2}\left(\vec{\beta}\cdot\vec{k'}\right)\right]. \tag{F.12d}$$

We define now the photon director cosines $\eta^{\mu} = k^{\mu}/k^0$, in the laboratory frame, and $\eta^{'\mu} = k^{'\mu}/k^{'0}$, in the comoving frame. From the Eqs. (F.11), the director cosines in the comoving frame become (naturally $\eta^0 = \eta^{'0} = 1$)

$$\eta^{'1} = \frac{k^{'1}}{k^{'0}}\frac{k^0}{k^0} = \frac{\eta^1 - \beta_x\left[\gamma - \frac{(\gamma-1)}{\beta^2}\left(\vec{\beta}\cdot\vec{\eta}\right)\right]}{\gamma\left[1 - \left(\vec{\beta}\cdot\vec{\eta}\right)\right]}, \tag{F.13a}$$

$$\eta^{'2} = \frac{k^{'2}}{k^{'0}}\frac{k^0}{k^0} = \frac{\eta^2 - \beta_y\left[\gamma - \frac{(\gamma-1)}{\beta^2}\left(\vec{\beta}\cdot\vec{\eta}\right)\right]}{\gamma\left[1 - \left(\vec{\beta}\cdot\vec{\eta}\right)\right]}, \tag{F.13b}$$

$$\eta^{'3} = \frac{k^{'3}}{k^{'0}}\frac{k^0}{k^0} = \frac{\eta^3 - \beta_z\left[\gamma - \frac{(\gamma-1)}{\beta^2}\left(\vec{\beta}\cdot\vec{\eta}\right)\right]}{\gamma\left[1 - \left(\vec{\beta}\cdot\vec{\eta}\right)\right]}. \tag{F.13c}$$

The inverse transformation to the laboratory frame gives

$$\eta^1 = \frac{k^1}{k^0}\frac{k^{'0}}{k^{'0}} = \frac{\eta^{'1} + \beta_x\left[\gamma + \frac{(\gamma-1)}{\beta^2}\left(\vec{\beta}\cdot\vec{\eta'}\right)\right]}{\gamma\left[1 + \left(\vec{\beta}\cdot\vec{\eta'}\right)\right]}, \tag{F.14a}$$

$$\eta^2 = \frac{k^2}{k^0}\frac{k^{'0}}{k^{'0}} = \frac{\eta^{'2} + \beta_y\left[\gamma + \frac{(\gamma-1)}{\beta^2}\left(\vec{\beta}\cdot\vec{\eta'}\right)\right]}{\gamma\left[1 + \left(\vec{\beta}\cdot\vec{\eta'}\right)\right]}, \tag{F.14b}$$

$$\eta^3 = \frac{k^3}{k^0}\frac{k^{'0}}{k^{'0}} = \frac{\eta^{'3} + \beta_z\left[\gamma + \frac{(\gamma-1)}{\beta^2}\left(\vec{\beta}\cdot\vec{\eta'}\right)\right]}{\gamma\left[1 + \left(\vec{\beta}\cdot\vec{\eta'}\right)\right]}. \tag{F.14c}$$

We can write the vector $\vec{\eta}$ and $\vec{\eta'}$ in spherical coordinates for both systems (remember that $|\vec{\eta}| = |\vec{\eta'}| = 1$):

$$\eta = \left(\eta^1, \eta^2, \eta^3\right) = (\sin(\theta)\cos(\phi), \sin(\theta)\sin(\phi), \cos(\theta)),$$

and

$$\eta' = \left(\eta^{'1}, \eta^{'2}, \eta^{'3}\right) = (\sin(\Theta)\cos(\Phi), \sin(\Theta)\sin(\Phi), \cos(\Theta)).$$

Then we can rewrite Eqs. (F.11a) (F.13) as

$$k^{'0} = \gamma k^0 \left[1 - \left(\beta_x \sin(\theta)\cos(\phi) + \beta_y \sin(\theta)\sin(\phi) + \beta_z \cos(\theta)\right)\right], \tag{F.15a}$$

$$\eta^{'1} = \frac{\sin(\theta)\cos(\phi) - \beta_x \left[\gamma - \frac{(\gamma-1)}{\beta^2}\left(\beta_x \sin(\theta)\cos(\phi) + \beta_y \sin(\theta)\sin(\phi) + \beta_z \cos(\theta)\right)\right]}{\gamma\left[1 - \left(\beta_x \sin(\theta)\cos(\phi) + \beta_y \sin(\theta)\sin(\phi) + \beta_z \cos(\theta)\right)\right]}, \tag{F.15b}$$

$$\eta^{'2} = \frac{\sin(\theta)\sin(\phi) - \beta_y \left[\gamma - \frac{(\gamma-1)}{\beta^2}\left(\beta_x \sin(\theta)\cos(\phi) + \beta_y \sin(\theta)\sin(\phi) + \beta_z \cos(\theta)\right)\right]}{\gamma\left[1 - \left(\beta_x \sin(\theta)\cos(\phi) + \beta_y \sin(\theta)\sin(\phi) + \beta_z \cos(\theta)\right)\right]}, \tag{F.15c}$$

$$\eta^{'3} = \frac{\cos(\theta) - \beta_z \left[\gamma - \frac{(\gamma-1)}{\beta^2}\left(\beta_x \sin(\theta)\cos(\phi) + \beta_y \sin(\theta)\sin(\phi) + \beta_z \cos(\theta)\right)\right]}{\gamma\left[1 - \left(\beta_x \sin(\theta)\cos(\phi) + \beta_y \sin(\theta)\sin(\phi) + \beta_z \cos(\theta)\right)\right]}, \tag{F.15d}$$

while Eqs. (F.12a) (F.14) become

$$k^0 = \gamma k^{'0} \left[1 + \left(\beta_x \sin(\Theta)\cos(\Phi) + \beta_y \sin(\Theta)\sin(\Phi) + \beta_z \cos(\Theta)\right)\right], \tag{F.16a}$$

$$\eta^1 = \frac{\sin(\Theta)\cos(\Phi) + \beta_x \left[\gamma + \frac{(\gamma-1)}{\beta^2}\left(\beta_x \sin(\Theta)\cos(\Phi) + \beta_y \sin(\Theta)\sin(\Phi) + \beta_z \cos(\Theta)\right)\right]}{\gamma\left[1 + \left(\beta_x \sin(\Theta)\cos(\Phi) + \beta_y \sin(\Theta)\sin(\Phi) + \beta_z \cos(\Theta)\right)\right]}, \tag{F.16b}$$

$$\eta^2 = \frac{\sin(\Theta)\sin(\Phi) + \beta_y \left[\gamma + \frac{(\gamma-1)}{\beta^2}\left(\beta_x \sin(\Theta)\cos(\Phi) + \beta_y \sin(\Theta)\sin(\Phi) + \beta_z \cos(\Theta)\right)\right]}{\gamma\left[1 + \left(\beta_x \sin(\Theta)\cos(\Phi) + \beta_y \sin(\Theta)\sin(\Phi) + \beta_z \cos(\Theta)\right)\right]}, \tag{F.16c}$$

$$\eta^3 = \frac{\cos(\Theta) + \beta_z \left[\gamma + \frac{(\gamma-1)}{\beta^2}\left(\beta_x \sin(\Theta)\cos(\Phi) + \beta_y \sin(\Theta)\sin(\Phi) + \beta_z \cos(\Theta)\right)\right]}{\gamma\left[1 + \left(\beta_x \sin(\Theta)\cos(\Phi) + \beta_y \sin(\Theta)\sin(\Phi) + \beta_z \cos(\Theta)\right)\right]}. \tag{F.16d}$$

The first specific case is when the emission is in the equatorial plane of the comoving frame ($\Theta = \pi/2$).

For this case, Eqs. (F.16) become:

$$k^0 = \gamma k'^0 \left[1 + \left(\beta_x \cos(\Phi) + \beta_y \sin(\Phi)\right)\right], \tag{F.17a}$$

$$\eta^1 = \frac{\cos(\Phi) + \beta_x \left[\gamma + \frac{(\gamma-1)}{\beta^2}\left(\beta_x \cos(\Phi) + \beta_y \sin(\Phi)\right)\right]}{\gamma\left[1 + \left(\beta_x \cos(\Phi) + \beta_y \sin(\Phi)\right)\right]}, \tag{F.17b}$$

$$\eta^2 = \frac{\sin(\Phi) + \beta_y \left[\gamma + \frac{(\gamma-1)}{\beta^2}\left(\beta_x \cos(\Phi) + \beta_y \sin(\Phi)\right)\right]}{\gamma\left[1 + \left(\beta_x \cos(\Phi) + \beta_y \sin(\Phi)\right)\right]}, \tag{F.17c}$$

$$\eta^3 = \frac{\beta_z \left[\gamma + \frac{(\gamma-1)}{\beta^2}\left(\beta_x \cos(\Phi) + \beta_y \sin(\Phi)\right)\right]}{\gamma\left[1 + \left(\beta_x \cos(\Phi) + \beta_y \sin(\Phi)\right)\right]}. \tag{F.17d}$$

We can get the values of the observer angles, for this specific case, over which the emission can be seen:

$$\sin(\theta) = \frac{\sqrt{1+\left(\beta_x^2+\beta_y^2\right)\left[\gamma+\frac{(\gamma-1)}{\beta^2}\left(\beta_x \cos(\Phi)+\beta_y \sin(\Phi)\right)\right]^2 + 2\left(\beta_x \cos(\Phi)+\beta_y \sin(\Phi)\right)\left[\gamma+\frac{(\gamma-1)}{\beta^2}\left(\beta_x \cos(\Phi)+\beta_y \sin(\Phi)\right)\right]}}{\gamma\left[1+\beta_x \cos(\Phi)+\beta_y \sin(\Phi)\right]}, \tag{F.18}$$

and

$$\tan(\phi) = \frac{\eta^2}{\eta^1} = \frac{\sin(\Phi) + \beta_y \left[\gamma + \frac{(\gamma-1)}{\beta^2}\left(\beta_x \cos(\Phi) + \beta_y \sin(\Phi)\right)\right]}{\cos(\Phi) + \beta_x \left[\gamma + \frac{(\gamma-1)}{\beta^2}\left(\beta_x \cos(\Phi) + \beta_y \sin(\Phi)\right)\right]}, \tag{F.19}$$

or

$$\sin(\phi) = \frac{\eta^2}{\sin(\theta)} = \left\{\sin(\Phi) + \beta_y \left[\gamma + \frac{(\gamma-1)}{\beta^2}\left(\beta_x \cos(\Phi) + \beta_y \sin(\Phi)\right)\right]\right\} \times$$
$$\left\{1 + \left(\beta_x^2+\beta_y^2\right)\left[\gamma + \frac{(\gamma-1)}{\beta^2}\left(\beta_x \cos(\Phi) + \beta_y \sin(\Phi)\right)\right]^2 + 2\left(\beta_x \cos(\Phi) + \beta_y \sin(\Phi)\right)\left[\gamma + \frac{(\gamma-1)}{\beta^2}\left(\beta_x \cos(\Phi) + \beta_y \sin(\Phi)\right)\right]\right\}^{-\frac{1}{2}}. \tag{F.20}$$

Assuming $\Phi = \pi/2$, we can rewrite $\tan(\phi)$, $\sin(\phi)$ and $\sin(\theta)$ as, with $\nu \equiv \gamma + \frac{(\gamma-1)}{\beta^2}\beta_y$:

$$\tan(\phi) = \frac{1}{\nu\,\beta_x} + \frac{\beta_y}{\beta_x}, \tag{F.21a}$$

$$\sin(\phi) = \frac{1 + \beta_y \nu}{\sqrt{1 + \left(\beta_x^2 + \beta_y^2\right)\nu^2 + 2\beta_y \nu}}, \tag{F.21b}$$

$$\sin(\theta) = \frac{\sqrt{1 + \left(\beta_x^2 + \beta_y^2\right)\nu^2 + 2\beta_y \nu}}{\gamma\left(1 + \beta_y\right)}. \tag{F.21c}$$

If the motion of the particle occurs almost in one-direction, that we assume to be along η^3 and then $\beta_x \sim \beta_y \sim 0$, we get the known results for the beaming effect for photons emitted by relativist particles:

$$\sin(\phi) \sim 1 \Longrightarrow \phi = \frac{\pi}{2}, \tag{F.22a}$$

$$\sin(\theta) \sim \frac{1}{\gamma} \Longrightarrow \theta \sim \frac{1}{\gamma}. \tag{F.22b}$$

The general expression for $\sin(\theta)$ and $\sin(\phi)$ (for any Φ and Θ) are:

$$\sin(\theta) = \frac{\sqrt{\sin^2(\Theta) + \left(\beta_x^2 + \beta_y^2\right)\Sigma^2 + 2\sin(\Theta)\left(\beta_x \cos(\Phi) + \beta_y \sin(\Phi)\right)\Sigma}}{\gamma(1+\Delta)}, \tag{F.23a}$$

$$\sin(\phi) = \frac{\eta^2}{\sin(\theta)} = \frac{\sin(\Theta)\sin(\Phi) + \beta_y\Sigma}{\sqrt{\sin^2(\Theta) + \left(\beta_x^2 + \beta_y^2\right)\Sigma^2 + 2\sin(\Theta)\left(\beta_x \cos(\Phi) + \beta_y \sin(\Phi)\right)\Sigma}}, \tag{F.23b}$$

with $\Sigma = \left[\gamma + \frac{(\gamma-1)}{\beta^2}\Delta\right]$ and $\Delta = \beta_x \sin(\Theta)\cos(\Phi) + \beta_y \sin(\Theta)\sin(\Phi) + \beta_z \cos(\Theta)$.
For $\Theta = 0$ (emission along the third axis $e^{'3}$), we get

$$\sin(\theta) = \frac{\sqrt{\beta_x^2 + \beta_y^2}}{1+\beta_z}\frac{\gamma(1+\beta_z) - 1}{\gamma - 1}, \tag{F.24a}$$

$$\sin(\phi) = \frac{\beta_y}{\sqrt{\beta_x^2 + \beta_y^2}}. \tag{F.24b}$$

A third specific case is when the emission in the comoving frame is on the $\left(e^{'2}, e^{'3}\right)$ direction, namely $\Phi = \pi/2$. Eqs. (F.16) become

$$k^0 = \gamma k^{'0}\left[1 + \left(\beta_y \sin(\Theta) + \beta_z \cos(\Theta)\right)\right], \tag{F.25a}$$

$$\eta^1 = \frac{\beta_x\left[\gamma + \frac{(\gamma-1)}{\beta^2}\left(\beta_y \sin(\Theta) + \beta_z \cos(\Theta)\right)\right]}{\gamma\left[1 + \left(\beta_y \sin(\Theta) + \beta_z \cos(\Theta)\right)\right]}, \tag{F.25b}$$

$$\eta^2 = \frac{\sin(\Theta) + \beta_y\left[\gamma + \frac{(\gamma-1)}{\beta^2}\left(\beta_y \sin(\Theta) + \beta_z \cos(\Theta)\right)\right]}{\gamma\left[1 + \left(\beta_y \sin(\Theta) + \beta_z \cos(\Theta)\right)\right]}, \tag{F.25c}$$

$$\eta^3 = \frac{\cos(\Theta) + \beta_z\left[\gamma + \frac{(\gamma-1)}{\beta^2}\left(\beta_y \sin(\Theta) + \beta_z \cos(\Theta)\right)\right]}{\gamma\left[1 + \left(\beta_y \sin(\Theta) + \beta_z \cos(\Theta)\right)\right]}. \tag{F.25d}$$

In this case we have:

$$\sin(\theta) = \frac{\sqrt{\sin(\Theta)^2 + \left(\beta_x^2 + \beta_y^2\right)\Sigma^2 + 2\sin(\Theta)\Sigma\beta_y}}{\gamma(1+\Delta)}, \tag{F.26a}$$

$$\sin(\phi) = \frac{\sin(\Theta) + \beta_y\Sigma}{\sqrt{\sin(\Theta)^2 + \left(\beta_x^2 + \beta_y^2\right)\Sigma^2 + 2\sin(\Theta)\Sigma\beta_y}}, \tag{F.26b}$$

with $\Delta = \beta_y \sin(\Theta) + \beta_z \cos(\Theta)$ and $\Sigma = \gamma + \frac{\gamma-1}{\beta^2}\Delta$.
For $\Theta = \pi/4$ and considering that $\beta_x \sim 0$, we get

$$\sin(\phi) = 1 \Longrightarrow \phi = \frac{\pi}{2}, \tag{F.27a}$$

$$\sin(\theta) = \frac{\frac{\sqrt{2}}{2} + \beta_y\left[\gamma + \frac{\sqrt{2}}{2}\frac{(\gamma-1)}{\beta^2}\left(\beta_y + \beta_z\right)\right]}{\gamma\left[1 + \frac{\sqrt{2}}{2}\left(\beta_y + \beta_z\right)\right]}. \tag{F.27b}$$

Eq. (F.27b), can be rewritten as

$$\sin(\theta) \simeq \frac{\frac{\sqrt{2}}{2}}{\gamma\left[1 + \frac{\sqrt{2}}{2}\left(\beta_y + \beta_z\right)\right]} + \beta_y. \tag{F.28}$$

Appendix G

Production rate for other configurations of $\vec{E}$ and $\vec{B}$ fields

In this appendix, we try to build up the set of equations that need to be solved in order to study the screening effect for configurations of the magnetic and electric fields different from the orthogonal configuration studied in Ch. (4). Firstly (Sec. (G.1)), we concetrate on the case with parallel fields, namely both $\vec{E}$ and $\vec{B}$ oriented along the $\hat{z}-$ axis. Secondly (Sec. (G.2)), we concentrate our attention to the general configuration of $\vec{E}\cdot\vec{B}\neq 0$. For the first study, we would like to use the pair production rate for parallel fields in [39]. For the second study, we wouyld like to use the production rate in [38] (the same that we have used for the perpendicular configuration of the fields).

The work for these two other configurations is still going on, so we do not put any results, but only the general equations that need to be used. In order to finish these calculations, we need only to find some proper Lorentz transformations in such a way that we can apply the two formula for the rate correctly. These Lorentz transformations will bring the fields or the photon momentum vector in the configuration necessary for the applicability of the rate formula:

1. **for the case of parallel fields:** one needs to find the proper Lorentz transformation to a frame where the photon momentum vector (directed in any direction in the laboratory frame) becomes perpendicular to the parallel fields and, obviously, that let the equations for the fields unchanged;

2. **for the configuration with $\vec{E}\cdot\vec{B}\neq 0$:** we need to make two Lorentz transformations: the first is necessary to move in a reference frame where the fields appear to be perpendicular; the second one, as done in Ch. (4), needs to be done in order to move in a frame where only the magnetic field is present and the photon momentum vector becomes perpendicular to this field.

G.1 Set of equations for $\vec{E}$ parallel to $\vec{B}$

In this configuration the components of the fields are: $\vec{B}=(0,\ 0,\ B_z)$ and $\vec{E}=(0,\ 0,\ E_z)$. Let's write all the equations necessary for our problem in this configuration. Here $B_{tot}(t)=B_{0,z}-B_{ind,z}(t)$ and $E_{tot}(t)=E_{0,z}-E_{ind,z}(t)=\Upsilon B_{tot}(t)$. The equations for the particles positions can be obtained from

$$\begin{cases}\frac{d\tilde{x}}{d\tilde{t}}=\beta_x,\\ \\ \frac{d\tilde{y}}{d\tilde{t}}=\beta_y,\\ \\ \frac{d\tilde{z}}{d\tilde{t}}=\beta_z.\end{cases} \tag{G.1}$$

While the equations for the particles velocity, from Eq. (4.8), becomes

$$\begin{cases} \frac{d\beta_x}{d\tilde{t}} = \frac{[\beta_y \tilde{B}_{tot} - \beta_x \beta_z \tilde{E}_{tot}]}{\gamma}, \\ \frac{d\beta_y}{d\tilde{t}} = -\frac{[\beta_x \tilde{B}_{tot} + \beta_y \beta_z \tilde{E}_{tot}]}{\gamma}, \\ \frac{d\beta_z}{d\tilde{t}} = \tilde{E}_{tot} \frac{[1-\beta_z^2]}{\gamma}. \end{cases} \tag{G.2}$$

The equation for the Lorentz factor, which contains the acceleration and the energy loss terms, becomes

$$\frac{d\gamma}{d\tilde{t}} = \beta_z \, \tilde{E}_{tot} - \frac{1}{\sqrt{3}\,\pi} \alpha_f \overline{H}(\tilde{\chi}), \tag{G.3}$$

where

$$\tilde{\chi} = \frac{3}{4} \gamma \sqrt{\tilde{B}_{tot}^2 \left(\beta_x^2 + \beta_y^2\right) + \tilde{E}_{tot}^2 \left(1 - \beta_z^2\right)}, \tag{G.4}$$

and $\overline{H}(\tilde{\chi})$ is given in Eq. (4.17).
The photon energy, normalized to the electron mass, is

$$\tilde{\varepsilon}_\gamma = \frac{\varepsilon_\gamma}{m\,c^2} = \frac{3}{2} \gamma^2 \sqrt{\tilde{B}_{tot}^2 \left(\beta_x^2 + \beta_y^2\right) + \tilde{E}_{tot}^2 \left(1 - \beta_z^2\right)}. \tag{G.5}$$

The equation for the number of photons can be written as

$$\frac{dN_\gamma(\tilde{t})}{d\tilde{t}} = \frac{2}{3\,\pi\,\sqrt{3}} \alpha_f \frac{N_\pm(\tilde{t})}{\gamma^2} \frac{\overline{H}(\tilde{\chi})}{\sqrt{\tilde{B}_{tot}^2 \left(\beta_x^2 + \beta_y^2\right) + \tilde{E}_{tot}^2 \left(1 - \beta_z^2\right)}}, \tag{G.6}$$

while the one for the pairs is, for any value of the Λ parameter (see Eq. (G.8)),

$$\frac{dN_\pm(\tilde{t})}{d\tilde{t}} = N_\gamma \zeta(t) \tag{G.7}$$

In the following expressions, the quantities with the prime symbol refer to their values in the K' frame (the frame where we move by means of a Lorentz transformation). The rate of pair-production, averaged over the polarization states of the photons (parallel and perpendicular to the fields) in the $K^{'}$ frame (where the photon momentum is perpendicular to the fields) is given by (see [39]):

$$\langle \zeta^{'} \rangle = \frac{9}{\sqrt{3}} \frac{\alpha_f}{\hbar} \frac{\varepsilon'_\gamma}{\Lambda^2} \int_0^1 dv \, \frac{K_{2/3}\left(\frac{4}{\Lambda'(1-v^2)}\right)}{1-v^2} \left[\frac{3}{2} - \frac{v^2}{6} + \frac{E'^2}{B'^2}\left(\frac{3}{2} - \frac{v^2}{6}\right)\right] \left(\frac{B'}{B_{cr}}\right)^2, \tag{G.8}$$

where $\varepsilon^{'}{}_\gamma = \hbar k^{'0}$ and $\Lambda = \frac{3}{2}\left(\frac{\varepsilon^{'}{}_\gamma}{mc^2}\right)\left(\frac{\hbar\omega^{'}{}_0}{mc^2}\right)$, with

$$\omega^{'}{}_0 = \frac{e}{mc} \sqrt{E^{'2} + B^{'2}}. \tag{G.9}$$

As we stated in the introduction of this appendix, in order to apply this formula for the rate, we need to find the proper Lorentz transformation to the $K^{'}$ frame (where all the variables in Eq. (G.8) are considered) where the photon momentum becomes perpendicular to the parallel fields and the form of the fields remains unchanged. After, we need to transform the rate in the laboratory frame through $\zeta = \zeta^{'}/\gamma^*$, where γ^* is the Lorentz factor of the $K^{'}$ frame.

The normalized curvature radius can be written as

$$\tilde{R}_c(\tilde{t}) = \frac{R_c}{\lambda_c} = \frac{\gamma}{\sqrt{\tilde{B}_{tot}^2\left(\beta_x^2+\beta_y^2\right)+\tilde{E}_{tot}^2\left(1-\beta_z^2\right)}}. \tag{G.10}$$

Finally, we can write the equation for the magnetic field variation as

$$\frac{d\tilde{B}_{tot}}{d\tilde{t}} = -\alpha_f\frac{\sqrt{\beta_x^2+\beta_y^2}}{\gamma^2}\frac{dN_\pm}{d\tilde{t}}\left[\tilde{B}_{tot}(\tilde{t})^2\left(\beta_x^2+\beta_y^2\right)+\tilde{E}_{tot}(\tilde{t})^2\left(1-\beta_z^2\right)\right]. \tag{G.11}$$

G.2 Set of equations for $\vec{E}\cdot\vec{B}\neq 0$

In this configuration we consider $\vec{B}=(0,0,B_z)$ and $\vec{E}=\left(0,E_y,E_z\right)=(0,E\sin(\psi),E\cos(\psi))$, with ψ the polar angle and E the strength of the electric field. With this configuration of the fields, we would like to use the pair production rate derived in [38], namely Eq. (4.30). In order to use that formulation, as we already stated in the introduction of the appendix, we need to transform the fields in order to get their same configuration. This means that: firstly, since here $\vec{E}\cdot\vec{B}\neq 0$, we need to make a Lorentz transformation to a frame, $K^{'}$, where $\vec{E}\cdot\vec{B}=0$, namely orthogonal fields; secondly, we need to move from $K^{'}$ to another frame, $K^{''}$, where only the magnetic field component is present. At this point, once we have transformed all the quantities (as the photon energy, the photons director cosines and the magnetic field), in the frame $K^{''}$, we can apply Eq. (4.30) for the pair production rate and transform it back to the K frame by the relation

$$\zeta = \frac{\zeta^{''}}{\gamma^{'}\,\gamma^{''}}, \tag{G.12}$$

where $\zeta^{''}$ and $\gamma^{''}$ is the production rate and the Lorentz boost, respectively, of the $K^{''}$ frame, while $\gamma^{'}$ is the boost of the $K^{'}$ frame.

The equations for this case are similar to the other analyzed cases. The only changes are in the equations for the motion of the particles (β) and the photon energy (and, consequently, the curvature radius, the equation for the magnetic field, the equation for the number of created photons and the parameter χ). Here we give only these two equations (the other can be derived easily as we have done before in Ch. (4) and Sec. (G.1)):

$$\begin{cases} \frac{d\beta_x}{dt} = \frac{e}{m\,c\,\gamma}\left[E_x+\beta_y B_z-\beta_x\,\mu\right], \\ \frac{d\beta_y}{dt} = \frac{e}{m\,c\,\gamma}\left[E_y-\beta_x B_z-\beta_y\,\mu\right], \\ \frac{d\beta_z}{dt} = \frac{e}{m\,c\,\gamma}\left[E_z-\beta_z\,\mu\right], \end{cases} \tag{G.13}$$

where $\mu\equiv|\vec{E}\cdot\vec{\beta}| = E_x\,\beta_x+E_y\,\beta_y+E_z\,\beta_z$ and

$$\varepsilon_\gamma = \frac{3}{2}\frac{e\,\hbar}{m\,c}\gamma^2\sqrt{E^2+B^2\left(\beta_x^2+\beta_y^2\right)-2\,\beta_x BE\sin(\psi)-\mu^2}, \tag{G.14}$$

where $E=\sqrt{E_x^2+E_y^2+E_z^2}$. The other equations can be derived from this form of ε_γ.
We emphasize that we still need to finish the calculations for these other two configurations of the fields. We only wanted to give the idea how to proceed for these other two cases.

Appendix H

Preliminary work on magnetic field screening

H.1 Introduction

The process of screening of a strong electric field through the creation of electron-positron pairs by QED vacuum polarization process, it has been studied for many years. One of the last studies about this argument was presented in [43], where they shown that an electric field as high as $E \sim \alpha_f E_c$, where α_f is the fine structure constant and $E_c = m_e^2 c^3/e\hbar$ the critical field, cannot be maintained because the creation of particles shower deplete the field.

Until now, no arguments came out about the screening of a magnetic field. In this appendix we study the process of screening of a magnetic field, for the case of a Kerr Black Hole. We emphasize that the model is not restricted only to BH, but can be applied in any other extreme astrophysical system (as neutron stars or magnetars) which satisfy the basic conditions of the problem, namely: strong magnetic and electric fields, proportionality between the fields strength (see Eq. (H.1)), pairs creation by vacuum polarization process. The aim is to show that the presence of electrons (already present in the system at the beginning, created via the magnetic pair production or vacuum polarization processes) and the consequent emission of synchrotron radiation, which will bring to a particles shower, can decrease the magnetic field even of a few order of magnitude. Our approach is based on the following relation between the already existing background magnetic field and the induced electric field:

$$E(t) = B(t)\frac{J}{2M^2}\frac{c^2}{G} = B(t)\frac{\bar{J}}{2\bar{M}^2}c \tag{H.1}$$

[1](see [130]). The proportionality factor J/M^2 represents the spin of the black hole (in SI units) [2] and the barred quantities are in geometric units.

Because of the relation in Eq. (H.1), correspondingly to the screening of the magnetic field, the screening of the electric field happens simultaneously. The two screening effects are correlated, but based on two different mechanisms. The $B(t)$ screening it is due to the creation of an induced magnetic field (with orientation opposite to the background one) by the accelerated electrons. The $E(t)$ screening it is due to the creation itself of these electrons (through electromagnetic showers), which deplete the electric field.

We will show that, for our particular case related to a BH, the lowest value of a magnetic field that can be attained is proportional to α_f and in inverse proportion to the spin of the BH, hereafter, $\eta \equiv \bar{J}/\bar{M}^2$. This conclusion corroborates the result that, in presence also of one initial pair, an electric field with strength as high as $\sim \alpha_f E_c$ cannot be maintained due to the depletion caused by creation of electromagnetic showers.

[1] The orientation of this magnetic field is along the $z-$axis ($B_x = B_y = 0$).

[2] All the quantities in this appendix are in SI units. Different units are explicitly indicated.

H.2 Main equations

The screening process of an electromagnetic field proceed through the following steps:

1. initial electrons are accelerated by the electric field and emit synchrotron radiation due to the presence of the magnetic field;
2. each of these synchrotron photons creates an e^+e^- pair via the magnetic pair production (MPP) process;
3. these new pairs start to be accelerated, emit synchrotron radiation and circularize around the magnetic field lines generating an induced magnetic field, B_{ind}, oriented in the opposite direction to the electron motion. This B_{ind} decreases the background magnetic field;
4. the previous processes occurs at every time t and, then, a particles shower develops.

This series of steps will end when the magnetic field decreases too much that the MPP process will not occur any more.
Now we derive all the equations that describe the steps of the entire process. The dynamic of an electron immersed in an electromagnetic field, under the approximation of $\gamma \gg 1$ (valid for our high energy regime), is given by

$$m_e^{\mathrm{eV}} c^2 \frac{d\gamma_e}{dt}(t,\alpha) = eE\,(t,\alpha)\,cA - \frac{2}{3}\frac{\mu_0}{6\pi}\frac{e^4 c \sin(\alpha)^2 A \gamma_e^2\,(t,\alpha)\,B^2\,(t,\alpha)}{m_e^2}, \tag{H.2}$$

where $A = 6.24 \times 10^{18}$ is the transformation constant between Joule to eV and μ_0 the vacuum permeability constant. The first term on the right side in Eq. (H.2) corresponds to the energy gain by each electron due the electric field, while the second term represents the energy lost by synchrotron emission (see, for example, [138])

$$P_{synch,e}(t,\alpha) \equiv \frac{dE_{synch,e}}{dt} = \frac{2}{3}\frac{\mu_0}{6\pi}\frac{e^4 c \sin(\alpha)^2 A}{m_e^2}\gamma_e^2\,(t,\alpha)\,B^2\,(t,\alpha)\,, \tag{H.3}$$

where α is the "*pitch angle*" between the electrons and the magnetic field. Since we are in the relativistic regime, the synchrotron photons are beamed along the direction of motion of the electrons. Then we can easily assume that α is also the angle between the emitted synchrotron photons and the magnetic field.
As we can guess, by the synchrotron and the MPP mechanism, a particles shower can develops. The evolution of the number of synchrotron photons with time can be written as

$$\frac{dN_\gamma}{dt}(t,\alpha) = N_\pm(t,\alpha)\,\frac{P_{synch,e}(t,\alpha)}{\varepsilon_\gamma^e(t,\alpha)}, \tag{H.4}$$

where

$$\varepsilon_\gamma^e(t,\alpha) = (0.29)\frac{3}{4\pi}\frac{ehA}{me}\gamma_e^2(t,\alpha)B(t,\alpha)\sin(\alpha) = D_e\gamma_e^2(t,\alpha)B(t,\alpha)\sin(\alpha), \tag{H.5}$$

is the peak energy of synchrotron photons and $N_\pm$ is the number of created pairs by MPP process. The number of pairs are strictly related to the number of photons. Then, the equation for the evolution of the number of created pairs $N_\pm$ can be written as

$$\frac{dN_\pm}{dt}(t,\alpha) = N_\gamma\,(t,\alpha)\,R_A\,(t,\alpha)\,c. \tag{H.6}$$

In Eq. (H.6) the term R_A^e is the attenuation coefficient (see [40]) defined as

$$R_A(t,\alpha) = (0.23)\frac{\alpha_f}{\lambda}\frac{B\,(t,\alpha)}{B_{cr}}\sin(\alpha)\exp\left[-\frac{4}{3\chi\left(\varepsilon_\gamma, B\right)}\right], \tag{H.7}$$

where α_f is the fine structure constant and $\lambda\!\!\!^{-} = \lambda/2\pi = \hbar/2\pi m_e c$ is the reduced Compton wavelength. The attenuation coefficient gives us the scale where the MPP process becomes important and it has the dimension of cm^{-1}. Then R_A^{-1} represents the photon mean free path for magnetic pair production. Another important quantity that measures the strength of the MPP process is the parameter χ_e, defined as $\chi_e(t,\alpha) = \left(\varepsilon_\gamma / 2m_e^{\text{eV}} c^2\right) \sin(\alpha)\,(B(t,\alpha)/B_{cr})$ [3].
At this point, in order to complete the set of our equations, we need another differential equation that describe the evolution with time of the magnetic field. We can derive it starting to consider the current created by the accelerated electrons $I = e v_\perp n_\lambda$, where n_λ is the linear number density of pairs $(\#/cm)$ and $v_\perp$ the perpendicular velocity of the electrons (with respect to the magnetic field). $v_\perp$ is the most important variable of this work, because is the perpendicular velocity that allows the particles to circularize around the magnetic field lines and produce an induced magnetic field. The pair linear number density can be calculated from the definition of the total number of the created pairs

$$N_\pm = \int n_\lambda dl \Longrightarrow n_\lambda(t) = \frac{dN_\pm}{dl} = \frac{dN_\pm}{cdt}. \tag{H.8}$$

The electrons move around orbits of radius given by the Larmor radius

$$R_L(t,\alpha) = \frac{p_\perp(t,\alpha)}{eB(t,\alpha)} = \frac{\gamma_e(t,\alpha) m_e c \beta_\perp(t,\alpha)}{eB(t,\alpha)} = \frac{\gamma_e(t,\alpha) m_e c \sin(\alpha)}{eB(t,\alpha)}.$$

[4]Then, the induced magnetic field can be calculated as:

$$\vec{B}_{ind}(t,\alpha) = \frac{\mu_0 I}{2R_L(t,\alpha)}\hat{z} = \frac{\mu_0 e^2}{2m_e c}\frac{B(t,\alpha)}{\gamma_e(t,\alpha)}\frac{dN_\pm(t,\alpha)}{dt}. \tag{H.9}$$

Here we have considered that the Larmor's radius evolves with time not only because of $\gamma_e(t,\alpha)$, but also thanks to $B(t,\alpha)$. This is because the motion of the pairs creates this induced magnetic field and, consequently, their motion is perturbed by this effect.
Then the total magnetic field $B(t,\alpha) = B_0 - B_{ind}(t,\alpha)$ becomes

$$B(t,\alpha) = \frac{B_0}{\left[1 + \frac{\mu_0 e^2}{2m_e c}\frac{1}{\gamma_e(t,\alpha)}\frac{dN_\pm(t,\alpha)}{dt}\right]}. \tag{H.10}$$

We need to solve at the same time the system of equations composed by Eqs. (H.2) (H.3) (H.4) (H.6). Since every equation of this system depends on the evolution of the magnetic field, we need to study the evolution with time of $B(t,\alpha)$ and, then, to write a differential equation for it $\frac{dB(t,\alpha)}{dt} = \frac{d}{dt}\left(B_0 - B_{ind}(t,\alpha)\right) = -\frac{dB_{ind}(t,\alpha)}{dt}$, where B_0 is the initial background magnetic field. We derive the complete formula for the evolution of the magnetic field in the next section.

H.3 Normalization

In order to integrate our system of equations, it is better to work with normalized quantities. We introduce two useful quantities: 1) the dimensionless time $\tilde{t} = t/\tau_c$; 2) B_c a normalization factor for the magnetic field. This normalization it has been made only to delete all the constants in the equations and does not have any physical meaning. Let's start from Eq. (H.2). Introducing these two quantities in the equation and calling $\tilde{B} = B/B_c$, we get

$$\frac{1}{B_c^2 \tau_c}\frac{d\gamma_e}{d\tilde{t}}(\tilde{t}\tau_c,\alpha) = \frac{K_e}{B_c}\tilde{B}(\tilde{t}\tau_c,\alpha) - Z_e^{'}\tilde{B}^2(\tilde{t}\tau_c,\alpha)\,\gamma_e^2(\tilde{t}\tau_c,\alpha)\sin^2(\alpha), \tag{H.11}$$

[3] The $\sin(\alpha)$ here considers the inclination between the photon vector and the magnetic field.
[4] Where we assume $\beta = 1$ since we are working in the high energy regime.

where $K_e = \left(ec^2A/m^{\rm eV}c^2\right)\left(\bar{J}/2\bar{M}^2\right)$ and $Z_e^{'} = 2/3\,(\mu_0/6\pi)\left(e^4cA/m_e^2m^{\rm eV}c^2\right)$.
In complete generality, we can define $\tilde{\gamma}_e\,(\tilde{t},\alpha) \equiv \gamma_e(\tilde{t}\tau_c,\alpha)$ and $\tilde{B}^{'}(\tilde{t},\alpha) \equiv \tilde{B}(\tilde{t}\tau_c,\alpha)$ (we will make the same definition for the others variables in the set of equations).
The two quantities τ_c and B_c are defined in such a way that:

$$\tau_c B_c K_e = 1 \implies \tau_c = \frac{1}{B_c K_e} = \frac{Z_e^{'}}{K_e^2}, \tag{H.12a}$$

$$Z_e^{'}\tau_c B_c^2 = 1 \implies B_c = \frac{K_e}{Z_e^{'}}. \tag{H.12b}$$

Finally we can write

$$\frac{d\tilde{\gamma}_e}{d\tilde{t}}(\tilde{t},\alpha) = \tilde{B}^{'}(\tilde{t},\alpha)\left(1 - \tilde{B}^{'}(\tilde{t},\alpha)\sin^2(\alpha)\tilde{\gamma}_e^2(\tilde{t},\alpha)\right). \tag{H.13}$$

For the electrons synchrotron power, Eq. (H.3), defining Z_e as the coefficient in front of $(B(t,\alpha),\gamma_e(t,\alpha)\sin(\alpha))^2$ and operating the same procedure as before, we get

$$\frac{d\widetilde{E}_{\rm synch,e}(\tilde{t},\alpha)}{d\tilde{t}} = m_e^{\rm eV}c^2\widetilde{B^{'}}^2(\tilde{t},\alpha)\widetilde{\gamma_e^2}(\tilde{t},\alpha)\sin^2(\alpha). \tag{H.14}$$

Defining $\widetilde{E^{'}}_{\rm synch,e}(\tilde{t},\alpha) = \widetilde{E}_{\rm synch,e}(\tilde{t},\alpha)/m_e^{\rm eV}c^2$, we have

$$\frac{d\widetilde{E^{'}}_{\rm synch,e}(\tilde{t},\alpha)}{d\tilde{t}} = \widetilde{B^{'}}^2(\tilde{t},\alpha)\widetilde{\gamma_e^2}(\tilde{t},\alpha)\sin^2(\alpha). \tag{H.15}$$

The equation for the number of created photons dN_γ/dt can be written as

$$\frac{dN_\gamma}{dt}(t,\alpha) = N_\pm(t,\alpha)\frac{P_{synch}}{\varepsilon_\gamma^e} = N_\pm(t,\alpha)\frac{Z_e\sin^2(\alpha)B^2\gamma_e^2}{D_e\gamma_e^2 B\sin(\alpha)} = \frac{Z_e}{D_e}B\sin(\alpha)N_\pm \times \frac{B_c}{B_c} = \frac{Z_eB_c}{D_e}\sin(\alpha)\tilde{B}N_\pm. \tag{H.16}$$

Before to continue with the normalization of the equation for the number of photons, we need to take into account the equation for the pairs. Before we rewrite firstly the χ_e parameter as

$$\tilde{\chi}_e(\tilde{t},\alpha) \equiv \frac{\chi_e}{G_e} = \tilde{\gamma}_e^2(\tilde{t},\alpha)\tilde{B^{'}}^2(\tilde{t},\alpha)\sin^2(\alpha), \tag{H.17}$$

with $G_e = \left(D_eB_c^2\right)/\left(2m_e^{\rm eV}c^23B_{cr}\right)$, where B_{cr} is the critical magnetic field.
Now, defining $S = (0.23)\left(\alpha_f c/\lambda\right)(B_c/B_{cr})$, we can write the attenuation coefficient as

$$R_A c = S\,\tilde{B}\sin(\alpha)\exp\left[-\frac{4}{3G_e\tilde{\chi}_e}\right], \tag{H.18}$$

and then, defining $\tilde{R}_A^{'} \equiv R_A c/S$, we get

$$\tilde{R}_A^{'} = \tilde{B}^{'}\sin(\alpha)\exp\left[-\frac{4}{3G_e\tilde{\chi}_e}\right]. \tag{H.19}$$

Then, we can write the equation for the pairs as

$$\frac{dN_\pm^{'}}{d\tilde{t}}(\tilde{t},\alpha) = N_\gamma\tau_c S\tilde{R}^{'}(\tilde{t},\alpha). \tag{H.20}$$

Defining $\tilde{N^{'}}_\pm = N_\pm^{'}/S\,\tau_c$, we get

$$\frac{d\tilde{N^{'}}_\pm}{d\tilde{t}} = N_\gamma\tilde{R^{'}}_A. \tag{H.21}$$

Going back the equation for the number of photons, we can write it as

$$\frac{dN_\gamma^{'}}{d\tilde{t}} = \frac{Z_e\tau_c B_c}{S\,D_e\tau_c}\sin(\alpha)\tilde{B}^{'}(\tilde{t},\alpha)\tilde{N}^{'}{}_{\pm} = \frac{Z_e B_c}{S\,D_e}\sin(\alpha)\tilde{B}^{'}(\tilde{t},\alpha)\tilde{N}^{'}{}_{\pm} = F_e\sin(\alpha)\tilde{B}^{'}(\tilde{t},\alpha)\tilde{N}^{'}{}_{\pm}, \tag{H.22}$$

and then, defining $\tilde{N}^{'}{}_{\gamma} \equiv \tilde{N}_\gamma/F_e = N_\gamma/F_e$, we get finally

$$\frac{d\tilde{N}^{'}{}_{\gamma}}{d\tilde{t}} = \sin(\alpha)\tilde{B}^{'}(\tilde{t},\alpha)\tilde{N}^{'}{}_{\pm}(\tilde{t},\alpha). \tag{H.23}$$

Consequently, the equation for the number of pairs becomes

$$\frac{d\tilde{N}^{'}{}_{\pm}}{d\tilde{t}} = F_e\tilde{N}^{'}{}_{\gamma}\tilde{R}^{'}{}_{A}. \tag{H.24}$$

At this point we need to make the derivative of the magnetic field. Dividing by B_c the equation for the magnetic field Eq. (H.10), substituting Eq. (H.21) and make the derivative, we have

$$\frac{d\tilde{B}^{'}}{d\tilde{t}}(\tilde{t},\alpha) = -\frac{d}{d\tilde{t}}\left(V_e\frac{\tilde{B}^{'}}{\tilde{\gamma}_e}\frac{d\tilde{N}^{'}{}_{\pm}}{d\tilde{t}}\right), \tag{H.25}$$

where we have defined $V_e = \mu_0 e^2 S/2m_e c$. The derivative gives

$$\frac{d\tilde{B}^{'}}{d\tilde{t}} = -V_e\left[\left(\frac{d\tilde{B}^{'}}{d\tilde{t}}\frac{1}{\tilde{\gamma}_e} + \tilde{B}^{'}\frac{d\tilde{\gamma}_e}{d\tilde{t}}\frac{1}{\tilde{\gamma}_e^2}\right)\frac{d\tilde{N}^{'}{}_{\pm}}{d\tilde{t}} + F_e\frac{\tilde{B}^{'}}{\tilde{\gamma}_e}\left(\frac{d\tilde{N}^{'}{}_{\gamma}}{d\tilde{t}}\tilde{R}^{'}{}_{A} + \tilde{N}^{'}{}_{\gamma}\frac{d\tilde{R}^{'}{}_{A}}{d\tilde{t}}\right)\right]. \tag{H.26}$$

The derivative of $\tilde{R}^{'}{}_{A}$ is

$$\frac{d\tilde{R}^{'}{}_{A}}{d\tilde{t}} = \sin(\alpha)\exp\left[-\frac{4}{3G_e\tilde{\chi}_e}\right]\left(\frac{d\tilde{B}^{'}}{d\tilde{t}} + \frac{4}{3G_e}\tilde{B}^{'}\frac{\dot{\tilde{\chi}}_e}{\tilde{\chi}_e^2}\right), \tag{H.27}$$

while the derivative of $\tilde{\chi}_e$ is

$$\dot{\tilde{\chi}}_e = 2\tilde{\gamma}_e\tilde{B}^{'}\sin^2(\alpha)\left(\dot{\tilde{\gamma}}_e\tilde{B}^{'} + \tilde{\gamma}_e\dot{\tilde{B}}^{'}\right). \tag{H.28}$$

Making all the derivatives, in the end we get

$$\frac{d\tilde{B}^{'}}{d\tilde{t}} = -\frac{\frac{V_e}{\tilde{\gamma}_e}\left[\frac{\tilde{B}^{'}}{\tilde{\gamma}_e}\frac{d\tilde{\gamma}_e}{d\tilde{t}}\frac{d\tilde{N}^{'}{}_{\pm}}{d\tilde{t}} + F_e\exp\left[-\frac{4}{3G_e\tilde{\chi}_e}\right]\left(\tilde{B}^{'2}\sin(\alpha)\frac{d\tilde{N}^{'}{}_{\gamma}}{d\tilde{t}} + \frac{8}{3G_e}\frac{\tilde{N}^{'}{}_{\gamma}}{\sin(\alpha)\tilde{\gamma}_e^3}\frac{d\tilde{\gamma}_e}{d\tilde{t}}\right)\right]}{1 + \frac{V_e}{\gamma_e}\left(\frac{d\tilde{N}^{'}{}_{\pm}}{d\tilde{t}} + F_e\tilde{N}^{'}{}_{\gamma}\exp\left[-\frac{4}{3G_e\tilde{\chi}_e}\right]\left(\tilde{B}^{'}\sin(\alpha) + \frac{8}{3G_e}\frac{1}{\tilde{\gamma}_e^2\tilde{B}^{'}\sin(\alpha)}\right)\right)}. \tag{H.29}$$

The set of equations that we need to integrate at the same time is composed by the Eqs. (H.13), (H.15), (H.23), (H.24) and (H.29). In the next section we will show the results of this integration.

H.4 Results

In this section we show the results of the integration of the equations presented in the previous sections. The integrations are made with different values of initial parameters: we select four pitch angles $\alpha = \pi/3, \pi/9, \pi/18, \pi/30$; four initial magnetic field $B_0 = 6.7B_{cr}$, $0.1B_{cr}$, $0.01B_{cr}$, 2×10^{11} Gauss; three initial number of pairs $N_\pm = \left(1, 10^5, 10^{10-13}\right)$ [5]. The initial value of $B_0 = 2\times10^{11}$ Gauss has a particular meaning because it is the lowest initial value for the magnetic field that can be screened. For $B_0 < 2\times10^{11}$ Gauss there is no screening effect since no pairs are produced by the MPP process.
We are going to show the results for the four different B_0, varying the pitch angles and the initial number

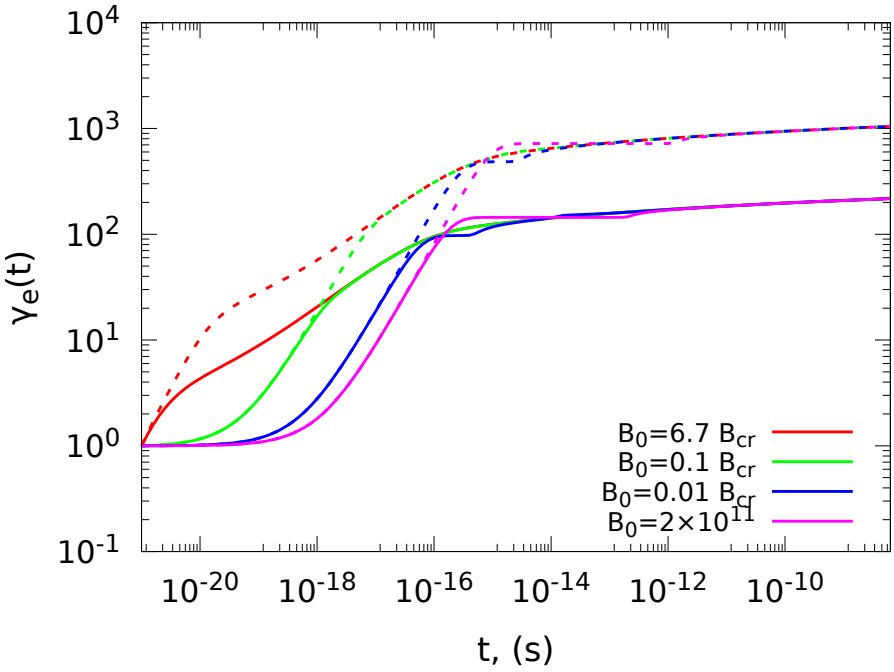

Figure H.1. Electron Lorentz factor for $B_0 = 6.7B_{cr}$, $0.1\,B_{cr}$, $0.01\,B_{cr}$ and $B_0 = 2 \times 10^{11}$ G, for $N_{\pm,0} = 1$ and $\alpha = \pi/3$ (solid lines), $\pi/18$ (dashed lines).

of pairs. In Fig. (H.1) we show the electron Lorentz factor with the four values of B_0, for $\alpha = \pi/3$, $\pi/18$ and $N_{\pm,0} = 1$. Increasing the number of pair does not change the shape of the curve of γ_e.

As it is clear from Eq. (H.2) and Fig. (H.1), there is an asymptotic value of γ_e that depends only by the pitch angle α. Varying the initial magnetic field can change only the dynamic of the electrons. Indeed, for higher value of B_0, the electrons gain energy more smoothly but constantly. Instead, for lower values of B_0 the growth toward the asymptotic value occurs at longer time and it is more steep. This behaviour is strictly correlated with the evolution of the magnetic field with time. The latter is shown in Fig. (H.2), where the result for the magnetic field screening is presented for the same initial values of B_0, but for $N_{\pm,0} = 1$, 10^{10} and $\alpha = \pi/3$. We can see that, decreasing the initial value of the magnetic field, $\gamma_e(t)$ reaches the balance at longer time and starts to increase its value towards the asymptotic one when the screening effect starts to operate (namely $B(t)$ decreases). From this figure we can see how the magnetic field decrease changes depending on the initial values of the parameters. Indeed we notice that when $N_{\pm,0} = 1$ the decreases is only due to the MPP process and the circularization of these pairs around the magnetic field lines. If one increases the initial number of pairs, the magnetic field initially decreases faster and, later, starts to decreases slower. This characteristic derives from the fact that, for the second case, the faster decreases of $B(t)$ is made by the initial particles. When the MPP process starts to have a significant impact, $B(t)$ starts to decrease slower. Another characteristic is that, independently by the initial conditions, there is a common asymptotic value that $B(t)$ reaches at longer time. We will explain below how to derive this asymptotic value and will show that it depends only by the spin of the BH.
The number of synchrotron photons and the consequent number of pairs are shown in Fig. (H.3) and Fig. (H.4), respectively, with the same values for the initial parameters as in Fig. (H.2).

Figs. (H.3) and (H.4) suggest us that not all the photons are converted in a pairs via the MPP process. Moreover, since all the equations of the model are coupled, also $N_\gamma(t)$ and $N_\pm(t)$ reach asymptotic values independently of B_0, $N_{\pm,0}$ and α. Consistently with the evolution of $B(t)$, for different initial parameters,

[5] The highest value of the initial number of pairs depends on of the others initial parameters (α, B_0) that we choose for the specific integration.

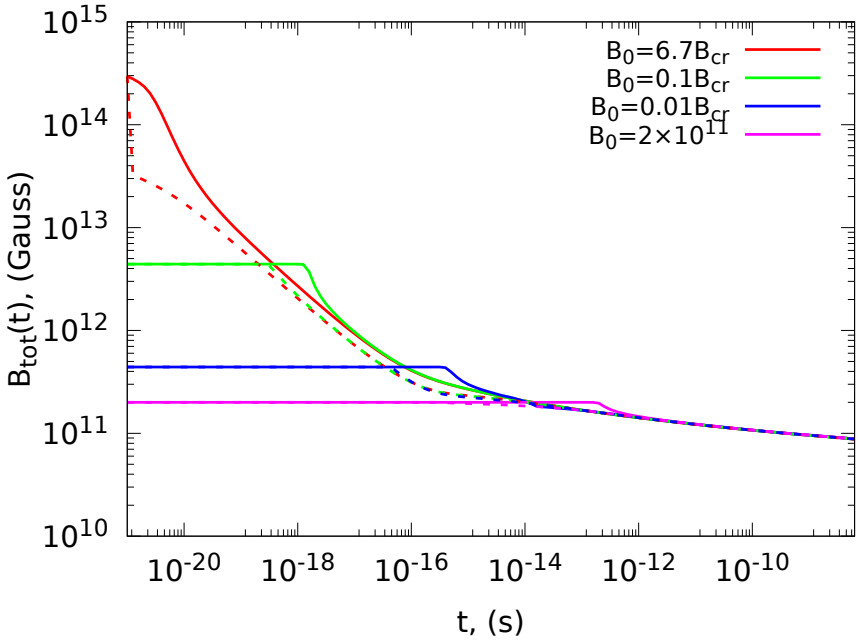

Figure H.2. The decrease of the magnetic field is shown for the four selected B_0, $N_{\pm,0} = 1$ (solid lines) and $N_{\pm,0} = 10^{10}$ (dashed lines), for $\alpha = \pi/3$.

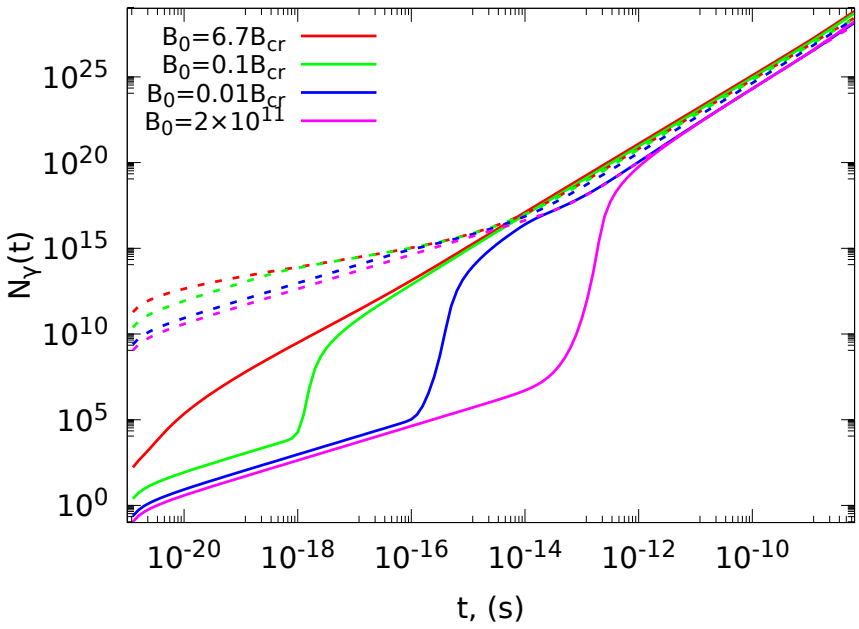

Figure H.3. Number of synchrotron photons for the same parameter of Fig. (H.2).

we note that both N_γ and $N_\pm$ start to increase at longer times if we decrease B_0 .
In Figs. (H.5), (H.6) and (H.7) are shown the same variables of Figs. (H.2), (H.3), (H.4), respectively, for the same parameters but for $\alpha = \pi/18$ and, instead of $N_{\pm,0} = 10^{10}$, here we use $N_{\pm,0} = 10^{13}$.

In Fig. (H.8), we show the electron synchrotron total energy emitted by the accelerated electrons, for the four values of the magnetic field selected above, for $N_{\pm,0} = 1$ (increasing the number of particles does not change the shape of the curves), for $\alpha = \pi/3$ (solid lines) and $\alpha = \pi/18$ (dashed lines). As we

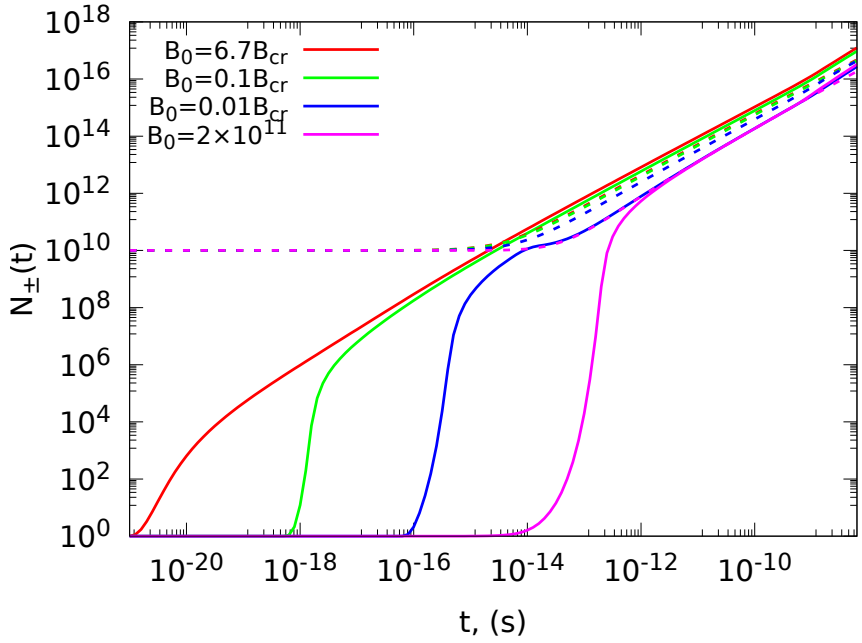

Figure H.4. Number of pairs created by MPP process, for the same initial parameters as in Fig. (H.2).

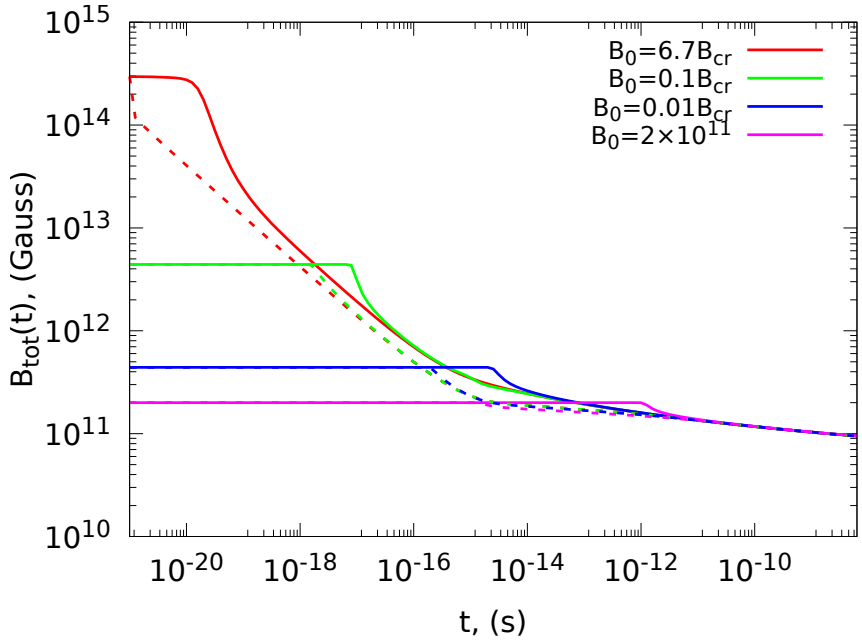

Figure H.5. The decrease of the magnetic field is shown for the four selected B_0, $N_{\pm,0} = 1$ (solid lines) and $N_{\pm,0} = 10^{13}$ (dashed lines), for $\alpha = \pi/18$.

noticed above, there is a common asymptotic value of the magnetic field, that does not depend on the initial number of pairs, the pitch angle and the initial magnetic field. As we can see, at longer times, all the curves tend to coincide to a common value. Then, this value is general and can be derived considering Eq. (H.18) for the attenuation factor. At longer times, the magnetic pair production is less efficient because the photons have less probability to interact with lower intense magnetic field (after the reduction). This implies that $R_A \to 0 \Longrightarrow R_A^{-1} \longrightarrow \infty$. This condition occurs when the exponential factor in Eq. (H.18)

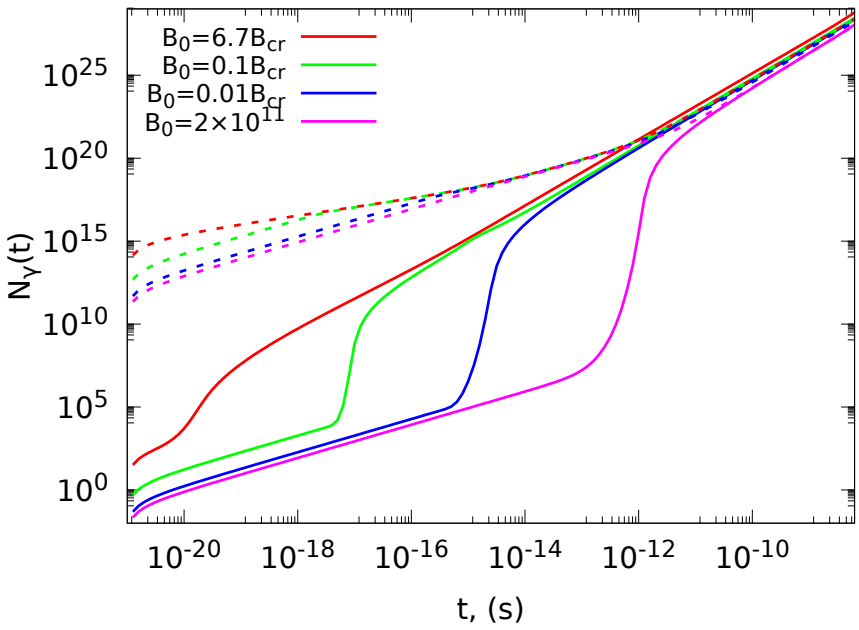

Figure H.6. Number of synchrotron photons for the same parameter of Fig. (H.5).

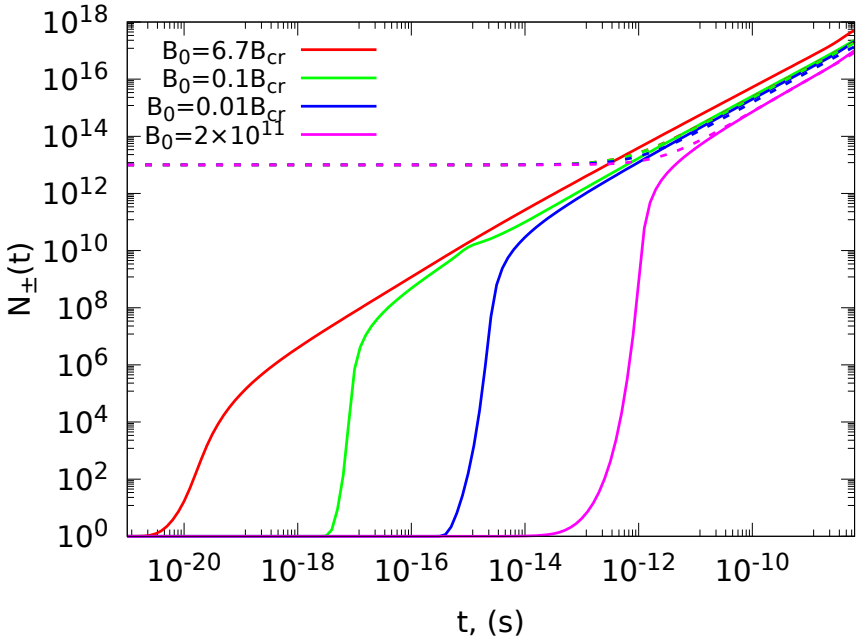

Figure H.7. Number of pairs created by MPP process, for the same initial parameters as in Fig. (H.5).

tends to $0 \Longrightarrow \chi_e \ll 1$. From this condition we get

$$B^2 \ll \frac{8\pi}{3(0.29)} \frac{m_e m_e^{\mathrm{eV}} c^2 B_{cr}}{ehA} \frac{1}{\gamma_e^2 \sin^2(\alpha)}. \tag{H.30}$$

Since we are looking to the asymptotic value of the variables, we need to derive the one for γ_e. This can be get requiring the balance between the energy gain and the energy loss in Eq. (H.2). Indeed, at longer

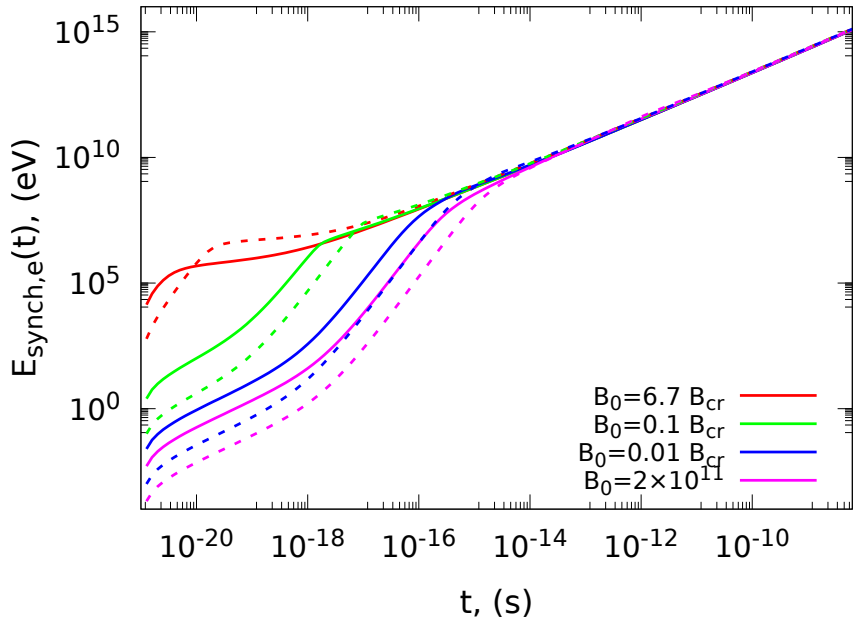

Figure H.8. Total synchrotron energy emitted by the accelerated electrons, for the four selected values of B_0, $N_{\pm,0} = 1$, $\alpha = \pi/3$ (solid lines) and $\alpha = \pi/18$ (dashed lines).

time, $d\gamma_e/dt \to 0$ and, then, the asymptotic value for γ_e is given by

$$\gamma_{e,asympt} = \sqrt{\frac{\xi(\eta)}{B\sin^2(\alpha)}}, \tag{H.31}$$

where $\xi(\eta) = \frac{9\pi}{2}\left(cm_c^2/\mu_0 e^3\right)\eta$, with $\eta = \bar{J}/\bar{M}^2$ is the spin of the BH. Inserting Eq. (H.31) in Eq. (H.30), we get an upper limit for the asymptotic magnetic field:

$$B \ll B^* \equiv \frac{16}{27(0.29)}\frac{m_e^{\rm eV}c^2 B_{cr}\mu_0 e^2}{hAcm_e}\frac{1}{\eta} = 4.088\,\frac{\alpha_f B_{cr}}{\eta}\,G, \tag{H.32}$$

where we have used the definition of $\mu_0 = 1/(\varepsilon_0 c^2)$ and $\alpha_f = e^2/(4\pi\varepsilon_0\hbar c)$. The real asymptotic value of the magnetic field B_{asympt}, derived from the simulations, at fixed values of the BH spin, for the four chosen pitch angles, are tabulated in Tab. (H.1). We see that, for a fixed value of the spin, the asymptotic magnetic field enhances increasing the pitch angle and, changing the spin with fixed pitch angle, it enhances decreasing the spin. This behaviour is consistent with Eq. (H.30). From the results of the simulations exposed in Tab. (H.1), we notice that between B^* and B_{asympt} there is a proportionality relation with a coefficient that varies between 41 and 47, which decreases if one increases the spin of the BH. This relation can be derived from Eq. (H.31) if one derives B_{asympt} as a function of γ_{asympt} and where the value of the latter is taken from the simulations. The ratio between B^* and this B_{asympt} results:

$$\frac{B^*}{B_{asympt}} = \Theta\,\alpha_f B_{cr}\left(\frac{\gamma^e_{asympt}\sin(\alpha)}{\eta}\right)^2, \tag{H.33}$$

where $\Theta = (64/243(0.29)\pi)\left(\mu_0 e^3 m_e^{\rm eV}c^2/Am_e^3c^3\right)$. The coefficient above is the right side of Eq. (H.33).

We should note that notwithstanding the plots of the electron Lorentz factor γ_e seems to suggest us that, after a time interval when $\gamma_e = const$ due to the balance between the energy gain and loss in Eq. (H.2), there is an increase of the energy gain since the γ_e increases, this is not true because at each

	$\eta = 0.7$	$\eta = 0.46$	$\eta = 0.23$
$\frac{\pi}{3}$	4.23	6.27	12
$\frac{\pi}{9}$	4.36	6.45	12.4
$\frac{\pi}{18}$	4.12	6.58	12.6
$\frac{\pi}{30}$	4.54	6.7	12.8

Table H.1. Asymptotic values of the magnetic field (in units of 10^{10} Gauss) for BH spin $\eta \equiv \bar{J}/\bar{M}^2 = 0.7, 0.46, 0.23$, for four pitch angles $\alpha = \pi/3, \pi/9, \pi/18, \pi/30$. The values of the spin are indicative only, they can be changed.

point of this grow the electron Lorentz factor is the asymptotic one given by Eq. (H.31). Indeed, from these results, we can see that γ_e starts to increase when the magnetic field starts to decrease. Then, the Lorentz factor increases in order to maintain the energy balance.

H.4.1 Screening time scale

Here we derive an useful formula for the screening time scale t_{screen}, namely the time scale neccassary for the magnetic field to be screened. The screening time scale is defined as $t_{screen} = \left|B/\dot{B}\right|$. In order to derive it, we require that, for $t \to \infty$, $t_{screen} \to \infty$. Under this limit $d\tilde{\gamma}_e/d\tilde{t} \to 0$. Then, from the definition of t_{screen} and Eq. (H.29), we get

$$\tilde{t}_{screen} = \left[\frac{2}{\tilde{B}'\sin(\alpha)} + \frac{8}{3G_e}\frac{1}{\tilde{\gamma}_e^2 \tilde{B}'^3 \sin^3(\alpha)}\right]\frac{\tilde{N}'_\gamma}{\tilde{N}'_\pm}. \tag{H.34}$$

This expression approximates well the behaviour of the screening process evolution. In Fig. (H.9) t_{screen} is plotted as a function of B for the four selected pitch angles (with $N_{\pm,0} = 1$), while in Fig. (H.10) we show t_{screen} as function of time for the four selected B_0 (with $\alpha = \pi/3$ and $N_{\pm,0} = 1$). As one can see

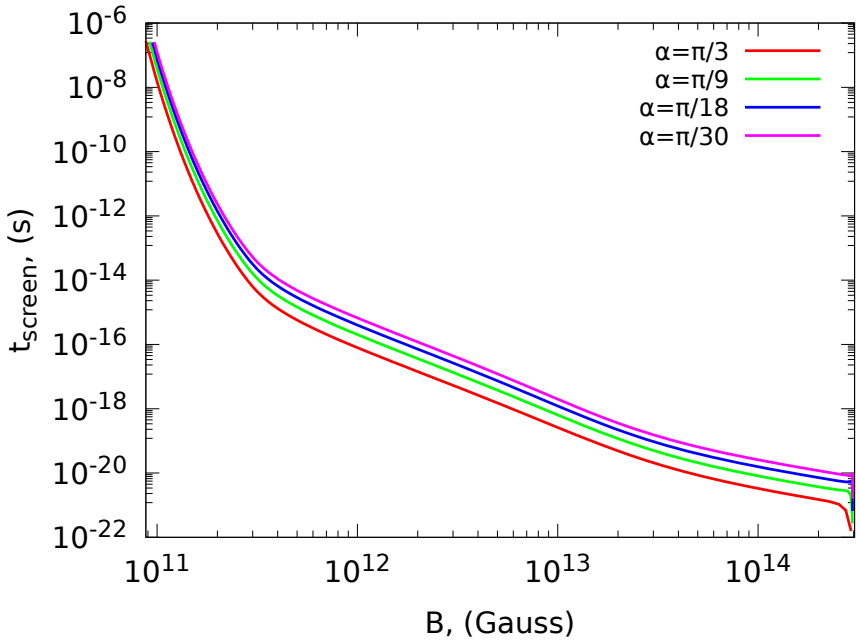

Figure H.9. t_{scren} as a function of the magnetic field, for the four selected pitch angles (as before) and with $N_{\pm,0} = 1$.

from Fig. (H.9), when the magnetic field decreases, t_{screen} tends to diverge (independently by the pitch angle), as we expected. Instead from Fig. (H.10), we can see that, depending on the different B_0, the

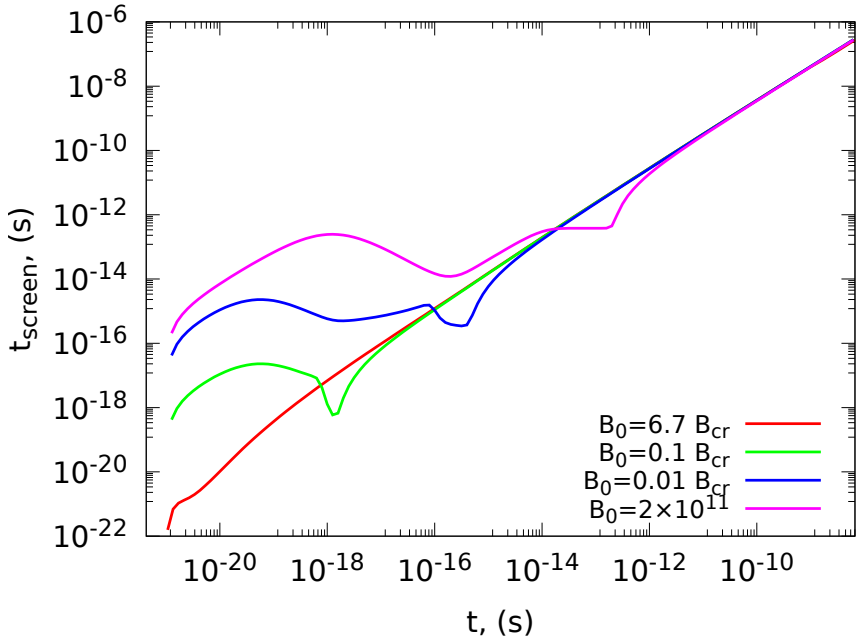

Figure H.10. t_{screen} as a function of time, for the four selected initial magnetic field B_0 at a fixed pitch angle $\alpha = \pi/3$ and $N_{\pm,0} = 1$.

screening starts to act at different times (at short time for high B_0; at longer time for low B_0). This is in good agreement with the results exposed in Fig. (H.5). By these considerations, we deduce that the formula for t_{screen} that we derived in Eq. (H.34), even if it is an approximated one, it fits well the dynamic of the process at each time.

H.5 Summary and Discussion

In this appendix, we have studied to screening process of an electromagnetic field, near a Kerr BH, due to the creation of a huge number of e^+e^- pairs emerging from the MPP process. The magnetic pair production process occurs through the interaction between synchrotron photons, emitted by accelerated electrons/positrons, and a background magnetic field B_0. We write down the equations that: 1) govern the dynamic of the accelerated pairs in this system; 2) the particles shower ruled by the MPP process and the synchrotron emission by the initial and the new created pairs; 3) the screening effect of the magnetic and electric field. We made simulations varying the values of the following initial parameters: magnetic field B_0, number of pairs $N_{\pm,0}$, pitch angle α and the spin η of the BH. The principal results that we got from these simulations can be resumed as follow:

1. the results does not depend much on $N_{\pm,0}$. The only effect that we get enhancing the initial number of pairs consists to the fact that the magnetic field starts to decrease faster in the beginning (where the screening work is done by the initial number of pairs) and, consequently, decreases smoothly (where the screening work is done by the new created pairs plus the initial one).

2. varying the pitch angle affects only the asymptotic value of the electron Lorentz factor: the smaller is the pitch angle the higher is γ^e_{asympt}.

3. the decrease of the magnetic field occurs at longer time if one decreases the B_0 or α. The first characteristic can be understood if we take into account the cross-section for the MPP process σ_{MPP}(see [15]). Indeed, if one decreases the magnetic field, the cross-section and, then, the

probability of interaction between photons and magnetic field becomes low. This problem is easily solved if one enhances the number of photons. We can appreciate this behaviour looking at Figs. (H.3) (H.6), in correlation with Figs. (H.4) (H.7). We can see that only when the number of photons becomes huge, the MPP process starts to act (with the consequent decrease of $B(t)$). In Fig. (H.11) is shown σ_{MPP} as a function of B, for the four selected pitch angles [6].
The second characteristic can be understood easily since, if we decrease the pitch angle, the particles have smaller tangential velocity, which is the component that produce the screening effect.

4. there is a common value for the magnetic field that is reached at longer time, independently by B_0, $N_{\pm,0}$ and α. This value depends only by the spin of the BH (see Eq. (H.32)).

5. there is a common value also for the variables (γ_e, N_γ, $N_\pm$, $E_{\rm synch,e}$, t_{screen}), independently by the initial parameters. The only asymptotic value that depends on the pitch angles is the electrons Lorentz factor.

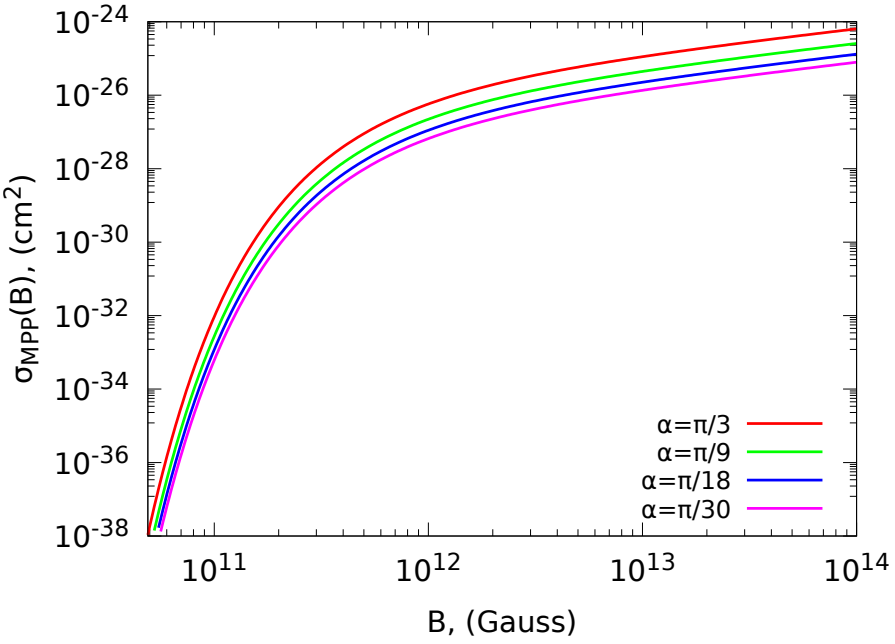

Figure H.11. MPP cross-section as a function of B, for some fixed pitch angles.

From these results we deduce that the screening effect can have a strong impact in the reduction of a strong electromagnetic field for extreme astrophysical systems as BH or NS.

[6] In order to get this $\sigma_{MPP}(B)$, we needed to integrate the equation for the differential cross-section $d\sigma_{MPP}/dB$ fixing the value of the synchrotron photon energy (given by Eq. (H.5)), which depends only by the pitch angles, since (as we explained in the derivation of Eq. (H.31)) when $B(t)$ decreases, γ_e increases in order to maintain the energy balance. This means that the synchrotron photons remains with a constant energy.

Bibliography

[1] Available from: http://pdg.lbl.gov/2014/hadronic-xsections/hadron.html.

[2] Available from: http://pdg.lbl.gov/2018/html/computer_read.html.

[3] Particle Data Group.

[4] Aartsen, M., et al. The search for transient astrophysical neutrino emission with icecube-deepcore. *The Astrophysical Journal*, **816** (2016), 75.

[5] Aasi, J., et al. Advanced ligo. *Classical and quantum gravity*, **32** (2015), 074001.

[6] Abbasi, R., et al. The design and performance of icecube deepcore. *Astroparticle physics*, **35** (2012), 615.

[7] Abbasi, R., et al. Search for sub-tev neutrino emission from transient sources with three years of icecube data. *arXiv preprint arXiv:2011.05096*, (2020).

[8] Abbott, B. P., et al. Gravitational waves and gamma-rays from a binary neutron star merger: Gw170817 and grb 170817a. *The Astrophysical Journal Letters*, **848** (2017), L13.

[9] Abbott, B. P., et al. Gw170817: observation of gravitational waves from a binary neutron star inspiral. *Physical Review Letters*, **119** (2017), 161101.

[10] Acernese, F., et al. Advanced virgo: a second-generation interferometric gravitational wave detector. *Classical and Quantum Gravity*, **32** (2014), 024001.

[11] Ackermann, M., et al. Fermi-LAT Observations of the Gamma-Ray Burst GRB 130427A. *Science*, **343** (2014), 42. arXiv:1311.5623, doi:10.1126/science.1242353.

[12] Aharonian, F. A. and Atoyan, A. M. Broad-band diffuse gamma ray emission of the galactic disk. *A&A*, **362** (2000), 937. arXiv:astro-ph/0009009.

[13] Aimuratov, Y. *Gamma-Ray Bursts within Fireshell Model*. Ph.D. thesis, Universitá di Roma "La Sapienza", International Center for Relativistic Astrophysics (ICRANeT) (2020).

[14] Amaro-Seoane, P., et al. Laser interferometer space antenna. *arXiv preprint arXiv:1702.00786*, (2017).

[15] Anguelov, V. and Vankov, H. Electromagnetic showers in a strong magnetic field. *Journal of Physics G: Nuclear and Particle Physics*, **25** (1999), 1755.

[16] Arcavi, I., et al. Optical emission from a kilonova following a gravitational-wave-detected neutron-star merger. *Nature*, **551** (2017), 64.

[17] Bahcall, J. N. and Mészáros, P. 5–10 gev neutrinos from gamma-ray burst fireballs. *Physical Review Letters*, **85** (2000), 1362.

[18] Bartos, I., Beloborodov, A., Hurley, K., and Marka, S. Detection prospects for gev neutrinos from collisionally heated gamma-ray bursts with icecube/deepcore. *Physical Review Letters*, **110** (2013), 241101.

[19] Becerra, L., Bianco, C. L., Fryer, C. L., Rueda, J. A., and Ruffini, R. On the Induced Gravitational Collapse Scenario of Gamma-ray Bursts Associated with Supernovae. *The Astrophysical Journal*, **833** (2016), 107. arXiv:1606.02523, doi:10.3847/1538-4357/833/1/107.

[20] Becerra, L., Cipolletta, F., Fryer, C. L., Rueda, J. A., and Ruffini, R. Angular Momentum Role in the Hypercritical Accretion of Binary-driven Hypernovae. *The Astrophysical Journal*, **812** (2015), 100. arXiv:1505.07580, doi:10.1088/0004-637X/812/2/100.

[21] Becerra, L., Ellinger, C. L., Fryer, C. L., Rueda, J. A., and Ruffini, R. SPH Simulations of the Induced Gravitational Collapse Scenario of Long Gamma-Ray Bursts Associated with Supernovae. *The Astrophysical Journal*, **871** (2019), 14. arXiv:1803.04356, doi:10.3847/1538-4357/aaf6b3.

[22] Becerra, L., Guzzo, M. M., Rossi-Torres, F., Rueda, J. A., Ruffini, R., and Uribe, J. D. Neutrino Oscillations within the Induced Gravitational Collapse Paradigm of Long Gamma-Ray Bursts. *The Astrophysical Journal*, **852** (2018), 120. arXiv:1712.07210, doi:10.3847/1538-4357/aaa296.

[23] Berger, E., Fong, W., and Chornock, R. An r-process Kilonova Associated with the Short-hard GRB 130603B. *The Astrophysical Journal Letters*, **774** (2013), L23. arXiv:1306.3960, doi:10.1088/2041-8205/774/2/L23.

[24] Bianco, C. L., Ruffini, R., and Xue, S. S. The elementary spike produced by a pure e^+e^- pair-electromagnetic pulse from a Black Hole: The PEM Pulse. *A&A*, **368** (2001), 377. arXiv:astro-ph/0102060, doi:10.1051/0004-6361:20000556.

[25] Blattnig, S. R., Swaminathan, S. R., Kruger, A. T., Ngom, M., and Norbury, J. W. Parametrizations of inclusive cross sections for pion production in proton-proton collisions. *Phys. Rev. D*, **62** (2000), 094030. Available from: https://link.aps.org/doi/10.1103/PhysRevD.62.094030, doi:10.1103/PhysRevD.62.094030.

[26] Burrows, D., Garmire, G., Ricker, G., Bautz, M., Nousek, J., Grupe, D., and Racusin, J. Chandra Searches for Late-Time Jet Breaks in GRB X-ray Afterglows. In *Chandra's First Decade of Discovery* (edited by S. Wolk, A. Fruscione, and D. Swartz) (2009).

[27] Caito, L., Bernardini, M. G., Bianco, C. L., Dainotti, M. G., Guida, R., and Ruffini, R. Grb060614: a "fake" short grb from a merging binary system. *Astronomy & Astrophysics*, **498** (2009), 501.

[28] Christodoulou, D. and Ruffini, R. Reversible transformations of a charged black hole. *Physical Review D*, **4** (1971), 3552.

[29] Cipolletta, F., Cherubini, C., Filippi, S., Rueda, J. A., and Ruffini, R. Fast rotating neutron stars with realistic nuclear matter equation of state. *Physical Review D*, **92** (2015), 023007. arXiv:1506.05926, doi:10.1103/PhysRevD.92.023007.

[30] Cipolletta, F., Cherubini, C., Filippi, S., Rueda, J. A., and Ruffini, R. Last stable orbit around rapidly rotating neutron stars. *Physical Review D*, **96** (2017), 024046. arXiv:1612.02207, doi:10.1103/PhysRevD.96.024046.

[31] Collaboration, I. et al. Multimessenger observations of a flaring blazar coincident with high-energy neutrino icecube-170922a. *Science*, **361** (2018), eaat1378.

[32] Connolly, A., Thorne, R. S., and Waters, D. Calculation of high energy neutrino-nucleon cross sections and uncertainties using the martin-stirling-thorne-watt parton distribution functions and implications for future experiments. *Physical Review D*, **83** (2011), 113009.

[33] Coulter, D., et al. Swope supernova survey 2017a (sss17a), the optical counterpart to a gravitational wave source. *Science*, **358** (2017), 1556.

[34] Covino, S., Malesani, D., Tagliaferri, G., Vergani, S. D., Chincarini, G., Kann, D. A., Moretti, A., Stella, L., and Mistici Collaboration. Achromatic breaks for Swift GRBs: Any evidence? *Nuovo Cimento B Serie*, **121** (2006), 1171. arXiv:astro-ph/0612643, doi:10.1393/ncb/i2007-10239-4.

[35] Cowperthwaite, P., et al. The electromagnetic counterpart of the binary neutron star merger ligo/virgo gw170817. ii. uv, optical, and near-infrared light curves and comparison to kilonova models. *The Astrophysical Journal Letters*, **848** (2017), L17.

[36] Damour, T. and Ruffini, R. Quantum electrodynamical effects in kerr-newmann geometries. *Physical Review Letters*, **35** (1975), 463.

[37] Danzmann, K., Team, L. S., et al. Lisa: laser interferometer space antenna for gravitational wave measurements. *Classical and Quantum Gravity*, **13** (1996), A247.

[38] Daugherty, J. and Lerche, I. On pair production in intense electromagnetic fields occurring in astrophysical situations. *Astrophysics and Space Science*, **38** (1975), 437.

[39] Daugherty, J. and Lerche, I. Theory of pair production in strong electric and magnetic fields and its applicability to pulsars. *Physical Review D*, **14** (1976), 340.

[40] Daugherty, J. K. and Harding, A. Pair production in superstrong magntic fields. *ApJ 761-773,1983*, (1983).

[41] Della Valle, M., et al. An enigmatic long-lasting γ-ray burst not accompanied by a bright supernova. *Nature*, **444** (2006), 1050. arXiv:arXiv:astro-ph/0608322, doi:10.1038/nature05374.

[42] Dominik, M., Belczynski, K., Fryer, C., Holz, D. E., Berti, E., Bulik, T., Mandel, I., and O'Shaughnessy, R. Double Compact Objects. I. The Significance of the Common Envelope on Merger Rates. *The Astrophysical Journal*, **759** (2012), 52. arXiv:1202.4901, doi:10.1088/0004-637X/759/1/52.

[43] Fedotov, A., Narozhny, N., Mourou, G., and Korn, G. Limitations on the attainable intensity of high power lasers. *Physical review letters*, **105** (2010), 080402.

[44] Fishman, G. J., Meegan, C. A., Parnell, T. A., Wilson, R. B., Paciesas, W., Mateson, J. L., Cline, T. L., and Teegarden, B. J. Burst and Transient Source Experiment (BATSE) for the Gamma Ray Observatory (GRO). *International Cosmic Ray Conference*, **3** (1985).

[45] Fletcher, R. S., Gaisser, T. K., Lipari, P., and Stanev, T. sibyll: An event generator for simulation of high energy cosmic ray cascades. *Phys. Rev. D*, **50** (1994), 5710. Available from: https://link.aps.org/doi/10.1103/PhysRevD.50.5710, doi:10.1103/PhysRevD.50.5710.

[46] Fryer, C., Benz, W., Herant, M., and Colgate, S. A. What Can the Accretion-induced Collapse of White Dwarfs Really Explain? *The Astrophysical Journal*, **516** (1999), 892. arXiv:astro-ph/9812058, doi:10.1086/307119.

[47] Fryer, C. L. Neutrinos from Fallback onto Newly Formed Neutron Stars. *The Astrophysical Journal*, **699** (2009), 409. arXiv:0711.0551, doi:10.1088/0004-637X/699/1/409.

[48] Fryer, C. L. Neutrinos from fallback onto newly formed neutron stars. *The Astrophysical Journal*, **699** (2009), 409.

[49] Fryer, C. L., Benz, W., and Herant, M. The Dynamics and Outcomes of Rapid Infall onto Neutron Stars. *The Astrophysical Journal*, **460** (1996), 801. arXiv:astro-ph/9509144, doi:10.1086/177011.

[50] Fryer, C. L., Herwig, F., Hungerford, A., and Timmes, F. X. Supernova Fallback: A Possible Site for the r-Process. *The Astrophysical Journal Letters*, **646** (2006), L131. arXiv:astro-ph/0606450, doi:10.1086/507071.

[51] Fryer, C. L., Oliveira, F. G., Rueda, J. A., and Ruffini, R. Neutron-Star-Black-Hole Binaries Produced by Binary-Driven Hypernovae. *Physical Review Letters*, **115** (2015), 231102. arXiv:1505.02809, doi:10.1103/PhysRevLett.115.231102.

[52] Fryer, C. L., Rueda, J. A., and Ruffini, R. Hypercritical Accretion, Induced Gravitational Collapse, and Binary-Driven Hypernovae. *The Astrophysical Journal Letters*, **793** (2014), L36. arXiv:1409.1473, doi:10.1088/2041-8205/793/2/L36.

[53] Fryer, C. L., Woosley, S. E., and Hartmann, D. H. Formation Rates of Black Hole Accretion Disk Gamma-Ray Bursts. *The Astrophysical Journal*, **526** (1999), 152. arXiv:astro-ph/9904122, doi:10.1086/307992.

[54] Gaisser, T. K., Engel, R., and Resconi, E. *Cosmic rays and particle physics*. Cambridge University Press (2016).

[55] Gehrels, N., Kniffen, D. A., and Ormes, J. F. The Compton Gamma Ray Observatory. In *Current Topics in Astrofundamental Physics* (edited by N. Sanchez and A. Zichichi) (1992).

[56] Goldstein, A., et al. The Fermi GBM Gamma-Ray Burst Spectral Catalog: The First Two Years. *The Astrophysical Journal Supplement Series*, **199** (2012), 19. arXiv:1201.2981, doi:10.1088/0067-0049/199/1/19.

[57] Goldstein, A., et al. An ordinary short gamma-ray burst with extraordinary implications: Fermi-gbm detection of grb 170817a. *The Astrophysical Journal Letters*, **848** (2017), L14.

[58] Guetta, D. and Della Valle, M. On the Rates of Gamma-Ray Bursts and Type Ib/c Supernovae. *The Astrophysical Journal Letters*, **657** (2007), L73. arXiv:astro-ph/0612194, doi:10.1086/511417.

[59] Harding, A. K., Tademaru, E., and Esposito, L. A curvature-radiation-pair-production model for gamma-ray pulsars. *The Astrophysical Journal*, **225** (1978), 226.

[60] Hayato, Y. A neutrino interaction simulation program library neut. *Acta Phys. Polon.*, **40** (2009), 2477.

[61] Hyper-kamiokande official website. http://www.hyperk.org/?page_id=59.

[62] Izzo, L., Rueda, J. A., and Ruffini, R. GRB 090618: a candidate for a neutron star gravitational collapse onto a black hole induced by a type Ib/c supernova. *A&A*, **548** (2012), L5. arXiv:1206.2887, doi:10.1051/0004-6361/201219813.

[63] Izzo, L., Ruffini, R., Penacchioni, A. V., Bianco, C. L., Caito, L., Chakrabarti, S. K., Rueda, J. A., Nandi, A., and Patricelli, B. A double component in GRB 090618: a proto-black hole and a genuinely long gamma-ray burst. *Astronomy & Astrophysics*, **543** (2012), A10. arXiv:1202.4374, doi:10.1051/0004-6361/201117436.

[64] Izzo, L., Ruffini, R., Penacchioni, A. V., Bianco, C. L., Caito, L., Chakrabarti, S. K., Rueda, J. A., Nandi, A., and Patricelli, B. A double component in GRB 090618: a proto-black hole and a genuinely long gamma-ray burst. *A&A*, **543** (2012), A10. arXiv:1202.4374, doi:10.1051/0004-6361/201117436.

[65] Jackson, J. D. Classical electrodynamics (1999).

[66] Joseph, J. and Rohrlich, F. Pair production and bremsstrahlung in the field of free and bound electrons. *Reviews of Modern Physics*, **30** (1958), 354.

[67] Kalmykov, N., Ostapchenko, S., and Pavlov, A. Quark-gluon-string model and eas simulation problems at ultra-high energies. *Nuclear Physics B - Proceedings Supplements*, **52** (1997), 17 . Available from: http://www.sciencedirect.com/science/article/pii/S0920563296008468, doi:https://doi.org/10.1016/S0920-5632(96)00846-8.

[68] Kaneko, Y., Preece, R. D., Briggs, M. S., Paciesas, W. S., Meegan, C. A., and Band, D. L. The Complete Spectral Catalog of Bright BATSE Gamma-Ray Bursts. *The Astrophysical Journal Supplement Series*, **166** (2006), 298. arXiv:astro-ph/0601188, doi:10.1086/505911.

[69] Kelner, S. and Aharonian, F. Energy spectra of gamma rays, electrons, and neutrinos produced at interactions of relativistic protons with low energy radiation. *Physical Review D*, **78** (2008), 034013.

[70] Kelner, S. R., Aharonian, F. A., and Bugayov, V. V. Energy spectra of gamma rays, electrons, and neutrinos produced at proton-proton interactions in the very high energy regime. *Phys. Rev. D*, **74** (2006), 034018. Available from: https://link.aps.org/doi/10.1103/PhysRevD.74.034018, doi:10.1103/PhysRevD.74.034018.

[71] Kelner, S. R., Prosekin, A. Y., and Aharonian, F. A. Synchro-curvature radiation of charged particles in the strong curved magnetic fields. *The Astronomical Journal*, **149** (2015), 33.

[72] Kerr, R. P. Gravitational field of a spinning mass as an example of algebraically special metrics. *Physical review letters*, **11** (1963), 237.

[73] Klebesadel, R. W., Strong, I. B., and Olson, R. A. Observations of Gamma-Ray Bursts of Cosmic Origin. *The Astrophysical Journal Letters*, **182** (1973), L85. doi:10.1086/181225.

[74] Landau, L. D. and Lifshitz, E. M. The classical theory of fields. (1971).

[75] Landau, L. D. and Lifshitz, E. M. *The classical theory of fields* (1975).

[76] Lazzati, D. Precursor activity in bright, long BATSE gamma-ray bursts. *Monthly Notices of the Royal Astronomical Society*, **357** (2005), 722. arXiv:astro-ph/0411753, doi:10.1111/j.1365-2966.2005.08687.x.

[77] Li, L.-X. and Paczyński, B. Transient Events from Neutron Star Mergers. *The Astrophysical Journal Letters*, **507** (1998), L59. arXiv:astro-ph/9807272, doi:10.1086/311680.

[78] Lipari, P. Lepton spectra in the earth's atmosphere. *Astroparticle Physics*, **1** (1993), 195 . Available from: http://www.sciencedirect.com/science/article/pii/0927650593900226, doi:https://doi.org/10.1016/0927-6505(93)90022-6.

[79] Maoz, D. and Hallakoun, N. The binary fraction, separation distribution, and merger rate of white dwarfs from SPY. *Monthly Notices of the Royal Astronomical Society*, **467** (2017), 1414. arXiv:1609.02156, doi:10.1093/mnras/stx102.

[80] Maoz, D., Hallakoun, N., and Badenes, C. The separation distribution and merger rate of double white dwarfs: improved constraints. *Monthly Notices of the Royal Astronomical Society*, **476** (2018), 2584. arXiv:1801.04275, doi:10.1093/mnras/sty339.

[81] Mazets, E. P., et al. Catalog of cosmic gamma-ray bursts from the KONUS experiment data. Part I and II. *Astrophysics and Space Science*, **80** (1981), 3. doi:10.1007/BF00649140.

[82] Melon Fuksman, J. D. and Mignone, A. A Radiative Transfer Module for Relativistic Magnetohydrodynamics in the PLUTO Code. *The Astrophysical Supplement Series*, **242** (2019), 20. arXiv:1903.10456, doi:10.3847/1538-4365/ab18ff.

[83] Meszaros, P., Laguna, P., and Rees, M. J. Gasdynamics of relativistically expanding gamma-ray burst sources - Kinematics, energetics, magnetic fields, and efficiency. *The Astrophysical Journal*, **415** (1993), 181. arXiv:astro-ph/9301007, doi:10.1086/173154.

[84] Mészáros, P. and Rees, M. J. Multi-gev neutrinos from internal dissipation in gamma-ray burst fireballs. *The Astrophysical Journal Letters*, **541** (2000), L5.

[85] Metzger, B. D., et al. Electromagnetic counterparts of compact object mergers powered by the radioactive decay of r-process nuclei. *Monthly Notices of the Royal Astronomical Society*, **406** (2010), 2650. arXiv:1001.5029, doi:10.1111/j.1365-2966.2010.16864.x.

[86] Mignone, A., Zanni, C., Tzeferacos, P., Van Straalen, B., Colella, P., and Bodo, G. The pluto code for adaptive mesh computations in astrophysical fluid dynamics. *The Astrophysical Journal Supplement Series*, **198** (2011), 7.

[87] Muccino, M., Ruffini, R., Bianco, C. L., Izzo, L., and Penacchioni, A. V. GRB 090227B: The Missing Link between the Genuine Short and Long Gamma-Ray Bursts. *The Astrophysical Journal*, **763** (2013), 125. arXiv:1205.6600, doi:10.1088/0004-637X/763/2/125.

[88] Muccino, M., Ruffini, R., Bianco, C. L., Izzo, L., and Penacchioni, A. V. GRB 090227B: The Missing Link between the Genuine Short and Long Gamma-Ray Bursts. *The Astrophysical Journal*, **763** (2013), 125. arXiv:1205.6600, doi:10.1088/0004-637X/763/2/125.

[89] Newman, E. T., Couch, E., Chinnapared, K., Exton, A., Prakash, A., and Torrence, R. Metric of a rotating, charged mass. *Journal of mathematical physics*, **6** (1965), 918.

[90] Nicholl, M., et al. The electromagnetic counterpart of the binary neutron star merger ligo/virgo gw170817. iii. optical and uv spectra of a blue kilonova from fast polar ejecta. *The Astrophysical Journal Letters*, **848** (2017), L18.

[91] Nordstrom, G. On the energy of gravitation field in einstein's theory. *Proc. Ned. Ac. Wet.*, **20** (1918), 1238.

[92] Page, K. L., et al. GRB 090618: detection of thermal X-ray emission from a bright gamma-ray burst. *Monthly Notices of the Royal Astronomical Society*, **416** (2011), 2078. doi:10.1111/j.1365-2966.2011.19183.x.

[93] Patricelli, B., Bernardini, M. G., Bianco, C. L., Caito, L., de Barros, G., Izzo, L., Ruffini, R., and Vereshchagin, G. V. Analysis of GRB 080319B and GRB 050904 within the Fireshell Model: Evidence for a Broader Spectral Energy Distribution. *The Astrophysical Journal*, **756** (2012), 16. arXiv:1206.5605, doi:10.1088/0004-637X/756/1/16.

[94] Patricelli, B., Bernardini, M. G., Bianco, C. L., Caito, L., de Barros, G., Izzo, L., Ruffini, R., and Vereshchagin, G. V. Analysis of GRB 080319B and GRB 050904 within the Fireshell Model: Evidence for a Broader Spectral Energy Distribution. *The Astrophysical Journal*, **756** (2012), 16. arXiv:1206.5605, doi:10.1088/0004-637X/756/1/16.

[95] Penacchioni, A. V., Ruffini, R., Bianco, C. L., Izzo, L., Muccino, M., Pisani, G. B., and Rueda, J. A. GRB 110709B in the induced gravitational collapse paradigm. *Astronomy & Astrophysics*, **551** (2013), A133. arXiv:1301.6014, doi:10.1051/0004-6361/201220679.

[96] Penacchioni, A. V., Ruffini, R., Izzo, L., Muccino, M., Bianco, C. L., Caito, L., Patricelli, B., and Amati, L. Evidence for a proto-black hole and a double astrophysical component in GRB 101023. *Astronomy & Astrophysics*, **538** (2012), A58. arXiv:1112.2970, doi:10.1051/0004-6361/201118403.

[97] Penacchioni, A. V., Ruffini, R., Izzo, L., Muccino, M., Bianco, C. L., Caito, L., Patricelli, B., and Amati, L. Evidence for a proto-black hole and a double astrophysical component in GRB 101023. *A&A*, **538** (2012), A58. doi:10.1051/0004-6361/201118403.

[98] Piran, T., Shemi, A., and Narayan, R. Hydrodynamics of Relativistic Fireballs. *Monthly Notices of the Royal Astronomical Society*, **263** (1993), 861. arXiv:astro-ph/9301004, doi:10.1093/mnras/263.4.861.

[99] Postnov, K. A. and Yungelson, L. R. The Evolution of Compact Binary Star Systems. *Living Reviews in Relativity*, **17** (2014), 3. arXiv:1403.4754, doi:10.12942/lrr-2014-3.

[100] Preparata, G., Ruffini, R., and Xue, S.-S. The dyadosphere of black holes and gamma-ray bursts. *arXiv preprint astro-ph/9810182*, (1998).

[101] Preparata, G., Ruffini, R., and Xue, S.-S. The dyadosphere of black holes and gamma-ray bursts. *A&A*, **338** (1998), L87. arXiv:astro-ph/9810182.

[102] Rees, M., Ruffini, R., and Wheeler, J. A. Black holes, gravitational waves, and cosmology: an introduction to current research. *bhgw*, (1974).

[103] Reissner, H. Über die eigengravitation des elektrischen feldes nach der einsteinschen theorie. *Annalen der Physik*, **355** (1916), 106.

[104] Rodríguez, J., Rueda, J., and Ruffini, R. Strong-field gravitational-wave emission in schwarzschild and kerr geometries: some general considerations. In *EPJ Web of Conferences*, vol. 168, p. 02006. EDP Sciences (2018).

[105] Rueda, J. and Ruffini, R. The blackholic quantum. *European Physical Journal C*, **80** (2020), 1.

[106] Rueda, J., Ruffini, R., Wang, Y., Bianco, C., Blanco-Iglesias, J., Karlica, M., Lorén-Aguilar, P., Moradi, R., and Sahakyan, N. Electromagnetic emission of white dwarf binary mergers. *Journal of Cosmology and Astroparticle Physics*, **2019** (2019), 044.

[107] Rueda, J., et al. The binary progenitors of short and long grbs and their gravitational-wave emission. In *EPJ Web of Conferences*, vol. 168, p. 01006. EDP Sciences (2018).

[108] Rueda, J., et al. Grb 170817a-gw170817-at 2017gfo and the observations of ns-ns, ns-wd and wd-wd mergers. *Journal of Cosmology and Astroparticle Physics*, **2018** (2018), 006.

[109] Rueda, J. A. and Ruffini, R. On the Induced Gravitational Collapse of a Neutron Star to a Black Hole by a Type Ib/c Supernova. *The Astrophysical Journal Letters*, **758** (2012), L7. arXiv:1206.1684, doi:10.1088/2041-8205/758/1/L7.

[110] Rueda, J. A., Ruffini, R., and Wang, Y. Induced Gravitational Collapse, Binary-Driven Hypernovae, Long Gamma-ray Bursts and Their Connection with Short Gamma-ray Bursts. *Universe*, **5** (2019), 110. arXiv:1905.06050, doi:10.3390/universe5050110.

[111] Rueda, J. A., et al. GRB 170817A-GW170817-AT 2017gfo and the observations of NS-NS, NS-WD and WD-WD mergers. *Journal of Cosmology and Astroparticle Physics*, **10** (2018), 006. arXiv:1802.10027, doi:10.1088/1475-7516/2018/10/006.

[112] Ruffini, R. Beyond the critical mass: The dyadosphere of black holes. In *Frontiers Science Series 23: Black Holes and High Energy Astrophysics*, vol. 23, p. 167 (1998).

[113] Ruffini, R. Fundamental Physics from Black Holes, Neutron Stars and Gamma-Ray Bursts. *International Journal of Modern Physics D*, **20** (2011), 1797. arXiv:1107.0862, doi:10.1142/S0218271811019876.

[114] Ruffini, R., Bianco, C. L., Fraschetti, F., Xue, S.-S., and Chardonnet, P. On a Possible Gamma-Ray Burst-Supernova Time Sequence. *The Astrophysical Journal Letters*, **555** (2001), L117. doi:10.1086/323177.

[115] Ruffini, R., Bianco, C. L., Fraschetti, F., Xue, S.-S., and Chardonnet, P. On the interpretation of the burst structure of gamma-ray bursts. *The Astrophysical Journal Letters*, **555** (2001), L113.

[116] Ruffini, R., Bianco, C. L., Fraschetti, F., Xue, S.-S., and Chardonnet, P. Relative spacetime transformations in gamma-ray bursts. *The Astrophysical Journal Letters*, **555** (2001), L107.

[117] Ruffini, R., Karlica, M., Sahakyan, N., Rueda, J. A., Wang, Y., Mathews, G. J., Bianco, C. L., and Muccino, M. A GRB Afterglow Model Consistent with Hypernova Observations. *The Astrophysical Journal*, **869** (2018), 101. arXiv:1712.05000, doi:10.3847/1538-4357/aaeac8.

[118] Ruffini, R., Melon Fuksman, J. D., and Vereshchagin, G. V. On the Role of a Cavity in the Hypernova Ejecta of GRB 190114C. *The Astrophysical Journal*, **883** (2019), 191. doi:10.3847/1538-4357/ab3c51.

[119] Ruffini, R., Salmonson, J. D., Wilson, J. R., and Xue, S.-S. On evolution of the pair-electromagnetic pulse of a charged black hole. *Astronomy and Astrophysics Supplement*, **138** (1999), 511.

[120] Ruffini, R., Salmonson, J. D., Wilson, J. R., and Xue, S.-S. On the pair electromagnetic pulse of a black hole with electromagnetic structure. *arXiv preprint astro-ph/9907030*, (1999).

[121] Ruffini, R., Salmonson, J. D., Wilson, J. R., and Xue, S.-S. On the pair-electromagnetic pulse from an electromagnetic black hole surrounded by a baryonic remnant. *A&A*, **359** (2000), 855. arXiv:astro-ph/0004257.

[122] Ruffini, R., Vereshchagin, G., and Xue, S. Electron-positron pairs in physics and astrophysics: From heavy nuclei to black holes. , **487** (2010), 1. arXiv:0910.0974, doi:10.1016/j.physrep.2009.10.004.

[123] Ruffini, R., Wang, Y., Enderli, M., Muccino, M., Kovacevic, M., Bianco, C. L., Penacchioni, A. V., Pisani, G. B., and Rueda, J. A. GRB 130427A and SN 2013cq: A Multi-wavelength Analysis of An Induced Gravitational Collapse Event. *The Astrophysical Journal*, **798** (2015), 10. arXiv:1405.5723, doi:10.1088/0004-637X/798/1/10.

[124] Ruffini, R., et al. On Gamma-Ray Bursts. In *The Eleventh Marcel Grossmann Meeting On Recent Developments in Theoretical and Experimental General Relativity, Gravitation and Relativistic Field Theories* (edited by H. Kleinert, R. T. Jantzen, and R. Ruffini), pp. 368–505 (2008). arXiv:0804.2837, doi:10.1142/9789812834300_0019.

[125] Ruffini, R., et al. On binary-driven hypernovae and their nested late X-ray emission. *A&A*, **565** (2014), L10. arXiv:1404.3946, doi:10.1051/0004-6361/201423812.

[126] Ruffini, R., et al. GRB 140619B: a short GRB from a binary neutron star merger leading to black hole formation. *The Astrophysical Journal*, **808** (2015), 190. arXiv:1412.1018, doi:10.1088/0004-637X/808/2/190.

[127] Ruffini, R., et al. GRB 090510: A Genuine Short GRB from a Binary Neutron Star Coalescing into a Kerr-Newman Black Hole. *The Astrophysical Journal*, **831** (2016), 178. arXiv:1607.02400, doi:10.3847/0004-637X/831/2/178.

[128] Ruffini, R., et al. On the classification of grbs and their occurrence rates. *The Astrophysical Journal*, **832** (2016), 136.

[129] Ruffini, R., et al. Early x-ray flares in grbs. *The Astrophysical Journal*, **852** (2018), 53. Available from: http://stacks.iop.org/0004-637X/852/i=1/a=53.

[130] Ruffini, R., et al. The inner engine of gev-radiation-emitting gamma-ray bursts. *arXiv preprint arXiv:1811.01839*, (2018).

[131] Ruffini, R., et al. On the Rate and on the Gravitational Wave Emission of Short and Long GRBs. *The Astrophysical Journal*, **859** (2018), 30. doi:10.3847/1538-4357/aabee4.

[132] Ruffini, R., et al. On the rate and on the gravitational wave emission of short and long grbs. *The Astrophysical Journal*, **859** (2018), 30.

[133] Ruffini, R., et al. On the role of the kerr-newman black hole in the gev emission of long gamma-ray bursts. *arXiv preprint arXiv:1803.05476*, (2018).

[134] Ruffini, R., et al. On the Ultra-relativistic Prompt Emission, the Hard and Soft X-Ray Flares, and the Extended Thermal Emission in GRB 151027A. *The Astrophysical Journal*, **869** (2018), 151. arXiv:1712.05001, doi:10.3847/1538-4357/aaee68.

[135] Ruffini, R., et al. The inner engine of GeV-radiation-emitting gamma-ray bursts. *arXiv e-prints*, (2018). arXiv:1811.01839.

[136] Ruffini, R., et al. On the gev emission of the type i bdhn grb 130427a. *The Astrophysical Journal*, **886** (2019), 82.

[137] Ruffini, R., et al. Self-similarity and power-laws in GRB 190114C. *arXiv e-prints*, (2019). arXiv:1904.04162.

[138] Rybicki, G. and Lightman, A. Book-review-radiative processes in astrophysics. *AstQ*, **3** (1979), 199.

[139] Ryde, F. Is Thermal Emission in Gamma-Ray Bursts Ubiquitous? *The Astrophysical Journal Letters*, **625** (2005), L95. arXiv:astro-ph/0504450, doi:10.1086/431239.

[140] Ryde, F. and Pe'er, A. Quasi-blackbody Component and Radiative Efficiency of the Prompt Emission of Gamma-ray Bursts. *The Astrophysical Journal*, **702** (2009), 1211. arXiv:0811.4135, doi:10.1088/0004-637X/702/2/1211.

[141] Sato, G., et al. Swift Discovery of Gamma-Ray Bursts without a Jet Break Feature in Their X-Ray Afterglows. *The Astrophysical Journal*, **657** (2007), 359. arXiv:astro-ph/0611148, doi:10.1086/510610.

[142] Shemi, A. and Piran, T. The appearance of cosmic fireballs. *The Astrophysical Journal Letters*, **365** (1990), L55. doi:10.1086/185887.

[143] Super-kamiokande official website. http://www-sk.icrr.u-tokyo.ac.jp/sk/index-e.html.

[144] Smartt, S. J. Progenitors of Core-Collapse Supernovae. *Annual Review of Astronomy and Astrophysics*, **47** (2009), 63. arXiv:0908.0700, doi:10.1146/annurev-astro-082708-101737.

[145] Smartt, S. J. Observational Constraints on the Progenitors of Core-Collapse Supernovae: The Case for Missing High-Mass Stars. *Publications of the Astronomical Society of Australia*, **32** (2015), e016. arXiv:1504.02635, doi:10.1017/pasa.2015.17.

[146] Solares, H., et al. Multimessenger gamma-ray and neutrino coincidence alerts using hawc and icecube sub-threshold data. *arXiv preprint arXiv:2008.10616*, (2020).

[147] Sturrock, P. A model of pulsars. *The Astrophysical Journal*, **164** (1971), 529.

[148] Tanvir, N. R., Levan, A. J., Fruchter, A. S., Hjorth, J., Hounsell, R. A., Wiersema, K., and Tunnicliffe, R. L. A 'kilonova' associated with the short-duration γ-ray burst GRB 130603B. *Nature*, **500** (2013), 547. arXiv:1306.4971, doi:10.1038/nature12505.

[149] Tauris, T. M., Langer, N., Moriya, T. J., Podsiadlowski, P., Yoon, S.-C., and Blinnikov, S. I. Ultra-stripped Type Ic Supernovae from Close Binary Evolution. *The Astrophysical Journal Letters*, **778** (2013), L23. arXiv:1310.6356, doi:10.1088/2041-8205/778/2/L23.

[150] Tauris, T. M., Langer, N., and Podsiadlowski, P. Ultra-stripped supernovae: progenitors and fate. *Monthly Notices of the Royal Astronomical Society*, **451** (2015), 2123. arXiv:1505.00270, doi:10.1093/mnras/stv990.

[151] Tursunov, A., Stuchlík, Z., Kološ, M., Dadhich, N., and Ahmedov, B. Supermassive Black Holes as Possible Sources of Ultrahigh-energy Cosmic Rays. *The Astrophysical Journal*, **895** (2020), 14. arXiv:2004.07907, doi:10.3847/1538-4357/ab8ae9.

[152] Wald, R. M. Black hole in a uniform magnetic field. *Physical Review D*, **10** (1974), 1680. doi:10.1103/PhysRevD.10.1680.

[153] Wang, Y., Rueda, J. A., Ruffini, R., Becerra, L., Bianco, C., Becerra, L., Li, L., and Karlica, M. Two Predictions of Supernova: GRB 130427A/SN 2013cq and GRB 180728A/SN 2018fip. *The Astrophysical Journal*, **874** (2019), 39. arXiv:1811.05433, doi:10.3847/1538-4357/ab04f8.

[154] Wang, Y., Ruffini, R., Kovacevic, M., Bianco, C. L., Enderli, M., Muccino, M., Penacchioni, A. V., Pisani, G. B., and Rueda, J. A. Predicting supernova associated to gamma-ray burst 130427a. *Astronomy Reports*, **59** (2015), 667. doi:10.1134/S1063772915070148.

[155] Waxman, E. and Bahcall, J. High energy neutrinos from cosmological gamma-ray burst fireballs. *Physical Review Letters*, **78** (1997), 2292.

[156] Waxman, E. and Bahcall, J. High energy neutrinos from astrophysical sources: An upper bound. *Physical Review D*, **59** (1998), 023002.

[157] Waxman, E. and Bahcall, J. N. Neutrino afterglow from gamma-ray bursts:˜ 1018 ev. *The Astrophysical Journal*, **541** (2000), 707.

[158] Yakovlev, D. G., Kaminker, A. D., Gnedin, O. Y., and Haensel, P. Neutrino emission from neutron stars. , **354** (2001), 1. arXiv:astro-ph/0012122, doi:10.1016/S0370-1573(00)00131-9.

[159] Zhang, B. *The Physics of Gamma-Ray Bursts* (2018). doi:10.1017/9781139226530.